Computational studies of vascularized tumors

DISSERTATION

zur Erlangung des Grades des Doktors der Naturwissenschaften der
Naturwissenschaftlich-Technischen Fakultät der
Universität des Saarlandes

von

Thierry Fredrich

Saarbrücken
2019

Tag des Kolloquiums: 11. November 2020

Dekan: Univ.- Prof. Dr. Jörn Walter

Vorsitzender des
Prüfungsausschusses: Univ.- Prof. Dr. Romanus Dyczij-Edlinger

Berichterstatter:

Univ.- Prof. Dr. Dr. h.c. Heiko Rieger
Univ.- Prof. Dr. Ludger Santen

Akademischer Beisitzer: Dr. Christian Spengler

"In theory, there is no difference between theory and practice. In practice there is."

— quoted from Yogi Berra

Preface

During my PhD studies, I contributed to four original research articles ([1, 2, 3, 4]), one review ([5]) and one book (not yet published, December 2019). Being first author of three publications ([2, 3, 4]) and second author of one publication ([1]) satisfies the requirements for a cumulative dissertation stated by Saarland University (copy of the valid version of the regulations at time of submission is reprinted in the appendix on page 199 of this dissertation).

In the first chapter of my dissertation "State of the Art", I provide an introduction to the field of computational tumor modeling. In the second chapter "Own work", I elaborate on the relevant original publications reprinted in the third chapter "Original publications" and finish the third chapter with a "Summary and Discussion" section. In the last chapter, I provide the "Demarcation from the coauthors" for the reprinted original publications.

Contents

Chapter 1

State of the Art

Tumor growth is a complicated and delicate issue touching all fields of life sciences — and beyond. Starting with pure mathematical and theoretical models over all kinds of biology up to the clinical routine, all collective efforts feature a common goal: try to understand, predict and eventually handle cancer.

In this first chapter of my dissertation, I provide background knowledge from biology (section 1.1 "Cancer Biology") and computational modeling (section 1.2 "Computer simulations in cancer research") enabling the reader to follow the original research reported in chapter 3 "Computer simulations in cancer research". In section 1.3 "Sparse matrices", I highlight the importance of sparse matrices in computational modeling and numerics before I end this introductory chapter with a personal reflection about state of the art "Model, Code and Data sharing" in section 1.4.

For a comprehensive overview on the broad field of cancer research, the interested reader is referred to the cited resources.

Contents

1.1 Cancer Biology

The notion *cancer* is very general and usually the notion refers to cells or an agglomeration of cells (tissue) fulfilling the following characteristics [6, 7]:

- Cell growth and division absent the proper signals,

- Continuous growth and division even given contrary signals,

- Avoidance of programmed cell death,

- Limitless number of cell divisions,

- Promoting blood vessel construction,

- Invasion of tissue and formation of metastases.

The progression from normal cells to cells forming a detectable mass (a tumor) to outright cancer involves multiple steps known as malignant progression [6, 7]. During the progression, the tumors usually affect different types of cells advising of the tumors names: sarcomas develop from mesenchymal tissue, or connective tissue, carcinomas develop from epithelial cells and lymphoma develop from lymphocytes. Malignant progression, however, does not always result in solid tumors. For example, in Leukemias [8, 9, 10] (cancers of the blood) the malignant progression affects the blood cells. In my dissertation, I restrict the discussion to solid tumors.

1.1.1 Cells

Cells are the basic units of all living organisms. The prokaryotic cells in simpler organisms (like bacteria) feature a simpler structure compared to the more complex structure of eukaryotic cells in animals or humans. The plasma membrane (lipid bilayer) outlines the eukaryote separating the cell from the environment (see section 1.1.2 and section 1.1.3). A typical eukaryotic cell spans from 10 to 100 μm being about 100 times larger than a prokaryotic cell. Aside from the difference in size, the Eukaryote is highly structured compared to the Prokaryote and the Eukaryote contains a nucleus.

The spherical or ovoidal shaped nucleus of an eukaryotic cell spans about 6 μm in diameter centering in the cell surrounded by the cell body or the cytoplasm. The nuclear membrane separates the nucleus from the cytoplasm comprising solid and liquid (cytosol) contributions. The cytosol contains soluble proteins, sugars, salts, etc. and engulfs numerous organelles with well-defined functions (figure 1.1). I discuss four important organelles with their functions [11]:

- **the cytoskeleton** is a complex network of polymeres crossing through the cytosol (figure 1.2) maintaining cell shape and playing an important role in both, intracellular transport and cellular division;

- **the mitochondria** (plural of mitochondrion) are responsible for converting sugar molecules into adenosine triphosphate (ATP) providing the energy to drive biological processes;

- **the endoplasmic reticulum (ER)** extends the nuclear membrane and is involved in the synthesis and sorting of proteins;

- **the Golgi apparatus** is a set of membranes composed of flattened sacs responsible for protein maturation and protein transport by labeling the proteins depending of their cellular or even extracellular destination.

Cells reproduce and the nucleus of an eukaryotic cell contains the genetic information required during the reproduction step. I summarize the essential steps of the reproduction in a simplified cell cycle (depicted in figure 1.3). Numerous checks (not discussed here) precede the evolution from one stage to another ensuring that the cell is ready to enter the next stage [15]. The simplified cell cycle starts in the quiescence state (G_0) where the cell is not actively dividing. Note that most cells (expect some liver, stomach, kidney cancer cells) exit the G_0 stage early and keep actively dividing throughout their entire lifespan. Cells spend about 90% of their entire lifespan taking up nutrients (interphase) in preparation for the replicating division step (mitosis). The interphase happens in three successive steps: Gap 1 (G_1), synthesis (S) and Gap 2 (G_2). First, the stock of proteins and organelles increases during G_1. Second, the deoxyribonucleic acid (DNA) carrying the genetic information duplicates during the synthesis (S) and third, the cell increases in volume during G_2. During the mitotic division, the cell separates the DNA into two nuclei and organizes the duplicated
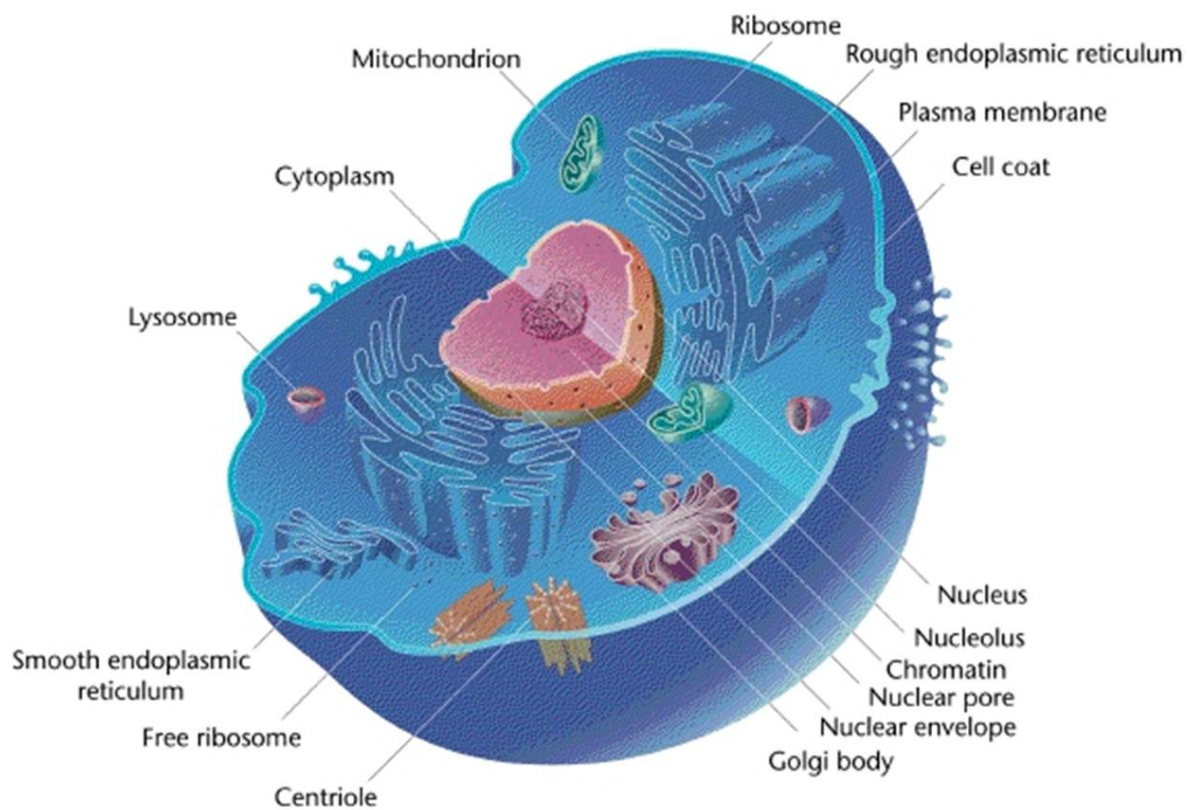
Figure 1.1: A schematic of the typical cell structure of an eukaryotic cell surrounded by the plasma membrane with a nucleus at the center and filled with cytoplasm comprising a Golgi apparatus or Golgi body and a endoplasmic reticulum [12].
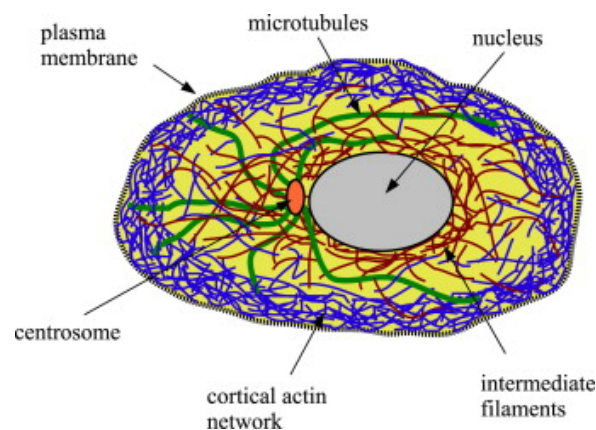
Figure 1.2: A schematic of the typical organisation of the cytoskeletal filaments inside an eukaryotic cell comprising the surrounding plasma membrane next to the cortical actin network, the nucleus in the center, the centrosome or main microtubule organizing center (MTOC) and the intermediate filaments.
Reprinted with permission (section G) from figure 1 of [13]
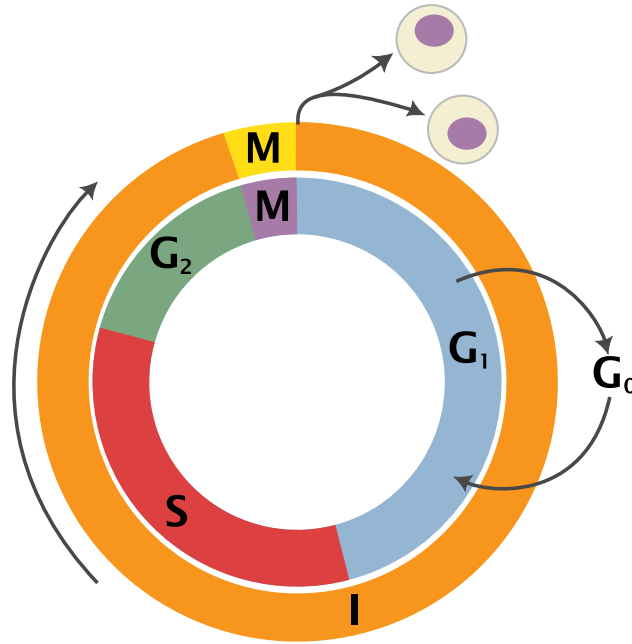
Figure 1.3: Schematic of simplified cell cycle. Outer ring: interphase (I) and mitosis (M); inner ring: mitosis (M), Gap 1 (G_1), synthesis (S), Gap 2 (G_2); not in ring: Gap 0/ resting (G_0) [14]

organelles in preparation for the physical division, which finally separates the mother cell into two daughter cells. Each daughter cell comprises the same structure than the mother and the cell cycle starts from the beginning [11, 16].

Recently, Sakaue-Sawano et al. reported a method to visualize the cell cycle dynamics [17]. Fluorescent ubiquitination-based cell cycle indicator imaging (FUCCI) labels cells in G_1 phase in red, cells in S phase in yellow and cells in G_2 and M phase in green. By using this method, first results obtained in animal models confirm that chemotherapeutant targeting cancer cells in $S/G_2/M$ phase are ineffective in solid tumors which dominantly contain quiescent cells in the G_0 phase [18].

It should be noted that the current understanding of the cell in terms of molecular biology is far more complicated than the description presented in this section. In particular, each molecular process is prone to errors resulting in mutations of the cell and some consider these mutations as the cause of cancer [19].

1.1.2 Tumors and Multicellular Tumor Spheroids (MTS)

Although tumor growth deregulates the interplay between intrinsic cellular programs (section 1.1.1), tumors are multicellular objects. In multicellular objects, the structural support and biochemical interaction between individual cells contributes to the collective behavior. In tissue, the extracellular matrix (ECM) mediates both, the structural support and the biochemical interaction. Although the detailed composition of the ECM varies between different lineages of multicellular objects, the ECM of different multicellular objects features common functions: supporting cell adhesion, cell-to-cell communication and differentiation [20].

While tumors emerge from molecular and genetic abnormalities, their growth always happens embedded in a tumor specific environment. Since tumors enhance cell proliferation, cell motility and cell differentiation, the local microenvironment changes continuously impairing cell death, cell adhesion and the microenvironmental architecture. For example: a hypoxic microenvironment modifies survival, growth and metastatic efficiency of some cancer cells; mechanical stresses in the tumor stroma modify the gene expressions and the cell phenotype; tumors co-opt inflammatory cells, vascular cells and fibroblasts to reset the balance between ECM degradation and ECM biosynthesis. In essence, tumor growth takes place in a highly dynamic landscape developing from a multifactorial environmental response to tumor growth itself.

Cell migration heavily depends on the ECM. In general, the random migration of cells is complemented by guided migration due to chemicals (chemotaxis) and mechanical cues (mechanotaxis) like fluidic shear

Figure 1.4: Schematic cross-section of a multicellular spheroid. Within the spherical shape, a concentric arrangement of large proliferating tumor cells is found in the periphery, while smaller non-proliferating cells concent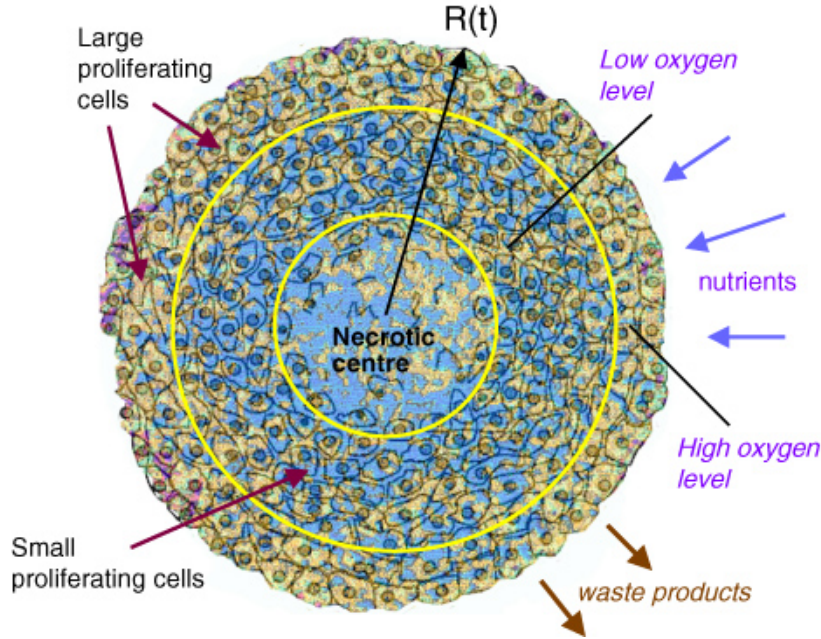rate in deeper regions. Diffusional constraints to oxygen and nutrients supply increase with spheroid size and a central necrotic core emerges as a result of cell death for a characteristic time-dependent spheroid radius $R(t)$. The value of the spheroid radius, which largely depends on the cell type and on cell culture conditions, is one of the main variables considered in MTS growth models.
Reprinted figure 8 of [21] (with permission see appendix G).

stress, substrate stiffness gradients (durotaxis) or cellular adhesion site gradients (haptotaxis). Experimental findings [21] indicate that tumor growth alters the guiding mechanisms and therefore the dynamics of normal and cancer cells is differentially affected.

The ECM provides not only the necessary structural support for cell migration, but is also part of a deformable continuum transmitting chemical signals. The plasma membrane of each cell is a multi-component mechanosensory switch. Since the plasma membrane interlaces with the ECM, mechanical stresses and strains convert into biochemical information influencing the cellular response. To understand the cellular response to mechanical forces in the presents of solid tumor growth requires an understanding of the mechanosensory machinery and the chemical signaling processes.

Although the understanding of single cell processes increases, studying realistic tumor growth is extremely difficult because the dynamically changing microenvironment is an integral part of the problem. For in vivo studies, the resolution of most imaging technique exceeds the cell level and therapy compromises wide-ranging studies. For animal models, the studies match reality closely, but the imaging techniques at cellular resolution require the immolation of individual animals. Therefore, time resolved studies in animal models are subjected to intersubject variability of the microenvironment, however, studying tumor growth demands an identical microenvironment. Experimentally, it is straight forward to investigate the growth process of cells on a homogeneous 2D substrate. Although the genetic information of cultured cells is identical to the genetic information the of cells in real tissue, a homogeneous 2D substrate fails to mimic the complicated characteristics of a 3D tumor microenvironment. To overcome some limitations of 2D substrates, experimentalists developed a technique to culture cells in 3D [22].

Since the first successful growth of in vitro multicellular tumor spheroids (MTSs) in 1971 [23, 24], MTSs became a well established method in cancer research and developed to a main tool in studying tumor growth and drug evaluation in oncology. Today, there are a lot of different techniques to commence the growth of a MTS. All techniques promote the cell-to-cell interaction and suppress interactions with confining walls. We divide the growing concepts in active and passive techniques. The passive techniques involve non-adherent surfaces disabling the adhesive contact and thereby promoting the cell-to-cell interaction inside the conglomerate of cells. The active techniques involve physical forces like surface tension, rotation or flow to prevent the cells from connecting to the walls an thereby also promoting the cell-to-cell interaction. An extensive list of experimental techniques is discussed in [22].

Similar to in vivo tumors, MTSs feature a network of structural and adhesive ECM proteins embedded in a gel. Further, the cell-to-cell and the cell-to-microenvironment interaction, the different cell proliferation rates, the specific gene expressions, and the drug response generate a suitable 3D model system to study not only the tumor growth more realistically, but also to evaluate drugs in a more realistic setting. Large spheroids ($\approx$ 400-500 μm in diameter) display an spherical symmetric layered cell distribution analogous to the observed structure in solid tumors (figure 1.4). The structure mainly results from mass transport limitations interfering with the diffusion of oxygen, nutrients and metabolic wastes through the spheroid creating specific gradients. In the outermost layer, the close contact of the cells to the substrate (agar is a common choice of substrate) provides easier access to oxygen and nutrients resulting in a layer of large actively proliferating cells. For in vivo tumors, this layer corresponds to cells close to the capillaries (section 1.1.3). The access to oxygen and nutrients decreases progressively with increasing distance from the spheroid periphery and, consequently, the cell metabolism decreases resulting in a middle layer of small proliferating cells followed by quiescent cells. At the spheroid center, oxygen depletion (i.e. hypoxia), acidosis and nutrient shortage cause cell necrosis. Since the tumor cell type characterizes the necrotic core, the characteristics at the center vary profoundly. Although the MTS model systems mimic the avascular tumor growth phase nicely, they neglect relevant aspects of the vascular tumor growth phase in real tumorgenesis such as the vascular remodeling, the immune system components and the fluid dynamics. Since spheroids naturally vascularize when implanted into animals, the cell-to-microenvironment interactions must be added into an integral model of tumor growth. However the vascularization of MTSs would be a first step in this direction, literature lacks reports about successful experiments of this type. [21, 22, 25]

1.1.3 Vasculature

As discussed in section 1.1.2, tumors comprise the interaction between cells and their microenvironment. An integral understanding of cancer requires the understanding of the involved interactions. For solid tumors in vivo or in animal models, these interactions include the vasculature.

The vasculature or the circulatory system of every mammalian is a highly optimized biological transport network distributing nutrients (such as amino acids and electrolytes), oxygen, hormones and collecting the metabolic waste (such as carbon dioxide) [27]. The high diffusivity of oxygen in tissue [28] limits the transport of oxygen by diffusion to short distances (100 to 200 μm [29]) although oxygen plays a major role in cell metabolism and energy production. Because of the high importance of oxygen, life requires an efficient oxygen transport method and a homogeneous distribution of oxygen inside tissue. Nature's way of transporting oxygen beyond the diffusion limit in a fast way is remarkably. The natural approach builds upon the vasculature carrying a complex fluid comprising liquid and solid components: the blood. The liquid blood plasma contributes about 55 % to the blood volume and different cells contribute the remaining 45 %. While white blood cells (leukocytes) and platelets (thrombocytes) contribute only little to the cellular volume, the majority of cells in the blood are red blood cells (RBCs, erythrocytes)[30]. The protein hemoglobin covers the surface of each RBC allowing to bind an oxygen molecule to the RBC. By binding the oxygen to the RBCs, the RBCs transport the oxygen as "cargo" successively along the blood stream enabling transport beyond the diffusion limit.

To optimize the oxygen transport, evolution optimized the architecture of the vascular system, in turn, towards an optimal transport of blood (section 3.4 or [4]). Starting with few feeding arteries, the systemic circuit pumps the blood with high oxygen content from the arteries to the arterioles, to the capillaries. At the capillaries, the oxygen and nutrient exchange takes place before the blood with low oxygen content enters the venous branch and returns via venules to the veins, and finally to the heart again. From the heart, the blood with the low oxygen content enters the pulmonary circuit where the oxygen content of the blood increases before the blood with a high oxygen content enters the systemic circuit again closing the loop of blood circulation.

Many blood vessels of different sizes and type build up the hierachical structure of a mature vasculature. During vasculargenesis, mesoderm and endothelial cells (EC) form single blood vessels which later connect. Under physiological conditions, vasculargenesis occures transiently in embriogenesis and wound healing. In maturated blood vessels, a homogeneous layer of ECs is covered by a perivascular layer of cells forming the blood vessel wall. Depending on the type of the vessel (artery, vein, capillary), the perivascular layer consists of pericytes, smooth muscle cells or other components (figure 1.5). After the establishment of first microvascular networks (vasculargenesis), blood vessel networks grow by successively extending mature vessels by splitting (intussusceptive) and sprouting angiogenesis. The balance between pro- and antiangiogenic factors regulates angiogenesis. The most prominent examples upregulating angiogenesis are the vascular endothelial growth factor (VEGF) and tumor angiogenic factors (TAFs). On the other side, the most prominent exam-
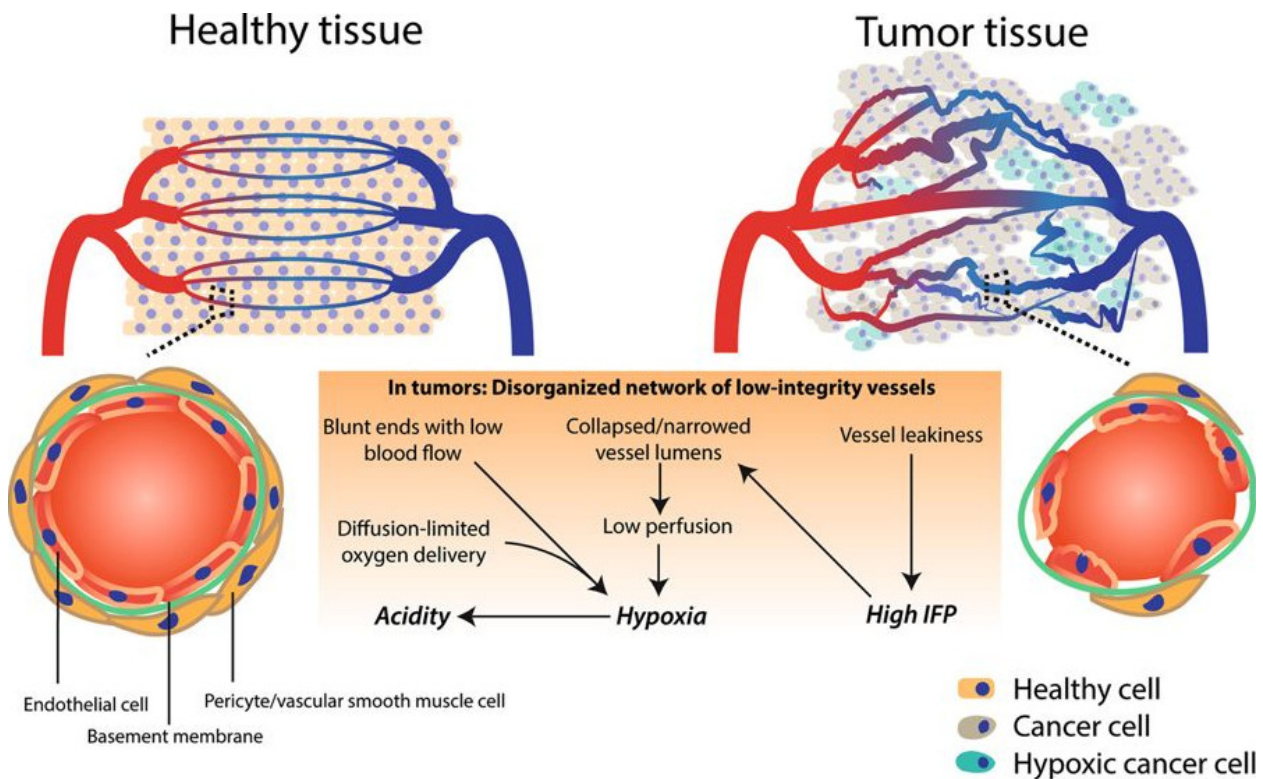
Figure 1.5: Healthy vs. Tumor tissue.(Upper left panel) A well-organized vessel network ensures full-covering of nutrient supply. (Lower left panel) These vessels are matured with an endothelial cell layer surrounded by a basement membrane and pericytes (like smooth muscle cells). The endothelial layer is characterized by tight intercellular junctions. Oppositely, due to high pro-angiogenic signaling, the network of tumor-associated blood vessels (upper right panel) is chaotic, low in pericyte coverage and has loose inter-endothelial cell junctions (lower right panel). This generates leaky vessels that increases interstitial fluid (IFP) pressure. Common blunt-ended or collapsed vessels result in tumor regions that are starved from nutrients including oxygen (hypoxic cells indicated in green). Moreover, the glycolytic nature of the (hypoxic) tumor cell acidifies the pH in the tumor microenvironment. Reprinted figure 1 of [26].
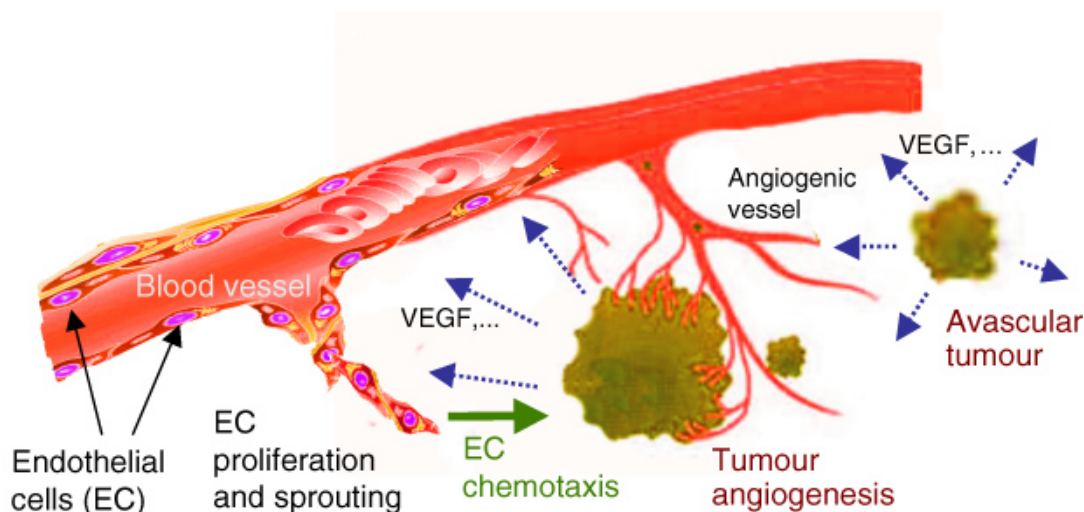
Figure 1.6: Schematic of tumor induce blood vessel growth, i.e. angiogenesis, by secreting various growth factors like vascular endothelial growth factor (VEGF), which binds to receptors present on Endothelial cell (EC) membrane. ECs then release proteases, escape from the original parent vessel walls (sprouting) and migrate by chemotaxis toward the tumor where they form new vessels. Single tumor cells can break away from the tumor mass and enter one of the blood vessels, being then carried to a distant site where they can initiate the growth of a secondary tumor (metastatis). Reprinted of figure 5 from [21] with permission (see appendix G).

ple for downregulating angiogenesis is the angiopoietin (Ang) family (figure 1.6). During the progression of solid tumors, sprouting angiogenesis dominates splitting angiogenesis. Similar to the situation in MTSs (see section 1.1.2), metabolic stresses (low pO_2, low pH or hypoglycaemia) or mechanical stresses (proliferating cells) unbalance the pro- and antiangiogenic factors, but in contrast to the avascular growth phase, the interaction with the blood vessels in the vascular phase results in a more complex behaviour of tumor growth in vivo or in animal models. During tumor growth: holes in the endothelial layer form, the interendothelial junctions widen and the basement membranes become discontinuous or absent resulting in leaky vessels. In addition, most tumor vessels lack the layer of functional perivascular cells protecting against changes in oxygen, accommodating metabolic needs and inducing vascular quiescence [29].

Tumor cells segregate VEGF (and other chemicals) establishing a spatial gradient between the tumor and the surrounding vasculature. In case a blood vessel experiences an increase in VEGF, the basement membranes of the endothelial cells degrades until some of the endothelial cells eventually become tip cells. Tip cells sense VEGF gradients using a filopodia and migrate towards an increasing VEGF concentration (chemotaxis). Behind the leading tip cells, more endothelial cells (stalk cells) follow the migration while proliferating and elongating to form snail trails of capillary sprouts [21, 31] (figure 1.6). At this point, the tumor growth crosses the point from the avascular growth phase to the vascular growth phase (angiogenic switch [32, 33]). During the progression of solid tumor growth, sprouting angiogenesis, vessel dilation and regression remodels the regular hierarchical structure, geometry and organization of the vasculature towards aberrancy affecting the delivery of nutrients, oxygen and other substances mediated by the blood. In healthy tissue, cells distribute within the diffusion range of oxygen (100 to 200μm [29]) around blood vessels. As discussed previously (section 1.1.1), maintaining the cell metabolism homogeneously inside the tissue requires a homogeneous distribution of oxygen inside the tissue. Since blood carries and delivers the oxygen, maintaining a homogeneous cell metabolism requires a homogeneous distribution of blood vessels, too. On average, the distance between two blood vessels is on the same order than the diffusion range of oxygen in tissue (50 μm for brain, 150 μm for breast [34]). This relationship between blood vessels and oxygen supply restricts the size of avascular tumors to the order of a few millimeters [35].

The tissue fluid or interstitial fluid (IF) surrounds all cells in multicellular organisms. The IF consists of similar molecules than the blood plasma allowing water-soluble nutrients to extravasate across the capillary walls from the blood plasma into the IF [36]. Since the spacial arrangement of the blood vessel networks including the topology and the wall integrity of blood vessels in tumors differs from their healthy counterpart, the interstitial fluid pressure (IFP) varies accordingly [37]. Figure 1.5 concisely summarizes the situation culminating in necrotic tumor core with elevated acidity as observed in in vitro systems and in in vivo tumors [21].

Understanding the topology of blood vessel networks, or transport networks in general, is still part of current research [38]. Generically, transport networks face geometric constrains while the transportation happens. Although the time scales and geometric boundary conditions differ, traffic or river bed formation faces similar problems than the blood vessel network formation. For the vasculature, Cecil D. Murray observed and analyzed the hierarchical structure in 1926 [39] proposing a formula to determine the blood vessel radii at vessel branches. In his theoretical derivation of the formula, he considered two energies with opposed dependency on the vessel radius and required the mutual minimization of the two energies. For each vessel branching point, his model proposes that the sum of the cubes of the daughter vessel's radii equals the cube of a parent vessel's radius. The derivation of Murray's law incorporates an optimality criterion, but gives no further advice on how the vasculature achieves this optimality (see section 3.4 or [4]).

1.2   Computer simulations in cancer research

Tumors emerge from the complicated interaction between cells and their microenvironment. As discussed in section 1.1, tumors communicate biochemically and biomechanically with the surrounding tissue. In contrast to other modeling approaches (animal, in vivo, in vitro, etc.), the mathematical modeling approach provides fully controlled conditions to investigate the individual contributing interactions and the emergent clinical behavior. The development of realistic mathematical models describing cells, cell clusters or whole tumors involves equations describing non linear effects in complicated geometries. Since finding solutions for non linear equations in complicated geometries ensues a very hard problem, computational methods help to obtain predictions from the equations.

In general, computer simulations of biological systems split into two major approaches: bottom up and top down. Bottom up approaches use minimal entities (atoms, molecules, cell constituents or cells) and their mutual interaction to build up the structure of interest. In bottom up or cell-based approaches (subsection 1.2.1), the length scale of interest is similar to the length scale over which the buildup structure or property
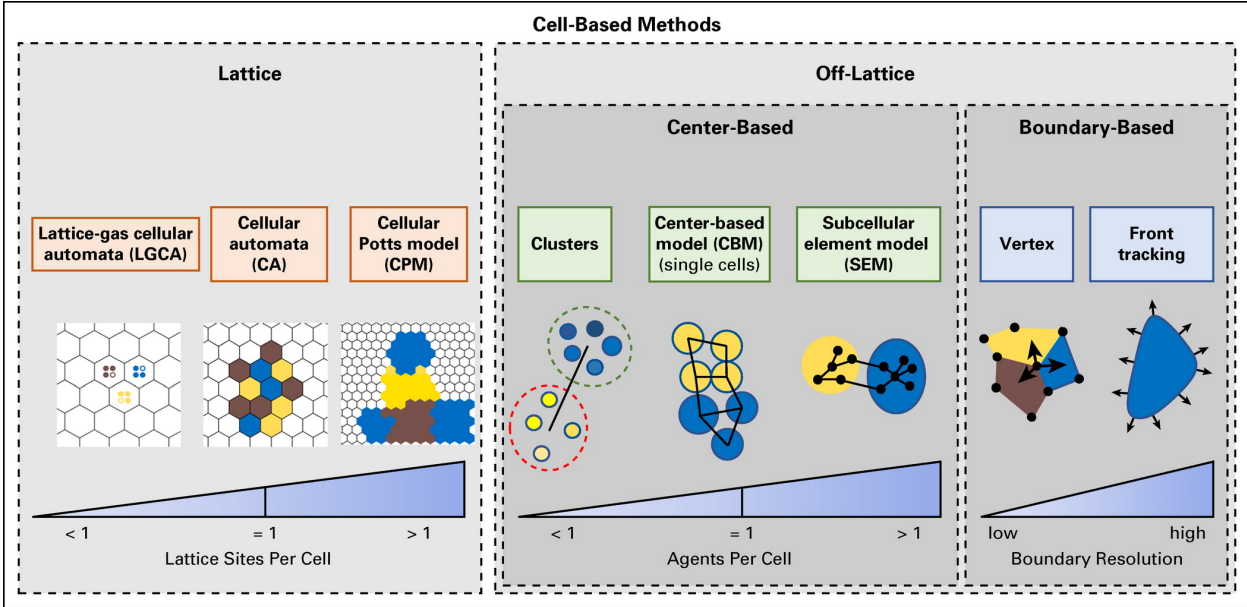
Figure 1.7: A schematic classification of cell-based modeling approaches. Reprinted figure 1 of [47].

varies e.g. the transport of a vesicle across a membrane in a molecular dynamics simulation. The opposite approach (top down) seeks for equations describing macroscopic observations of tissue compartments or cell clusters e.g. using Navier-Stokes equations to describe the necrotic core inside a tumor spheroid. Subsequently, the top down or continuum approach (subsection 1.2.2) aims at solving the governing modeling equations. A successful application of a top down approach requires that the smallest length scale of interest exceeds the length scale over which the considered property of the tissue compartment or cell cluster varies e.g. for the oxygen transport: the diffusion length of oxygen exceeds the diameter of a single cell (section 3.1 or [1]). Since a well adapted discretization always satisfies this restriction, the real problem dwells in finding the level of discretization that provides a trade off between computational resources and new information. Current state of the art research features hybrids between the two approaches (section 3.3 or [3]). In the following I describe the cell-based and the continuum approach in more detail with special focus on cancer and discuss the multi scale issue in subsection 1.2.3 [21, 40, 41, 42, 43, 44, 45, 46].

1.2.1 Cell-based models

With increasing computational resources, the relevance of cell-based, discrete, agent-based or individual based models in cancer research increased. Current models reach out for simulated tumors of clinical relevant dimensions.

Cell-based models track individual cells either along a rigid grid (lattice-based models) or without spatial restrictions (lattice-free or off-lattice models).

Lattice-based Methods use regular structured (e.g. Cartesian, Dodecahedral) or unstructured grids. Implementation, visualization and combination with partial differential equation solvers integrates easily with structured meshes, but these meshes suffer artifacts when the discretization falls behind the required resolution. Unstructured meshes avoid discretization biases at the cost of high complexity.

I discuss three examples for the lattice-based methods categorized by the number of cells associated with each lattice point (left of figure 1.7). In **cellular automaton (CA)** models, a single cell occupies a single lattice site. Discrete lattice-based rules (remain, move to a neighboring lattice site, free a lattice site, or divide to place a daughter cell in a nearby site) update each lattice site in a random order to reduce grid artifacts. In **lattice gas cellular automaton (LGCA)** models, more than a single cell occupies one lattice site. By neglecting the dynamics of individual cells and tracking the dynamics of cell clusters, LGCA models simulate very large numbers of cells efficiently over long periods of time. Similar to statistical mechanics,

building grid averages allow LGCA models to link the discrete model to continuum equations describing cell densities or populations instead of single cells [48]. In **Cellular Potts Models (CPMs)**, a single cell occupies more than one lattice site reversing the situation compared to LGCA models. Since more than one lattice site models a single cell, CPMs track the individual cell morphology in more detail compared to CA or LGCA models and, therefore, CPMs require much more computational effort.

Off-Lattice Methods   Off-Lattice methods require no a priori grid structure. The lack of the grid makes them more realistic, but also more complex and computationally expensive compared to the Lattice-based methods. I categorize the **Center-based models (CBMs)** by the number of software agents associated to each cell and start with typical CBM models associating a single software agent per cell. Some CBMs represent cells as point-like objects and other (more sophisticated) models explicitly include cell volumes modeled as spheres or deformable ellipsoids. The exchange of adhesive, repulsive, locomotive and drag-like forces between the cell centers results in dynamic cell repositioning. Using more than one software agent per cell approximates the cell biomechanics and the cell morphology in more detail (the method is called **subcellular element model (SEM)**), but at increased computational costs. Building **clusters** of cells and using one software agent per cluster eases the computational costs compared to traditional CBMs still incorporating heterogeneous details.

A different off-lattice method, the **boundary-based method**, focuses more on the morphology of cells or cell clusters than on the functional aspects. Two examples of boundary-based methods are: the **vertex-based method** and the **front tracking method**. The vertex-based method outlines cells by polygons in 2D or polyhedra in 3D and compute forces acting on the vertices of the polygons. This approach particularly helps in modeling confluent tissues. For greater spatial resolution compared to the vertex-based method, front-tracking methods solve partial differential equations (PDEs) describing fluid flow inside and between cells. The calculated flow advects the boundary points along the cell membranes. A similar technique, the immersed boundary method (IBM) [49], considers cells as infinitely thin shells filled with liquid. The shells respond to deformation with elastic restoring forces transmitted into the fluid establishing a coupling between the PDE describing the liquid and the cells. Level set methods define surfaces implicitly via the value of an auxiliary function. Depending on the model, the surface outlines a single cell, a cell cluster or a tumor and adjusts according to the PDEs modifying the auxiliary function. Theoretically, the combination and hybridization between of different methods is possible e.g. the implementation in VCell [50] recently connected the level set method with the front tracking method. Table 1.1 lists available software categorized by the discussed methods.

In cell-based models, the mutual interactions between individual constituents and the mutual interaction between individual constituents and the environment heavily depends on the modeling assumptions. Since the modeling assumptions spread widely depending on the scope of the study, I will not attempt a general review, but refer to the interaction model of the virtual biology lab (VBL) as example (presented in section 2.3.3).

Figure 1.8 summarizes a computational study reproducing the porous necrotic microstructure in a hanging drop spheroid experiment in vitro. In particular, the figure 1.8 compares two different implementations of cell necrosis in a cell-based model: deterministic cell necrosis in the left and stochastic cell necrosis in the right. In the widely used deterministic model, cells become instantly (and deterministically) necrotic whenever the oxygenation drops below a threshold value. In contrast, the stochastic necrosis model allows cells to survive hypoxic conditions at random. Although both approaches find the porous microstructure known from biopsy, the deterministic approach (left column) features a sharp perinecrotic boundary between the viable and nectrotic tissues while the stochastic approach (right column) features a perinecrotic transition zone with substantial mixing of viable and nectrotic cells (best visible at 8 days of simulated tumor growth in figure 1.8). Immunological surveillance and immunotherapy entered cancer treatment recently [**?**]. During the formation of tumors, the body naturally deals with malignant cells using the immune system and kills the majority of tumors before progression. Unfortunately cancer cells have ways to avoid destruction by the immune system. One way is to coat the surface of a malignant cell with proteins down-regulating the immune response such as PD-1. Therefore new therapies attempt to prevent the down-regulation of the immune response by malignant cells using immune checkpoint inhibitors. Since the immunohistochemistry of immune checkpoint inhibitors depends on the spatial distribution of the cells/ molecules (tumor immunoarchitecture) the immuno-architecture is of great interest. In [51], the authors focus on immunotherapy using immune checkpoint inhibitors in a cell-based model. Their computational model captures the temporal and spatial dynamics of cytotoxic T cells (CD8$^+$) during the development of a tumor.

Other recent computational studies using cell-based models investigated hypoxia in breast cancer [52, 53], tumor-induced angiogenesis and drug delivery [54, 55, 56, 57, 58, 59], cancer stem cells [60, 61, 62], the "Go

or Grow" hypothesis for glioblastoma multiforme [63, 64, 65], cancer invasion and epithelial-mesenchymal transition [66, 67, 68, 69] and multiple variants of tumor immunosurveillance [51, 70, 71]. [47] [72]

Method	Open Source Toolkits
Cellular automata (CA)	Repast: https://repast.github.io
	Chaste: http://www.cs.ox.ac.uk/chaste
	NetLogo: https://ccl.northwestern.edu/netlogo
Lattice gas CA	Repast: https://repast.github.io
Cellular Potts model	CompuCell3D: http://compucell3d.org
	EPISIM: http://tigacenter.bioquant.uniheidelberg.de/episim.html
	Morpheus: http://imc.zih.tu-dresden.de/wiki/morpheus/doku.php
	Tissue Simulation Toolkit: https://biomodel.project.cwi.nl/software/software#TST
Vertex based	Chaste: http://www.cs.ox.ac.uk/chaste
	Tyssue: https://github.com/DamCB/tyssue
Center based	Biocellion*: https://biocellion.com
	Chaste: http://www.cs.ox.ac.uk/chaste
	FLAME: http://flame.ac.uk
	PhysiCell: http://PhysiCell.MathCancer.org
	Timothy: https://timothy.icm.edu.pl
	VBL: https://github.com/edymil/VBL
Immersed boundary	IBCell*: https://labpages.moffitt.org/rejniakk/LabsTools.html#LabIAD
Other	BioFVM: http://BioFVM.MathCancer.org
	Microvessel Chaste: https://jmsgrogan.github.io/MicrovesselChaste
	VCell: http://vcell.org
	CaTSiT: http://bioinformatics.fh-stralsund.de/catsit/

Table 1.1: Computational methods of cell-based models and open source toolkits.

NOTE: Many computational approaches are available in open source toolkits contributing to open science (section 1.4). Because their source code is available with standard licenses, they have clear reuse rights. Users can tailor the codes to meet their particular need, publish the modified source (for greater reproducibility), and contribute bug fixes and new capabilities to the benefit of the scientific community. Adapted from Table 1 of [47] under license. * indicates packages with nonstandard (not Open Source Initiative-compliant) licences or are posted online for free but with unclear licenses.
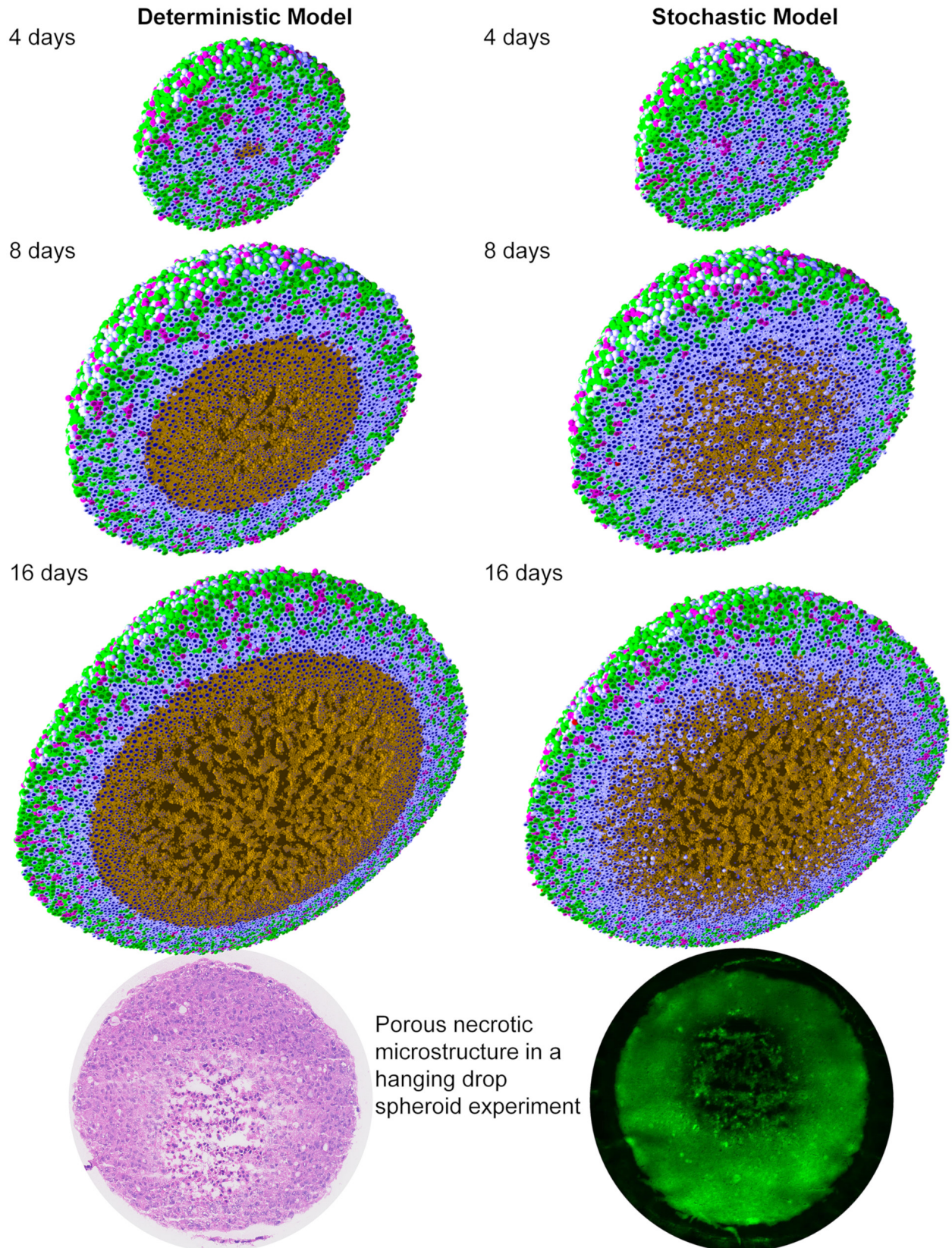
Figure 1.8: Example of cell-based modeling with PhysiCell. The left column shows a deterministic and the right column a stochastic modeling approach both implemented in PhysiCell. In all simulation time snapshots, the colors represents the following cell state: green before and magenta after mitosis, pale blue quiescence, red apoptotic and brown necrotic. The cell nuclei are shown in dark blue.

The bottom row shows a hanging drop spheroid experiment demonstrating a similar necrotic core microstructure. Image courtesy Mumenthaler lab, Lawrence J. Ellison Center for Transformative Medicine, University of Southern California. Reprinted figure 2 of [70]. This work is licensed under the Creative Commons Attribution 4.0 International License. To view a copy of this license, visit http://creativecommons.org/licenses/by/4.0/ or send a letter to Creative Commons, PO Box 1866, Mountain View, CA 94042, USA.
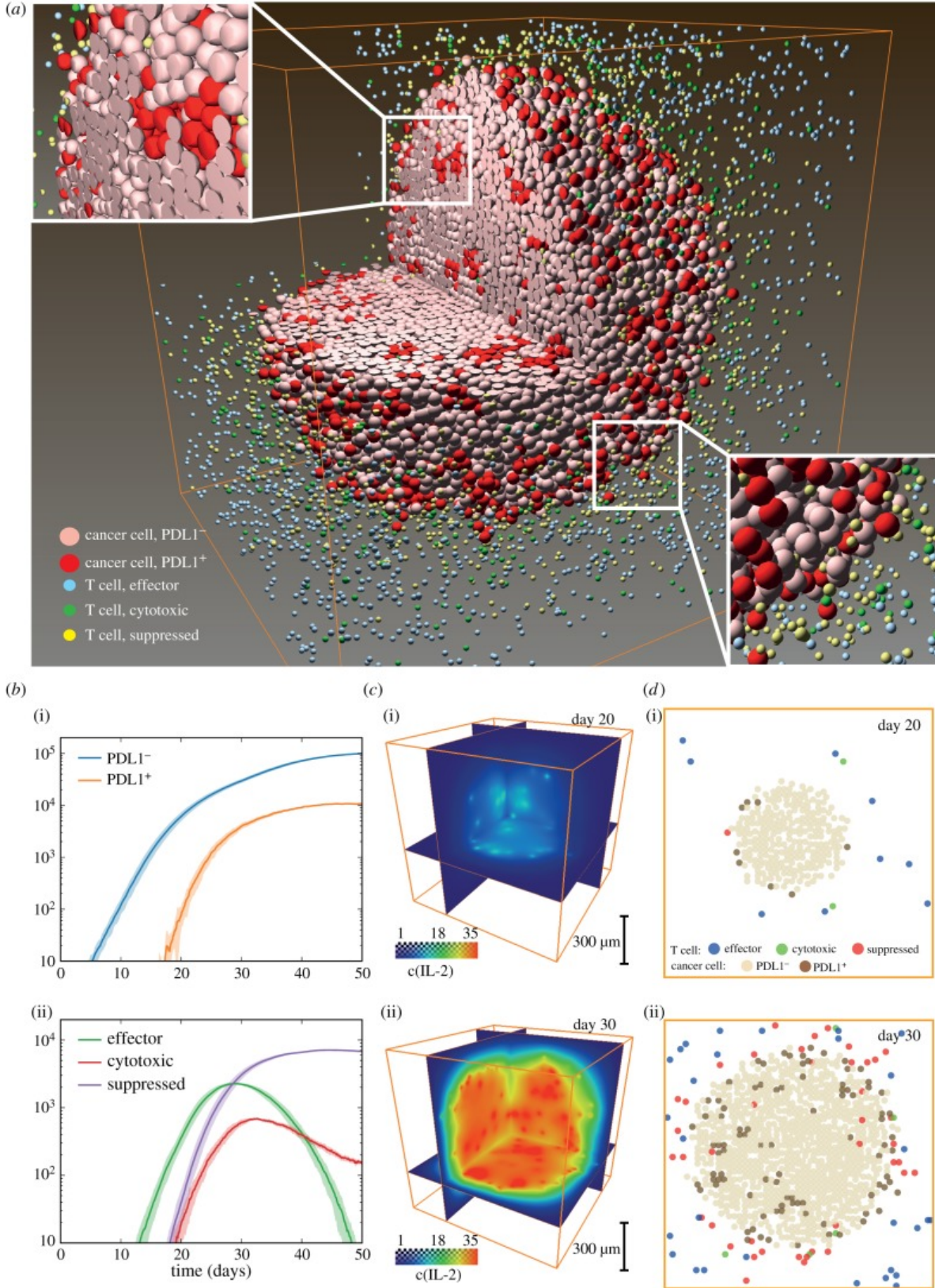
Figure 1.9: Example of a cell-based model including immune and cancer cells. (a) Three-dimensional distribution of different cell subsets. Insets show relative locations of T cells and cancer cells in the interior and at the tumour boundary. (b)(i) Time courses of cancer cell (PDL1$^+$ and PDL1$^-$) statistics tracked during simulation. (b)(ii) Time course of T-cell statistics tracked during simulation. Shadow indicates $\pm$ standard deviation. (c) Distribution of IL-2 (T cell activator signaling molecule in the immune system) concentration on days (i) 20 and (ii) 30. (d) 2D slices through the orange box shown in (a) at a simulated tumor time of (i) 20 days and (ii) 30 days. Reprinted figure 2 of [51].

1.2.2 Continuum models

Continuum models describe the behavior of cell densities or cell populations neglecting cellular details discussed in the previous subsection. In biological growth processes, changes of cell densities with respect to space inherently affect changes with respect to time and vice versa. The math of partial differential equations suits this kind of problem well.

Single-phase models (section 1.2.2.1) consider tumors of a single cell phenotype while multiphase models (section 1.2.2.2) describe multiple types of healthy and/or cancerous tissues and their mutual interaction at the same instance.

1.2.2.1 Single-phase modeling

Simplest single-phase models describe a tumor as an expanding sphere which simplifies solid tumor growth drastically, but also simplifies the math. Describing the tumor by a single scalar value R (the radius of the spheroid) requires the solution of an ordinary differential equation of the following form:

$$\frac{dR}{dt} = ? \tag{1.1}$$

to determine the temporal evolution of the spheroid. The question mark in equation 1.1 indicates the different model assumptions.

Using a constant cell volume density links the spheroid radius to total tumor mass. Since clinicians utilize and measure the total tumor mass frequently, available in vivo data allows to check model predictions and to compare model assumptions to realistic tumor growth curves [73, 74, 75, 76, 77, 78].

In general, continuum models depend critically on the choice of the underlying material laws and the 2D or 3D geometry with the associated boundary conditions. Since tissue (and similar biological material) resembles a viscous fluid, the description of the tissue dynamics often follows the Navier-Stokes equations. Established models of tumors adopt material laws describing fluids, poroelastic, viscoelatic and elasto-viscoplastic media. Naturally, the modeling of biological tissue includes concentrations of cell substrates such as glucose, lactate, oxygen, growth factors, inhibitors, hydrogen ions, drugs and their mutual interactions.

In contrast to passive physical systems, strict mass conversation does not apply to active biological systems. Therefore a more general mass conservation equation should include a reaction term f as introduced by Turing in 1952 [79] (equation 1.2). Let $\Phi(\vec{x}, t)$ describe the tumor cell density depending on space coordinate $\vec{x}$ and time t and $\vec{J}$ describe the local volume flux of tumor cells, than the mass conservation equation reads:

$$\frac{d\Phi}{dt} = -\nabla \cdot \vec{J} + f \tag{1.2}$$

Here, the reaction term f acts as additional source or sink for tumor cells. Usually, the local volume flux is modeled proportional to the local density gradient using the diffusion constant D (Fick's first law). Application of Fick's first law and the expansion of the total derivative with respect to time from $\frac{d\Phi}{dt}$ to $\frac{d\Phi}{dt} = \frac{\partial \Phi}{\partial t} + \vec{u}\nabla\Phi$ results in the generalize form of a diffusion equation, the diffusion reaction equation (DRE):

$$\frac{\partial \Phi}{\partial t} + \nabla \cdot (\Phi\vec{u}) = \nabla \cdot (D\nabla\Phi) + f \tag{1.3}$$

where $\vec{u}$ describes the local speed of the tumor cell density at space coordinate $\vec{x}$ and time t. Meanwhile DREs are studied carefully in divers fields [80, 81, 82].

However active biological systems (like tumors) violate mass conservation, cell division and cell death still obey momentum conservation. The general momentum equation (equation 1.4):

$$\frac{d(\Phi\vec{u})}{dt} = \nabla\sigma + \vec{F} \tag{1.4}$$

for a viscous fluid includes the Cauchy stress tensor σ and the total body force $\vec{F}$ accounting for gravity and other external forces. Tumor growth models neglect the elastic behavior of tissue on short time scales (minutes), because relevant processes of tumor growth happen on long time scales (days). On the tissue time and length scale, the residual stresses relax by rearrangement of extracellular matrix fibers leading to viscous behavior including solid pressure, friction and adhesion forces. Since biological growth and migration happens in a regime of very low Reynolds numbers (Re $\ll$ 1), tumor growth model neglect inertial forces. The direction and the speed of cell migration depend on environmental stimuli (section 1.1), especially on:

- **chemotaxis** i.e. gradients of soluble chemicals;

- **haptotaxis** i.e. gradients of substrate-attached molecules;

- **mechanotaxis** i.e. modifications of the ECM mechanical properties;

- **durotaxis** i.e. gradients of the matrix rigidity.

A crucial point in biophysical cancer modeling is to determine whether the coupling between tumor microenvironment evolution, cellular forces and active cell migration sustains or prevents tumor growth. Theoretical models have included different degrees of complexity to account for cell motility. The book of J D Murray [81] exhaustively presents such models. In unguided cellular diffusion, the diffusive cell flux $\vec{J}_d(\vec{r})$ at location $\vec{r}$ adjusts proportional to the local cell gradient $\nabla\Phi(\vec{r}, t)$:

$$\vec{J}_d(\vec{r}) = -D\nabla\Phi(\vec{r}, t) \tag{1.5}$$

Assuming a constant isotropic diffusion results in random cell motility. In more sophisticated models, the proportionality factor D depends on cell density $\Phi(\vec{r}, t)$ itself, strain, different substrate gradients or even on anisotropic reactions. In the most prominent example regarding tumor growth, the cells move up the gradient of vascular endothelial growth factor (VEGF) [83, 84].

In first approximation, the chemotactic cell flux $\vec{J}_g$ is proportional to the cell density $\Phi(\vec{r}, t)$ by a factor α defining the cell's sensitivity to the VEGF:

$$\vec{J}_g = \alpha\Phi(\vec{r}, t)\nabla g \tag{1.6}$$

Equations similar to equation 1.6 follow for haptotaxis, mechanotaxis and durotaxis, and have been considered in a large class of continuous differential tumor models coupling DREs with chemotactic and possibly haptotactic cell migration processes in 1D [85, 86], 2D [87] and 3D [88, 89].

Since tumor growth includes biomechanical processes with multiple facets ranging from inherent balance between proliferative pressure and resistive force of surrounding host tissue to the far more complex processes of mechanical control of cell dynamics and tumor vascularization, growing tumors actively contribute mechanical signals to the biological system. Continuum models lack the possibility to include direct cell-cell mechanics. Instead, authors considered coarse grained quantities like adhesion and surface tension [90, 91, 92] as source of intratumoral pressure gradients ∇p driving the tumor growth. Since the speed of molecular diffusion of the nutrients surpasses the speed of a growing tumor by several orders of magnitude, the steady state assumption for the nutrients simplifies the DREs describing the nutrients. I discuss a generalized model assumption (equation 1.7) in the following.

The balance between cell proliferation and death produces additional contributions to the cellular movement depending on the nutrient distribution. Let $n(\vec{r}, t)$ describe a nutrient distribution (e.g. oxygen field) and $\Gamma(n)$ describe the net balance between the nutrient-dependent proliferating rate and the cell death rate [92, 93]. Considering the tumor as an incompressible fluid, the continuity equation:

$$\nabla \cdot \vec{u}(\vec{r}, t) = \Gamma(n) \tag{1.7}$$

links the nutrient concentration to the velocity field $\vec{u}(\vec{r}, t)$ of the cell population. A constitutive equation links the velocity field to the internal pressure p. Usually, models consider the tumor as a porous media and apply Darcy's law to obtain the velocity from the pressure:

$$\vec{u} = -\gamma\nabla \cdot p \tag{1.8}$$

In Darcy's law (equation 1.8), the proportionality factor γ characterized the hydrostatic, viscous-like properties of the tumor cells [94, 95]. Together with assumptions on the boundary conditions, the above equations provide a closed set of partial differential equations enabling numerical studies of the tumor growth. [21]

1.2.2.2   Multiphase modeling

Up to now, the discussion assumed a single cell phenotype per cell population (single-phase models). The mixing or simultaneous consideration of multiple cell phenotypes (mixed-phase or multiphase models) offers the possibility to study healthy, cancerous and other populations of phenotypes at the same time and thereby considerably improving the tumor simulations regarding heterogeneity.

The description of a solid tumor in a multiphase model comprises usually at least one solid phase (necrotic tissue, viable tissue, ECM, ...) and one liquid phase (water, interstitial fluid, ...). The equations used in multiphase modeling are similar to the equations used in single-phase modeling (section 1.2.2.1), but consist
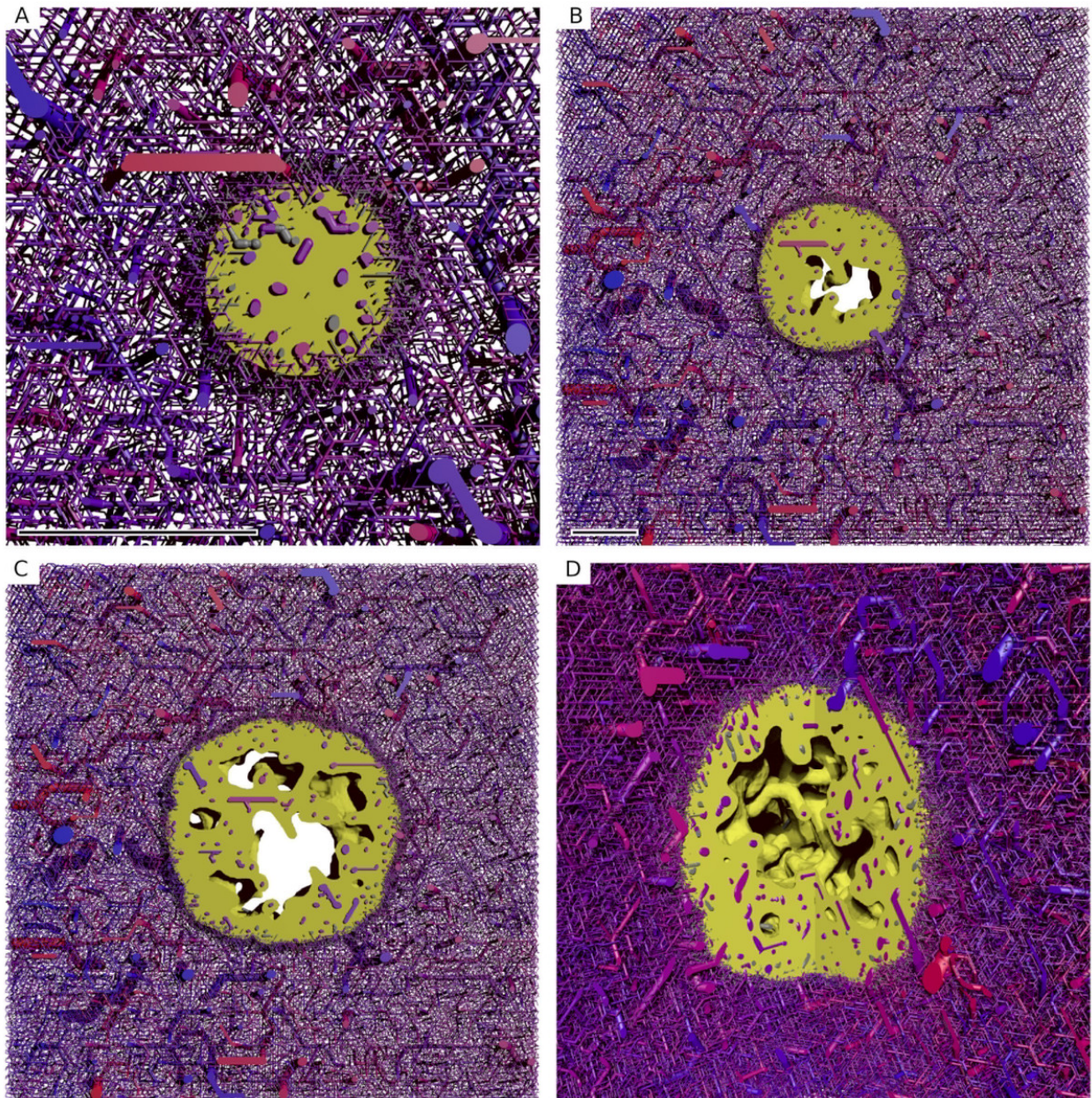
Figure 1.10: (A) to (C) depict a 400 μm thick slice through the origin of a 3D simulation box with lateral extension of about 8 mm. The scale bar indicates 1 mm. (A) is a close-up. (B) and (C) have the same scale. The snapshots were taken after 100 h, 400 h, 700 h. (C) and (D) show the same time but from a different point of view where a quadrant was cut out. The boundary to the viable tumor phase is rendered as solid yellow surface. Necrotic phases appear as void spaces within the tumor. The blood vessel network is rendered as collection of cylinders, color coded by blood pressure. Red represents high blood pressure (arteries), and blue represents low blood pressure (veins).
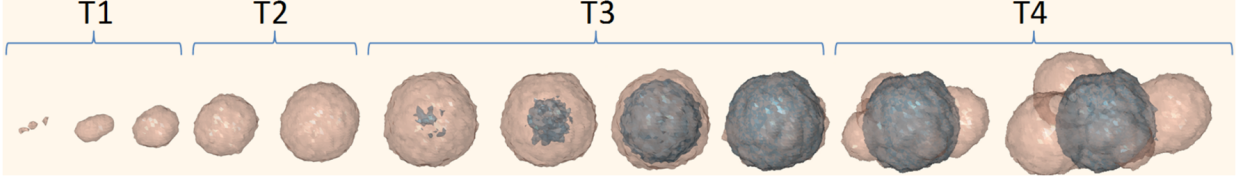
Figure 1.11: Tumor volume and morphology changes during progression including exponential growth (T1), linear expansion (T2), stasis (T3), and secondary growth processes (T4). Brown region: Viable cells; Black region: Necrotic cells.

of mass and momentum balance equations for each phase separately in combination with an interphase mass and momentum exchange. Similar to the single-phase models, appropriate constitutive laws and boundary conditions close the model equations. In contrast to the single-phase models, however, the total volume in multiscale models splits for the different phenotypes or species. Considering N species with each of the species occupying a volume fraction ϕ_i, the assumption of no voids constrains the total volume at each point in space and time to $\sum_{i=0}^{N} \phi_i = 1$. Equation 1.9 shows the general mass conservation law for each of the species in a multiphase model.

$$\rho_i \left(\frac{\partial \phi_i}{\partial t} + \nabla \cdot (\vec{u}_i \phi_i) \right) = -\nabla \cdot \vec{J}_i + S_i \tag{1.9}$$

ρ_i describes the density, σ_i the stress and $\vec{u}_i$ the velocity of component i. The source terms S_i generalize the reaction term f of equation 1.3 to account for inter-component mass exchange. Assuming mass conservation of the mixture, the summation of equation 1.9 requires that $\sum_{i=0}^{N} \vec{J}_i$ equals a constant and $\sum_{i=0}^{N} S_i$ equals zero. Together with these two consistency equations, the multiphase method allows to compute quantities of the system such as velocities, forces, stresses or interaction energies. [40]

In [37], Welter et al. used a multiphase model to study the influence of the interstitial fluid pressure on chemotherapy. In their model, the solid phase comprised tumor tissue, normal tissue, necrotic tissue and ECM in combination with the liquid interstitial phase as illustrated in figure 1.10.

In [96], Tang et al. proposed a mathematical model coupling 3D tumor growth and angiogenesis to simulate tumor progression for chemotherapy evaluation. Their model combines cell-based features with continuum equations to model tumor progression through multiple stages including tumor initiation, avascular growth, and transition from avascular to vascular growth (shown in figure 1.11). Using cell- and vascular-mediated interstitial pressure, mass transport, angiogenesis, cell proliferation, and vessel maturation, allowed them to simulate realistic drug distributions during chemotherapy (compare figure 1.12).

Recently, Vavourakis et al. [97] studied intravenous delivery of cytotoxic drugs in a model accounting for chemo-, hapto- and mechanotactic vessel sprouting, extracellular matrix remodeling, mechano-sensitive vascular remodeling and collapse, intra- and extravascular drug transport, and tumour regression as an effect of a cytotoxic cancer drug (see figure 1.13).

[98] [72] [99] [34] [100, chapter 3: Computer Simulations of the Tumor Vasculature: Applications to Interstitial Fluid Flow, Drug Delivery, and Oxygen Supply]
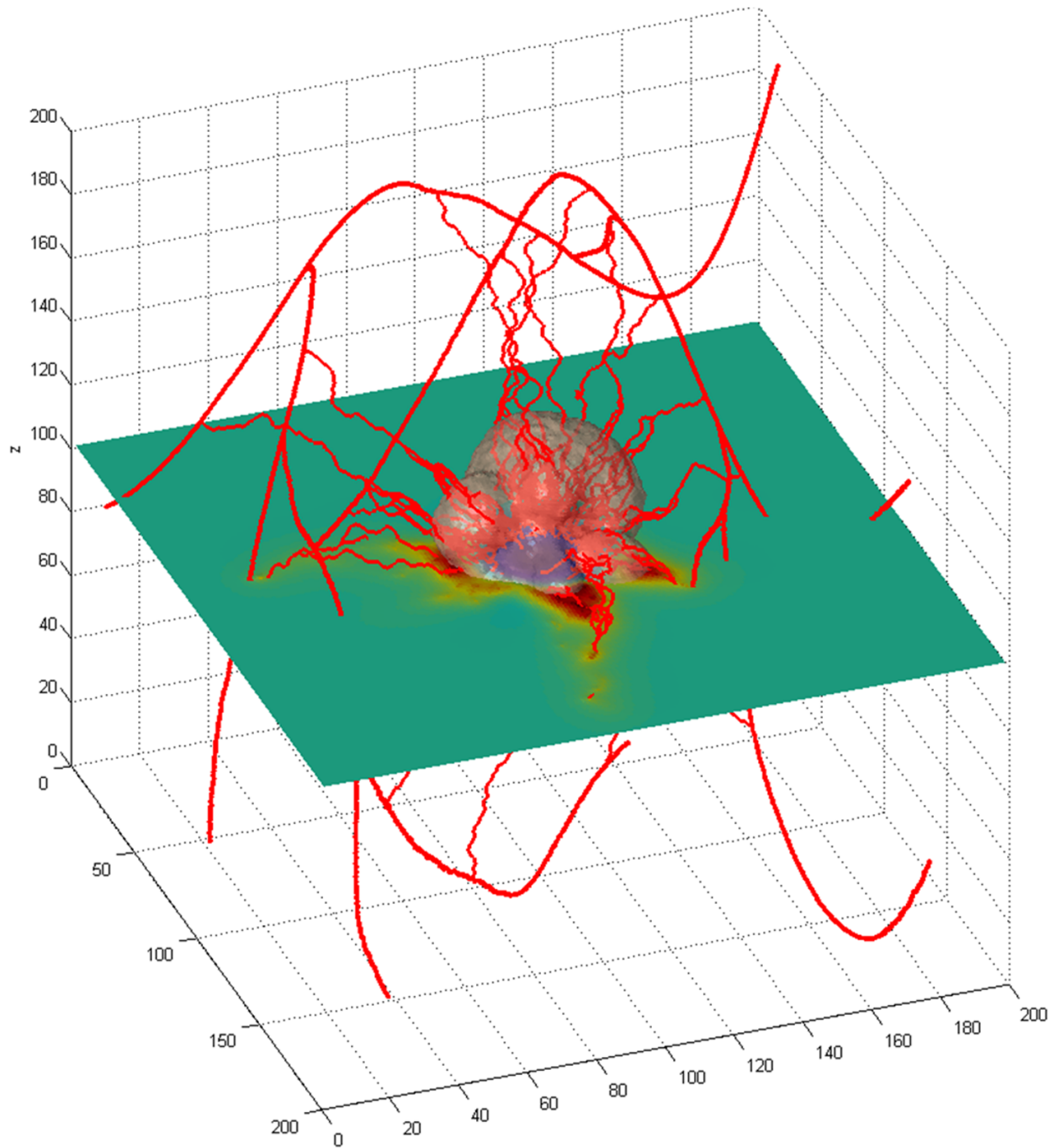
Figure 1.12: Solid tumor growth simulation with angiogenesis from a virtual 3D vasculature. The cross-sectional plane shows the nutrient availability within the simulation area.
Reprinted figure 9 of [96] available at https://doi.org/10.1371/journal.pone.0083962.g009.
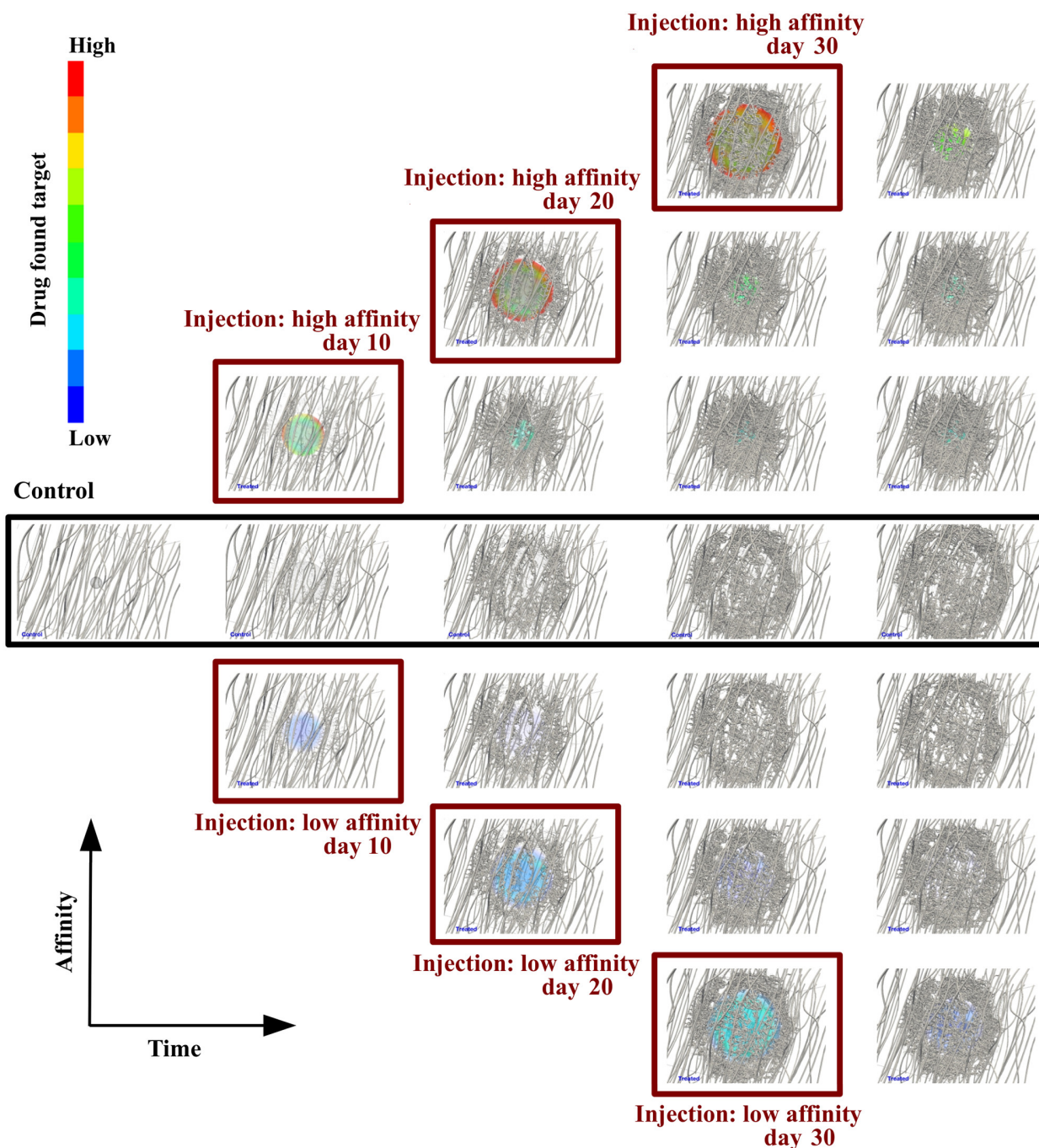
Figure 1.13: Snapshots of tumor growth and angiogenesis over time. Simulation results visualisation comparison of the control (center row) versus the treated case for low poresize, and two extreme drug affinity ratios. From left to right, the snapshots at the second column correspond to day 11, the third column to day 21, the fourth column to day 31, and the last column to day 40. Note for low drug affinity (bottom three rows) the low drug concentration in the tumor and for high affinity (top three rows) the significant concentration of the cytotoxic drug. Notably, the drug distribution is very heterogeneous for early-stage injections due to the non-hierarchical structure of the immature tumor vessels supporting the argument of the the spatio-temporal variability of the vascular tree in mammary tumors. Comparing the top right snapshot with the bottom counterpart, the tumor regresses for high drug affinity.

1.2.3 The multi scale issue

As presented in the previous two subsections (subsection 1.2.1 "Cell-based models" and 1.2.2 "Continuum models") and discussed by others [21, 101, 102, 40], cancer acts on many length and time scales. To integrate the knowledge across different scales (and disciplines) is a major challenge in cancer research.

The past two decades shed a lot of light on the subcellular processes in a single cell and the mere complexity of the single cell processes drives a huge branch of modern biological research. Literature even established a new notion — the "omics" family of research — to summarize the emerging subdisciplines in system biology. The "omics" family of research covers (not exclusively) genomics, epigenomics, proteomics, metabolomics and mechanomics acting on length scales as small as *nanometers* and time scales as fast as *nanoseconds*. Since the typical cell cycle of a healthy cell lasts about one day [103], I consider one day as the upper limit of the time scale for a single cell phenomena. Considering multicellular processes (cell migration, proliferation) lifts the length scale to *micrometers* and time scale to several *hours* or multiple *days* defining the meso scale. The meso scale bridges between the subcellular micro scale and the clinical observable macro scale. The macro scale completely lacks single cell aspects considering collective cell or tissue phenomena only. Tissue extends up to several *centimeters* forming whole organs including the vasculature, which is peculiar to macro level. Blood vessels sustaining a blood stream with enough nutrients and a lymphatic network disposing metabolic wast allows living tissue to maintain the "status quo" for *decades* or even a whole *century* (compare figure 1.14).

Unfortunately science lacks **the** reason for cancer, but scientists widely believe [21] that tumors originate from a malfunctioning within the "omic" family. However a malfunctioning single cell might cause problems, tumors comprise multiple cells dynamically interacting with each other and the local environment similar to the interaction in non cancerous tissue. To incorporate and modify the vasculature is a hallmark of solid tumor growth. During the progression of solid tumor growth, a cohort of processes such as chemotaxis, haptotaxis, mechanotaxis combine with topological properties of the cell cluster and form the natural habitat of the "omic" processes. In other words: feedbacks from the tissue to cell and from the cell to the sub cellular level establish.

We started to understand some of the processes at their characteristic scale (macro, meso and micro), but we are just getting an idea about the complicated and diverse feedbacks between the different scales. As described in [21], solid tumor growth involves processes at all scales and the authors of [101] even gave the name "cancer system biology" to this emerging field of research.

Combining cell-based models with continuum models into hybrid models enables in silico modeling to deal with the multiscale issue.
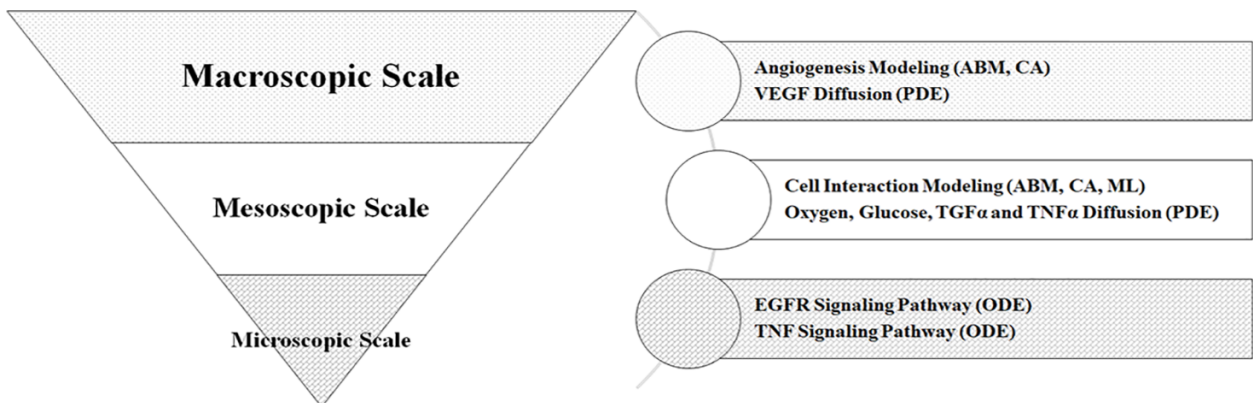
Figure 1.14: Multiscale model techniques overview showing characteristic techniques for each scale of cancer modeling: ML = Machine Learning, CA = Cellular Automata, ABM = Agent Based Modeling, PDE = Partial Differential Equation, ODE = Ordinary Differential Equation.
Relevant biological abbreviations: TGF = Transforming growth factor (member of the epidermal growth factor family), TNF_α = Tumor Necrosis Factor α (important during inflammation), EGFR = Epidermal growth factor receptor.
Reprinted figure 1 of [104] available at https://doi.org/10.1371/journal.pone.0183810.g001.

1.3   Sparse matrices

Finding a vector x satisfying the linear equation

$$Ax = b \tag{1.10}$$

is a well known and studied problem in math [105] — in pure math as well as in numerics. With increasing computational power, numerical methods became increasingly relevant for finding solutions to equation 1.10. In practical, real-world problems occurring in science and engineering, the matrices A are very large and sparsely populated meaning only a few matrix entries differ from zero ($\frac{\#\{a_{i,j} \neq 0\}}{\#\{a_{i,j} = 0\}} \ll 1$). Studying sparse matrices intersects numerical linear algebra and graph theory.

In general, a graph represents connection between variables in a mathematical model such as physical forces between two points inside a mechanical structure or the voltage across a circuit being similar to the blood pressure at each intersection in a blood vessel network (compare section "2.2 Computation of blood flow and hematocrit" in [5]). The emerging field of machine learning heavily uses sparse matrix techniques because data categorization and counting smoothly integrates with sparse matrices e.g. in natural language processing a nonzero entry at (i,j) means that document i contains word j (http://faculty.cse.tamu.edu/davis/research.html, [106]).

More classical applications of (sparse) linear systems occure when computationally solving differential equations. As presented in section 1.2.2.2, Partial Differential Equations (PDEs) facilitate continuum descriptions of physical problems based on suitable material laws. Since finding analytical solutions fails for practical applications, numerical methods find approximative solutions for the PDEs under consideration. Current state of the art numerics features two different methods to solve PDEs: Finite Elements Methods (FEM) and Finite Difference Methods (FDM). FEMs assume that the function solving the PDE could be represented as a superposition from a suitable set of basic functions defined on small patches ("Finte Elements") of the total domain. Therefore, finding a solution to the global PDE reduces to finding the appropriate coefficients for each of the basic functions in superposition on each patch. Finding the coefficients converts into solving linear equations where the matrix A is sparse. In contrast to the sophisticated FEMs, Finite Difference Methods (FDMs) simply divide the domain of the PDE turning derivatives into "Finite Differences" [107, 108, 109, 110] . I describe the transformation of a PDE into sparse linear system explicitly for the 1D diffusion equation [107].

The diffusion equation for scalar function u depending on space and time reads as follows (Dirichlet boundary conditions):

$$\begin{aligned}
\frac{\partial u}{\partial t} &= \alpha \frac{\partial^2 u}{\partial x^2}, \quad x \in (0, L), \ t \in (0, T] \\
u(x, 0) &= I(x), \quad x \in [0, L] \\
u(0, t) &= 0, \quad t > 0, \\
u(L, t) &= 0, \quad t > 0
\end{aligned} \tag{1.11}$$

where $\alpha > 0$ is a real parameter and the prescribed function $I(x)$ determines the initial condition at $t = 0$. To treat the problem numerically, we discretize the domain $[0, L] \times [0, T]$ with equally spaced mesh points at

$$x_i = i \Delta x, \quad i = 0, \dots, N_x \text{ where } \Delta x = \frac{L}{N_x}$$

and

$$t_n = n \Delta t, \quad n = 0, \dots, N_t \text{ where } \Delta t = \frac{T}{N_t}$$

Using the standard shortcut u_i^n for $u(x_i, t_n)$ together with backward difference in time and central difference in space (known as "Backward Euler Method" [108]), the discretization of equation 1.11 becomes a coupled system of algebraic equations

$$\frac{u_i^n - u_i^{n-1}}{\Delta t} = \alpha \frac{u_{i+1}^n - 2u_i^n + u_{i-1}^n}{\Delta x^2} \tag{1.12}$$

for each point on the mesh. Defining $F = \alpha \frac{(\Delta t)}{(\Delta x)^2}$ and sorting the unknowns in equation 1.12 to the left hand side, equation 1.12 rewrites to

$$-Fu_{i-1}^n + (1 + 2F)\, u_i^n - Fu_{i+1}^n = u_{i-1}^{n-1}, \tag{1.13}$$

Considering the boundary conditions $u_0^n = 0$ and $u_{N_x}^n = 0$, equation 1.13 restates in matrix form ($Ax = b$) where

$$
A = \begin{pmatrix}
1 & 0 & 0 & \cdots & \cdots & \cdots & \cdots & \cdots & 0 \\
-F & 1+2F & -F & \ddots & & & & & \vdots \\
0 & -F & 1+2F & -F & \ddots & & & & \vdots \\
\vdots & \ddots & & \ddots & \ddots & 0 & & & \vdots \\
\vdots & & \ddots & \ddots & \ddots & \ddots & \ddots & & \vdots \\
\vdots & & & 0 & -F & 1+2F & -F & \ddots & \vdots \\
\vdots & & & & \ddots & \ddots & \ddots & \ddots & 0 \\
\vdots & & & & & \ddots & \ddots & \ddots & -F \\
0 & \cdots & \cdots & \cdots & \cdots & \cdots & 0 & 0 & 1
\end{pmatrix}
\tag{1.14}
$$

,

$$
x = \begin{pmatrix} u_0^n \\ \vdots \\ u_{N_x}^n \end{pmatrix} \text{ and } b = \begin{pmatrix} b_0 \\ \vdots \\ b_i \\ \vdots \\ b_{N_x} \end{pmatrix}, \text{ with } b_0 = 0, b_i = u_i^{n-1}, b_{N_x} = 0
\tag{1.15}
$$

At this point, finding a function solving the diffusion equation (equation 1.11) turned in to finding the inverse matrix of A (written as A^{-1}) to obtain the unknowns in equation 1.13. The explicit representation of the matrix A (see equation 1.14) shows the sparsity for the discussed 1D problem.

For a PDE of a function defined over 2D- or 3D-dimensional space, the presented reasoning requires an
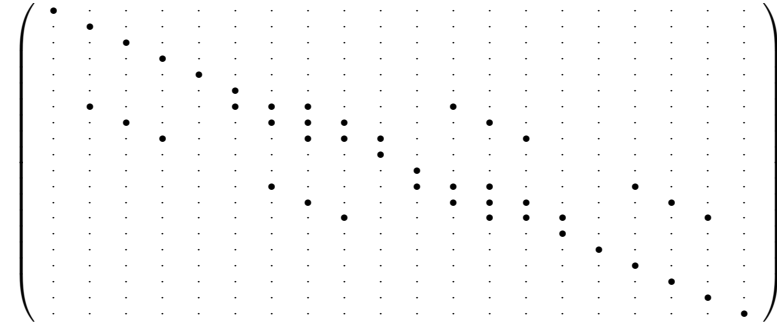
Figure 1.15: Sparsity pattern for the 2D diffusion equation. The bullets refer to the nonzero entries and the dots represent entries with zeros.

additional mapping of the two- or three-dimensional grid points to the matrix. Similar to the 1D case, the resulting matrices are sparse, but with more complicated sparsity patterns. Figure 1.15 illustrates the sparsity pattern for the matrix obtained from the 2D diffusion equation.

The mentioned "Backward Euler" time-stepping scheme is one of the most simplest approaches. Different possibilities of mixing forward and backward time-stepping or to approximate the derivatives in the discretized form of the equation exist. The "best" choice depends on the problem, but often the Runge- Kutta method derived from the described "Backward Euler" method is a good starting point.

Now the problem of finding a function satisfying a differential equation turned into finding a vector x satisfying the (sparse) matrix equation $Ax = b$ and we find lots of tools for this task in computational mathematics or computer science. During the course of my PhD studies I used "Trilinos" ([111], https://trilinos.github.io/) and "PETSc" ([112, 113, 114], https://www.mcs.anl.gov/petsc/). Both packages are highly flexible and implement the latest techniques to solve linear and even non-linear sparse matrix equations. The techniques include parallel computing with distributed memory using MPI (Message Passing Interface, https://www.mpi-forum.org) and shared memory multiprocessing using openMP (www.openmp.org).

1.4 Model, Code and Data sharing

Computers dramatically affect our daily life. More digital data than ever is acquired and stored on ever increasing storing devices. Data storage in combination with fast distribution of information via the internet accelerated our communication. The possibility to easily store large amounts of data and the new pace of communication affects also the scientific community. For example: today, one website hosts a lifetime of writings from a single person (http://www.alberteinstein.info/) or today, a medical doctor in Europe could almost instantly evaluate a Magnetic Resonance (MR) scans of a person located in the United States or vice versa.

Prior to computers and the internet, the library was the place to find the latest science communicated in professional journals, but the previously well accepted ways of communicating scientific results slowly adapt to the pace of the digital world. The peer review process managed by the professional journals like the physical review letters (https://journals.aps.org/prl/) maintained quality standards, improved performance, and provided credibility in academia. However these advantages, a peer review process raises the cost for a journal concerning staff members, mail and storage. A critical point of the peer review process is to find an appropriate peer executing the review of the article. Knowing, finding and contacting an expert on the scope of an article requires a well established network of the journal's editor. The internet eased the efforts to find and contact an expert quickly. Therefore a lot of researchers started questioning whether the classical journals including their form of the peer review process are still worth the gains [115, 116, 117] with wikipedia being one successful counter example.

In wikipedia, the review process follows a concept know from open source software development (https://opensource.org/) where not only a few experts judge the contributions, but everybody interested contributes. This way, numerous people with diverse backgrounds and contrary opinions find a common consensus resulting in high quality articles similar to the high quality obtained in open source software development. Preprint servers like arXiv (https://arxiv.org) and bioRxiv (www.biorxiv.org) offer the possibility to share research in a form that is independent of classical journals and the classical peer review process [118]. Instead of a classical peer review process, preprint servers feature different metrics to judge contributions. The simplest form of a metric counts the response to an article (altmetric) similar to the facebook's thumb up or thumb down approach. Current investigations focus on the scientific reliability of this metric [119].

Computers changed not only the communication in the sciences, but also a lot of the sciences itself. Current life sciences rely on a lot of techniques indispensable connected with computers during data acquirement and data analysis. Proper science requires reproducibility of the digital methods and to ensure reproducibility, sciences relying on computers request reliable data storage. To this end, the community established the FAIR Principles for scientific data management and stewardship: research data should be Findable, Accessible, Interoperable and Reusable [120].

The discussed aspects are part of the open science movement [121, 122] calling for

- Open Methodology
- Open Source
- Open Data
- Open Access
- Open Peer Review
- Open Educational Resources.

Several publisher accepted the call for open science with a serious of open access journals. For example the nature publishing group with the journal Scientific Reports or the royal society publishing group with the journal ROYAL SOCIETY OPEN SCIENCE. On top, "nonprofit" publishers like the public library of science PLoS (www.plos.org) or eLife Sciences Publications (www.elifesciences.org) became an established resource in the scientific community. To contribute to an open access journal, the authors (or their hiring institutions) pay an article processing charge (APC) covering the expenses of the journal. In return, the hiring institution of an author avoids journal subscription rates for the open access journals. Therefore paying an APC is not a drawback for the institution and as a consequence, the science reported in the manuscript becomes accessible to everybody. To ensure the public availability, manuscripts passing the peer review of an open access journal usually appear under creative commons licenses https://creativecommons.org/licenses/

allowing other scientists to access and adapt the already reported research focusing on new scientific results rather than copyrights.

Like wikipedia being the most prestigious achievement of an open review process, the linux kernel is the most prestigious achievement of the open source community. Except of the desktop computer segment (where Microsoft's Windows is still leading), the linux kernel drives supercomputers, (web-) servers and embedded devices — also the Android operating system relies on the linux kernel. Although the idea that everybody can contribute to software (the kernel) was present at the early days of the linux kernel, integrating and merging code from multiple developer became more tedious the more developer a project had. To automatically coordinate a lot of contributions and to smoothly integrate modifications into the source code of the kernel, the head developer of the linux kernel, Linus Torvalds, developed a distributed version control system to track changes in the source code: git. In my opinion, git and other version control systems (VCS) such as CVS or subversion contributed to the current success of open source software [123].

In the context of open science, the scientific community became aware that source code (e.g. www.github.com) and data (e.g. www.zenodo.org and Scientific DATA https://www.nature.com/sdata/) sharing is an advantage [97, 124] rather than bearing the risk of being scooped. Today scientists upload and share their software including documentation and example data to platforms like https://simtk.org/ or www.openhub.net. In the context of this dissertation, I worked with three listings:

"SimVascular" [125](http://simvascular.github.io/) providing a complete pipeline from medical image data segmentation to patient specific blood flow simulation and analysis;

"Chaste" [126, 127] (http://www.cs.ox.ac.uk/chaste/) providing a cell-based simulation framework extended by a simple 2D vasculature in

"MicrovesselChaste" [128] (http://jmsgrogan.github.io/MicrovesselChaste/) .

A more general example of data sharing and integration is the human brain project (https://www.humanbrainproject.eu) attempting to merge knowledge, software and data from multiple disciplines into a single platform accessible for everybody or the story of the open source approach to drug design [129].

Chapter 2

Own work

In this second chapter of my dissertation, I summarize my personal contributions to the scientific community by reviewing my contributions to the original research papers reprinted in chapter 3.

Contents

2.1 Computational Model for Tumor Oxygenation Applied to Clinical Data on Breast Tumor Hemoglobin Concentrations Suggests Vascular Dilatation and Compression

The original research article entitled *Computational Model for Tumor Oxygenation Applied to Clinical Data on Breast Tumor Hemoglobin Concentrations Suggests Vascular Dilatation and Compression* was published at 22nd of August 2016 in PLoS ONE. I reprinted the article with permission (see appendix G at page 215 of this dissertation) in section 3.1 starting on page 55 of this dissertation.

2.1.1 Background

Although oxygen plays a major role in cell biology, the oxygenation of tumors is not well understood and focus of current research.

Since oxygen plays a key role in the creation of ATP, oxygen also plays a key role in driving biological life on the molecular level, but only few measurement techniques are available [130] to study oxygen in vivo. In [131], the authors presented an in silico model to obtain the oxygen distribution in arbitrary shaped tissue domains based on the blood vessels crossing the domain. Inspired by their work, we propagated the oxygen from artificial blood vessel networks into the sourrounding tissue to study oxygen saturation of the tissue during vascular remodeling due to breast cancer.

In contrast to conventional mammography, optical or infrared (IR) mammography scans the tissue with low energy radiation serving as a none invasive scanning technique and providing information about the average oxygen distribution in vivo. In detail, IR mammography accesses the average concentration of total hemoglobin c_{Hb}, oxyhemoglobin c_{HbO} and deoxyhemoglobin c_{HbD} [132]. The ratio between oxyhemoglobin c_{HbO} and deoxyhemoglobin c_{HbD} determines the average blood oxygen saturation $Y = c_{HbO}/c_{HbD}$ as a derived quantity. In [133], the authors scanned a cohort (87) of patients with carcinomas using IR mammography and reported that the total hemoglobin concentration in tumors exceeds the total hemoglobin concentration in healthy control tissue (second breast).

Cancer leads to dilated blood vessels increasing the available volume for the blood. Assuming a constant hemoglobin concentration in the blood, the observed increase in hemoglobin concentration follows from the increased blood volume. However the total hemoglobin concentration (c_{Hb}) increased, the measurements revealed variations in the blood oxygen saturation Y. High hemoglobin concentrations correlate with high blood oxygen saturations, but tumors with a low hemoglobin concentration exhibit a wide range of blood oxygen saturations (see figure 5 in [133]).

In the original research paper [1] (reprinted in section 3.1.1), we provide reasoning for the variation.

2.1.2 Summary of the paper

After the introduction, we explain the theoretical and computational models to calculate the blood vessel and tissue oxygen saturation. The implementation of these models is part of the Tumorcode software published in 2018 ([2] and section 3.2 of this dissertation). In the Tumorcode software, the models described in the publication "Computational Model for Tumor Oxygenation Applied to Clinical Data on Breast Tumor Hemoglobin Concentrations Suggests Vascular Dilatation and Compression" are named "detailedO2".

The model development started with previously published models from Hsu, Secomb and Goldman ([134],[135]). Our approach [1] assumes a constant intravascular partial pressure of oxygen (P) at the cross section area of a blood vessel. Therefore, the propagation of the intravascular oxygen parallel to the blood vessel axis (longitudinal) becomes an effectively one dimensional problem. The coupling between vessels and the surrounding tissue is the most elaborate part of our model. Since the intravascular oxygen acts as source for the oxygen field inside the tissue surrounding the blood vessel (P_t), the intravascular oxygen pressure P reduces accordingly as the blood propagates along the vessel axis similar to fluid extravasation. Fluid extravasation requires a driving pressure gradient, and in analogy, we model the transvascular flux density of oxygen per unit length j_{tv} proportional to the gradient of oxygen partial pressure inside the vessel P and outside the vessel (i.e. inside the tissue) P_t.

$$2\pi r j_{tv} = 2\pi r \gamma (P - P_t) \tag{2.1}$$

In equation 2.1, r denotes the vessel radius and γ describes a phenomenological mass transfer coefficient determined from current literature values (details listed in the supporting information "S1 Appendix: Model details and validation" reprinted in chapter 3.1.2 starting on page 98 of this dissertation). We modeled the

Dataset type	Hierarchical Iterations	Lateral Extent	Runtime greens function	Runtime Tumorcode	Number of circulated segments	g0method
Mesent28_10_subset	-	2350 μm	0m47s	0m19s	445	2
artificial	0	0550 μm	2m47s	0m10s	83	1
	1	1200 μm	0m58s	0m31s	154	1
	2	2200 μm	5m52s	1m39s	352	1

Table 2.1: Simulation details for comparing the Green's function based method with the finite differences based method. Runtimes measure on standard desktop computer (Intel(R) Core(TM) i7-4770K CPU @ 3.50GHz) and Ubuntu 16.04.

tissue oxygen consumption rate $M(P_t)$ according to the standard Michaelis- Menten relation [135].
For our computational study, we used 90 different artificial blood vessel networks: 10 samples for each of the 9 root node configurations (see figure 3 of [1]). Given the initial vasculature, we simulated our oxygen model in three different variants: the case *BASE* with no additional assumptions, the case *CMPR* including vascular compression by the tumor and the case *METAB* varying the oxygen consumption rate inside the tumor tissue. After validating the simulations by comparing them to available literature values, we conclude that: 1) the variance of tissue hemoglobin concentration, tissue blood oxygen saturation and perfusion results from individual initial vascular configurations; 2) vascular compression causes low tumor oxygen saturation and 3) the high tumor blood flow rates outweigh the increased oxygen demand.

Our published paper links the statistical variations observed in [133] to the topology and spatial distribution of blood vessel networks confirming several other conjectures about solid tumor (see "Results and Discussion" of the paper).

2.1.3 Personal contributions

I revised the manuscript and assisted Dr. Michael Welter during software development by testing and debugging his implementations. In his implementation, Dr. Michael Welter modified the presumably more accurate numerical methods described in [131] and [135] towards faster execution, but more coarse grained resolution. Using "small" (discussed in the following) synthetic blood vessel networks enables a direct comparison of the two implementations with each other and was executed by the author of this dissertation (see supplemental information "S1 Appendix" of [1] and section 3.1.2 starting on page 98 of this dissertation). Supplementing the already published data, I will discuss my comparison in more detail here.

I downloaded the program implementing the numerical method described in [131] from https://physiology.arizona.edu/people/secomb/greens and applied minor modifications allowing execution of the software on current linux systems (tested with Ubuntu 16.04, Ubuntu 18.04 and archlinux 4.18.14). I host the modified version of the software together with data format modifying scripts on my GitHub site (https://github.com/thierry3000/green_function_method). The scripts convert data files into each others counterpart with the correct file structure considering two main points: 1) Secomb et. al. used units common in medicine (pressures in mmHg and flows in $\frac{nl}{min}$) while Tumorcode uses SI units (kPa for pressure and $\frac{\mu m^3}{s}$ for flows) and 2) the indexing of the boundary conditions differs. However both programs index fixed flow boundary conditions by "2", the Tumorcode software indexes fixed pressure boundary conditions by "1" (see "*calcflow_linsys.h*") and the implementation of Secomb et al. labels fixed pressure boundary conditions by "0". With the converting scripts at hand, I set up a comparison of the two implementations by applying the Green's function based method [131] to artificial blood vessel networks created by the Tumorcode software and applying the finite differences based approach described in [1] to the data set *Mesent28_10_subset* measured by Secomb et al. (see table 2.1, figure 2.1 and figure 2.2).
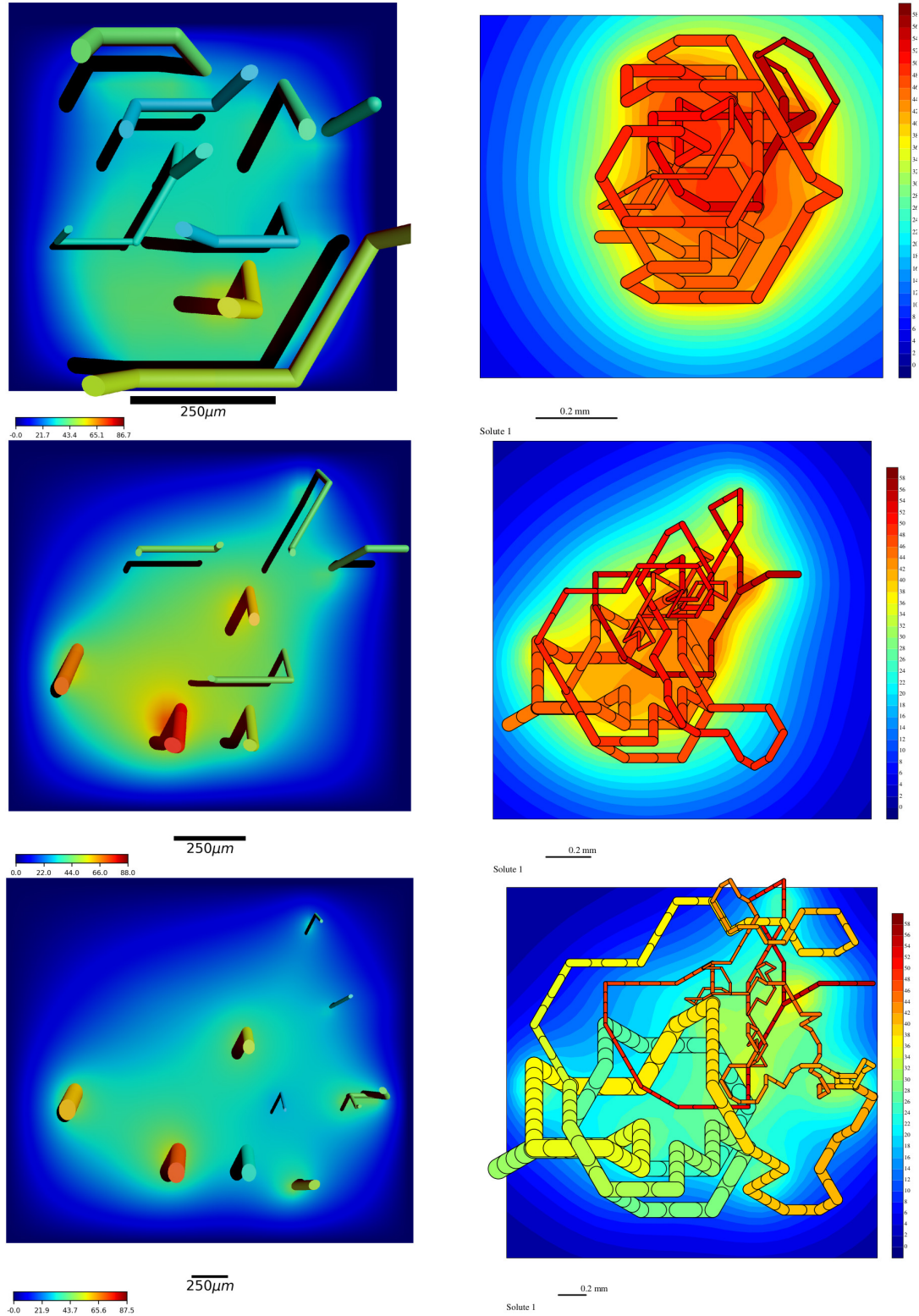
Figure 2.1: Plot of pO$_2$ field for artificial blood vessel networks created by the Tumorcode software. From top to bottom the number of hierarchical iterations during the network creation step increases from 0 to 2. Note the increasing lateral size (550 μm to 2200 μm). All color codes represent mmHg. Left column: pO$_2$ field calculated by the finite difference method described in [1] and implemented in the Tumorcode software. For a clear view on the distribution, the visualization with with POV-Ray truncates the vessels above the data slice. Right column: pO$_2$ field calculated by the Greens function based method [131] and visualized by their code.

CHAPTER 2. OWN WORK

2.1. COMPUTATIONAL MODEL FOR TUMOR OXYGENATION APPLIED TO CLINICAL DATA
ON BREAST TUMOR HEMOGLOBIN CONCENTRATIONS SUGGESTS VASCULAR DILATATION
AND COMPRESSION

(a) Finite Differences based method implemented by the Tumorcode software. Colors scale between minimum and maximum value of pO$_2$.

(b) Green's function based method implemented by Secomb et. al. Colors scale continuously according to the pO$_2$ color bar on the right.

Figure 2.2: Plot of oxygen partial pressure (pO$_2$) distribution for the mesentery data set (*Mesent28_10_subset*) measured by Secomb et al. All color codes represent mmHg.

Green's function based method to artificial vasculature I created three artificial blood vessel networks with root node configuration 5 (RC5, see figure 3 in [1]), increasing lateral size and hierachical iterations ([2]) using the Tumorcode script "*submitVesselgeneration.py*" with the parameter set "asymmetric" ("*parameterSetsVesselGen_generic.py*"). After construction of the blood vessel networks, I applied the finite difference based method ("detailedO2" in the Tumorcode software) to calculate the oxygen field of the constructed vessel networks with the parameter set "Artificial_tumorcode" ("*parameterSetsO2_generic.py*"). The left column of figure 2.1 displays a visual representation of the pO$_2$ fields calculated by the finite difference based implementation. Next, I exported the artificial blood vessel networks created by the Tumorcode software to the vessel network data format used in the implementation of Secomb et al. ("*vesselhdfToSecombNetwork.py*"). By manually adjusting the file "SoluteParams.dat" and the total inflow of blood into the network for each vessel network separately, I converted the parameter set of the Tumorcode software ("Artificial_tumorcode") to the equivalent required by the implementation of Secomb et al. A complete list of the parameters is stored at my GitHub repository. The right column of figure 2.1 displays a visual representation of the pO$_2$ fields calculated by the Green's function based implementation.

With increasing hierarchical level (from top to bottom), the variation in intravessel pO$_2$ increases because of the increasing length scale. Note that the overall lateral size increases from 550 μm to 2200 μm similar to the length scale of the data sets released with Secomb's software (e.g. *Mesent28_10_subset*). In contrast to the finite difference method of the Tumorcode software, the runtime for the Green's function method does not scale with the system size in the presented examples. As discussed in [131], the implementation of the coupling between vessel and tissue depends on the spatial vessel arrangement in the network and therefore variation of the vessel networks significantly affects the runtime. This is where the mean field approach of the finite difference method outperforms the Green's function based approach. With increasing system size, the deviation between the two methods becomes smaller. With a single hierarchical iteration at the network creation step (central row of figure 2.1), the outline of the two pO$_2$ distributes are similar and with two hierarchical iterations at the network creation step, (bottom row row of figure 2.1) the details overlap.

Finite differences method to the data set *Mesent28_10_subset* The dataset *Mesent28_10_subset* was measured from a rat mesentery network [131] (available for download at http://www.physiology.arizona.edu/people/secomb/greens_c3). I exported the dataset *Mesent28_10_subset* to a format compatible with the Tumorcode software ("*secomb2hdf2.py*"). After exporting, I applied the finite difference based method (implemented in "*submitDetailedO2.py*") using the parameter set "Artificial_tumorcode" (see "*parameterSetsO2_generic.py*") to the *Mesent28_10_subset* dataset. Figure 2.2 compares the two pO_2 fields obtained with the different methods (Green's function based method and finite differences based method).

The finite difference based method runs more than twice as fast as the Green's function based method (19 seconds vs. 47 seconds, compare table 2.1). A visual difference between the two images shown in figure 2.2 appears along the major veins at the periphery because of two main reasons: First, the Green's function approach uses a hematocrit stored in the measurement file (in the case of *Mesent28_10_subset*, 40% for all segments) while the artificial blood vessel networks lack a measured value of hematocrit. Instead the Tumorcode software calculates the hematocrit from the physiological assumption that the hematocrit propagates downstream in the arterial branch. Fixing the hematocrit at all arterial inlets of the network allows successive calculation of all vessel's hematocrit. In the calculation, the Tumorcode software includes the Fåhræus–Lindqvist effect [136] and the phase separation effect [137]. Second and similar to the hematocrit problem, the Tumorcode software neglects any measured pO_2 value along the vessel network, but solely relies on the fixed pO_2 values at the arterial inlets. The Green's function based method follows a more sophisticated approach including the measured pO_2 values along the blood vessels (compare equation 20 in [131]). In summary, the pO_2 distributions shown in figure 2.2 are qualitatively similar however figure 2.2b shows stepper gradients compared to figure 2.2a.

The two considered programs implement different methods to solve similar, albeit not the same, equations describing the partial oxygen pressure in tissue penetrated by blood vessel networks. A qualitative data comparison is not compelling, but I showed that the results agree with each other. In addition, further testing confirmed that calculating the pO_2 saturation with the Green's function based approach exceeds moderate memory and time limitations for large synthetic blood vessel networks.

2.2 Tumorcode - A framework to simulate vascularized tumors

The original research article entitled "*Tumorcode - A framework to simulate vascularized tumors*" was published at the 26th of April 2018 in the European Physical Journal E. I reprinted the article with permission (see appendix G) in section 3.2 starting on page 115 of this dissertation.

2.2.1 Background

When I started my PhD in 2013, the Tumorcode software was already present albeit not in the current form. Dr. Michael Welter successively developed large parts of the software base on original work from Bartha et. al. ([34, 138]). During our common time in the research group of Prof. Dr. Dr. h.c. Heiko Rieger, Dr. Welter introduced me to the relevant algorithms and taught me how to use the code in personal communication. Bearing the idea of open science in mind (section 1.4), I realized that a written introduction to the code and some examples would be helpful for other scientists in the field.

The European Physical Journal E "Soft Matter and Biological Physics" features a section called Tips and Tricks (T&T) sharing previously unpublished state of the art research methods which the Tumorcode software in fact was.

2.2.2 Summary of the paper

After a short introduction to the topic, I described the "Design and implementation" principles of the Tumorcode software in section 2 of [2] (reprinted in section 3.2). Most importantly, the Tumorcode software presents a hybrid between the two programming languages *C++* and *Python*. Executable machine code build from *C++* source code tailored to the underling hardware results in optimal performance. However the optimal performance, the code development and compilation of the *C++* programming language is often tedious. In contrast to the *compiler based* approach of *C++*, the *interpreter based* approach of the *Python* programming language simplifies implementation effort because *Python* scripts instruct the *Python* kernel rather than creating real machine-readable executables. Without thinking too much about the struggles present in classical programming languages like datatypes and memory layout, *Python* allows fast prototyping of problems and the scientific community offers a lot of packages optimized for different situations.

In the Tumorcode software, computational extensive tasks such as solving sparse matrices to obtain the hydrodynamics of the blood flow network; solving diffusion convection reaction equations modeling the tumor growth, nutrient and oxygen transport (section 1.3); and various demanding measurement tasks are forwarded to a computational core written in *C++*. This way, the Tumorcode software benefits from the high performance of the *C++* programming language and the handy features of the *Python* programming language at the same time.

In section 3 "Workflow", I described the typical workflow of the simulations conducted with the Tumorcode software: 1) we create an artificial blood vessel network (algorithmic details reported in [5]); 2) we grow a tumor, either by continuum diffusion reaction equations (section 1.2) or by a fake tumor simulation that comprises a homogeneously expanding spherical tumor mass including the full vessel remodeling procedure; 3) we apply one of the sophisticated biological models to the vessel network snapshots stored during the tumor simulation, before we 4) optionally analyze or visualize any simulation step.

In section 4 "Applications", I summarize the two cases ([1] and [37]) where step 3) (the application of the sophisticated biological models) resulted in original research publications. The interstitial fluid pressure (IFP) is an experimentally hardly accessible quantity, which is highly relevant in chemotherapy because the extravascular drug transport is driven by the IFP gradient. One of the biological models calculates the interstitial fluid pressure based on the vessel arrangement, vessel wall conductivity parameters and Darcy's law. Assuming convective transport of drugs driven by the IFP gradient, the interstitial fluid flow module estimates drug distributions in vascularized solid tumors [37].

Oxygen is a key player in cell metabolism. The transport of oxygen in animals or humans is a complicated problem by itself (see section 1.1.3) happening in two distinct phases: in bound state where the oxygen molecule couples to red blood cells (RBCs) streaming along in the blood and in a diffusive state when the oxygen molecule uncouples from the RBCs. Similar to the IFP distribution, the distribution of unbound oxygen inside tissue heavily depends on the arrangement and condition of blood vessels. We modeled the two kinds of oxygen transport and traced the oxygen saturation during the progression of cancer. With this model we explained the variation in blood oxygen saturation dependent on the total haemoglobin concentration as measured by Grosenick et al. ([133]) in 87 breast carcinomas (see section 2.1).

In addition to the main text, I compiled 8 supplements (3 digital supplements "suppl-file1.zip", "suppl-file2.mov", "suppl-file3.avi" and 5 supplements in text form "suppl-file4.pdf" to "suppl-file8.pdf"). "suppl-

file1.zip" contains a snapshot of the source code at time of publishing the article, "suppl-file2.mov" illustrates the network creation process in a movie and "suppl-file3.avi" shows a growing tumor simulated and rendered by the Tumorcode software. The remaining five supplements (reprinted in subsection 3.2.2 of this dissertation starting on page 124) illustrate how the data used in main text (vessel networks, tumor simulations, IFP distribution, oxygen distribution) was obtained by the Tumorcode software:

suppl-file4.pdf describes how to create vessel networks with Tumorcode;

suppl-file5.pdf describes how to run tumor simulations with Tumorcode;

suppl-file6.pdf describes how to calculate interstitial fluid pressure and drug transport with Tumorcode;

suppl-file7.pdf describes how to calculate detailed oxygen distributions with Tumorcode;

suppl-file8.pdf describes how to use the visualization tools implemented in Tumorcode.

2.2.3 Personal contributions

I conceived and wrote the manuscript of [2], provided the data comprising all figures and illustrations, and communicated with the editor and referees of the publishing journal (The European Physical Journal EPJ). During my Ph.D. studies, I made considerable contributions to the Tumorcode software package illustrated in the following.

2.2.3.1 Software development

I eased the required technical background to use the Tumorcode software. Since a very broad community studies cancer, the knowledge about (linux) software development required to use the Tumorcode software should be as moderate as possible. To this end I:

- created a cmake installation routine allowing inexperienced users to build and install the software,

- trimmed the source code to the standard folder structures and to the standard naming conventions used in other open source ($C++$) projects,

- added lots of comments to the source code in the doxygen style helping other software developers to understand the algorithms

- used python's "argparse" concept (see https://docs.python.org/2.7/library/argparse.html) to include help messages for command line arguments of the main routines (e.g. "submitVesselgeneration.py", "submitBulkTissue.py" and "submitPovrayRender.py")

- tested the source code on different standard operating systems (Ubuntu 16.04, Ubuntu 18.04, ArchLinux, Hardened Gentoo 4.1.7) and provided corresponding installation scripts.

As mentioned earlier, an important feature of the Tumorcode software is the simultaneous usage of two programming languages: the $C++$ language used in the computational core and the *Python* programming language used for fast and straight forward prototyping of problems.
Numpy is the standard package for numerics in the *Python* programming language. In the past, Dr. Michael Welter used his code (https://github.com/DaWelter/numpycpp) to implement the interface between the computational core of the Tumorcode software and the numpy package. Starting with version 1.64, the boost library offered an interface to numpy called boost::numpy (see https://www.boost.org/doc/libs/1_64_0/libs/python/doc/html/numpy/index.html). Therefore I replaced the subproject "numpycpp" in the Tumorcode software with the newly available standard option provided by the boost library.
The Tumorcode software stores data in the HDF5 file format. The Hierarchical Data Format (HDF) stores and organizes large amounts of heterogeneous data while allowing easy sharing, cross platform usage and metadata storage within the same file. Dr. Michael Welter implemented an $C++$ interface to the HDF5 file format (https://github.com/DaWelter/HDF5-cpp-wrapper) and used his implementation throughout coding the computational core of the Tumorcode software. Starting with the minor release version 1.10, the HDF5 file format provided an interface to the $C++$ programming language. Therefore I replaced the subproject "HDF5-cpp-wrapper" in the Tumorcode software with the newly available default option.

2.2.3.2 Cartesian coordinates/ Boundary conditions

Before I joined the project, the hydrodynamic solver of the Tumorcode software worked with vessels on lattices and fixed pressure boundary conditions only. To deal with experimental data sets such as the one shown in figure 2.2, I extended the $C++$ simulation core to work with arbitrary Cartesian coordinates as input and extended the hydrodynamic solver to work with flow and mixed boundary conditions simultaneously.

2.2.3.3 Continuation of simulation runs

Typically, High Performance Computing (HPC) facilities assign a maximum "Wall time" $(< \infty)$ to computing jobs enabling them to maintain and fix hardware on the fly and to fairly distribute resources among the users.

The typically runtime of Tumorcode simulations exceeds maximal "Wall time"s preventing an execution of the Tumorcode software on HPC facilities. To overcome the drawback of runtimes exceeding maximal "Wall time"s, I implemented the possibility of consecutive runs of a single simulation. At runtime, the Tumorcode software buffers the current simulation state on the hard disk (in HDF5 file format) allowing to continue the simulation from the latest simulation state before exceeding the maximum wall time (rerun option in the "submit"- scripts).

I tested this option successfully on marconi at CINECA for the "fakeTum" simulation combined with Virtual Biology Lab (VBL, see section 2.3.3) tool.

2.2.3.4 Solver

Solving sparse linear systems (see section 1.3) naturally occurs when dealing with finite elements or finite difference methods ([139]) and solving the Hagen- Poiseuille equation in large flow networks ([2]). "Belos" ([111]) and "Ifpack2" ([140]) both contribute to the Trilinos project (https://trilinos.github.io/index.html), and in combination, they are well suited for the sparse matrix problems occurring the scope of the Tumorcode software. By replacing all solvers with these two options from Trilinos, the code became more structured and easier to maintain. Further, "Ifpack2" implements state of the art algorithms ready for parallel computing which will become an important aspect in future.

2.2.3.5 Data Cache

Analyzing large data sets could be tedious and very computational expensive. "Data caching" remembers costly obtained data. Subroutines equipped with a data cache store the input arguments and the output for every call. At each call of a cached subroutine, "the cache" checks for previous calls with identical arguments. In case the subroutine was called with identical arguments before, the data cache reads the output from disk instead of starting the (costly) computation again.

Dr. Michael Welter began to implement this concept in the Tumorcode software starting in 2015. Together we improved the implementation of the data cache and used data caching throughout the data analysis resulting in [1] (reprinted in section 3.1 on page 55 of this dissertation).

In successive code development, I applied the concept of data caching at plenty of appropriate locations.

2.2.3.6 Visualization

To communicate results effectively in an interdisciplinary environment, visualizations of the problems are obligatory. Computer graphic's methods of creating visualizations distinguish between two main fields approaching each other in recent years [141]: the realistic image synthesis and real time rendering. Realistic image synthesis aims at creating most realistic images including relevant physical details like illumination, light scattering and refraction. The artist describes a virtual scene in an abstract language and the computer translates the description of scene into pixels of an image ignoring computational costs. As the name suggests, real time rendering provides interactive scene modifications. To mimic "realtime", considering the computational costs is essential because real time rendering requires that the calculations run faster than the reaction time of the human visual stimulus (about 50 ms).

The Tumorcode software features both possibilities (realistic image synthesis and real time rendering). By means of realistic image synthesis, the Tumorcode software renders large vascular networks with hundreds of thousands of vessels outrunning real time rendering on current hardware devices. For the realistic image synthesis, the Tumorcode software uses the "Persistence of Vision Raytracer" (POV-Ray, http://www.povray.org/) as an open-source, high-quality software tool for creating stunning three-dimensional
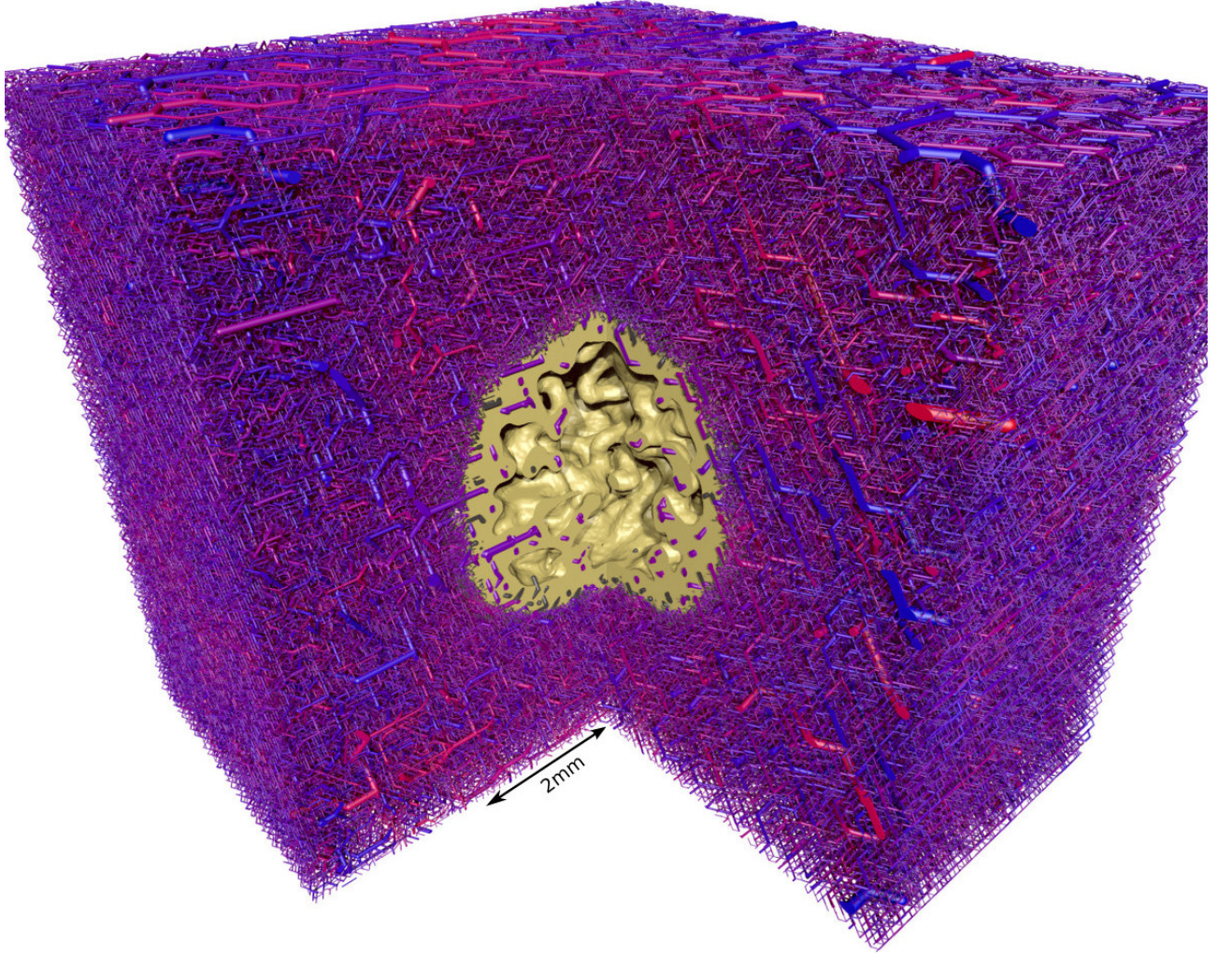
Figure 2.3: Visualization of the necrotic core inside a vascularized tumor rendered with the realistic image synthesis of POV-Ray. Depicted is a simulated tumor and tumor blood vessel network at the age of about one month (700 h). The full simulation cube of 8 mm lateral length is shown where a quadrant is cut out to improve visibility. The interface of viable tumor mass to the necrotic core is shown in yellow. The vessels are color coded according to their blood pressure. The bulk of volume surrounding the (yellow) tumor spheroid is filled with the initial vascular network. It appears solid due to the large amount of vessels (more than 3 million), but the vessels only fill about 10% of the available volume. Reprinted (with permission, see page 238 of this dissertation) from figure 6 of [5].

graphics [142]. Each single blood vessel is rendered as cylinder. To provide visual continuity at the intersection of two vessels in a blood vessel network, a sphere with the radius of the cylinder is added at each intersection. Figure 2.3 shows an example of a large vessel network rendered by POV-Ray.

For real time rendering, the Tumorcode software exports to the "Visualization Toolkit" (VTK) data format. VTK is open source software for manipulating and displaying scientific data using state-of-the-art tools in 3D rendering and data analysis. The graphical user interface based on VTK (called ParaView [143, 144], www.paraview.org) allows to explore small to intermediate size (depending on the graphic hardware) blood vessel networks in realtime. Figure 2.4 shows two images created by the VTK file export of the Tumorcode software and ParaView.

I maintained and updated the interface of the Tumorcode software to POV-Ray and to the VTK data format meeting the file structure of current POV-Ray, VTK and ParaView versions. In addition, I extended the interface by adding new features like:

- ParaView output for scalar fields such as growth factor distribution shown in orange in figure 2.4a to the Tumorcode software;

- new clipping, coloring, overlay, filter and camera options to the POV-Ray interface ("submitPovrayRen-
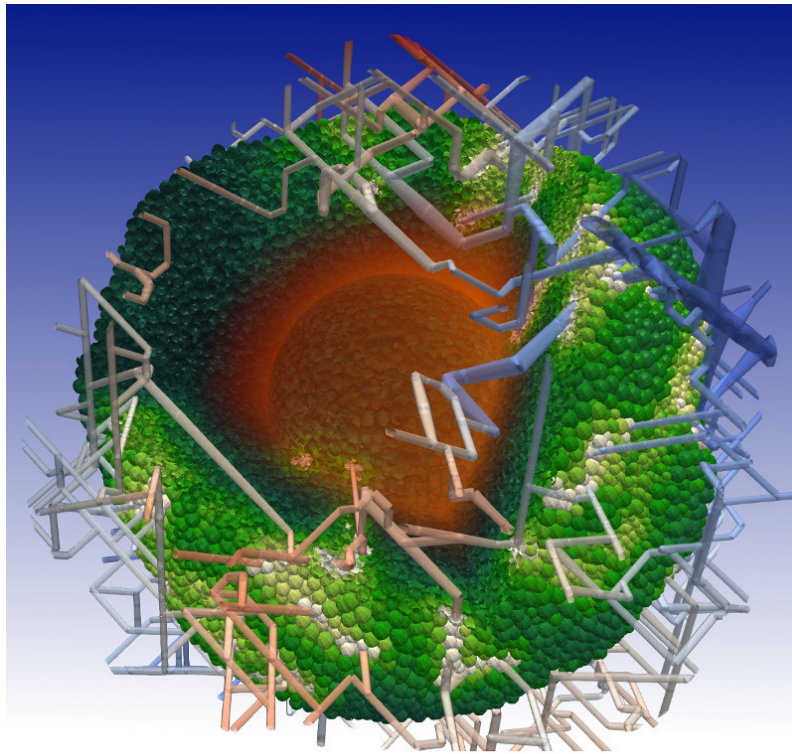
(a)
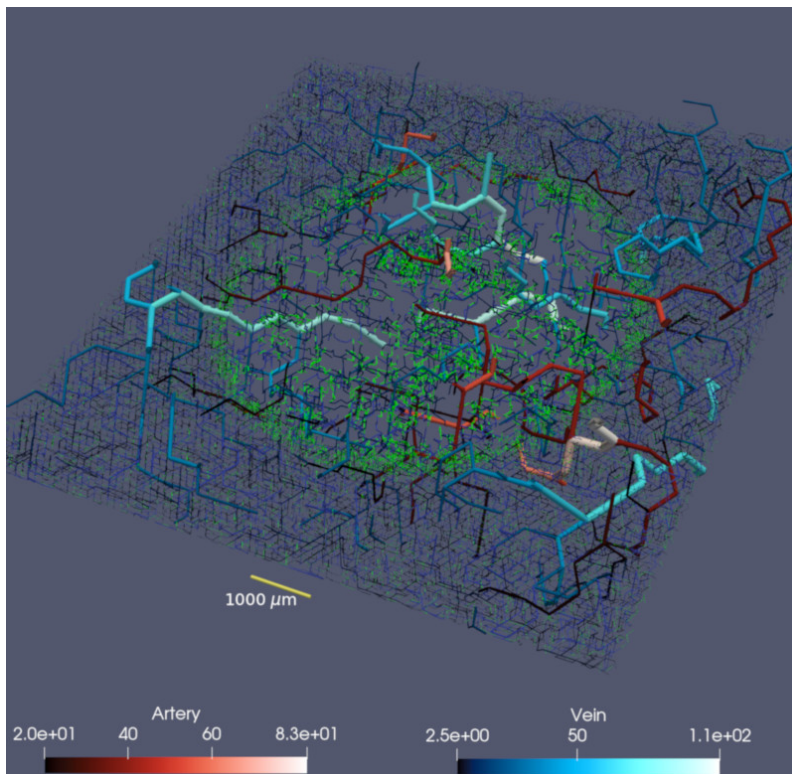
(b)

Figure 2.4: Two visualizations of vascularized tumors rendered with VTK and Paraview. The features of ParaView allow to extract and clip subsets, color data according to arbitrary color codes and interactive scaling and rotating.Top (a): pH level in vascularized tumor spheroid - vessels are color coded by blood pressure, cells by pH level, the fading orange in the center indicates the amount of vascular endothelial growth factor (VEGF) released by the cells.Bottom (b): $500\mu m$ thick slice through tumor vasculature of 1cm lateral size. For 3D illustration, vessels with radius bigger than $20\mu m$ are continued for another $750\mu m$ above and below the extracted slice. Vessels are colorcoded by their radius according to the lower panels: arteries are displayed in varying reddish color and veins in varying blueish color (unit of colorbar is μm). Capillaries and young vessels with radius of 2.5 μm are shown in green. Reprint figure 2 of [3] with permission.

der.py"). Some of them are used in the videos at https://doi.org/10.6084/m9.figshare.7406183.v1 and https://doi.org/10.6084/m9.figshare.7406180.v1 ([145, 146]);

- incorporation of information provided by the Virtual Biology Lab simulation ([3] and section 3.3) to the VTK/ParaView and the POV-Ray interface.

2.3 Fine-grained simulations of the microenvironment of vascularized tumours

The original research article entitled "*Fine-grained simulations of the microenvironment of vascularized tumours*" was published at the 12th of August 2019 in the journal "Scientific Reports". I reprinted the article with permission (see appendix G at page 215) in section 3.3 starting on page 141 of this dissertation.

2.3.1 Background

Although genetics certainly contributes to the diversity of cancer, the contribution of the diversity in the local environment to the diversity of cancer attracted the interest of the community recently. Meanwhile, it is well known ([101]) that the tumor microenvironment is a very complicated and heterogeneous entity affecting the progression of solid tumors. Moreover, the tumor microenvironment is often involved in cancer therapy e.g. in chemotherapy or in radiotherapy and therefore, an integral understanding of the tumor microenvironment is not only of scientific interest, but also of high clinical relevance.

Solid tumors grow in two phases: first, in an avascular phase not actively involving the vasculature for the nutrient transport and second, in a vascular phase actively involving the blood vessels for the nutrient transport. In the avascular phase, the tumor spheroid is typically smaller than the average distance between capillary vessels and the nutrient transport happens solely by diffusion resulting in a characteristic spherical symmetry of the tumor spheroid. Once the size of a tumor spheroid exceeds the average blood vessel distance, the topology of the blood vessel network breaks the spherical symmetry influencing the nutrient supply and modifying the further tumor growth process. During progression, solid tumors even remodel the structured blood vessel networks of healthy tissue towards irregular and unstructured networks comprising dilated and leaky vessels. Healthy tissue features a high oxygenation and, a balanced pH and interstitial fluid pressure levels. Tumor tissue, however, features hypoxia, acidosis and elevated interstitial fluid pressure level ([34]). The angiogenic switch [32] defines the moment when an avascular tumor spheroid turns into the vascular growth phase. In the publication "*Fine-grained simulations of the microenvironment of vascularized tumours*" ([3]), I simulated the growth of a multicellular tumor spheroid at the angiogenic switch looking at the oxygenation of the tumor microenvironment in more detail.

2.3.2 Summary of the paper

After the introduction, I give a brief outline of the two combined computer programs: the "Virtual Biology lab" (VBL) and the Tumorcode software. The VBL software simulates the growth of avascular tumor spheroids including the cell cycle of each individual cell. The Tumorcode software simulates solid tumor growth at large scales including realistic blood vessel networks and vascular remodeling dynamics during tumor growth. Both programs have been verified separately in previous publications. The results obtained by VBL were tested against data from in vitro experiments ([147]) and the results obtained by the Tumorcode software were tested against data from in vivo experiments ([1, 148]).

In the next section "The Merging of the Two Programs", I discuss the developed interface combining the two simulations before I describe the main simulation setup in the section "Development of the Microenvironment in Small Solid Tumours". I computationally studied the development of small solid tumors starting from three distinct locations inside a small synthetic arteriovenous network: at the center of the vessel network, in the middle of a venous bifurcation and in the middle of an arterial bifurcation. This way, I studied the early formation of the tumor microenvironment considering the vascular remodeling at the angiogenic switch.

I observed a large spatial and temporal variability inside the tumor microenvironment promoting the formation of ecological niches. In the "Conclusions" of the manuscript, I conjecture that the high niche diversity enables "Darwinian selection" in solid tumors supporting the clonal section hypothesis [149, 150].

2.3.3 Personal contributions

Solid tumors are multicellular entities. The Tumorcode software and the related earlier publications [1, 37, 148] modeled tumors by continuum equations (see section 1.2.2 "Continuum models") neglecting cellular details in favor of larger system sizes. Since inhomogeneities and large chemical gradients characterize the tumor microenvironment, a realistic tumor model necessitates the inclusion of the cellular details to explain the inhomogeneities and the chemical gradients.

In [147], Prof. Dr. Edoardo Milotti et al. simulated an avascular tumor spheroids by an off-lattice method (compare section 1.2.1) called Virtual Biology Lab (VBL). I combined the Tumorcode software and the VBL
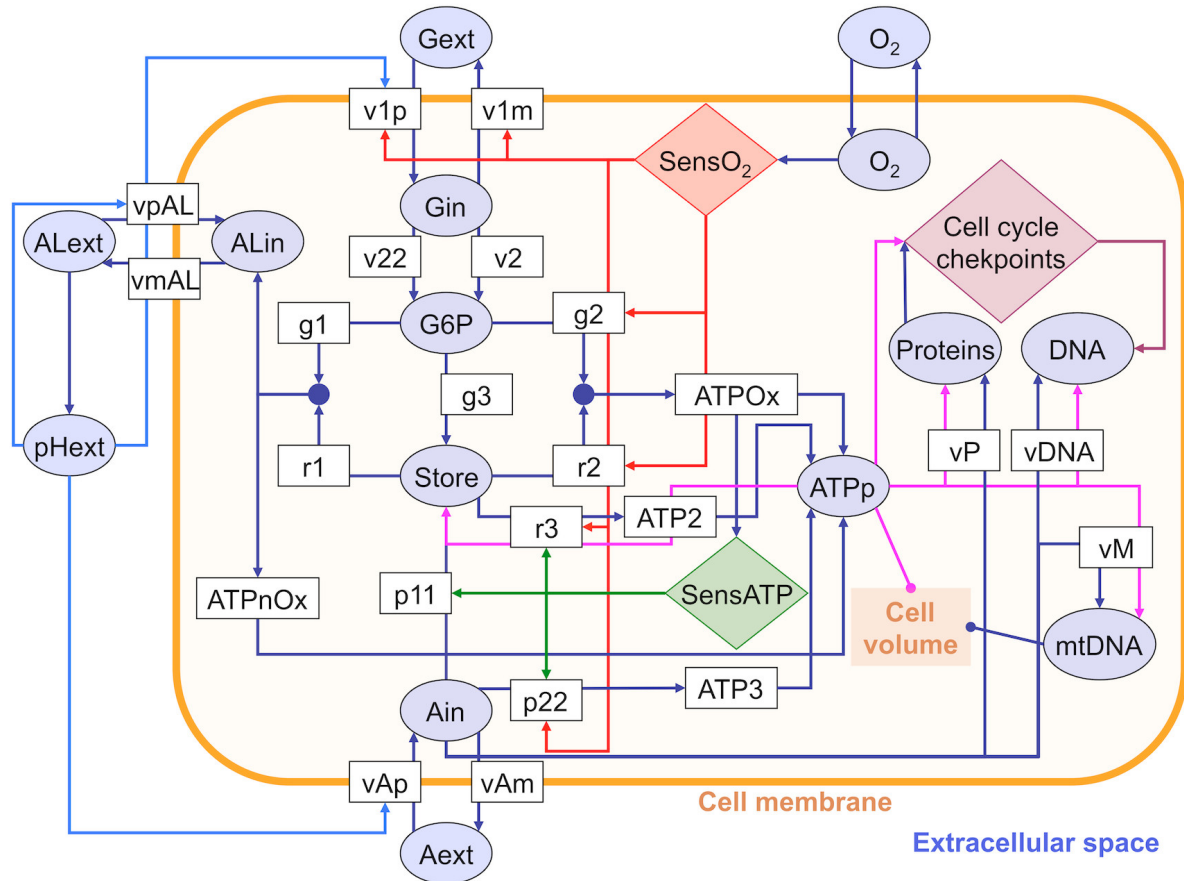
Figure 2.5: Sketch of the metabolic network used in VBL. Variables within circles represent molecular species. The suffixes ext and int indicate extracellular and intracellular variables respectively: G=glucose, G6P=glucose-6-phosphate, STORE=glucose stored in the form of glycogen, AL=lactic acid, A=glutamine, ATPp=pool of ATP molecules, DNA=nuclear mass of DNA (normalized to 1 for the whole genome), mtDNA=mitochondrial DNA. Variables within rectangles represent rates. The red circuit represents the oxygen sensor, whereas the green circuit represents the ATP sensor [151, 152]. "Cell cycle checkpoints" denotes the molecular circuit of cell cycle control that has been modeled on the basis of previous studies on the dynamics of the allosteric effect [153, 154]. The biological foundations of this simplified metabolic network have been given in [151, 152]. Recent improvements with respect to earlier previous models include: internalization rates of glucose, glutamine and lactate are sensitive to extracellular pH and this dependence is now described by smoothed functions [147]; synthesis of cellular proteins, nuclear DNA and mitochondrial DNA are now described by double-substrate Michaelis-Menten chemical reactions to take into account the dependence of protein and nucleic acid biosynthesis on glutamine (which stands phenomenologically for the wider class of aminoacids) and ATP availability.
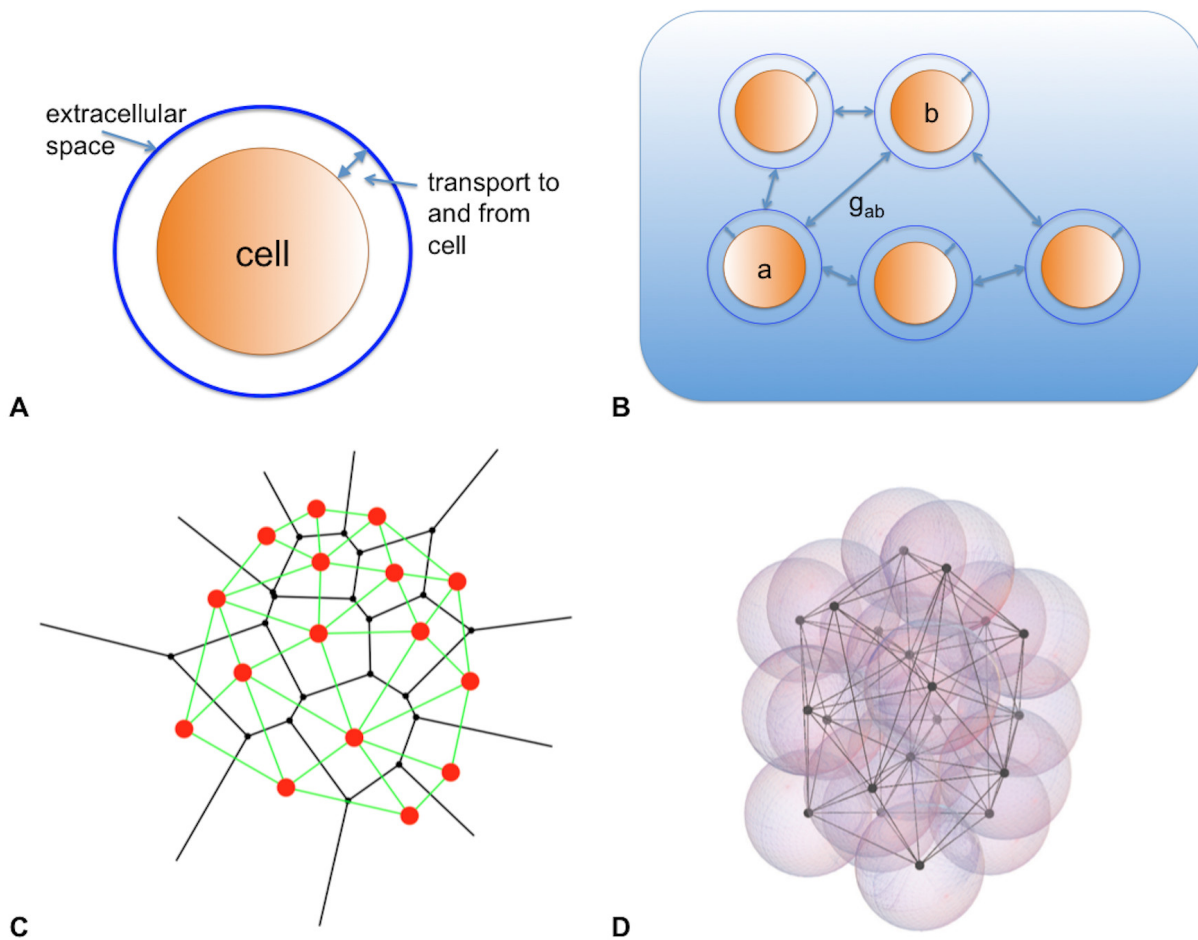
Figure 2.6: The geometry and topology of diffusion. a) Most substances are carried into and out of the cells by facilitated diffusion and there is an active mass exchange between cell and extracellular space. Each cell in the simulation program has its own extracellular space. b) Extracellular spaces are interconnected and there is a diffusion flow through the network of connections. c) The network of interconnected spaces is defined by a Delaunay triangulation. In this 2D representation, for any red dot we can define a Voronoy cell, i.e., the set of points in the plane that are closer to the given dot than to any other dot in the set. The dual structure is the Delaunay triangulation (Voronoy cells are black and Delaunay links are green). There is a Delaunay link between any two dots only if the respective Voronoy cells touch each other, therefore we can use the Delaunay triangulation to define proximity. This enables us to set up a discretized version of diffusion between extracellular spaces, like in b). In addition to the topology of contacts between cells we also keep into account geometry: g_{ab} in part b) is a geometric factor that modulates diffusion. d) The actual simulation is in 3D: here the Delaunay triangulation of a small cluster of cell centers shows up in transparency.
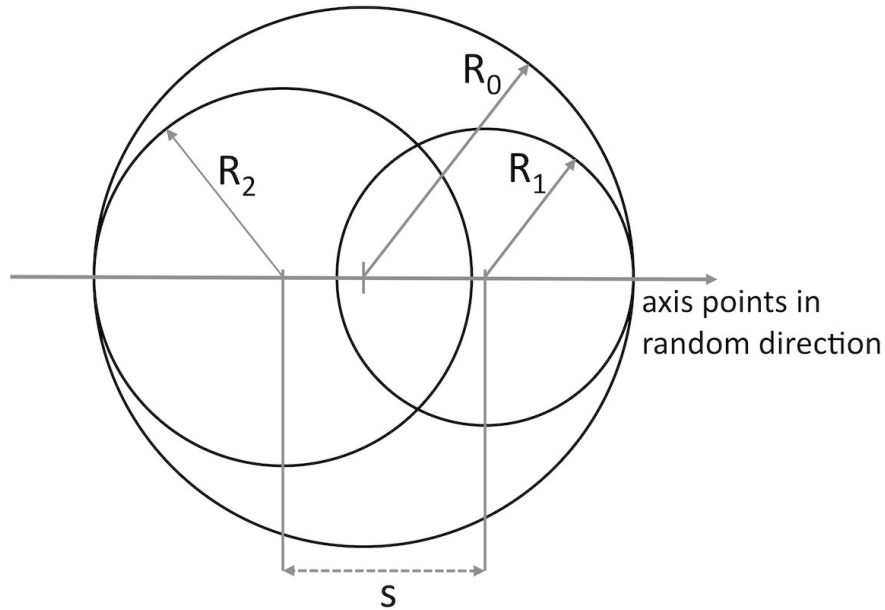
Figure 2.7: The geometry of mitosis in VBL. R_0 denotes the radius of the initial mother cell, while R_1 and R_2 denote the radii of two daughter cells. Because of random asymmetries during mitosis, the daughter cells usually have different sizes. The program places the two daughter cells inside the region initially occupied by the mother, and the axis connecting the centers points in a random direction. Placing the to daughters closer than R_0 forces the two cells to push against each other separating and rotating the axis. The new cells' centers separate by roughly 0.4 R_0.

Reprinted figure S5 of [147] available at https://doi.org/10.1371/journal.pone.0013942.s006.

software to a hybrid simulation including the cellular and the macroscopic level as reported in the main manuscript.

I performed data analysis and data visualization to provide the displayed figures. To present my analysis of the simulation runs, I wrote the results section and revised the manuscript together with all coauthors. As corresponding author, I communicated with the manuscript assistant, the publishing assistant, the editor and the referees of the publishing journal ("Scientific Reports").

Since I used the implementation of the VBL model extensively in [3] (section 3.1.1), I present the main modeling assumptions of VBL and comment on my personal implementation efforts in the following.

2.3.3.1 Modeling assumptions of VBL

VBL models individual cells as perfect spheres. Apart from the 3D position and the cell volume, 15 biochemical variables (circles inside the cell membrane illustrated in figure 2.5) such as nuclear mass of DNA or mass of glucose characterize the internal state of each cell. Figure 2.5 visualizes the equations linking the variables. Since VBL links the cellular volume to the present amount of DNA, to the present amount of ATP and to the number of mitochondria (equation S.22 in supporting text to [147]), the equations visualized in figure 2.5 model the cell volume correspondingly.

Except oxygen, other substances included in the model cannot diffuse freely across the cell membrane because of the complex structure of the membrane (section 1.1.1). Therefore VBL uses facilitated diffusion from the extracellular space into the cell volume. In the model, a slightly larger sphere surrounds each VBL cell mimicking the extracellular space (panel A in figure 2.6). The mass of glucose, the mass of lactic acid, the mass of glutamine and the pH (circles outside the cell membrane illustrated in figure 2.5) characterize the extracellular space in VBL. These four extracellular parameters and the oxygen content link to the internal biochemical pathways (figure 2.5) modeling the transport to and from a single cell across the cell membrane. The spheres modeling the extracellular space are linked to implement the multicellular interaction (panel B in figure 2.6). To link individual cells, VBL approximates the facilitated diffusion process between neighboring cells using a Delaunay triangulation. The Delaunay triangulation constructed from the centers of all spheres provides geometric information (Voronoy cell surfaces and distances to the neighboring cells) and the VBL software models the (facilitated) diffusion process proportional to the geometric information (g_{ab}
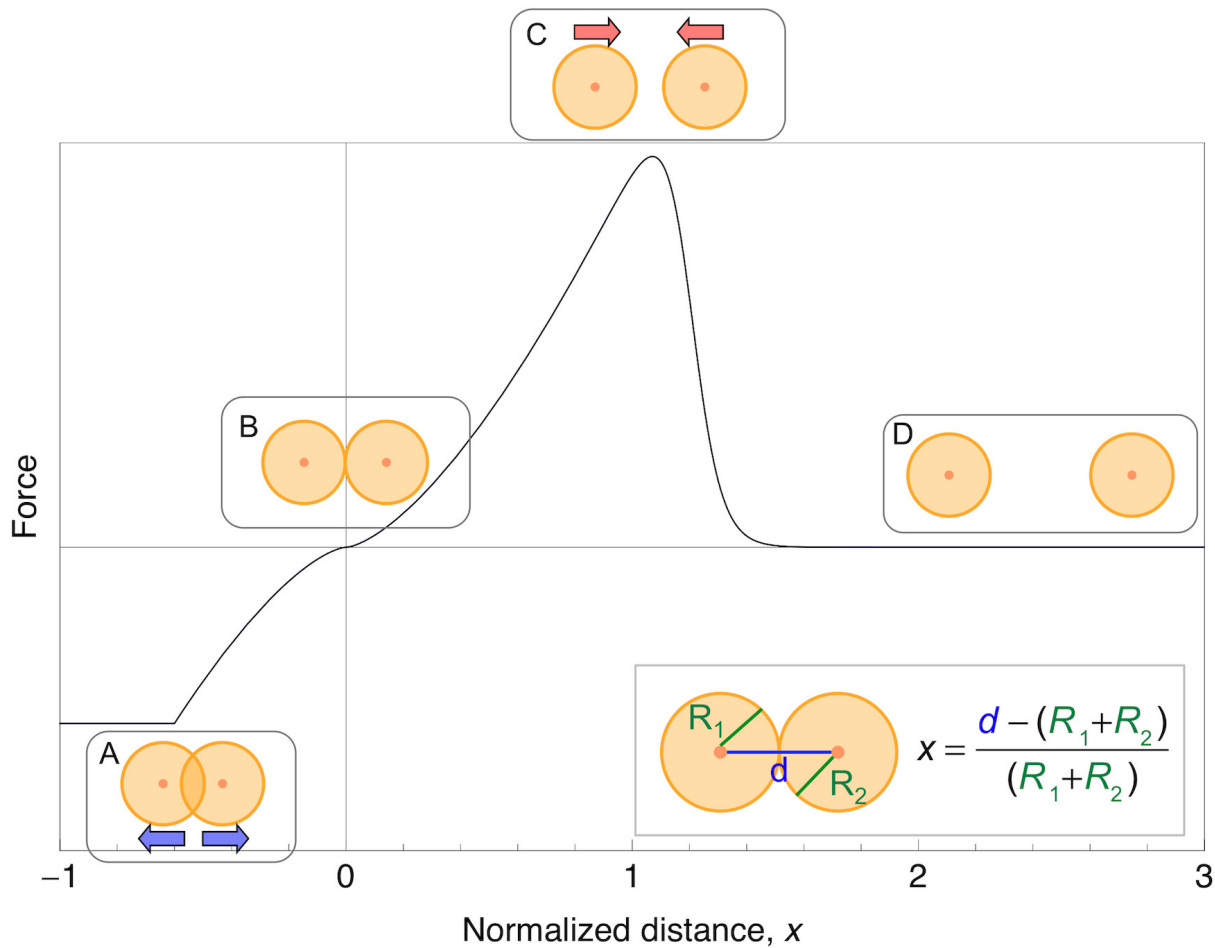
Figure 2.8: Pictorial representation of the interaction force between two cells in VBL. The solid curve shows qualitatively the behavior of the interaction force, while the insets depict the corresponding situations: A)cells are compressed against each other, force is repulsive; B)cells are in contact, the total force vanishes; C)cell centers are slightly apart, force is attractive because of adhesive molecules on the cell's membranes; D)cells are no longer in contact, the total force vanishes again. The inset on the lower right shows the definitions of the basic geometric variables.

in panel B of figure 2.6).

The biomechanical interaction between two VBL cells is derived from the Hertz problem [155, 156] known in contact mechanics. The Hertz problem deals with the interaction forces of two spherical membranes approximating the cell-cell interaction forces for small deformations quite well. For two cells with radii R_1 and R_2, Poisson's ratios $\nu_{1,2}$ and Young's moduli $E_{1,2}$ for cell 1,2 respectively (figure 2.8), the resulting force acting between the two VBL cells reads:

$$F = \frac{\sqrt{R_1 R_2}\,(R_1 + R_2)}{\frac{3}{4}\left(\frac{1-\nu_1^2}{E_1}\frac{1-\nu_2^2}{E_2}\right)}\left(\frac{R_1 + R_2 - d}{R_1 + R_2}\right)^{\frac{3}{2}} \tag{2.2}$$

Defining $k := \frac{\sqrt{R_1 R_2}(R_1+R_2)}{\frac{3}{4}\left(\frac{1-\nu_1^2}{E_1}\frac{1-\nu_2^2}{E_2}\right)}$ and $x := \frac{d-(R_1+R_2)}{R_1+R_2}$, the dependence of the forces on the deviation from the equilibrium position ($x = 0$) becomes more obvious as shown in equation 2.3.

$$F = k|x|^{\frac{3}{2}} \tag{2.3}$$

Under strong compression e.g. after mitosis, the formula for the force (equation 2.2) results in unrealistic values. Therefore, VBL assumes that the force flattens out towards a constant modulus for small separations ($x << 0$). The qualitative shape of the force is depicted in figure 2.8.

In addition to the deterministic equations of the biochemical pathway (figure 2.5) and the biomechanical forces (figure 2.8), the simulation considers two probabilistic cellular events: mitosis and cell death. The mitotic cell division in VBL happens inside the volume of the initial mother cell limiting the increase in volume during this step (situation depicted in figure 2.7). While limited by the size of the mother cell, the volume of both daughter cells and the direction connecting the new daughter cells are taken at random.

Milotti et al. report all computational details in a supporting text to [147] also available at https://doi.org/10.6084/m9.figshare.9878588.v1.

2.3.3.2 Implementation efforts

Prof. Dr. Edoardo Milotti released an implementation of the model described in [147] to the public domain via GitHub (https://github.com/edymil/VBL). I designed a cmake build environment to easily build the VBL software from the source code. Developing similar cmake build scripts for the VBL and the Tumorcode software eases the installation effort preceding the combined simulations. Further, I translated a lot of comments from Italian to English increasing the targeted audience. I arranged the VBL source code in a more object oriented fashion.

As documented in the main manuscript ([3] and section 3.3.1), I implemented an interface between the VBL and the Tumorcode software. Complementary to the interface, I conceived a way to store the simulation data in a common data format. After successfully establishing a communication of the two simulations via the interface and establishing a common data format, I performed simulation runs on a small beowulf cluster (named "snowden") at Saarland University and the high performance computing (HPC) facility in CINECA (Italy) with the login name "tfredric".

2.4 Dynamic vessel adaptation in synthetic arteriovenous networks

The original research article entitled "*Dynamic vessel adaptation in synthetic arteriovenous networks*" was published at the 31st of August in the Journal of Theoretical Biology. I reprinted the article with permission (see appendix G at page 229) in section 3.4 starting on page 157 of this dissertation.

2.4.1 Background

The vasculature is a highly dynamic object embedded in surrounding tissue and subjected to numerous biological regulatory mechanisms (section 1.1.3). Not all of the regulatory mechanism are fully understood today. Since measurements on alive vasculature are complex, computer simulations offer a non invasive way to test hypothetical regulatory mechanism. The vessel adaptation model described in [157] modulates the radii of blood vessels within a network based on biologically inspired stimuli (see main manuscript in section 3.4 or [4]).
As reported in [1], we found that an ad hoc dilation of cancerous blood vessels accounts for measured oxygen and hemoglobin concentrations in real patient's tumors. Conjecturing that an integration of the adaptation model into the Tumorcode software provides reasoning for the ad hoc vessel dilation, I studied the vessel adaptation model in more detail.
Unfortunately I failed with a successful application of the vessel adaptation model to tortuous, unstructured and cancerous blood vessel networks (see supplemental material to [4], section 3.4.2). Instead I focused on the adaptation model with respect to artificial blood vessel networks created by the Tumorcode software.

2.4.2 Summary of the paper

The "Introduction" reviews the biological motivation for a vessel adaptation model before the "Methods" section explains the details of "the adaptation algorithm", "the artificial blood vessel networks", the "parameter optimization" and the used "biophysical quantities". The "Results" section of the main manuscript (section 3.4 or [4]) starts by "reproducing the available data" from the measured rat mesentery network approving my own implementation of the adaptation algorithm.
The original work of the Pries et al. [157] obtained the required parameters of the vessel adaptation model by minimizing the deviation between predictions of the adaptation model and experimentally observed vascular networks. Since artificially constructed blood vessel networks by the Tumorcode software lack a comparison to measured blood vessel networks, the vessel adaptation model requires a different way to determine the free model parameters when applied to artificial blood vessel networks.
Therefore I applied a numerical parameter optimization to the problem of finding model parameters predicting realistic blood vessel networks. The main manuscript (see section 3.4.1 or [4]) describes two testing scenarios involving artificial blood vessel networks created by the Tumorcode software: "single topology with varying boundary conditions" and "varying topology with fixed boundary conditions". In the first scenario, I applied particle swarm optimization to find parameters of the adaptation algorithm minimizing the variation in capillary blood flow for a single fixed vessel arrangement. In the second scenario, I applied the adaptation algorithm together with the parameters obtained in the first scenario to varying vessel arrangements. Studying the two scenarios supports my assumption that a realistic blood vessel radii distribution satisfies an optimality criterion similar to the assumptions included in the derivation of Murray's law (section 1.1.3). I applied the vessel adaptation algorithm to artificial blood vessel networks created by the Tumorcode software, but failed in augmenting the biophysical principles of vascular remodeling during solid tumor growth (as implemented in the Tumorcode software) by the adaptation algorithm. Mainly due to two reasons: 1) the complexity in obtaining the free parameters for which the set of highly non linear equations converges and 2) the immediate loss of convergence due to the nonlinearities in the equations occuring when changing the topology of the vessel network by either adding or removing a vessel to or from the network — both are valid options during vascular remodeling occurring in solid tumors (supplemental material to [4] or section 3.4.2).

2.4.3 Personal contributions

I extended the Tumorcode software by a module implementing the vessel adaptation algorithm described in [157].

Dr. Michael Welter designed the numerical core of the Tumorcode software [2] to deal with lattice coordinates only. To include the vessel adaptation algorithm into the numerical core, I lifted this restriction allowing arbitrary 3D coordinates in the numerical core of the Tumorcode software. After implementing the adaptation algorithm, I validated the implementation by reproducing the numerical results published in [157]. To this end, I downloaded the measured blood vessel networks used in [157], converted the raw data to the data structure of the Tumorcode software and applied my implementation of the algorithm with parameters reported in [157].

At the time of conducting the experiments, the measured blood vessel network data was available for downloaded at:

http://ajpheart.physiology.org/highwire/filestream/95027/field_highwire_adjunct_files/1/network_546_segments.txt. *(Today on the 7th of October 2019, this link is broken, but I found the same data distributed as supplemental for* [158] *and hosted at:*

https://www.physiology.org/doi/suppl/10.1152/ajpheart.00757.2002/suppl_file/Table%201.txt.)

To convert the raw data into the data structure required by the Tumorcode software, I used the python script "*apj2hdf.py*" distributed with the Tumorcode software (in the folder "*py/krebs/adaption/*"). The exact parameters are stored in the file "*parameterSetsAdaption_generic.py*" (in the folder "*py/krebsjobs/parameters/*"). After successful validation of my implementation, I investigated the adaptation algorithm on artificial blood vessel networks created by the Tumorcode software. I identified relevant parameters influencing the stability of the adaptation algorithm and conducted an extensive parameter study to find applicable parameters for a single fixed vessel arrangement. Using a robust optimization method (particle swarm optimization), I considered several objective functions and different hydrodynamic boundary condition during the course of optimization. In the end, minimizing the variance in capillary blood flow turned out to produce realistic radii distribution of blood vessel networks (section "Single topology, varying boundary conditions" in [4]). Conducting the optimization was computationally expensive and demanding (more technical details listed in the supplemental text to [4]).

Next, I tested the influence of rearranging the vessels in space to the adaptation algorithm by creating an ensemble of networks featuring the same hydrodynamic boundary conditions, but different vessel radii and spatial arrangements. For the ensemble, I studied two biophysical observables: the relative blood volume (rBV) and the surface to volume ratio (s2v). I compared rBV and the s2v of blood vessel networks with radii obtained by vessel adaptation to the same blood vessel network with vessel radii fulfilling Murray's law (section "Varying topology, fixed boundary conditions" in [4]).

The Tumorcode software focuses on the vascular remodeling during the progression of solid tumor. I applied the adaptation algorithm to blood vessel networks subjected to vascular remodeling during the progression of solid tumor. As reported in the supplement to [4] (reprinted in section 3.4.2), I found that the highly nonlinear adaptation algorithm is not suited to describe dynamic vessel adaptation in topologically changing networks.

I provided all data comprising figures, tables and illustrations of [4]. Further I checked the relevant source code into my GitHub repository and uploaded the commented raw data to www.zenodo.org (section 3.4 or [4]).

As corresponding author, I communicated with the editor and referees of the publishing journal (Journal of Theoretical Biology).

2.5 Summary and Discussion

In this section, I summarize the contribution of my dissertation to the scientific community.

In the recent years, in silico modeling became a scientific tool helping to unveil the secrets behind the progression of solid tumors. Similar to conventional science without computers, results should be independent on the method used to obtain the results. By validating the implementation of the main numerical method used in [1] against a similar method (section 2.1), I confirmed the numerical method and contributed to [1] indicating that vascular network remodeling during the progression of breast cancer affects both, the tissue and blood vessel oxygen saturation.

The implementation of the numerical methods of used in [1] and similar preceding publications [37, 148, 159] were not well documented hindering other scientists in the broad field of cancer research to benefit from the developed numerical methods. Therefore I decided to report the main features of the software together with handy examples illustrating the logic of the simulations and released the source code under the name "Tumorcode" software to the public domain in 2018 [2] (section 2.2). My efforts created a sustainable software from previously unpublished source code contributing to open science (section 1.4).

Oxygen plays an essential role in cell metabolism. Since the vasculature delivers the oxygen (and other nutrients) to the place where the actual metabolism takes place, the vasculature plays an essential role in the progression of solid tumors, too. Prio to my work published in [3] (section 2.3), the Tumorcode software neglected cellular details. With increasing computational power, the consideration of cellular details in the macroscopic description of the Tumorcode software became feasible. I augmented the abilities of the Tumorcode software towards an integral model of realistic tumor growth by combining cellular details and vascular remodeling dynamics to study the tumor microenvironment at the angiogenic switch.

The volume flow of blood highly depends on the blood vessel radius and since blood comprises the nutrients, the volume flow of nutrients also highly depends on the blood vessel radius. The intriguing question on how the vasculature maintains its blood vessel radii is still under debate, but some responses to mechanical and metabolic stimuli have been identified lately. Since the progression of solid tumors is intrinsically tied to the vasculature, the question on the blood vessel radii affects also tumor growth. To observe vascular networks in vivo is a complicated issue for which reason a realistic in silico model of vascular networks would support drug and therapy development in cancer research. In [4](section 2.4), I provided a new tool to study blood vessel radii regulation in silico by means of the vessel adaptation algorithm.

Further I contributed to [5] reviewing relevant topics for my PhD studies. I replotted data of previous studies ([37]) in figure 10 of [5] and supplemented [5] by an extensive literature review on available biophysical parameters at that time.

The research conducted during my PhD studies in the past 6 years comprised multiple aspects of physical and computational modeling of solid tumors with respect to the vascular growth phase.

Chapter 3

Original publications

In this chapter, I reprint the relevant original publication (with permissions shown in appendix G).

Contents

3.1 Computational Model for Tumor Oxygenation Applied to Clinical Data on Breast Tumor Hemoglobin Concentrations Suggests Vascular Dilation and Compression

3.1.1 Main Manuscript

PLOS | ONE

RESEARCH ARTICLE

Computational Model for Tumor Oxygenation Applied to Clinical Data on Breast Tumor Hemoglobin Concentrations Suggests Vascular Dilatation and Compression

Michael Welter[1], Thierry Fredrich[1], Herbert Rinneberg[2], Heiko Rieger[1]*

1 Theoretical Physics, Saarland University, Saarbrücken, Germany, **2** Division of Medical Physics and Metrological Information Technology, Physikalisch Technische Bundesanstalt PTB Berlin, Germany

* h.rieger@mx.uni-saarland.de

Abstract

We present a computational model for trans-vascular oxygen transport in synthetic tumor and host tissue blood vessel networks, aiming at qualitatively explaining published data of optical mammography, which were obtained from 87 breast cancer patients. The data generally show average hemoglobin concentration to be higher in tumors versus host tissue whereas average oxy-to total hemoglobin concentration (vascular segment RBC-volume-weighted blood oxygenation) can be above or below normal. Starting from a synthetic arterio-venous initial network the tumor vasculature was generated by processes involving cooption, angiogenesis, and vessel regression. Calculations of spatially resolved blood flow, hematocrit, oxy- and total hemoglobin concentrations, blood and tissue oxygenation were carried out for ninety tumor and associated normal vessel networks starting from various assumed geometries of feeding arteries and draining veins. Spatial heterogeneity in the extra-vascular partial oxygen pressure distribution can be related to various tumor compartments characterized by varying capillary densities and blood flow characteristics. The reported higher average hemoglobin concentration of tumors is explained by growth and dilatation of tumor blood vessels. Even assuming sixfold metabolic rate of oxygen consumption in tumorous versus host tissue, the predicted oxygen hemoglobin concentrations are above normal. Such tumors are likely associated with high tumor blood flow caused by high-caliber blood vessels crossing the tumor volume and hence oxygen supply exceeding oxygen demand. Tumor oxy- to total hemoglobin concentration below normal could only be achieved by reducing tumor vessel radii during growth by a randomly selected factor, simulating compression caused by intra-tumoral solid stress due to proliferation of cells and extracellular matrix. Since compression of blood vessels will impede chemotherapy we conclude that tumors with oxy- to total hemoglobin concentration below normal are less likely to respond to chemotherapy. Such behavior was recently reported for neo-adjuvant chemotherapy of locally advanced breast tumors.

Introduction

Adequate supply of tissue with oxygen and nutrients critically depends on the structure and function of its vasculature. For tumors to grow beyond 2 *mm* in size, new vasculature must develop, i.e. angiogenesis must occur [1]. The vasculature of solid tumors, however, is known to differ distinctly from that of surrounding normal tissue. Whereas vasculature in normal tissue is arranged in a hierarchy of arteries, arterioles, capillaries, venules and veins and grows under tight control of inter-capillary distances, tumor vasculature develops in a chaotic manner without such control, leading to spatial vascular heterogeneity. In solid tumors necrotic regions and regions of low microvessel density (*MVD*) may occur, whereas tumor blood vessels are more abundant at the tumor-host interface [2]. Tumor vessels are known to be immature, fragile, tortuous, dilated, to form (large diameter) arterio-venous shunts and often it is even difficult to distinguish arterioles and venules, i.e. the classification of tumor vessels as arterioles, capillaries and venules is no longer adequate [2–8]. In addition, tumor vessels exhibit high permeability to macromolecules [3]. The structurally abnormal tumor vasculature results in spatially and temporally heterogeneous blood flow, affecting tissue oxygenation (acute or perfusion-limited hypoxia). From intravital dorsal window microscopy on tumor models it is known that blood flow through tumor capillaries is frequently sluggish and at times may even be stationary and reverse direction. It follows that blood flow through tumors may not follow a constant unidirectional path. In addition, red blood cell (RBC) flux varies greatly among tumor vessels, many tumor vessels do not carry RBCs but contain plasma only [2–4, 6, 7]. Furthermore, tissue solid pressure, generated by proliferating cancer cells and modifications of the extracellular matrix of tumors, may compress tumor blood vessels thus reducing or impairing blood flow [9–11]. Tumor cells separated from nearby capillaries beyond the diffusion limit of oxygen suffer from chronic (diffusion-limited) hypoxia. Hypoxic tumor cells are known to be resistant to ionizing radiation, since oxygen is needed to stabilize radiation-induced DNA defects and, in addition, are considered to be resistant to some anticancer drugs. Therefore, tumor hypoxia is associated with poor prognosis, because it causes resistance to standard therapies and promotes more aggressive phenotypes [12, 13].

Because of their limited spatial resolution present-day non-invasive imaging techniques used in clinical practice do not allow to visualize tumor vasculature, blood flow and distributions of oxygen and nutrients at the capillary and cellular level, despite the diagnostic relevance, e.g. of *MVD* and the presence of hypoxic tumor cells. Therefore, computational modeling is an appropriate tool to analyze the interrelation of clinically amenable characteristics of tumor vasculature and oxygenation.

Tissue oxygenation has been measured in human tumors by various methods such as needle electrodes [14]. In this way oxygen partial pressures were found to be highly heterogeneous in tumors with median oxygen pressures below that of the host tissue. More importantly, tumors often exhibit hypoxic regions with oxygen partial pressures below 10 *mmHg*. Today, non-invasive positron emission tomography (PET) is employed clinically to image oxygenation status of tumor tissue [15]. Complementary to tissue oxygenation measurements magnetic resonance imaging (MRI) [16, 17] and tissue optical imaging, such as optical mammography assess (RBC-volume weighted) blood oxygenation of vascular segments.

Optical mammography [18–20] has been developed over the past one to two decades and a large body of data on deoxy-,oxy-, and total hemoglobin concentrations c_{HbD}, c_{HbO} and c_{Hb} in normal breast tissue and breast tumors has been collected from many patients [21–24]. Because of light scattering photon trajectories through the breast are much (about 5 times) longer compared to the geometrical distance between the point of entry and point of exit of the photons,

resulting in high sensitivity towards absorption. However, spatial resolution is generally poor and only average hemoglobin concentrations can be deduced. Tissue hemoglobin concentration c_{Hb} equals the sum of hemoglobin mass of each vessel segment taken over the vessel network within a selected tissue volume per unit volume of tissue and approximately reflects fractional blood volume. The ratio of oxy- to total hemoglobin concentration, called tissue blood oxygen saturation Y, is the average of RBC-volume-weighted true blood oxygenation taken over all vessel segments of the tissue volume selected. Tissue blood oxygen saturation reflects the balance between vascular flux of oxygen that enters the tissue, i.e. oxygen supply, and oxygen flux from the vascular network into tissue, reflecting oxygen demand. Besides tissue hemoglobin concentration, tissue blood oxygen saturation is thus another parameter characterizing tumor and host vascular networks.

On average tissue hemoglobin concentration c_{Hb} of breast tumors was found to be larger than in host tissue by a factor of 3.5 [22]. This observation can qualitatively be explained by a larger blood volume in tumors compared to their host tissue. However, tissue blood oxygen saturation in breast tumors was observed by most authors to be both above or below normal [21–23] whereas some papers reported tissue blood oxygenation in tumors to generally be below that of their host tissue [25, 26]. Up to now, there were no microscopic theoretical models available to account for tissue blood oxygenation in tumors allowing to analyze clinical data. Computational models as the one we present in this paper contain detailed information about the vasculature as well as the emerging oxygen distributions of tumors and host tissue. By coarse graining the obtained detailed information and comparing it with low resolution clinical data, one can infer potential vascular structure in the tumor of patients—with some uncertainty of course.

Mathematical modeling and numerical simulation of growth of solid tumors has been actively pursued since many years, for a recent review see e.g. [27]. In this paper 3D host vasculature is obtained by applying stochastic vessel network generation algorithms (see S1 of [28]). During tumor growth, remodeling of the host vasculature occurs involving vessel cooption, angiogenesis, vessel circumferential growth, vessel regression and collapse, simulated by corresponding stochastic vessel network remodeling processes (see S1 of [28]). In the present paper we adopted a simplified tumor growth model where a spherical tumor is expanding at constant rate. Host tissue and tumor are represented as hybrid models consisting of their vascular network surrounded by a homogeneous medium, representing host cells or tumor cells, respectively. Intravascular and extravascular oxygen transport has been studied by several authors. Oxygen dissolved in plasma, being in chemical equilibrium with oxygen bound to hemoglobin, extravasates and diffuses in tissue, where it is metabolized. Oxygenation by isolated vascular tubes has been studied theoretically in detail since the originally proposed "Krogh" model [29], see e.g. [30]. Also in several works, simplified two-dimensional tumor tissues, supplied by point-sources of oxygen, were considered, and the resulting oxygen concentration distributions were analyzed [31–37]. However, these models require appropriate intravascular O_2 concentrations as input parameters. Previously, Goldman [38] coupled oxygen in a vascular network and tissue via boundary conditions which relate the radial transvascular oxygen flux at each point on the vessel surface to the PO2 gradient at the respective tissue location. For further reading focusing on skeletal muscle oxygenation, see [39] and the Refs. therein. Secomb and coworkers [40–43] used a Green's function method for solving the diffusion equation in tissue, treating vessels as distributions of oxygen sources and tissue represented as a distribution of oxygen sinks. We followed the computational method of Beard [44], discretizing the diffusion equation for oxygen by a finite difference approach with source terms added locally corresponding to the surface area of nearby vessels. Our computational method is sufficiently fast to simulate tissue volumes of

$0.5\ cm^3$. Only stationary solutions are sought, ignoring transient variations of blood flow through tissue discussed above. For each vascular network generated our model allows us to calculate various biophysical and metabolic quantities, in particular partial oxygen pressure distributions in tissue, blood flow (perfusion), true vessel length weighted blood oxygen saturation distribution in the vascular network, tissue hemoglobin concentrations and tissue blood oxygen saturation, the latter two quantities being dominated by high caliber vessel. Blood vessels that set themselves apart by their diameter (approx. 100 μm) from the bulk of other vessels were found in corrosion casts of blood vessels of leiomyomata [45]. Moreover, in mammary carcinoma vessels of up to 200 μm diameter were observed [46].

Recently it was reported [47] that breast cancer patients who underwent neoadjuvant chemotherapy before surgery and were not classified as complete responders by immuno-histo-chemistry at the end of chemotherapy, tended to initially exhibit tumor blood oxygenation below that of host tissue. On the other hand, patients who were ranked as pathological complete responders exhibited the same tissue blood oxygen saturation on average in tumor and host tissue. Thus, tissue blood oxygen saturation may have diagnostic value for therapy control and it is important to understand what causes tissue blood oxygen saturation in tumors to fall above or below normal.

It is the aim of the present paper to gain information on host and tumor vascular networks from clinical data on tissue hemoglobin concentration and tissue blood oxygen saturation of breast tumors and their surrounding host tissue. To this end various synthetic host and tumor vascular networks were generated and tissue total hemoglobin concentration as well as tissue blood oxygenation calculated. As expected, tumor total hemoglobin concentration was always found to be larger than that of host tissue, consistent with clinical data. Within reasonable limits of metabolic rates of oxygen consumption by normal and tumorous breast tissue, simulated tumor blood oxygen saturation always fell above normal, in contrast to clinical data, indicating that increased perfusion and hence increased oxygen supply outweighs higher oxygen consumption in tumorous tissue. Tumor blood oxygen saturation was simulated below normal depending on the degree of vascular compression of (high-caliber) tumor vessels assumed to be caused by tumor solid stress. Although qualitative agreement with clinical data on tissue blood oxygenation was achieved, other processes than compression of high-caliber tumor vessels may lead to perfusion impairment in at least parts of a tumor and hence tumor blood oxygen saturation to drop below normal.

The main part of this paper is organized as follows: first, we briefly explain our tumor growth model including the generation of host and tumor vasculature. Then we discuss the mathematical models used to account for blood flow, intravascular and extravascular oxygen transport, which are well known [30, 40] but reviewed here for clearness and readability. Further below we describe our method to solve the obtained coupled equations describing intra- and extravascular PO2 distributions efficiently. Section 'Theoretical models' concludes with a description of three model variants, the results of which are presented in the following section 'Results and Discussion'. There we initially provide examples of simulated PO2 and hematocrit distributions of host and tumor tissue, illustrating compartmentalization in tumors. Next we validate our model by comparing simulation results on host und tumorous tissue with biophysical and biochemical data available in the literature. Then we focus on clinical data on tissue hemoglobin concentration and tissue blood oxygenation of breast tumors, determining which simulation model variant provides qualitative agreement. Additionally, we correlate various simulated quantities of host and tumor that are not easily amenable to clinical measurements. Finally we discuss the limitations of our model and summarize our results in the conclusion section.

Theoretical models

Overview of tumor growth model for hemodynamic and oxygen transport simulations

Ideally, one would start from digitized 3D blood vessel networks of each breast cancer patient to simulate hemodynamic properties, as well as intravascular and extravascular oxygen transport in tumor and surrounding host tissue. Although 3D vascular networks of tumors grown in animal tumor models can be generated from μ-CT data [48, 49], such techniques are not applicable to humans. Therefore, 3D vascular trees of tumors and surrounding host tissue are algorithmically constructed, following methods developed by us previously and applied to model vasculature in melanomas and gliomas [28, 50–54]. The model described in detail in Ref. [28] represents an extension of the model used in [55] which is based on wall shear stress guided random growth of interdigitating vascular trees on a lattice. In contrast to previous work, the model of the tumor spheroid employed in this paper is very simplified.

Fig 1 illustrates the theoretical model of tumor growth used in the present paper. Starting from synthetic host vasculature, a small spherical nucleus ($R_{tum}(t = 0) = 250\ \mu m$) is inserted at the beginning ($t = 0$) of the growth process into host tissue. The tumor spherically expands and its radius is assumed to grow linearly in time with speed $v_{tum} = 2\ \mu m/h$ up to a preselected time t_{end}, taken to be 600 h. In real tumors, competition for space and nutrients causes confinement of cell proliferation to a few cell layers behind the invasive edge and therefore eventually leads to a linear expansion rate. The tumor tissue is assumed homogeneous. We surround the tumor with a concentric shell of thickness R_g, within which angiogenesis, i.e. sprouting of new vessels is activated. The distance R_g represents the diffusion length of vascular endothelial growth factors (VEGFs), i.e. the distance that growth factors diffuse, before their concentration drops to
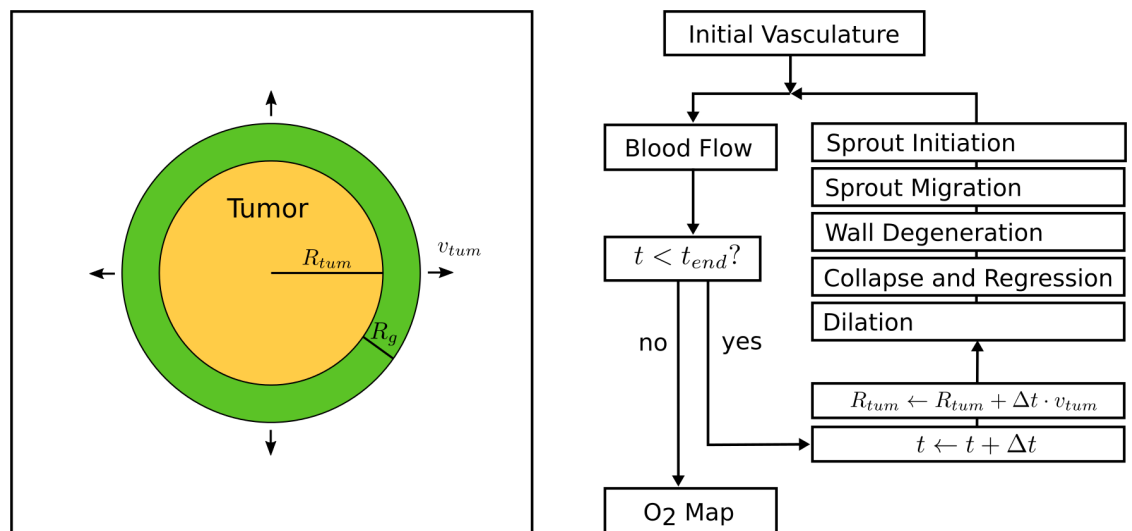
Fig 1. Model Overview. Left hand side: the tumor spheroid is represented by a homogeneous sphere, the radius of which R_{tum} grows at constant speed v_{tum} and is surrounded by a concentric shell of thickness R_g, the diffusion length of vascular endothelial growth factors. Vascular remodeling is thought to take place within the tumor and surrounding concentric shell. Right hand side: block diagram outlining basic simulation procedure. The modification of the present vasculature is implemented by stochastically applying the processed depicted in Fig 2. At the end of each time step, blood flow is recomputed, time t and tumor radius R_{tum} incremented. The iteration steps are repeated until the final simulated time t_{end} is reached.

doi:10.1371/journal.pone.0161267.g001

insignificant levels due to degradation and binding. Vascular remodeling takes place during each time step delta $t = 1\ h$, corresponding to the following biological processes: sprout initiation, sprout migration, vessel wall degeneration, vessel collapse and regression and vessel dilatation due to circumferential vessel growth. These biological processes are implemented as probabilistic addition (angiogenesis), deletion (collapse) of vessel segments, as well as probabilistic and deterministic changes of segment associated variables (e.g. wall thickness or vessel radius, see below). During each time step, we iterate over lattice sites or vessel segments as required and perform the local alterations. Since the probability for vessel collapse and regression depends on wall shear stress, blood flow through host and tumor vasculature is calculated as Poiseuille flow and updated after each time step. Furthermore, for angiogenesis (sprout initiation, sprout migration) to occur, VEGFs have to be present in tumor tissue. To this end more advanced growth models, such as the one described in [28], calculate a VEGF concentration field during each time step. For this purpose the (extravascular) oxygen concentration field is calculated in tumor tissue and hypoxic tumor cells are taken as sources for VEGF, assuming the same preset blood oxygen saturation throughout the entire vasculature, however. In the present work we focus on a realistic oxygen transport model taking the decrease of intravascular oxygen concentration due to oxygen extravasation into account. In order to reduce model complexity we assume vascular remodeling to take place within the tumor and surrounding concentric shell, i.e. assume sufficient VEGF to be within the tumor and its outer shell for angiogenesis to occur. The considerable simplification of our present tumor growth model is justified because vascular morphologies obtained in this way are consistent with data from real tumors [56, 57] and predictions of more detailed tissue models. The simulation growth process was deliberately stopped at $t = 600\ h$ when the tumor diameter had grown to ca. 3 *mm* to minimize boundary effects which would occur if the tumor was allowed to grow to the size of the simulation box.

By simulating tumor growth and vascular remodeling, a tumor-specific vascular network emerges at the end ($t = t_{end}$) of each growth process. Because of the stochastic nature of the growth processes involved, each simulation yields a different network. Based on the networks obtained, relative blood volume, tissue perfusion, hematocrit, and tissue hemoglobin concentration c_{Hb} are calculated. In addition, using a sophisticated model of oxygenation (see below), tissue blood oxygen saturation $Y = c_{HbO}/c_{Hb}$ and maps of oxygen partial pressure (PO2) were simulated. Note that the assumed spheroidal tumor region generally differs in its physiology, e.g. metabolic rate of oxygen consumption, from that of the surrounding host tissue. If not stated otherwise, results for host tissue refer to the entire (unaltered) network at $t = 0$.

Artificial blood vessel networks in normal breast tissue. We briefly review the generation of 3D host vascular networks and refer the reader to the supplemental material S1 of Ref. [28] for details. Simulations are performed on a cubical domain with lateral length of $L = 8$ *mm*. Starting point are arterial and venous root nodes, (endpoints of feeding arterioles and draining venules) located at boundary sites of the face centered cubic lattice. Structural elements of different shape (linear, tripod) are added to randomly selected terminal branches of the vascular trees one at a time. This process is continued until further addition of vessel segments causes segments to overlap, which is forbidden by definition. In the subsequent stage of the construction scheme, trees generated in this way are pruned and extended to obtain the final network. It comprises the following steps. Firstly, nearby open ends at terminal branches are temporarily connected by vessel segments representing capillaries. Radii of capillaries, of arterial and venous terminal segments are set to 2.5 *µm*, 2.5 *µm* and 3.8 *µm*, respectively, whereas radii of parent segments are determined from Murray's law, i.e. $r_c^{\alpha} = r_a^{\alpha} + r_b^{\alpha}$ with r_c being the radius of the parent vessel, r_a, r_b the radii of the two downstream vessels and $\alpha = 3$ has been selected. Secondly, blood flow through the temporary network is calculated, including

shear wall stress of segments. With the capillaries removed additional vessel segments are stochastically attached to or removed from terminal branches with probability based on wall shear stress, corresponding to wall shear stress guided random growth of interdigitating vascular trees on a lattice [55]. This process is repeated until the number of capillaries reaches a plateau, i.e. the lattice is filled with a interdigitating trees exhibiting a homogeneous distribution of capillaries. The resulting *MVD* is determined by the lattice constant h_{gen}, where $h_{gen} = 130$ μm has been selected in the present paper.

Variations of host vessel networks among patients of a cohort were introduced by arbitrarily adopting nine root node geometries, illustrated in Fig 3, differing in location and number of arterial (venous) inlet (outlet) vessels. Starting from each root node geometry ten host vascular networks were grown which differed among each other because of the statistical nature of the growth process. Thus a total of 90 different vascular networks were generated, representing normal tissue vasculature. Using these networks we demonstrated that the specific arrangement of host vessels prior to tumor growth can play a significant role for the outcome of tumor vascular remodeling. We believe that all generated vascular morphologies are physiologically plausible. However, we did not make an effort to determine the frequency with which configurations $RC1 - RC9$ might occur in real breast tissue (s. 'Limitations').

Details of vascular remodeling during growth of synthetic tumor blood vessel networks. Starting from one of the 90 vascular networks representing host tissue the associated tumorous vessel network is formed by following processes, also ilustrated in Fig 2:

1. Angiogenic sprouting: In normal tissue, lattice sites occupied by vessels, have a chance (probability $\Delta t / t_{EC}^{(sprout)}$) to spawn a sprout segment on an adjacent lattice bond provided the site is close enough to the tumor, i.e. within the growth factor diffusion distance R_g rather than requiring the growth factor concentration to be sufficiently high, as previously postulated [51]. Furthermore, no other branching points must be nearby, i.e. within the distance of $d^{(br, min)}$. Vessels within the tumor sphere, switch to circumferential growth (s. below). The direction of sprouting is chosen randomly, which is non-critical, since the net effect is either way an increase of vascular density near the invasive edge, extending R_g units into normal tissue.

2. Sprout growth: sprouting vessels have a chance (probability $\Delta t / t_{EC}^{(sprout)}$) to be extended by another lattice bond. Sprouts have a total life time of $t_{EC}^{(migr)}$. When sprouts hit an existing vessel during their lifetime, they are connected to it. Sprouts that are consequently circulated become normal vessels. Otherwise sprouts are prone to collapse after their lifetime.

3. Circumferential growth: vessels switch from sprouting to circumferential growth after their residence time $t_{EC}^{(switch)}$ within the tumor. After switching to circumferential growth we assume each endothelial cell ($10 \times 10 \ \mu m^2$ surface area) at the inner wall to duplicate every $t_{EC}^{(prol)}$ hours leading to an increase of vascular radius r. We impose an upper limit on the radius ($r^{(max)}$) after which circumferential growth stops.

4. Degradation of vessel wall stability: vessels possess a wall stability value w as an abstract measure of the state of degeneracy of their vessel wall. The stability measure w is initialized relating it to the wall thickness of healthy vessels [28, Suppl.1, Eq (2)]. The wall stability of tumor vessels decreases over time at the rate Δw until zero. Once zero, vessels are allowed to collapse and regress (see below).

5. Vessel collapse and regression: If the wall shear stress f of a segment falls below a threshold ($f^{(coll)}$) and $w = 0$, then the segment is removed from the network at probability $p^{(coll)}$,

62
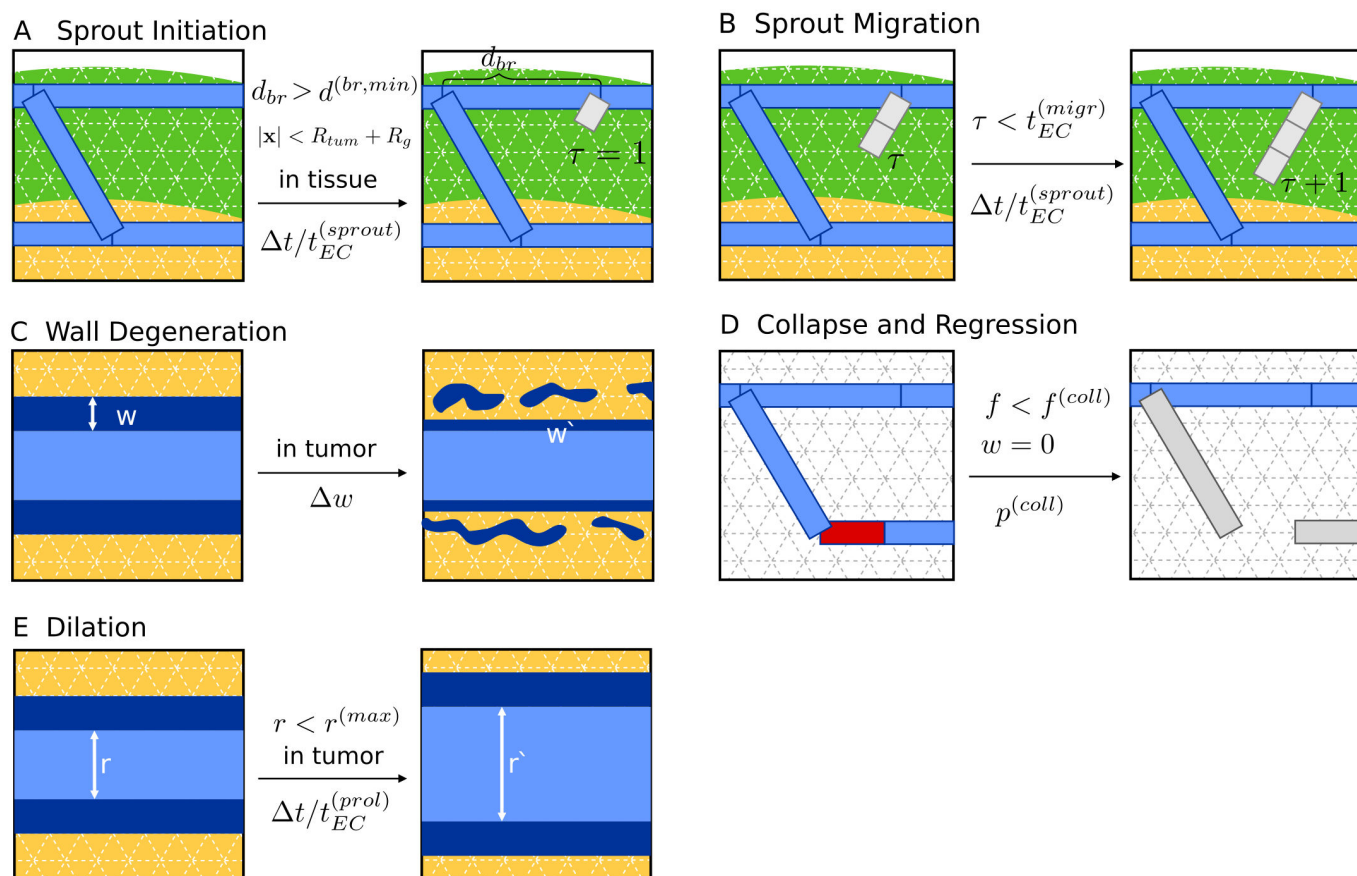
Fig 2. Vascular Remodeling Processes. The dynamical processes of vascular network remodeling (A-E) are illustrated by exemplary state transitions with the current state shown in the left hand side box and the resulting state on the right. Preconditions are indicated above the center arrows, and transition probabilities are denoted below, respectively. (A) depicts the start of a new sprout (gray) which can happen on any site on the network provided that given preconditions are true. Here, one of several preexisting segments (blue) is split to create a new branching point. Space occupied by the tumor spheroid (orange), and space where angiogenic sprouting may take place (green), i.e. where $R_{tum} < |\mathbf{x}| < R_{tum} + R_g$, is indicated by colored background. "In tissue" refers to the exterior of the spheroid, i.e. where $|\mathbf{x}| > R_{tum}$. "In tumor" means the opposite, obviously. The path length on the network to the next branching point d_{br} must be larger than the lower limit $d^{(br, min)}$. The new segment is initialized with an associated life-time of $\tau = 1$. (B) depicts the further extension of the sprout from (A). Additional segments inherit τ from the parent segment. Moreover τ is incremented, globally, for all sprouts once per time step Δt. (C) depicts the degradation of vessel walls. The variable w represents the stability of the vessel wall, here depicted as varying wall thickness. It decreases continuously at the rate Δw, resulting in a value of w' at the next time step. In (D) an unstable vessel (red) is removed, representing occlusion of blood flow and complete disintegration. Such event is assumed to happen only to vessels with maximally degenerate walls $w = 0$ and low wall shear-stresses f, where $f < f^{(coll)}$. The emerging dead ends (gray) trivially have $f < f^{(coll)}$, and therefore collapse rapidly, resulting in a long ranged effect. Since collapses can happen anywhere, we left the background blank. (E) depicts the dilation of tumor vessels. Their radii increase at rate Δr up to the upper limit $r^{(max)}$.

representing collapse, occlusion and complete regression. In this study we set $p^{(coll)}$ to 1, making collapses deterministic.

The vasculature obtained at the end of the tumor growth process ($t = 600\ h$) comprises the part of the network altered by the tumor and the remaining normal vasculature. Parameters used for simulations of oxygen transport (s. Table 1) are to a large extent taken from [58], compiled from various sources, not specifically for breast tissue.
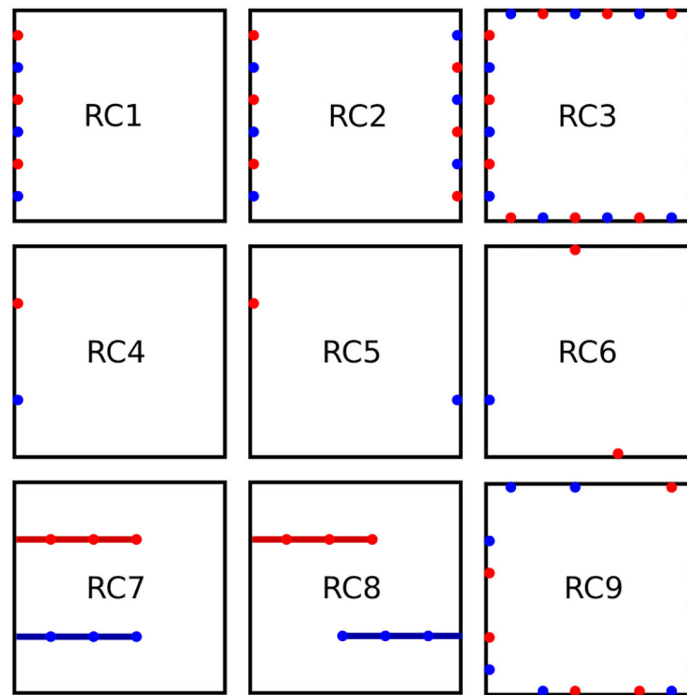
Fig 3. Illustration of vascular tree configurations. Schematic views from above on simulation cubes indicate vascular tree root locations for configurations denoted RC1 to RC9. In RC1 to RC3 boundary sites are occupied in alternating order either with arterial or venous nodes. In RC1 only one face of the simulation cube is used, in RC2 two opposing sides are used and in RC3 four faces are used. In RC4, RC5 and RC6 we place nodes at 33% and 66% of the length of the cube faces diagonals on the diagonals. As before, one, two and four faces are used, where in total only two (RC4, RC5) and four nodes (RC6) are placed. In RC7 and RC8 we first create fixed parent vessels protruding along the x-axis to 60% of the cube length into the interior. On each site occupied by these parent vessels a regular root node is created for further growth. Flow boundary conditions are specified at the actual inlets and outlets at the cube boundaries. In RC9 each boundary site of the lattice is occupied with a root node with probability p_{root}. Before a network is created, p_{root} is drawn equally distributed between 0 and 1, however a configuration is only accepted if there is at least one arterial and one venous node.

doi:10.1371/journal.pone.0161267.g003

Mathematical modeling of oxygen transport in networks and tissues

Hemodynamic and blood oxygen transport model. The concentration of oxygen dissolved in blood plasma or in tissue is proportional to the oxygen partial pressure, i.e. $c_p = \alpha_p P$ and $c_t = \alpha_t P_t$, where P, P_t are the oxygen partial pressures in plasma and tissue, respectively, and α_p, α_t are the oxygen solubilities. Conventionally, the partial pressures are measured in $mmHg$ and solubilities in $mlO_2/ml/mmHg$, yielding the oxygen concentrations expressed as oxygen gas volume at standard conditions (STP 0°C, 1 bar) per unit volume of plasma or tissue. In blood, oxygen, besides being dissolved in plasma, is bound to hemoglobin. Up to 4 molecules of oxygen can be bound per hemoglobin molecule. The chemical equilibrium between dissolved oxygen and oxygen-carrying hemoglobin depends on the number of oxygen molecules bound to hemoglobin, and the reaction is sufficiently fast, that the equilibrium state needs to be considered only. The cooperativity of oxygen-hemoglobin binding leads to the well-known oxygen dissociation curve [59], that can be approximated by the Hill equation [30]

$$S(P) = \frac{P^n}{P^n + P_{S50}^n},$$

(1)

Table 1. Oxygen transport parameters.

Symbol	Unit	Value	Ref/Note
n		2.7	[58]
P_{S50}	$mmHg$	27	[58]
α_p	$mlO_2\ ml^{-1}\ mmHg^{-1}$	$3.1 \cdot 10^{-5}$	[58] (a)
α_t	$mlO_2\ ml^{-1}\ mmHg^{-1}$	$2.8 \cdot 10^{-5}$	[58] (a)
c_0	mlO_2/ml	0.5	[60] (b)
D_t	$\mu m^2/s$	2410	[58]
D_p	$\mu m^2/s$	2750	[58]
$P_{M50}(normal)$	$mmHg$	4	(c)
$P_{M50}(tumor)$	$mmHg$	2	(c)
$M_0(normal)$	$\mu lO_2\ ml^{-1}\ min^{-1}$	3.7	(d)
$M_0(tumor)$	$\mu lO_2\ ml^{-1}\ min^{-1}$	14.8	(d)
γ	$\mu m^3\ O_2\ \mu m^{-2}\ s^{-1}\ mmHg^{-1}$	0.0033 – 0.021	(e)
η_{plasma}	mPa	1.2	[61]
$H^{(BC)}$		0.45	
$P_c^{(BC)}$	$mmHg$	100	[62]
$\Delta P^{(BC)}$	$mmHg/\mu m$	1	[62]
$P_0^{(BC)}$	$mmHg$	55	[62]
h_v	μm	4	
h	μm	40	

Shows parameters for throughout all simulations except case METAB where $M_0(tumor)$ is picked at random, for each simulation. n is the Hill-Exponent, P_{S50} is the PO2 where the the Hill-curve $S(P)$ is 1/2, α_p, α_t denote the oxygen solubilities in plasma and tissue, respectively, c_0 is oxygen concentration in saturated red blood cells, D_p, D_t denote the diffusion coefficients in plasma and tissue, P_{M50} denotes the M-M pressure where $M(P) = M_0/2$, M_0 denotes the maximal oxygen consumption rate, γ is the transvascular mass transfer coefficient. For blood flow, η_{plasma} is the blood plasma viscosity, $H^{(BC)}$ is the inlet hematocrit, and $P_c^{(BC)}$, $\Delta P^{(BC)}$ and $P_0^{(BC)}$ are the coefficients of the radius dependency of the inlet PO2 $P^{(BC)}(r) = min\{P_0^{(BC)} + r\Delta P^{(BC)}, P_c^{(BC)}\}$. The lattice constants h and h_v refer to the numerical grid on which the tissue PO2 distribution is defined, and the step width with which Eq (5) is integrated.

(a) Assuming 22.4 l/mol under normal conditions.

(b) Computed as the product of the hemoglobin binding capacity (Hüfner factor) 1.36 $ml\ O_2/g$ and the $MCHC$ (mean corpuscular hemoglobin concentration) 0.34 g/ml.

(c) Literature [32, 37, 39, 41] values for P_{M50} range from 1 to 4 $mmHg$. P_{M50} represents a threshold below which cells become hypoxic. We lowered P_{M50} in tumor tissue by a factor of 1/2 because cancer cells are generally associated with a resistance to hypoxia.

(d) The maximal consumption rate M_0 was estimated assuming zeroth order kinetics $MRO_2 = M_0$, using that $MRO_2 \cdot MTT = \epsilon c_{Hb, blood} \cdot OEF$ with $MTT = rBV/rBF$, $rBV = 0.008$, $rBF = 0.06 min^{-1}$ [8], $c_{Hb, blood} = 14$ gHb/dl, and $OEF = 0.32$.

(e) The lower bound is obtained for $r = 60$ μm and the upper bound for $r = 3$ μm.

doi:10.1371/journal.pone.0161267.t001

where $S(P)$ is the blood oxygen saturation, P_{S50} denotes the partial pressure at 50% saturation and n is the Hill exponent (see Table 1). Consequently, the total blood oxygen concentration, denoted by c, is the sum of the concentrations of dissolved and bound oxygen.

$$c = c_p + c_b = \alpha_p P + H c_0 S(P), \tag{2}$$

where H is the hematocrit, i.e. the volume fraction of red blood cells (RBCs), and c_0 denotes the concentration of oxygen per unit volume of RBCs at maximal saturation (s. Table 1).

65

Oxygen transport within a single vascular cylindrical tube. The intravascular PO2 variation along the longitudinal axis of a cylindrical vascular tube is described by $P(x)$, where x is the spatial coordinate. Following [40], we make the zeroth order approximation that the variation of PO2, hematocrit, and flow velocity in the radial direction within vascular tubes are negligible. This approximation reduces the problem to advection in one dimension. Radial transport, i.e. transvascular oxygen exchange is accounted for by the addition of suitable mass transfer terms (see below). Hence, the product of the oxygen concentration with the blood flow rate q yields the oxygen flux ι representing the total amount of oxygen at any given point that flows per unit time through the tube's cross-sectional area

$$\iota(P) = qc(P). \tag{3}$$

While blood flows along the vessel, some oxygen is continuously lost through the vessel wall. The respective transvascular flux density j_{tv} is given in units of amount of oxygen per lumen surface area and time. It causes a change in the longitudinal oxygen flux, which is expressed as

$$\frac{d\iota}{dx} = q\left[Hc_0 \frac{dS}{dP}\frac{dP}{dx} + \alpha_p \frac{dP}{dx}\right] = -2\pi r j_{tv}(x), \tag{4}$$

where the second expression is just the evaluation of $d\iota/dx$, and r is the vessel radius. Reordering yields the derivative of P

$$\frac{dP}{dx} = \frac{-2r\pi j_{tv}(x)}{q\left[Hc_0 \frac{dS}{dP} + \alpha_p\right]}. \tag{5}$$

For simplicity only losses due to diffusion are considered. This is certainly a good approximation for normal vessels because oxygen is a light molecule and has a proportionately high diffusion speed. Its diffusion constant in water is ca. $2 \cdot 10^3 \ \mu m^2/s$. Walls of tumor vessels, on the other hand, are leaky e.g. for plasma which is why a significant convective transport is plausible. Interstitial fluid velocities of up to $v = 1 \ \mu m/s$ have been reported near tumor vessels [63–66]. In order to judge whether diffusive or convective transport in tissue is dominant, we calculated the Peclet number $P_e = vL/D$ which relates advective transport rate to diffusive transport rate over a certain distance L. A reasonable L is 100 μm, corresponding to typical intercapillary separations, yielding $P_e = 1/20$. It follows that the transport is diffusion dominated. Intravascular radial oxygen transport is in itself a complex problem. To make transvascular oxygen flux workable, the mass transfer coefficient (MTC) γ is introduced that relates the transvascular oxygen flux density with the PO2 difference between the plasma and tissue partial oxygen pressure P and P_t.

$$j_{tv}(x) = \gamma \cdot (P(x) - P_t(x)). \tag{6}$$

Since vessels are represented as lines, we also assume that P_t is constant over the entire circumference. Note that $\gamma 2\pi r = K^{-1}$, where K is the radial transport resistance used in [40, 41, 67]. The MTC depends on several factors like tube radius, blood oxygen saturation, hematocrit, RBC shape [30] and vessel morphology [68]. We consider a radius dependency according to a simple fit model, based on empirical data for radial oxygen transfer in vascular tubes [58, 69, 70]: This is typically characterized by the dimensionless flux density, denoted Nusselt number $Nu = 2rD_p^{-1}\alpha_p^{-1} \cdot \gamma$, where D_p and α_p are oxygen diffusion coefficient and solubility in blood plasma. We found that the data presented in the Refs. cited above, ranging up to $r = 50 \ \mu m$, is

well fit by an exponential function

$$Nu(r) = p_2(1 - \exp(-r/p_1)),$$ (7)

where $p_1 = 8 \ \mu m$ and $p_2 = 4.7$ are fit parameters. For simplicity we omitted the dependence of Nu on the saturation S, assuming an approximate $S = 0.9$.

Blood flow and hematocrit in vascular networks. The vascular network is represented by a graph where edges represent vessel segments each connected to two nodes, whereas nodes may be attached to one to three vessel segments. Following the work of Pries et al. [71] we calculated blood pressure p at each node as well as blood flow rate q and hematocrit H associated with each vessel segment. The primary unknowns are the nodal pressures and segment hematocrits. The hematocrit may differ between various vessel segments due to phase separation.

The flow rates are given by Hagen-Poiseuille's law for flow through pipes $q = \pi r^4 \Delta p/(8\eta l)$, where r denotes the radius of the segment, l its length, η the (apparent) blood viscosity, and Δp the difference of the blood pressure at both nodes the vessel segment is attached to. Mass conservation demands at each non-boundary node that

$$\sum_v q_v = 0$$ (8)

$$\sum_v H_v q_v = 0,$$ (9)

where the index variable v runs over vessels adjacent to the currently considered node. Note that depending on context, the flow rate q must be taken as a signed quantity, e.g. in Eq (8) to correctly account for flow into and out of the considered node. In contrast to Ref. [71] we use pressure boundary conditions (BCs) where p at root nodes is set to a fixed value $p(root) = p^{(BC)}(r)$ depending on the radius and the type of vessel (artery or vein) (s. Eq (3) in S1 Appendix). Eq (8) and BCs lead to a system of linear equations, the solution of which yields the nodal pressures. The system is very large, of the order of 10^6 unknowns. We found that the Conjugate Gradient algorithm with the Multilevel (ML) preconditioner from the Trilinos software library [72] solves it efficiently. The calculated nodal blood pressures impose flow directions upon vessel segments, i.e. blood flows from the end-point with higher pressure to the end with lower pressure.

The apparent blood viscosity in microvessels varies with r and H (Fahraeus-Lindqvist effect) and is expressed by decomposing it into $\eta = \eta_{plasma} \eta_{rel}(r, H)$, where η_{plasma} is the viscosity of pure blood plasma and $\eta_{rel}(r, H)$ is known as relative viscosity. We implemented the η_{rel} formula from more recent work of Pries et al. [73] where η_{rel} is based on in vivo data. For brevity we refer to the original publication for the expression for η_{rel}.

Furthermore RBCs at arterial bifurcations tend to flow into the faster perfused branch (phase separation effect) resulting in an uneven hematocrit distribution across the network. Pries et al. [71] devised a phenomenological formula which describes the hematocrit H in the downstream branches of a bifurcation as a function of q and r of all adjacent vessels. For details we refer to [71]. With the help of this formula we compute the RBC flow qH in down stream vessels of arterial bifurcations, i.e. where one vessels splits into two downstream vessels. On the other hand, venous bifurcations have only one downstream branch where H is determined by Eq (9). Host vascular networks contain by default only bifurcations and the trivial case of two adjacent vessels. In the present model of tumor vascular remodeling, we reject sprout connections to other vessels that resulted in junctions with more than three vessels attached, following [50]. The hematocrit over the entire network can thus be computed with a simple depth-first

search graph traversal algorithm [74] starting from the venous ends and determining the downstream H while backtracking.

The ansatz to solve this coupled system of equations is iterative. In each iteration, the nodal pressures are computed using the results for the vessel segment hematocrit of the previous iterations, followed by the computation of the hematocrit with new flow rates. Details can be found in [71] (see also sec. 'Numerical solution').

Oxygen in vascular networks. The ansatz to determine the PO2 across the vascular network is similar to the method followed for calculating the distribution of hematocrit. First we consider the distribution at an arbitrarily selected node. To this end we define the sets $\mathbb{I}$ and $\mathbb{O}$ that contain adjacent up-and downstream vessels. Let further P_i for $i \in \mathbb{I}$ be the PO2 at downstream ends of adjacent inlet vessels. Then P_j for $j \in \mathbb{O}$ at the upstream ends of outlet vessels are to be determined. The main assumption made is that RBCs flowing into the junction instantly assume a common equilibrium partial pressure $\tilde{P}$, that by definition equals the PO2 at all outlets $P_j = \tilde{P}$ for $j \in \mathbb{O}$. $\tilde{P}$ is determined with the help of the oxygen mass balance

$$\sum_{i \in \mathbb{I}} q_i(c_0 S(P_i)H_i + \alpha_p P_i) = \tilde{\imath} = \sum_{j \in \mathbb{O}} q_j(c_0 S(\tilde{P})H_j + \alpha_p \tilde{P}), \tag{10}$$

where the left hand side is known and provides the total oxygen flux $\tilde{\imath}$ at the node under discussion. The right hand side is rearranged as

$$\tilde{\imath} = \left[\sum_{i \in \mathbb{O}} H_i q_i\right] c_0 S(\tilde{P}) + \left[\sum_{i \in \mathbb{O}} q_i\right] \alpha_p \tilde{P}, \tag{11}$$

where quantities in brackets are known RBC, and blood, flow rates. Eq (11) was solved numerically for $\tilde{P}$ using a bisection search. At inlet (root) nodes, boundary conditions (BCs) must be specified. We use Dirichlet BCs where $P = P^{(BC)}$ is given according to a curve $P^{(BC)}(r)$ depending on the arteriolar radius.

$$P^{(BC)}(r) = \min\left(P_0^{(BC)} + \Delta P^{(BC)} r, P_c^{(BC)}\right). \tag{12}$$

For the parameter values of $P_0^{(BC)}$, $\Delta P^{(BC)}$, $P_c^{(BC)}$ see Table 1. The determination of PO2 across the entire network can be defined procedurally with the help of the depth-first search graph traversal [74] defined analogously to the propagation of hematocrit. Starting from venous root nodes, the network is traversed towards the upstream ends. Let us consider a given node while backtracking. P is known at the upstream ends of adjacent inlet vessels, and according to Eq (5) the down-stream P is determined. Hence, Eq (11) provides P for further backtracking downstream. This procedure holds under the caveat that j_{tv} is known, which is addressed below.

Oxygen in tissue. The oxygen concentration in tissue, denoted $c_t(\boldsymbol{y})$, as a function of position $\boldsymbol{y}$, is determined by the solution the following steady state diffusion equation, considering a cubic domain $\Omega = (0, L)^3$ with lateral size L and Neumann boundary conditions.

$$D_t \nabla^2 c_t - M + Q = 0 \tag{13}$$

$$\nabla c_t \cdot \boldsymbol{n} = 0 \text{ on } \partial\Omega, \tag{14}$$

where M is the oxygen consumption rate per unit volume of tissue and the last term Q represents the oxygen exchange with vessels. With the help of the solubility α_t this equation is

68

rewritten in terms of the partial pressure P_t.

$$\alpha_t D_t \nabla^2 P_t - M + Q = 0 \tag{15}$$

$$\nabla P_t \cdot \boldsymbol{n} = 0 \text{ on } \partial\Omega, \tag{16}$$

where the symbols $Q = Q(P_t, \boldsymbol{y})$ and $M = M(P_t)$ are redefined as functions of P_t. They emerge from their former versions by simple scaling of their arguments by α_t.

We model oxygen consumption according to the well-known Michaelis-Menten (M-M) model [30]. The M-M model takes into account that viable cells consume oxygen up to a maximal rate M_0 even at high (excess) oxygen availability, and that consumption must drop to zero when the local oxygen partial pressure drops to zero. M is consequently defined as

$$M(P) = M_0 \frac{P}{P + P_{M50}}, \tag{17}$$

where the subscript for P has been dropped. The partial pressure at which M equals 50% of its maximal rate M_0 is denoted by P_{M50}. $M(P)$ increases monotonously and approaches M_0 asymptotically. The advantage of the M-M model over zero-or first order kinetics is a realistic description of hyper-and hypoxic situations. Apart from their vasculature, we assume the tumor tissue and host tissue to be homogeneous and that it behaves according to the M-M relation. The selected parameters M_0 and P_{M50} are thus representative of the mixture of all tissue components. This assumption is justified by the small volume of the tumor grown. Otherwise the expression for $M(P)$ has to be weighted by the fraction of viable cells in tumor and host tissue.

To find the vascular contribution Q, representing sources and drains, we follow [40] where line-like sources are embedded into the volume (tissue) with a magnitude equal to j_{tv}. Symbolically written, this corresponds to

$$Q(\boldsymbol{y}) = \sum_{v \in \mathbb{V}} \int_v 2\pi r j_{tv}(\boldsymbol{x}, r) \delta(\boldsymbol{x} - \boldsymbol{y}) dx, \tag{18}$$

where the summation is taken over all vessels and the integration along their center lines. δ is the Dirac delta distribution and j_{tv} is given in Eqs (6) and (7).

Numerical solution.   The equation for the vascular oxygen distribution Eqs (5) and (11) together with the diffusion equation for tissue Eq (15) form a complicated non-linear system of equations with the partial pressures values as unknowns. The only practical way to treat this is through a numerical solution.

Previously a similar approach to ours was followed by Beard [44] who distributes the exchange flux with vessels to nearby sites of a discretization grid of the tissue domain. We justify this approach with a formulation based on a Finite Element Method (FEM) and in contrast to [44] also include hemoglobin binding dynamics. As a result we obtain a sparse system of equations which is efficiently solved by an iterative scheme.

The principal idea of the FEM is to seek an approximate solution within a finite dimensional vector space V that is spanned by basis functions φ_i. Various choices are possible, e.g. Fourier bases, but the common approach is to introduce a grid and organize the φ_i such that their contribution is centered around a corresponding grid site $\boldsymbol{x}_i$, requiring that $\varphi_i(\boldsymbol{x}_i) = 1$ and $\varphi_i(\boldsymbol{x}_j) = 0$ for $i \neq j$. Here the choice falls for simplicity on piecewise linear (P1) tensor product bases

which are defined on a regular cubic grid. Then φ_i reads

$$
\begin{aligned}
\tilde{w}(x) &= \max\left(0, 1 - |x|/h\right) \\
w(\boldsymbol{x}) &= \tilde{w}(x_0)\tilde{w}(x_1)\tilde{w}(x_2) \\
\varphi_i(\boldsymbol{y}) &= w(\boldsymbol{y} - \boldsymbol{x}_i),
\end{aligned}
$$

where h is the lattice constant and $\boldsymbol{y} = (y_0, y_1, y_2)$ and likewise $\boldsymbol{x}$ in three dimensions. Incidentally evaluation of a function $f(\boldsymbol{y}) = \sum f_i\,\varphi_i(\boldsymbol{y})$ with some coefficients f_i is equivalent to a (tri-) linear interpolation of the coefficients between grid sites that are nearest to $\boldsymbol{y}$. Hence, let the tissue PO2 be an element of V such that

$$
P_t = \sum_j P_{t,j}\varphi_j. \tag{19}
$$

At this point it is advisable to proceed with the treatment of the vascular system. It is by definition already represented as discrete collection of segments but these are implicitly further subdivided by the integration points that are introduced for the solution of the axial transport Eq (5) (see below). We impose an equidistant subdivision with step length of approximately $h_v = 4\,\mu m$. In general, the last point needs to coincide with the end of the vessel. Therefore the true step length is adapted to the vessel length, corresponding to $\lceil l_v/h_v \rceil + 1$ integration points. Smaller values of h_v, given all other parameters fixed, did not yield noticeably different predictions.

In the following indices k, l are used for points on the vessel network whereas i, j denote indices to sites on the tissue grid. Now it is convenient to introduce vector and matrix notations. Hence let coefficient vectors be denoted in bold face, such that $\boldsymbol{P_t} = \{P_{t,i}\}$ and $\boldsymbol{P} = \{P_k\}$. And let further linear operators (matrices) be denoted in bold face underlined $\underline{\cdot}$.

The solution procedure relies on an outer iteration where the tissue degrees of freedom $\{P_{t,i}\}$ and the vessel degrees of freedom $\{P_k\}$ are updated in alternating order. This can be written with the aid of two functions $\boldsymbol{F}(\boldsymbol{P_t})$ and $\boldsymbol{F_t}(\boldsymbol{P},\boldsymbol{P_t})$ determining $\boldsymbol{P}$ and $\boldsymbol{P_t}$ from the last known quantities. An iteration variable n is introduced denoting the current step number. This is not to be confused with n in the Hill-equation Eq (1).

$$
\begin{aligned}
&\text{for } n = 1, 2, 3, \cdots \\
&\quad \boldsymbol{P}^{(n+1)} = \boldsymbol{F}(\boldsymbol{P}_t^{(n)})
\end{aligned} \tag{20}
$$

$$
\begin{aligned}
\boldsymbol{P}_t^{(n+1)} &= \boldsymbol{F}_t(\boldsymbol{P}^{(n+1)}, \boldsymbol{P}_t^{(n)}) \\
\text{while } &||\boldsymbol{P}_t^{(n+1)} - \boldsymbol{P}_t^{(n)}||_\infty > \epsilon \text{ and } ||\boldsymbol{P}^{(n+1)} - \boldsymbol{P}^{(n)}||_\infty > \epsilon,
\end{aligned} \tag{21}
$$

where $||\cdot||_\infty$ denotes the maximum norm. We set the initial guess for tissue $\boldsymbol{P}_t^{(1)}$ to $P_{root,max}/2$ on all grid points, i.e. to half the maximal inlet PO2. $\boldsymbol{P}$ needs no initial value since it is entirely determined by $\boldsymbol{P_t}$. The iteration is stopped when the change between the updates becomes less than ϵ, where we consider $\epsilon = 0.1\,mmHg$ to be small enough. Usually 200 to 400 iterations are needed for convergence, when applied to our tumor networks.

Evaluation of $\boldsymbol{F}$: The vascular tree is traversed down stream as explained. At each vessel, first the upstream PO2 is determined according to Eq (11) or according to the boundary condition Eq (12) if it is an inlet node.

Then Eq (5) is integrated with the implicit Euler method [75]. Explicit methods are not well suited to the problem since their stability requirements [75] lead to a step size $h_v < const \cdot q$. Since many tumor vessels are slowly perfused this would lead to sub-micrometer steps, incurring a prohibitive performance penalty. Note that the representation of P_t as superposition of

basis functions readily provides a means to obtain its function value for the r.h.s of Eq (5). Since the bases φ_i have a small support this can be efficiently implemented. Moreover storage of all P_k values is not required. Instead we perform required operations "on the fly" when the vascular PO2 is computed in **F**. This means we either record oxygen exchange contributions for P_t into the system matrix Eq (35) or compute observables for final output. It is sufficient to just store P_k at the upstream end of each vessel which is just $\tilde{P}$ from Eq (11).

Evaluation of $\mathbf{F}_t$: Our approach for the solution of the diffusion Eq (15) can be derived from the Galerkin method, where in brief, the general idea is as follows. First, the standard scalar product over the space of integrable functions over Ω is introduced $(f, g) = \int fg d\,\boldsymbol{x}$. Furthermore instead of the true solution, an approximation within the vector space V is searched for. This solution is defined as $f \in V$ for which the residual R after evaluation of the differential equation w.r.t. f is minimal, i.e. we look for $f \in V$ such that $(R, R) = min$. Here P_t takes the role of f and we have

$$R = \alpha_t D_t \nabla^2 P_t - M(P_t) + Q(P_t). \tag{22}$$

It can be shown that minimization of $||R||$ is equivalent to finding the P_t where R is orthogonal to V

$$(R, \varphi_i) = 0 \quad \forall i. \tag{23}$$

Eventually this results in an equation per grid site i in the unknowns $\{P_{t,i}\}$. The l.h.s. of Eq (23) decomposes into the summands

$$\alpha_t D_t (\nabla^2 P_t, \varphi_i) \tag{24}$$

$$(M(P_t), \varphi_i) \tag{25}$$

$$(Q(P_t), \varphi_i), \tag{26}$$

for which algebraic expressions are needed.

The benefit of considering a finite element formulation lies in the straight forward treatment of the transvascular exchange Q with its Dirac delta. Also FEM makes it straight forward to use higher order elements for better accuracy. Here however we use P1 elements. Moreover, if the integration of Eqs (24)–(26) is performed by the trapezoidal rule, then the resulting discretized equations look identical to standard finite differences, s. e. g. [76]. We use this to obtain for a smooth function g

$$(g, \varphi_i) \approx h^3 g(\boldsymbol{x}_i), \tag{27}$$

i.e. g is sampled at grid points, where we have control values $g_i = g(\boldsymbol{x}_i)$. Likewise, one obtains for a sufficiently smooth function f

$$(\nabla^2 f, \varphi_i) \approx h^3 [\underline{\Delta}_h \boldsymbol{f}]_i + \text{ boundary terms}, \tag{28}$$

where

$$(\underline{\Delta}_h \boldsymbol{f})_i = \sum_{j \in \text{Neighbors of } i} (f_j - f_i)/h^2. \tag{29}$$

$\underline{\Delta}_h$ is the discrete Laplacian [75] known from finite differences. Neighbors of i denotes the 6 nearest grid neighbors. At the boundaries we modify $\underline{\Delta}_h$ to account for the missing neighbors [75]. The consumption term $M(P_t)$ is expanded to first order around the oxygen level from the

71

last step. Following the above rationale, it is evaluated per grid point which yields

$$\frac{1}{h^3}(M, \varphi_i) \approx M(P_{t,i}^{(n)}) + M'(P_{t,i}^{(n)})[P_{t,i}^{(n+1)} - P_{t,i}^{(n)}], \tag{30}$$

where $'$ denotes the first derivative. More conveniently in matrix notation and with dropped super scripts, we write for the right hand side of Eq (30)

$$\boldsymbol{MA} + \boldsymbol{MB}\,\underline{\boldsymbol{I}}\,\boldsymbol{P_t}, \tag{31}$$

where $\underline{\boldsymbol{I}}$ denotes the identity, and

$$MA_i = M(P_{t,i}^{(n)}) - M'(P_{t,i}^{(n)})P_{t,i}^{(n)} \tag{32}$$

$$MB_i = M'(P_{t,i}^{(n)}) \tag{33}$$

The last contribution is derived by expanding Eq (26). For better readability, the super scripts are dropped again. Also the dependence of r and γ on the current vessel v is implied but for readability not indicated.

$$
\begin{aligned}
(Q(P_t), \varphi_i) &= \int_\Omega \sum_{v \in \mathbb{V}} \int_v 2\pi r j_{tv} \delta(\boldsymbol{x} - \boldsymbol{y}) \varphi_i(\boldsymbol{y}) d\boldsymbol{x} d\boldsymbol{y} \\
&= \sum_{v \in \mathbb{V}} \int_v 2\pi r j_{tv} \varphi_i(\boldsymbol{x}) d\boldsymbol{x} \\
&= \sum_{v \in \mathbb{V}} \int_v 2\pi r \gamma [P(\boldsymbol{x}) - P_t(\boldsymbol{x})] \varphi_i(\boldsymbol{x}) d\boldsymbol{x} \\
&= \left[\sum_{v \in \mathbb{V}} \int_v 2\pi r \gamma P(\boldsymbol{x}) \varphi_i(\boldsymbol{x}) d\boldsymbol{x} \right] - \left[\sum_j \sum_{v \in \mathbb{V}} \int_v 2\pi r \gamma P_{t,j} \varphi_j(\boldsymbol{x}) \varphi_i(\boldsymbol{x}) d\boldsymbol{x} \right]
\end{aligned}
\tag{34}
$$

The expression given in Eq (34) approximates the total volume rate of oxygen that extravasates from the entire vascular system into the tissue volume associated with the basis function φ_i. Now the integral over the vessel network is approximated with a Riemann sum based on the integration points $\{P_k\}$ from step Eq (20). Each integration point k represents a finite length segment $\Delta x_k = h_v$ except at the end points of each segment where $\Delta x_k = h_v/2$. In order to achieve good accuracy, we require $h_v << h$. Else, the integration kernel $2\pi\gamma\varphi_i$ or $2\pi\gamma\varphi_i\,\varphi_j$ will be under-sampled. This limitation could be removed to some degree by interpolation of the numerical solution of $P(x)$, decoupling it from the integration quadrature formula. From Eq (34) one obtains for the total volume rate of extravasated oxygen per cell volume

$$\frac{1}{h^3}(Q(P_t), \varphi_i) \approx \underbrace{\sum_k \frac{\Delta x_k 2\pi r}{h^3} \gamma P_k \varphi_i(\boldsymbol{x}_k)}_{QA_i} - \sum_j P_{t,j} \underbrace{\left[\sum_k \frac{\Delta x_k 2\pi r}{h^3} \gamma \varphi_j(\boldsymbol{x}_k) \varphi_i(\boldsymbol{x}_k) \right]}_{QB_{ij}}. \tag{35}$$

The factor $\Delta x_k 2\pi r/h^3$ is intuitively understood as vessel surface area per cell volume associated with vessel centerline integration step k. Finally, the completely assembled system of equations reads

$$[\alpha_i D_i \underline{\Delta}_h - \boldsymbol{MB}\,\underline{\boldsymbol{I}} - \underline{\boldsymbol{QB}}]\boldsymbol{P_t} = \boldsymbol{MA} - \boldsymbol{QA}. \tag{36}$$

It is easy to see that this is a sparse symmetric system. The Laplacian gives rise to 6 off-diagonal entries. The operator $\underline{\boldsymbol{QB}}$ gives rise to 26 off-diagonal entries corresponding to the nearest

and second nearest grid neighbors. For points which are spaced further apart, φ_i and φ_j have no overlap so their product in Eq (35) becomes zero.

In order to improve the efficiency we approximate $P_t(\mathbf{x_k})$ with the value from the current site $P_{t,i}$. This approximation is justified physically since the oxygen diffusion length considerably exceeds the lattice spacing h. Consequently, $\underline{\mathbf{QB}}$ is diagonalized such that the new version, now denoted $\underline{\tilde{\mathbf{QB}}}$, reads

$$\tilde{\boldsymbol{B}}_{ij} = \sum_k \frac{\Delta x_k 2\pi r}{h^3} \gamma \varphi_i(\boldsymbol{x}_k) \delta_{ij}. \tag{37}$$

This is a sparse linear system where the only off-diagonal terms stem only from the Laplacian, removing the off-diagonal entries corresponding to the second nearest neighbors. We solved these systems with an algebraic multigrid method (Trilinos ML [72]). We found the difference between the $\underline{\tilde{\mathbf{QB}}}$ and $\underline{\mathbf{QB}}$ solutions negligible.

The computational cost of our method scales well in the number of discretization points since the obtained sparse systems can be solved in $O(n \log n)$ time. In contrast the Green's functions method [41] gives rise to dense systems and is therefore much more computationally demanding.

We take grid constants h of 40 μm, which is rather coarse for resolving the approximately exponential decay of the O_2 concentration around isolated tumor blood vessels. The therewith associated diffusion range can be estimated, assuming zeroth order kinetics in one dimension, by $l_{diff} = \sqrt{2D\alpha_t P_t/M_0}$. This estimate is obtained from $dP_t(x)/dx = -M_0/D\alpha_t$, under the boundary conditions that $P_t(0) = P_0$, $dP_t/dx(l_{diff}) = 0$, and $P_t(l_{diff}) = 0$. We obtain, $l_{diff} = 295$ μm in normal tissue, and 148 μm in tumor, using the parameters in Table 1 and assuming that $P_0 = 40$ $mmHg$. In two dimensions, the Krogh model for a capillary of 3 μm radius, yields approximately $l_{diff} = 150$ and 80 μm in normal and tumor tissue, respectively. However, we do not use Fick's law as in $j_{tv} = -D\alpha_t \nabla P_t$ to determine the amount of extravasated oxygen. Instead, j_{tv} is computed from the difference between P and P_t at the vessel center line. Therefore the result does not depend critically on the precise resolution of tissue $PO2$ gradients.

We repeated our calculations with a grid constant h of only 20 μm. As a result, the peaks of the calculated P_t distributions are better resolved. Concomitant changes in the predicted averages are rather small. For instance we obtain lower average OEF (0.1 versus 0.11), lower P_t (25 vs. 28 $mmHg$—the most significant change), and higher Y (0.75 vs. 0.73), in tumors of case CMPR. However, these variations are well within experimental uncertainties. Therefore, our overall results and conclusions are left unaltered.

In Fig D in S1 Appendix we investigated the convergence of the on-axis oxygen partial pressure $P(x)$ with decreasing lattice constant h and conclude that at $h = 40$ μm the accuracy is between 3 to 13% depending on the location along the vessel. Differences of the absolute values of the intravascular and extravascular partial oxygen pressures $P(x)$ and $P_t(\boldsymbol{y})$ with respect to the Green's function technique of Secomb et al. [41] are illustrated in Fig C in S1 Appendix. Overall, we estimate uncertainties of absolute intravascular and extravascular partial oxygen pressures to be in the order of 10 – 20%.

Simulation setup

Expressions for tissue hemoglobin concentration and tissue blood oxygen saturation.
For a comparision of simulated tissue hemoglobin concentration c_{Hb} and tissue blood oxygenation Y with clinical data we provide expressions for these quantities based on host and tumor vascular networks. Corresponding expressions for other quantities of interest are

PLOS ONE   Computation of Tumor Oxygenation with Application to Breast Cancer

given in S2 Appendix.

$$c_{Hb} = MCHC \cdot rRBCV = \frac{MCHC}{|\Omega|} \sum_{v \in \mathbb{V}} \pi r_v^2 l_v H_v \tag{38}$$

$$Y = \frac{c_{HbO}}{c_{Hb}} = \sum_{v \in \mathbb{V}} \left\{ \frac{\pi r_v^2 H_v l_v}{\sum_{u \in \mathbb{V}} \pi r_u^2 l_u H_u} \frac{1}{l_v} \int_v S_v(x) dx \right\}, \tag{39}$$

where $\mathbb{V}$ is the set of vessel segments of host or tumor tissue, $MCHC$ is the mean corpuscular hemoglobin concentration, $|\Omega|$ the relevant tissue volume, $r_v, l_v, H_v, S_v(x)$ designate radius, length, hematocrit and blood oxygen saturation of vessel segment v. In Eq (39) integration of blood oxygenation is taken over the length of the vessel segment.

Tissue total hemoglobin concentration c_{Hb} is the sum over the hemoglobin mass of all vessel segments per unit volume of tissue. Tissue blood oxygenation Y is the average of RBC-volume-weighted blood oxygen saturation taken over all vessel segments. It follows that high-caliber vessels contribute dominantly to c_{Hb} and Y, being less sensitive to the capillary plexus.

Simulation model variants. In the following we discuss three different scenarios denoted BASE, CMPR and METAB. Cases BASE and METAB use the same tumor vascular networks ($t = 600\ h$), but differ in their assumptions made to calculate tissue metabolic rate of oxygen consumption variables. CMPR, on the other hand, augments the processes that cause remodeling of the tumor vasculature by accounting for vascular compression by solid pressure, leading to tumor vascular networks at $t = 600\ h$ that differ from the networks of the scenarios BASE and METAB.

Case BASE This is our base case with parameters for growth of breast tumor vasculature listed in Table 2. Blood flow, hematocrit distribution, blood and tissue oxygen concentrations were calculated using each of the 90 realizations of tumor vasculature ($t = 600\ h$) together with

Table 2. List of parameters for tumor growth.

Parameter	Value	Unit	Description
$R_{tum}(t = 0)$	250	μm	Initial tumor radius
v_{tum}	2	$\mu m/h$	Tumor radius expansion rate
R_g	200	μm	Growth factor diffusion range
$t_{EC}^{(switch)}$	12	h	Circumferential growth switch delay
$t_{EC}^{(sprout)}$	2	h	Time between sprouting events
$t_{EC}^{(migr)}$	50	h	Sprout activity duration
$d^{(br,min)}$	80	μm	Sprout sites minimum separation
$t_{EC}^{(prol)}$	144	h	Endothelial cell proliferation time
$r^{(sprout)}$	2.6	μm	Initial sprout vessel radius
$r^{(max)}$	10 *, 14 **	μm	Maximum dilatation radius
$p^{(coll)}$	1		Vessel collapse probability
Δw	0.05	$\mu m/h$	Vessel stability (w) decrease rate
$f^{(coll)}$	0.25	Pa	Critical wall shear stress
$h_{(gen)}$†	130	μm	Lattice constant of initial network generation

* case BASE.

** case CMPR. Increased maximal dilatation radius compensated for by overall compression of tumor vessels (see text).

† The lattice constant $h_{(gen)}$ corresponds to the vessel segment length in the initial ($t = 0$) networks. Simulation of tumor growth and vascular remodeling is performed at only 10 μm lattice spacing. This is possible since segments of the initial $t = 0$ lattice coincide with bonds and sites of the finer 10 μm lattice.

doi:10.1371/journal.pone.0161267.t002

parameters related to oxygen transport given in Table 1. The maximal oxygen consumption rate of tumor tissue was assumed amounting to $M_0(tumor) = 4 \cdot M_0(normal)$ and $P_{M50}(tumor)$ was assumed equal to $1/2 \cdot P_{M50}(normal)$, reflecting the enhanced need for oxygen of proliferating tumor cells. Reports on measured oxygen consumption of solid tumors are scarce in the literature. We include a recent report on metabolic rate of oxygen consumption of viable multicellular spheroids of human colorectal carcinoma cells [77] indicating that $M_0(tumor)$ might even be underestimated. Compared to previous simulations concerning melanomas [28], changes in the tumor growth parameters (s. Table 2) include $d^{(br,min)}$, governing the *MVD* near the tumor rim, $f^{(coll)}$, and $r^{(max)}$ determining the central *MVD* and *rBV*. Other parameters such as the sprouting time $t_{EC}^{(sprout)}$, and vessel wall degradation rate Δw are unaltered.

Case CMPR: Vascular compression We allowed for compression of tumor vessels during tumor growth by extravascular stress on simulated tissue blood oxygen saturation Y_{tum} based on the final $t = 600\ h$ tumor vasculature. Compression of tumor vessels will change the relation of Y_{tum} and the tissue blood oxygen saturation of the surrounding normal breast tissue Y_{norm} obtained from the corresponding vascular network at $t = 0$. Elevated interstitial fluid pressure (IFP) is known to be a hallmark of tumors [10], primarily caused by the increased leakiness of tumor vessels and the lymph drain being impaired in solid tumors. Yet the precise mechanisms by which extravascular pressure compresses tumor vessels are still under debate [78, 79]. The uncontrolled proliferation and growth of tumor cells within a restricted volume generates extravascular solid stress. Solid stress accumulates within the tumor volume through an increase in tumor cell density and hyperproduction of interstitial matrix molecules such as collagen and hyaluronan [9–11]. Collagen fibers are resistant to tensile stress whereas hyaluronan resists compression thus transferring stress on tumor vessels. On the other hand water-loaded hyaluronan can be considered to be part of the relative immobile fluid phase of the interstitial fluid, contributing to IFP apart from contributions of the freely mobile fluid phase. Furthermore, solid stress can be exerted on the tumor volume by the surrounding normal tissue. It was estimated that solid stress becomes significant for tumor volumes larger than $0.065\ mm^3$, corresponding to a sphere of $R_{tum} = 250\ \mu m$ [80]. A detailed simulation of solid stress during progression of the tumor is beyond the scope of the present paper. Therefore we assume that all vessels of the tumor vasculature experience compression during the growth process, i.e. a reduction of their radius by a constant factor. The fundamental difference to the case BASE is that in this way high-caliber vessels experience a reduction in radius, which cannot be achieved by the previous model that predicts either growth or complete removal of vessels. Hence we introduce a new "compressed" vessel radius, denoted $\tilde{r}$ which enters the blood flow and oxygen computation. We consider a function $\psi(|\boldsymbol{x}|)$ of the spatial coordinate $\boldsymbol{x}$ that represents the magnitude of compression relative to the base radius, depending on the distance from the tumor center $|\boldsymbol{x}|$. Therefore we define $\tilde{r} = \psi \cdot r$. We let ψ describe a linear transition between full compression of magnitude $1 - \xi_{cpr}$, in the tumor center and zero in normal tissue. Thus, vascular radii $\tilde{r}$ within the tumor, with the exception of a small transition zone of width w_{cpr}, are reduced relative to r by a factor of ξ_{cpr}. Since compression affects all vessels, and to obtain a common mean capillary diameter of cases BASE and CMPR, $r^{(max)}$ was increased in case CMPR from $r^{(max)} = 10\ \mu m$ to $14\ \mu m$. This compensation helps to separate the effect of compression of large vessels from an overall compression of all radii.

$$\psi(x) = \begin{cases} \xi_{cpr} & \text{for } x < R - w_{cpr} \\ 1 & \text{for } x > R + w_{cpr} \\ \xi_{cpr} - \frac{x - R + w_{cpr}}{2 w_{cpr}} \cdot (\xi_{cpr} - 1) & \text{else,} \end{cases} \tag{40}$$

where $R = R_{tum}$ is short for the tumor radius and w_{cpr} is assumed 200 μm. We assume that varying degrees of compression are present in the tumors of the patient cohort due to phenotypical differences from tumor to tumor or differences in the micro environment of the host. Therefore a new ξ_{cpr} was drawn for each simulation from a uniform distribution over the interval between 0.5 and 1. The lower bound of 0.5 was deliberately chosen since it appears to be the lower bound of what was reported for experiments, i.e. relief of stress resulted in two times increase of vessel diameters [81].

Case METAB: Variation of tumor oxygen consumption rate In contrast to case CMPR scenario, METAB uses the identical tumor vascular networks as case BASE. However, rather than selecting the same maximal oxygen consumption rate M_0 for all tumors as in scenario BASE we consider variations of the maximal tumor oxygen consumption rate M_0 among various tumors reflecting phenotypical differences. In this way we probe the impact of tumor tissue oxygen consumption versus tumor vascular restructuring on intra-and extravascular oxygen distributions. Therefore, $M_0 / (ml\ O_2/ml/min)$ is drawn from a lognormal distribution with $mu = log(0.0149)$ and $sigma = 0.3$ on a tumor by tumor basis, yielding a median M_0 identical to case BASE and a standard deviation of 32% of the median. The oxygen consumption rate of normal tissue is kept at its original value (s. Table 1). Furthermore oxygen partial pressures P_{M50} were kept unchanged.

Results and Discussion

Tumor compartmentalization and contributions of tumor core to hemoglobin concentration, fractional blood volume and tissue blood oxygenation

Using the model parameters listed in Table 2 together with the root node geometries illustrated in Fig 3 we simulated vascular networks corresponding to normal breast tissue ($t = 0$, "initial") and tumors ($t = 600h$, case BASE, case CMPR). As can be seen from Fig 4, tumor vascular networks are highly compartmentalized, comprising a central core with low MVD and a highly
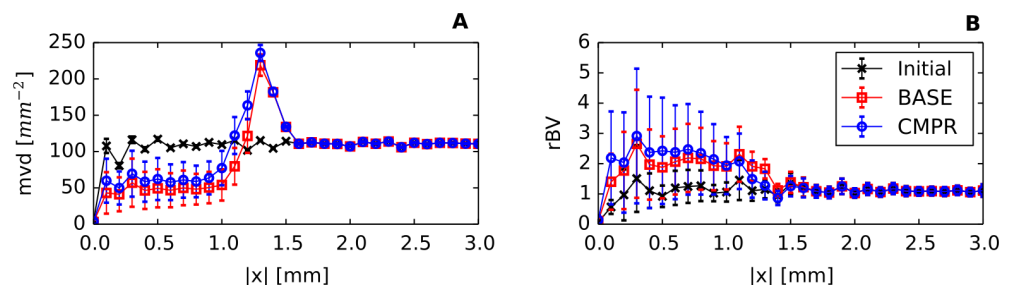
Fig 4. Radial distributions of the microvascular density, *MVD*, and the relative blood volume, *rBV*. The simulation box was divided in 100 μm thick concentric shells over which the regional *MVD* and *rBV* were determined to obtain radial profiles depending on the distance from the center |x|. Plotted is the ensemble mean of these profiles, where the error bars display the standard deviation (STD). As can be seen, a compartmentalization into varying degrees of vascularization (*MVD*) and vascular dilatation (*rBV*) exist which is typical for Melanoma [56] and Glioma [57]. Fig 4 provides evidence that these features are also present in breast tumors. The STD of *MVD* further shows that the *MVD* of the tumor core is below normal in most realizations of the ensemble which conforms to our expectations for tumors. Oscillations are an artifact of the confinement of the vessels to a lattice.

doi:10.1371/journal.pone.0161267.g004

vascularized peripheral shell of a few hundred micrometer thickness, consistent with previous results [28, 50–54]. The arterio-venous organization is lost, and the remaining high caliber vessel protruding into and through the tumor are connected with a chaotic network of dilated capillaries. Although central tumor *MVD* is lower than normal (s. Fig 4A), relative blood volume rBV is above normal within the tumor core (s. Fig 4B). It follows that vessels crisscrossing the tumor core are predominantly of high caliber. As was mentioned above, all vessel segments contribute to the average blood oxygen saturation $\langle S \rangle$ proper (s. S2 Appendix), independent of their volume.

Fig 5 provides examples for vascular networks corresponding to tumor model CMPR, and root node geometry RC9 (cf. Fig 3). Distributions of partial oxygen pressure (PO2) of blood vessels, P, and of tissue, P_t, as well as corresponding distributions of blood oxygen saturations S are shown at the start ($t = 0$, top row) and at the end ($t = 600$ h, bottom row) of the growth process. The other cases (BASE, METAB) and root node geometries exhibit similar looking distributions of PO2 and blood oxygen saturation S in normal tissue and tumor periphery. However, the vascularization at the tumor center can be lower or higher than for the example shown, which is accompanied with varying degrees of oxygenation. We made sure that in good approximation cases BASE and CMPR exhibited similar radial *MVD* and *rBV* profiles. This requirement is critical since we aim to analyze the effect on tissue blood oxygen saturation Y by varying the compression factors ξ_{cpr} among the ensemble of 90 tumor vascular networks (see below), while retaining agreement with clinical data on *MVD* and *rBV*. We consider details of the oxygen distribution shown for instance in Fig 5C. Immediately obvious, we see severe hypoxia at the tumor center due the sparse vasculature there. As one would expect, P_t is highest near vessels and falls off into non-vascularized spaces over a scale of 100 to 200 μm, corresponding to the oxygen diffusion-range.

Redirection of hematocrit modulates blood oxygen saturation

Tumor vessels in the central region of the tumor vary significantly in their oxygen content. Some vessels carry highly saturated blood, in particular when connected to nearby arterioles. When isolated vessels thread the tumor over distances of several hundred micrometers, blood oxygen saturation S visibly decreases to the point where vessels are completely depleted of oxygen. The tissue PO2 near such vessels follows this trend. Remarkably, the (neo-)vascular plexus around the tumor rim is dominated by severe oxygen deprivation. However, the few high caliber vessels which advance towards the tumor center carry normal amounts of oxygen. We explain this by the phase separation effect taken into account in our simulations. This means that red blood cells (RBCs) at bifurcations prefer to flow into the more strongly perfused branch [71]. Accordingly, simulated hematocrit distributions exhibit high hematocrit in central tumor vessels, as exemplarily shown in Fig 6. We conclude that RBCs are redirected into central vessels, consequently leading to a lack of RBCs in the peripheral capillary plexus and a drastically decreased oxygen carrying capacity. The impaired oxygen carrying capacity, in turn, results in fast oxygen depletion to hypoxic levels which could drive further invasive behavior in real tumors. On average, the hematocrit taken over the concentric core region 100μm beyond the invasive edge is elevated to 117% of baseline hematocrit in normal tissue. In contrast, the average taken over annular shells near the invasive edge of 50 μm thickness drops to 66%.

For some applications, such as models of tumor growth, it might be sufficient to implement a simplified model of tissue oxygenation, setting intravascular PO2 constant, thus treating it as input parameter. Therefore, in S1 Fig we briefly consider such a simplification and highlight qualitative differences to results obtained by our full model of oxygenation.
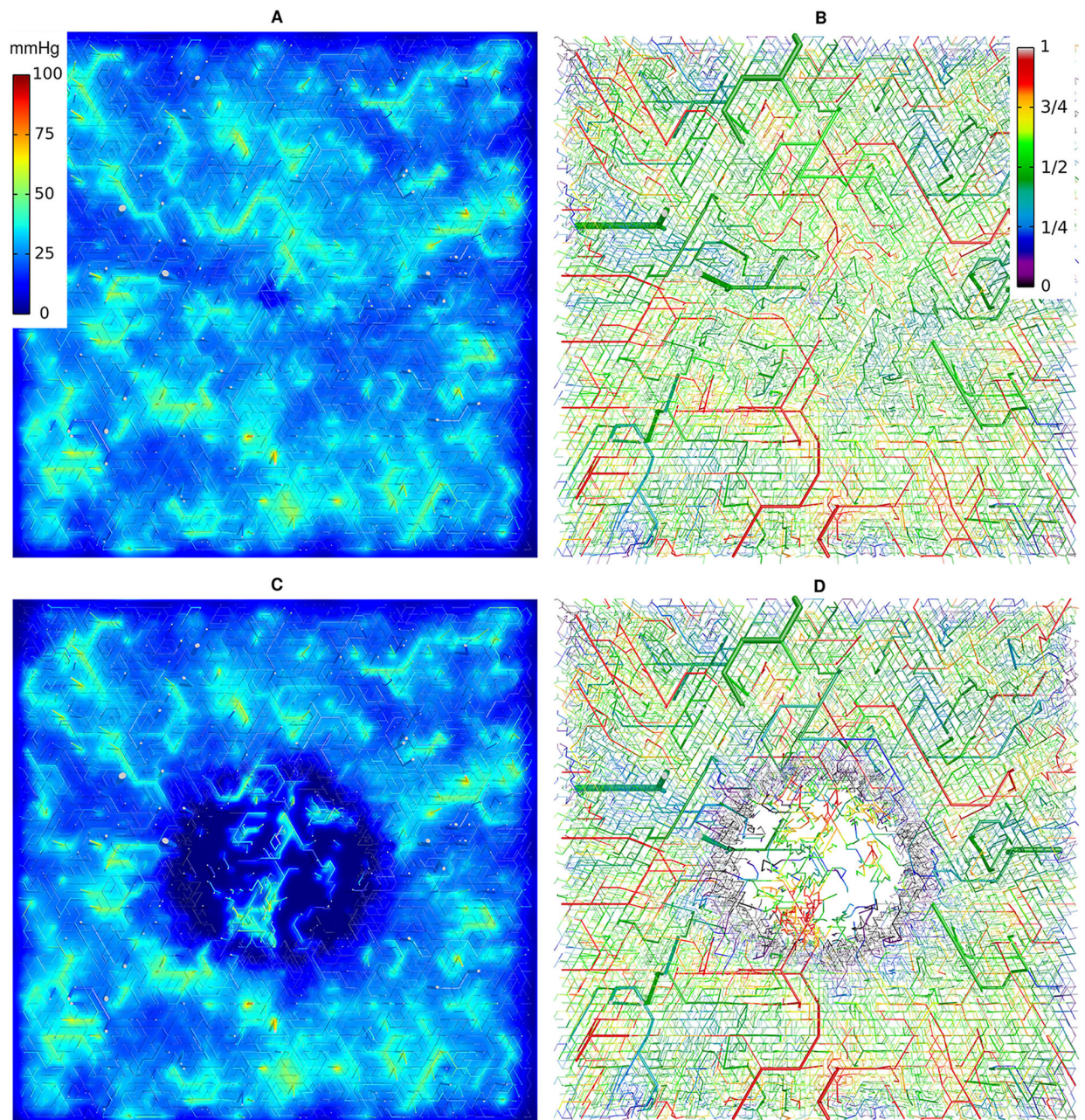
Fig 5. Blood oxygen saturation and oxygen partial pressure corresponding to case CMPR, root node configuration RC9. The left column (A, C) shows the PO2 of vessels, P and of tissue, P_t in a slice through the center of the simulation domain. The camera is looking vertically onto the horizontal cutting plane so that the whole lateral extent of 8 *mm* is shown. The vessel network is visualized as a collection of cylinders that have been truncated 100 *μm* above and below the central plane. The resulting cross sectional areas are light grey. Otherwise the color code indicates the PO2, P, of vessels and P_t of tissue, respectively. In the right column (B, D), only the network is shown color coded by saturation S. The top row (A, B) shows the initial state at t = 0. The bottom row (C, D) shows the final state at $t = 600\,h$.

doi:10.1371/journal.pone.0161267.g005

Fig 6. Hematocrit distribution corresponding to Fig 5D, showing the same slice of the vessel network, but color coded for *H*. Our blood flow model includes the phase separation effect which leads to a severe reduction of the hematocrit in the peripheral tumor network and an elevated hematocrit in the vessels at the tumor center.

doi:10.1371/journal.pone.0161267.g006

Model validation: vascular morphology, blood flow and oxygenation

In order to validate our simulation model we calculated various biophysical quantities and compared the results with data available in the literature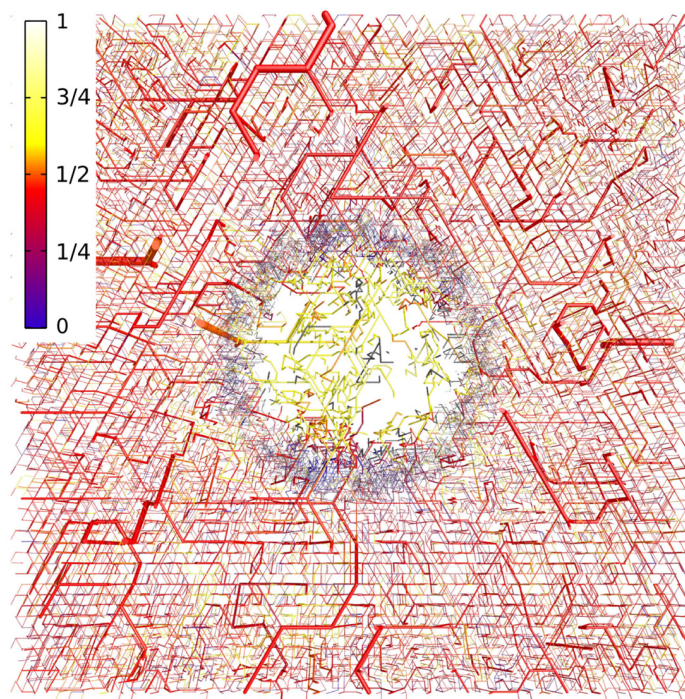. Values listed in Tables 3 and 4 represent averages (means) over the results of all 90 vascular networks, including standard deviations, at a given time. The initial networks ($t = 0$) are taken to represent vasculature in normal breast tissue, neglecting the influence of the small tumor of radius 250 μm at the center of the simulation domain. Data given in column "Initial" are therefore associated with normal breast tissue. Data for the cases BASE, CMPR and METAB were calculated at the end ($t = 600\ h$) of the tumor growth process.

Explicit formulas for the parameters listed are given in S2 Appendix. It should be kept in mind that for most biophysical variables, results corresponding to a particular vascular network represent (weighted) averages taken over all vessel segments of the network (s. S2 Appendix). For comparison, Tables 3 and 4 also include clinical data, data obtained from animal models and theoretical results taken from the literature. In the following we comment on some of the simulated and literature data. Additional details are provided in S4 Appendix.

In general, good to fair agreement was achieved between simulation results and corresponding literature data. In particular total hemoglobin concentration and tissue blood oxygenation Y, known from optical mammography were reproduced both for normal breast tissue and breast tumors. Likewise, simulated vascular volume densities fall within the range of *rBV* values reported in the literature. In Table 3 we take simulated length density L_D, i.e. the total length of

Table 3. Morphological data: Simulation results and literature values.

Symbol	Unit	Initial	Clin./Lit.	BASE/METAB	CMPR	Clin./Lit.
MVD, L_D	mm^{-2}	111 ± 0.4	115 ± 8 [84]	112 ± 19	133 ± 18	$88 (15 - 348)$ [85]
						$20 (0 - 157)$ [86]
						$21 (9 - 101)$ [7] (a)
rBV	%	0.98 ± 0.10	0.8 ± 0.3 [22] (b)	1.9 ± 0.6	1.8 ± 0.9	2.4 ± 1.5 [22] (b)
			3.4 ± 0.6 [87] (c)			4.3 ± 1.3 [87] (c)
						$0.67 (0.2 - 3.4)$ [7] (a)
r	μm	4.1 ± 0.1	-	5.9 ± 0.4	5.2 ± 1	9.23 ± 0.27 [7] (a)
S_D	mm^{-1}	2.8 ± 0.04	-	4.2 ± 1	4.4 ± 1.1	$0.5 - 5.4$ [7] (a)
S_D/rBV	μm^{-1}	0.29 ± 0.03	-	0.22 ± 0.03	0.27 ± 0.06	0.165 [7] (a)
rBF	$mlg^{-1} min^{-1}$	0.053 ± 0.014	0.06 [8]	1.6 ± 1.3	1.2 ± 1.3	0.32 [8]
			0.056 ± 0.014 [88]			0.19 ± 0.1 [87]
			0.04 ± 0.01 [87]			0.29 ± 0.17 [88]
			0.028 ± 0.017 [89]			$0.07 - 0.16$ [90] (d)
						$0.001 - 2$ [7] (a)
rBF_{scaled}	$mlg^{-1} min^{-1}$	-	-	0.12 ± 0.04	0.091 ± 0.050	-

Shows averages and standard deviations taken over 90 initial networks ($t = 0\,h$) and tumors ($t = 600\,h$) for cases BASE, CMPR and METAB. Morphological data for BASE is the same as METAB. We compiled clinical data, data from animal models and theoretical data taken from literature in the columns "Clin./Lit." for normal (left) and tumor tissue (last col.), respectively. Microvascular density obtained by our model and from [7] is given as the line density L_D whereas data from [85, 86] are the medians of histological MVD. rBF_{scaled} is the initial tissue rBF scaled by the ratio of perfusions, rBF, of the iso-volumetric tumor sphere at $t = 0$ and at $t = 600\,h$ (see text).

(a) Obtained from digitized animal model tumor network obtained by μ-CT.

(b) rBV estimated from c_{Hb} assuming 2.18 $\mu mol/l$ hemoglobin in blood.

(c) Data from [87] was obtained by PET of human breasts. Note that PET data from [87] for tumor tissues are considered unreliable (see text).

(d) obtained from human breast cancer xenografts in animal model.

doi:10.1371/journal.pone.0161267.t003

the vascular network divided by the tissue volume (s. S2 Appendix), as measure for microvessel density MVD, conventionally obtained by microscopically counting the number of microvessels per area of a tissue section. Simulated length density L_D and clinical MVD of normal breast tissue agree quantitatively and length densities L_D of the tumor model variants fall within the range of MVD reported for breast cancers in the literature. Average vessel radii corresponding to the tumor model variants BASE, CMPR and METAB are about 60% of those reported by Stamatelos, probably because the maximal dilatation radius was limited to 10 μm (BASE/METAB) and 14 μm (s. Table 2). Tumor vessel surface density S_D and tumor vessel surface density over tumor vascular volume density S_D/rBV are consistent with the data reported by Stamatelos et al. [7].

Regional blood flow, rBF, i.e. perfusion, is given by the ratio of total blood flow entering a selected tissue region Ω to its volume $|\Omega|$ (s. S2 Appendix). To calculate host perfusion rBF_{norm} of the entire simulation cuboid we sum the flow rates q over all arterial root nodes and divide by the volume of the simulation box $|\Omega| = L^3$. Good agreement between simulated perfusion rBF_{norm} and clinical data was achieved. However, for a partial volume, such as a small spherical tumor inside the tissue cuboid, some caution must be taken. Assuming a constant surface flux density of blood, the perfusion of the small spherical volume scales as $1/R_{tum}$. Indeed, perfusion rates rBF_{tum} predicted for the relatively small tumors, simulated here, are much larger than clinical rBF data from breast tumors which are typically of several cm^3 in volume. To estimate the perfusion rBF_{scaled} that corresponds to larger simulated tumors, we scale rBF_{tum} in the

Table 4. Oxygenation data: Simulation results and literature values.

Symbol	Unit	Initial	Clin/Lit.	BASE	CMPR	METAB	Clin/Lit.
$\langle S_{in}\rangle_q$		-	0.98 [91] (e)	-	-	-	-
rJ_{in}	$\mu l O_2\ ml^{-1}\ min^{-1}$	12 ± 3	-	331 ± 266	249 ± 282	331 ± 265	11 – 27 [90] (d)
$rJ_{in,scaled}$	$\mu l O_2\ ml^{-1}\ min^{-1}$	-	-	25 ± 10	18 ± 12	25 ± 10	-
j_{tv}	$\mu l O_2\ min^{-1}\ cm^{-2}$	0.12 ± 0.001	0.6 [92] (f)	0.24 ± 0.02	0.20 ± 0.02	0.24 ± 0.06	-
MRO_2	$\mu l O_2\ ml^{-1}\ min^{-1}$	3.3 ± 0.1	4.5 ± 1 [87]	12 ± 1	12 ± 2	13 ± 3	6.6 ± 2.8 [87] (c)
			33 ± 5 [93] (i)				40.6 ± 7.8 [77] (g)
							21 – 52 [83] (g)
							33.4 ± 8.3 [83] (h)
							4.5 – 11.8 [90] (d)
OEF		0.34 ± 0.10	0.65 ± 0.1 [87]	0.068 ± 0.050	0.11 ± 0.09	0.068 ± 0.051	0.23 ± 0.08 [87]
			0.44 ± 0.06 [93] (i)				0.3 – 0.52 [90] (d)
OEF_{scaled}		-	-	0.55 ± 0.19	0.88 ± 0.46	0.55 ± 0.22	-
c_{Hb}	$\mu mol/l$	24 ± 3	17.3 ± 6.2 [22]	47 ± 14	43 ± 19	47 ± 14	53 ± 32 [22]
			16 ± 4 [23]				70 ± 35 [23]
Y		0.70 ± 0.10	0.74 ± 0.14 [22]	0.81 ± 0.10	0.73 ± 0.14	0.81 ± 0.10	0.72 ± 0.14 [22]
			0.74 ± 0.09 [23]				0.71 ± 0.10 [23]
P	$mmHg$	39 ± 6	-	45 ± 11	34 ± 13	45 ± 12	-
P_t	$mmHg$	36 ± 6	30 [94] (k)	35 ± 14	29 ± 14	35 ± 14	30 (0 – 100) [14] (j)
			65 (12 – 100) [14] (j)				
			40 – 50 [95] (k)				

This is a continuation of Table 3 with data of tumor and normal tissue oxygenation. $\langle S_{in}\rangle_q$ denotes the flow-weighted blood oxygen saturation at input. rJ_{in} denotes the oxygen supply at input $rJ_{in} = c_0 H\langle S_{in}\rangle_q \cdot rBF$. For tumors, $rJ_{in,scaled}$ denotes the scaled quantity where rBF_{scaled} is used. In addition to the following notes, see Table 3 for further notes.

(e) Oxygen saturation of human arterial blood at sea level.

(f) Obtained by oxygen micro-electrode measurement in rat brains [92].

(g) Obtained from various human cancer cell spheroids, excluding breast cancer.

(h) Obtained from MDA-MB-468 human breast cell spheroids.

(i) Obtained from human brain by PET.

(j) Median and range; obtained from human breast cancer and normal tissue using polarographic needles.

(k) Obtained from peritumoral skin tissue [94] and muscle tissue in breast tumor-bearing rats [95].

following way: $rBF_{scaled} = rBF_{norm} \cdot rBF_{tum}/rBF_{sph,norm}$. Here, $rBF_{sph,norm}$ denotes the perfusion of the isovolumetric spherical volume V_{sph} of normal tissue ($t = 0$) that corresponds to the tumor spheroid at $t = 600\ h$. The perfusion rates rBF_{tum} and $rBF_{sph,norm}$ are obtained from summation of blood flow q over those vessels that penetrate the surface of the sphere V_{sph} and have a blood flow direction into the spherical tissue volume. Scaled perfusion rBF_{scaled} is lower by a factor 2—3 compared to clinical data on breast cancers. However, scaled perfusion falls within the range of perfusion values reported by Stamatelos [7] and Kallinowski et al [82] for human breast cancer animal models. In addition, Table 3 lists the regional blood flow of the small spherical tumor rBF_{tum} proper.

The metabolic rate of oxygen consumption MRO_2 of normal tissue is mainly determined by the assumed Michaelis-Menten maximal rate M_0 (s. Table 1), since (average) partial oxygen pressure P_t in tissue is considerably larger than the Michaelis-Menten oxygen half pressures. As a result, the simulated MRO_2 for normal breast tissue favorably compares with clinical data. To

our knowledge there are no reliable clinical data available on metabolic rates of oxygen consumption of breast cancers. Therefore, we considered a maximal consumption rate $M_0(tumor)$ for cases BASE and CMPR, consistent with the metabolic rates of oxygen consumption reported for xeno-transplanted human breast cancers in animal models [82] (see above for case METAB). More recently, metabolic rates of oxygen consumption, ranging from $21 - 52 \mu l O_2/g/min$, were determined from multicellular tumor spheroids of various human cancer cell lines, including breast cancer ($33 \pm 8 \mu l O_2/g/min$), serving as avascular in-vitro tumor models [77, 83], also consistent with our choice of M_0.

The cohort average of the predicted tumor O_2 consumption $M(P_t)$ proper is close to the assumed maximal rate M_0, indicating that predominantly $P_t > P_{M50}$, in spite of severely decreased PO2 levels. We explain this result by the assumed value of $P_{M50} = 2\ mmHg$ which is quite small. Furthermore, average partial oxygen pressures in normal breast tissue and breast tumors are consistent with clinical data.

We conclude that our model is in general capable to correctly account for the biophysical and physiological quantities simulated taking into account their considerable standard deviations and the considerable variations of clinical, animal and theoretical data available in literature.

Variance of tissue hemoglobin concentration, tissue blood oxygen saturation and perfusion due to individual initial vascular configurations

It is the focus of the present paper to simulate tissue total hemoglobin concentrations c_{Hb} and tissue blood oxygen saturation Y of tumors and host tissue and compare the results with the clinical data on breast tumors and surrounding normal breast tissue obtained from a cohort of 87 breast cancer patients using optical mammography, reported by Grosenick et al. ([22], cf. Figs 3A, B, Fig 5]). Since the present paper frequently refers to the clinical results, we reproduce the relevant figures, see Figs 7 and 8.

In Figs 9, 10 and 11 corresponding to the model variants BASE, CMPR and METAB, respectively, we likewise correlate simulated tissue hemoglobin concentration and tissue blood oxygenation in normal and tumorous tissue separately for each of the 90 network realizations at the beginning ($t = 0$) and at the end ($t = 600h$) of the tumor growth process, thus mimicking a patient cohort. Figs 9–13 illustrate that variations of normal vascular configurations in the
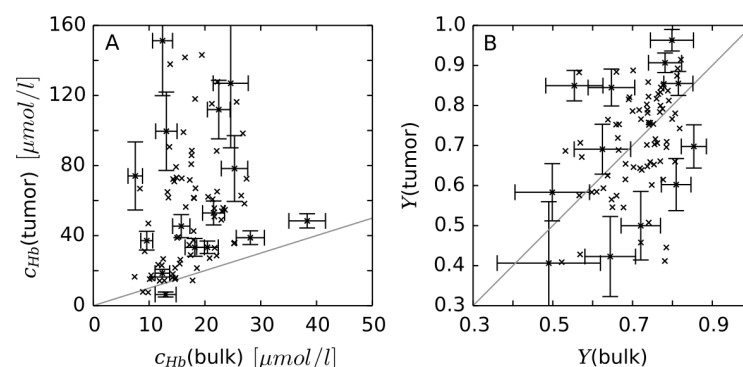

Fig 7. Physiological parameters of tumors versus those of corresponding healthy breast tissue for 87 patients. (A, left) total hemoglobin concentration c_{Hb}; (B, right) blood oxygen saturation Y. Reproduced from data shown in Ref. ([22], Fig 3A, B).

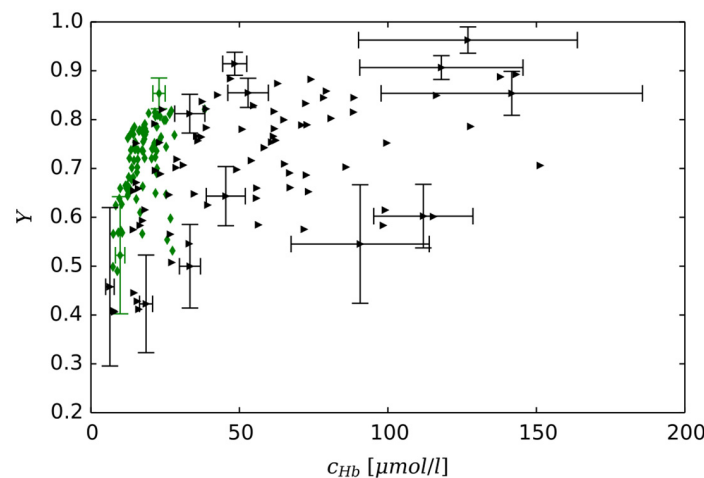doi:10.1371/journal.pone.0161267.g007

Fig 8. Blood oxygen saturation versus total hemoglobin concentration. Error bars ([22], cf. Fig 3a,b) on tumor data correspond to uncertainties of tumor radius a_T and location z_T along compression direction, besides statistical contributions, error bars on healthy breast tissue data reflect statistical uncertainties only. Reproduced from data shown in Ref. ([22], Fig 5).

doi:10.1371/journal.pone.0161267.g008

cohort result in considerable data scatter of simulated parameters, explaining the observed scatter in clinical data on the patient cohort. Additionally the root node configuration (cf. Fig 3), associated with a particular data point, is indicated by a colored symbol.

Depending on root node configuration, drastic variations in microvascular density MVD at the tumor center, vascular volume density rBV and tissue hemoglobin concentration c_{Hb} as well as perfusion and tissue blood oxygenation Y in tumors are observed. The same parameters are subject to fluctuations over the initial networks, yet in many cases to a much lesser relative magnitude. Our main finding, that vascular compression in solid tumors is responsible for low tissue oxygen saturation is supported by the sections below.

Perfusion and tissue hemoglobin concentration are positively correlated

Fig 12A and 12B show that perfusion rates rBF correlate positively with tissue hemoglobin concentration c_{Hb} in both normal tissue and tumors. According to Fig 12A, perfusion of the initial vasculature (normal tissue) is almost linearly dependent on c_{Hb}. Since we take c_{Hb} to be proportional to rBV, perfusion rBF and vascular volume density rBV are likewise well correlated, illustrated for scaled perfusion rBF_{scaled} in Fig 12C, exhibiting a linear dependence approximately. Since high caliber vessels crisscrossing the tumor core provide dominant contributions to c_{Hb} and rBV, and, at the same time, carry high blood flow due to low hydrodynamic resistance, such correlation is to be expected. Details of this correlation are determined not only by vascular morphology, e.g. the initial vessel network growth model, but also by boundary conditions at inlets and outlets, i.e. the assumed blood pressure-radius relation (s. Eq (3) in S1 Appendix).

To understand the relation between number of root nodes, vascular volume density rBV and radii of root nodes in initial networks ($t = 0$, normal tissue), we consider a simplified system in S3 Appendix. There, we calculate rBV assuming perfect binary vascular trees depending on the number of (identical) trees (i.e. number of root nodes), yet keeping the total number of vessel segments constant. Vessel radii, in our model of the initial vasculature, are governed by Murray's law. Thus, the radius of mother vessels grows by a factor of $2^{1/3}$ compared to their
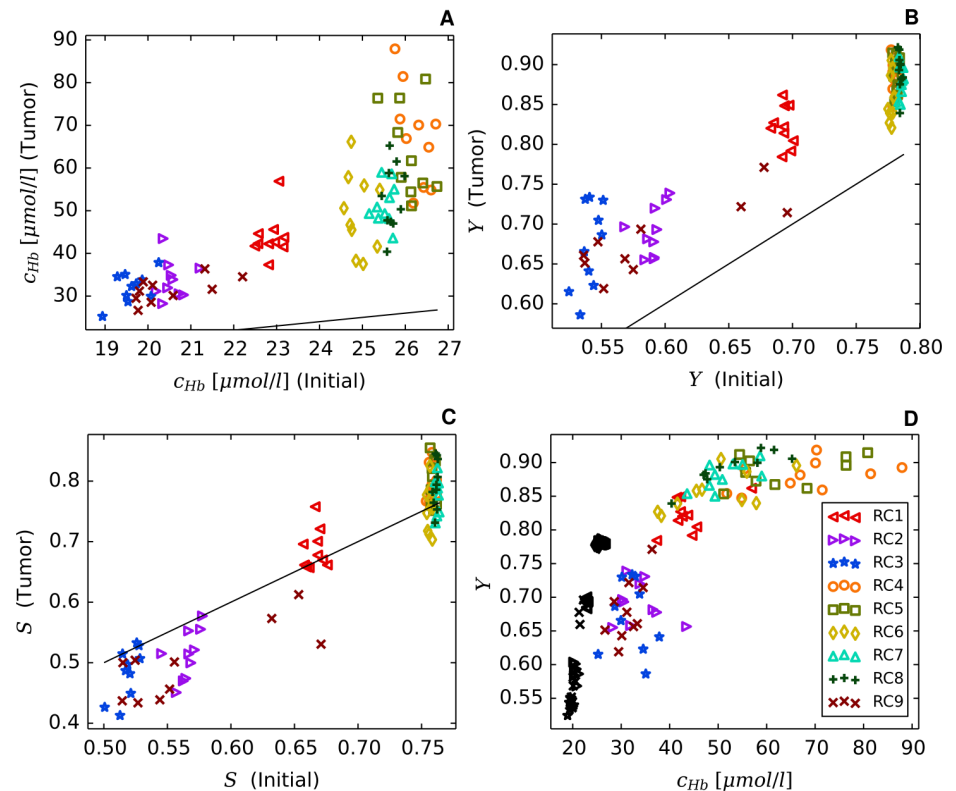
83

Fig 9. Tissue hemoglobin concentrations, volume-weighted tissue blood oxygen saturations *Y* and length-weighted blood oxygenation *S* (Case BASE). Each data point corresponds to a different simulation run, where the color code indicates the corresponding root node configuration (cf. Fig 3, see text). Panel A displays hemoglobin concentration c_{Hb} of tumor tissue versus c_{Hb} in normal tissue. Panel A also corresponds to case METAB, differing from case BASE in tissue oxygen metabolism only. Panel B correlates RBC-volume-weighted tissue blood oxygen saturation *Y*, Panel C length-weighted blood oxygenation *S* in tumorous and normal breast tissue. Panel D shows a plot of *Y* against tissue hemoglobin concentration c_{Hb} where tumor (colored symbols) and normal tissue (black symbols) are both shown as different point sets. Black lines in Panel A, B and C represent diagonals separating tumor data above from below normal.

doi:10.1371/journal.pone.0161267.g009

daughter vessels. Geometries with fewer root nodes (e.g. RC4 through RC8, s. Fig 3) correspond to more extended arterio-venous trees compared to configurations (e.g. RC1, RC2, and RC3) with many arterial and venous roots. It follows that *rBV* and root node radii are larger for geometries with fewer root nodes. Furthermore, according to the assumed blood pressure-radius relation, larger root node radii correspond to larger arterial-venous pressure differentials, increasing perfusion. Conversely, configurations with larger numbers of root nodes are associated with lower *rBV*, lower root vessel radii, and hence lower arterio-venous blood pressure differentials.

Thus, vascular network structure and pressure-radius relation of the feeding and draining vessels determine vascular volume and perfusion. In a cohort of real tissue sections we expect a similar multitude of vascular configurations with the therewith associated data scatter.

Vascular dilatation leads to elevated tumor oxygen saturation

The c_{Hb}(tumor)-c_{Hb}(normal) correlations for cases BASE and METAB (Fig 9A) and for case CMPR (Fig 10A) qualitatively agree with the clinically observed correlation between tissue
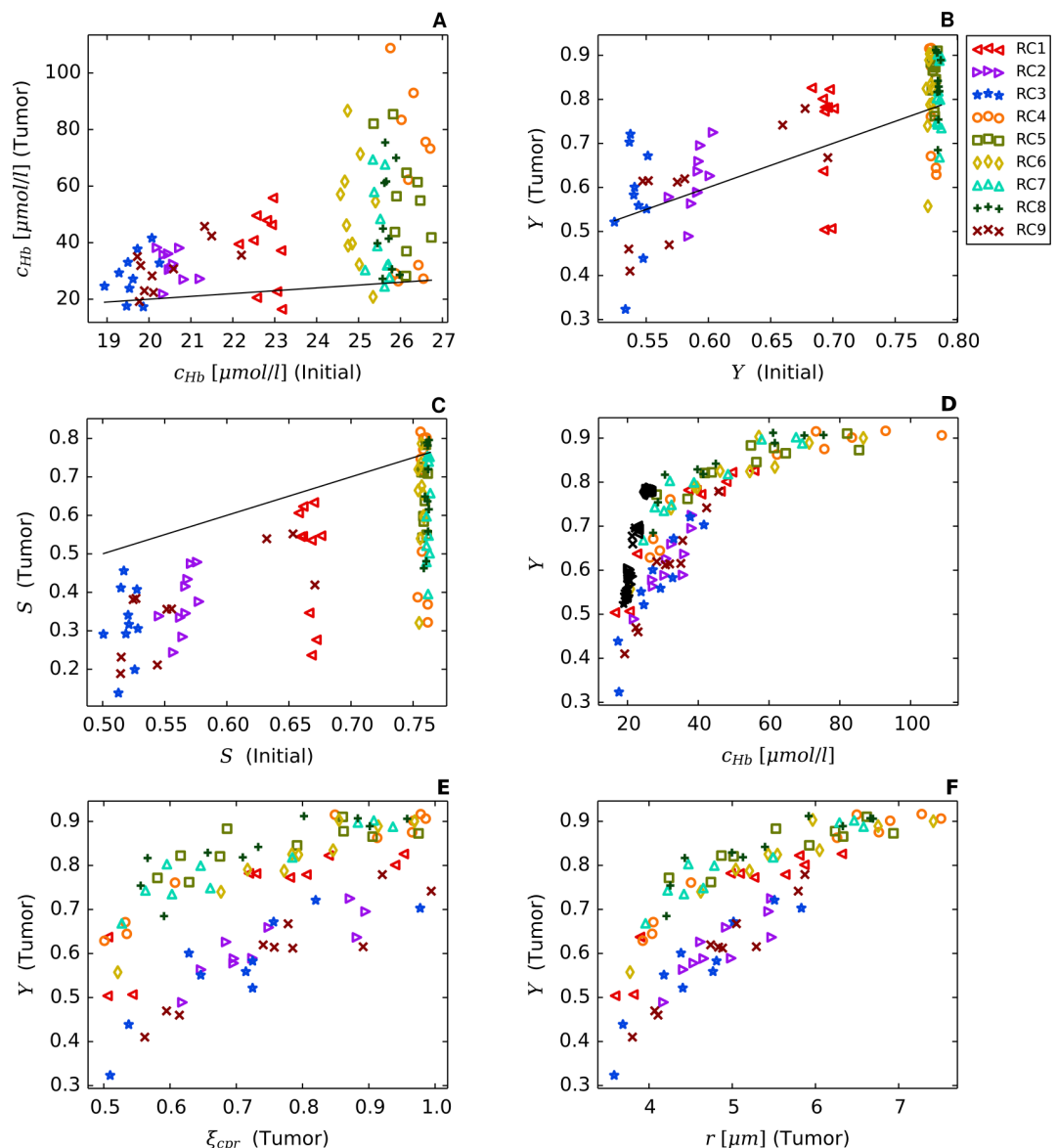
Fig 10. Tissue hemoglobin concentrations, volume-weighted tissue blood oxygen saturations *Y* and length-weighted blood oxygenation *S* (Case CMPR). This figure is the analog of Fig 9, but for case CMPR. Each of the 90 simulation runs was carried out with a different randomly selected factor ξ_{cpr} for reducing all tumor vessel radii (s. Eq (40)) simulating solid stress. Fig 10 Panel A-C correlate tissue hemoglobin concentration c_{Hb}, RBC-volume-weighted blood oxygen saturation *Y* and length-weighted blood oxygen saturation *S* of tumor ($t = 600\,h$) and normal ($t = 0\,h$) tissue, respectively. In Fig 10D tissue blood oxygenation *Y* is plotted versus tissue hemoglobin concentration c_{Hb} separately for tumors (colored) and normal tissue (black). Fig 10E and 10F correlate tissue blood oxygen saturation *Y* of tumors with factor ξ_{cpr} and average vessel radius *r*. Generally, Y_{tum} decreases with decreasing average *r* and decreasing ξ_{cpr}, corresponding to higher compression. Black lines in (A), (B) and (C) represent diagonals separating tumor data above from below normal. The color code to identify root node geometry is the same as in Fig 9.

doi:10.1371/journal.pone.0161267.g010
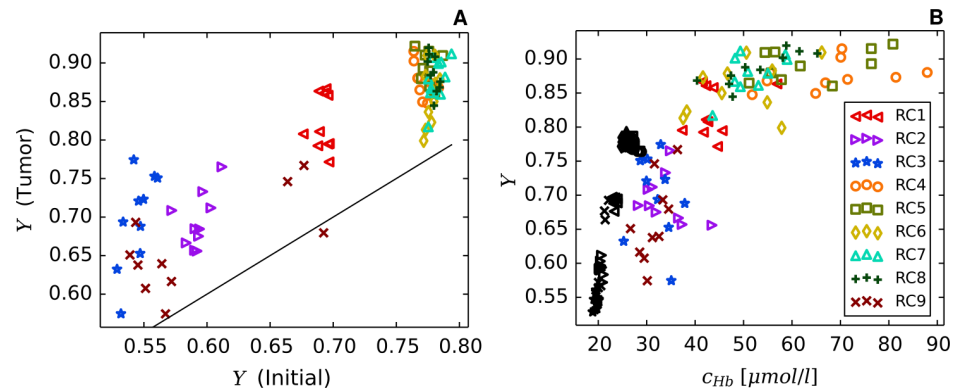
Fig 11. Volume-weighted tissue blood oxygen saturations Y and hemoglobin concentrations (Case METAB). This figure is the analog of Fig 9 for case METAB, using the same 90 vascular network realizations at $t = 0$ and $t = 600$ h as in case BASE. For each network realization at the end of the growth process, oxygen related parameters were simulated by randomly selecting M_0 from a lognormal distribution (see text). Fig 11A correlates tissue blood oxygen saturation in tumorous and normal tissue. In Fig 11B, tissue blood oxygenation is plotted versus tissue hemoglobin concentration for tumors (colored symbols) and normal tissue (black symbols) separately. The black lines in (A) represents the diagonal separating tumor data above from below normal. The color code to identify root node geometry is the same as in Fig 9.

doi:10.1371/journal.pone.0161267.g011

hemoglobin concentrations in breast tumors and surrounding normal breast tissue (Fig 7a, ([22], Fig 3a)). Since total hemoglobin concentration is approximately proportional to vascular volume density rBV, the higher hemoglobin concentration reflects the larger rBV of tumors, explained by neo-angiogenesis and vessel dilatation, outweighing vascular regression. For case CMPR we raised the maximum dilatation radius $r^{(max)}$ from 10 μm (BASE, METAB) to 14 μm (s. Table 2) in order to compensate for the decrease of vascular volume density rBV associated with an overall compression of tumor vessels. Consequently, the ensemble averages of rBV (BASE, METAB) and rBV(CMPR) are approximately the same (s. Table 3). Likewise, the correlation plots c_{Hb}(tumor)-c_{Hb}(normal) shown in Figs 9A and 10A agree qualitatively, although quantitative differences exist comparing individual representations.

For clarity we want to point out the difference between tissue blood oxygen saturation $Y = c_{HbO}/c_{Hb}$ and average vascular oxygen saturation $\langle S \rangle$. The latter quantity is the length-weighted average of blood oxygen saturation taken over all vessel segments of the vascular network (s. S2 Appendix). High caliber tumor vessels contribute to $\langle S \rangle$ according to their—likely higher— blood oxygen saturation, but contribute to Y additionally by their large relative RBC volume. A plot of $\langle S \rangle$(tumor) versus $\langle S \rangle$(normal) shows $\langle S \rangle$(tumor) to fall above and below normal for case BASE (Fig 9C), whereas $\langle S \rangle$(tumor) is generally lower than normal when M-M oxygen consumption rate is raised to M_0(tumor) = 24.6 $\mu lO_2/ml/min$ (s. Panel D of Fig A in S2 Fig) and in the compression case CMPR (Fig 10C).

Figs 9D, 10D and 11B, being qualitatively similar, illustrate the correlation between tissue blood oxygen saturation Y and tissue total hemoglobin concentration c_{Hb} for cases BASE, CMPR, METAB, respectively. Analogous to Fig 8, separate correlations are shown for normal and tumorous tissue. At an arbitrarily selected hemoglobin concentration c_{Hb} there exists a lower bound on Y, clearly discernible in Figs 9D, 10D and 11B despite considerable data scatter. For tumors, tissue blood oxygen saturation Y tends towards an upper limit at high tissue total hemoglobin concentration.
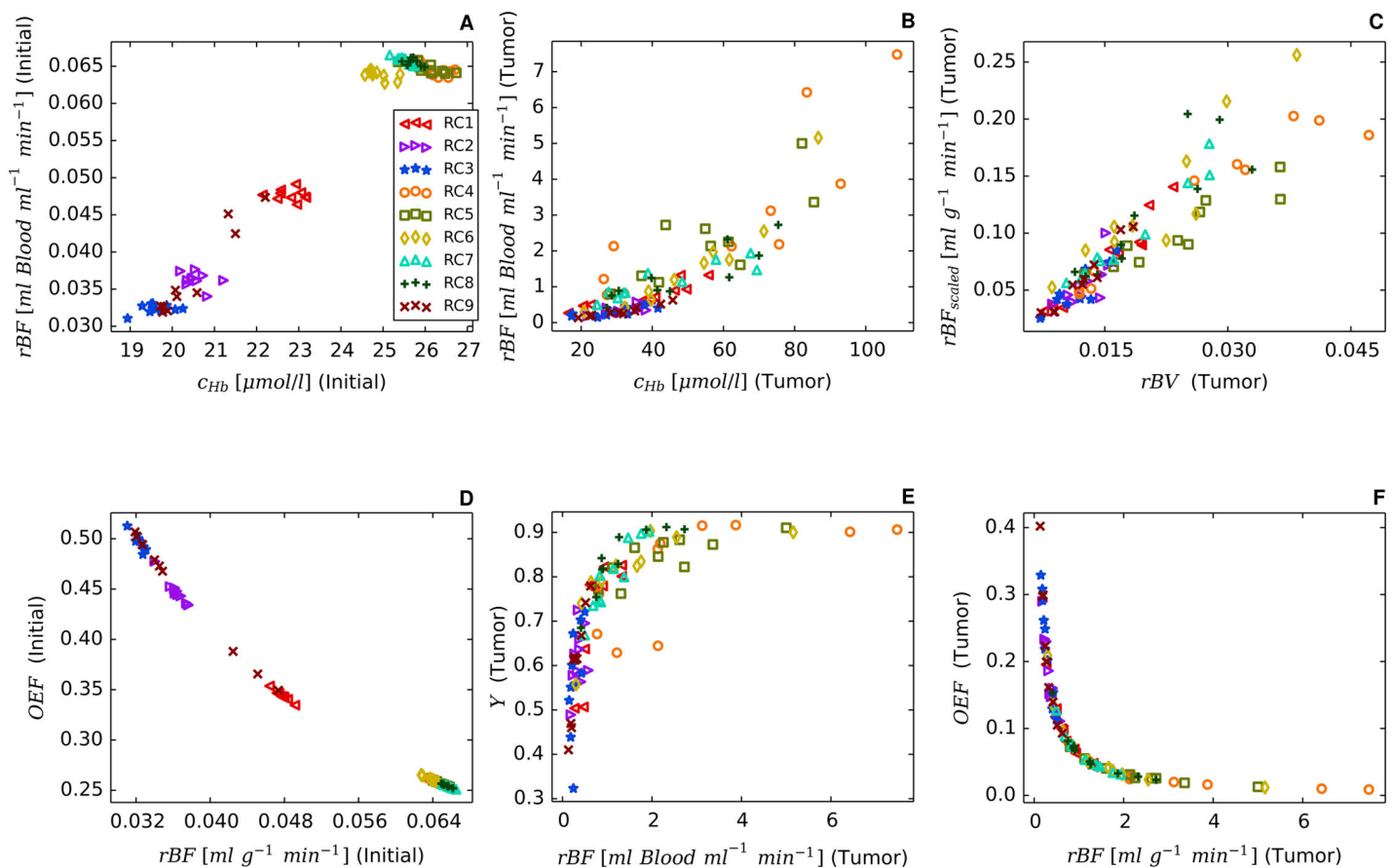
Fig 12. Correlation of other dynamic vascular and metabolic quantities (Case CMPR). Fig 12A and 12B relate perfusion to tissue hemoglobin concentration for normal tissue (t = 0) and tumors (t = 600 h), respectively, whereas Fig 12C correlates tumor scaled perfusion rBF_{scaled} (see text) with vascular volume density rBV. Fig 12D and 12F correlate oxygen extraction fraction OEF with perfusion rBF for normal (t = 0) and tumorous (t = 600 h) tissue, respectively. Fig 12E displays tissue blood oxygen saturation Y versus perfusion (t = 600 h). A comparison of Fig 12E and 12F shows implicitly the negative correlation of OEF and Y for normal tissue. Each data point corresponds to one of the 90 simulation runs, where the color code to identify the root node geometry is the same as in Fig 9.

We explain this asymptotic behavior of Y by first recognizing that vascular volume—essentially c_{Hb}—and perfusion rBF are positively correlated as shown in Fig 12A and 12B. An increase in vascular volume allows for stronger perfusion at given blood pressure boundary conditions. By definition, tissue blood oxygen saturation Y is negatively correlated with oxygen extraction fraction OEF. Moreover, the amount of oxygen extracted from the blood stream is bound from above by the rate of radial diffusion and the local metabolic oxygen demand of tissue. An increase of vascular oxygen influx $q \cdot c$ beyond what can be extracted, leads to luxurious perfusion. In this imbalanced state, most of the oxygen exits the system again through draining vessels. In this case the oxygen extraction fraction OEF is relatively low. This means, with increasing perfusion Y approaches asymptotically the blood oxygen saturation level at the input.

Luxurious perfusion is evidently predicted in tumors exhibiting high tissue hemoglobin concentrations c_{Hb}. We conclude that in such tumors particularly few and thick vessels crisscross the central tumor volume. Such vessels are associated with relative large blood flow rates
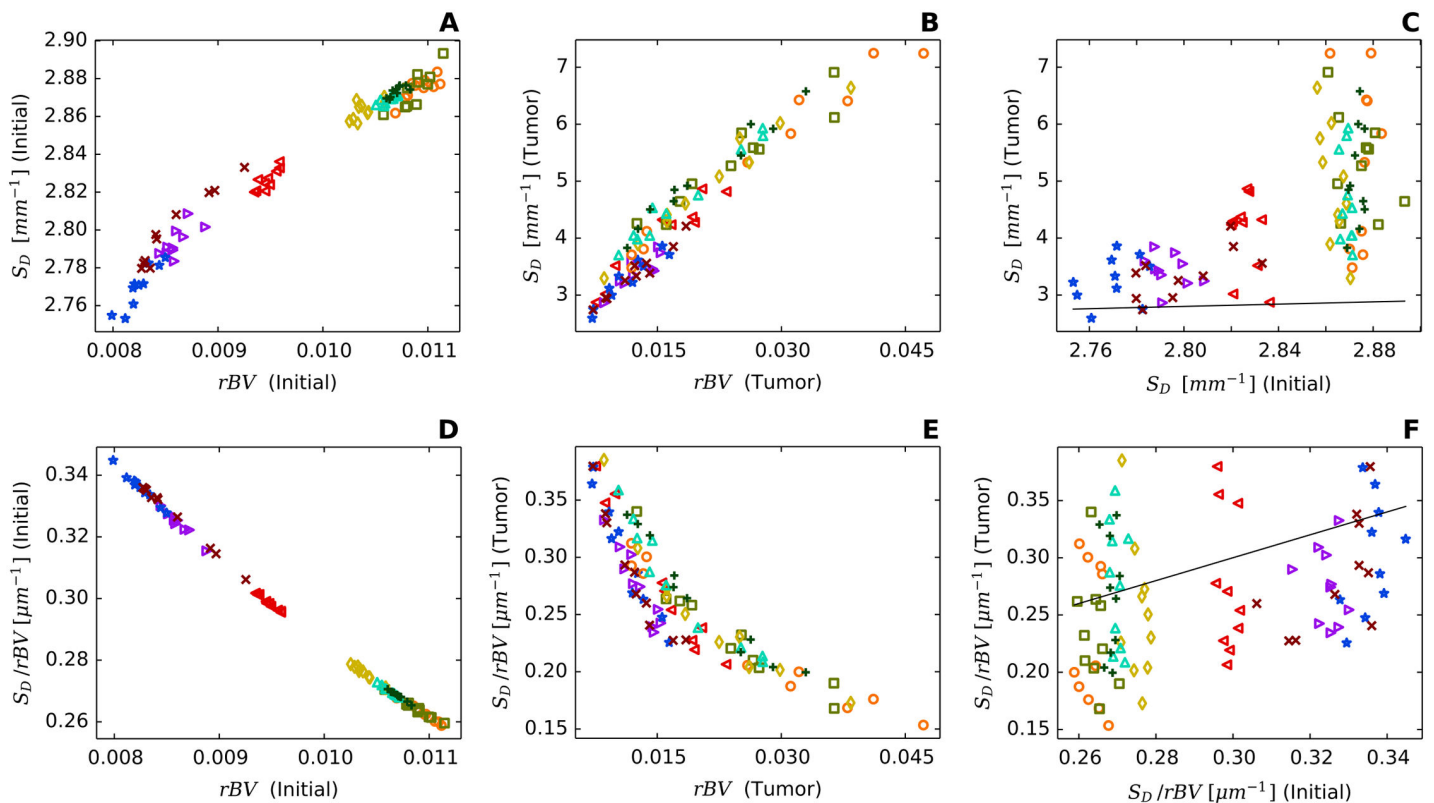
Computation of Tumor Oxygenation with Application to Breast Cancer

Fig 13. Correlation of geometric vascular quantities (Case CMPR). Fig 13A and 13B relate vessel surface with vessel volume densities for normal ($t = 0$) and tumorous ($t = 600\,h$) tissue, respectively, whereas Fig 13C compares vessel surface densities of tumors and normal tissue. Correlations of surface to volume ratios S_D/rBV with vessel volume density rBV are shown in Fig 13D and 13E for normal tissue ($t = 0$) and tumors ($t = 600\,h$), respectively. Fig 13F relates vessel surface to vessel volume densities for tumorous($t = 600\,h$) and normal ($t = 0$) tissue. Each data point corresponds to one of the 90 simulation runs, where the color code to identify the root node geometry is the same as in Fig 9. Black lines in (C), (F) represent diagonals separating tumor data above from below normal.

q, relatively high blood oxygen saturation S, besides enhanced hematocrit (s. Figs 5D and 6). Since tissue blood oxygen saturation Y is the RBC-volume-weighted average of blood oxygen saturation S taken over all vessel segments (s. Eq (39)), high caliber vessels predominantly contribute to Y.

Paradoxically, hypoxia is prevalent in many tumors, including our simulations. However, a physiologically normal oxygen supply requires a homogeneous distribution of a capillary bed exhibiting a physiological surface area per vascular volume. Instead, tumor blood vessels are very heterogeneously distributed.

The resulting simulated tissue blood oxygen saturation Y of tumors falls above normal (case BASE, METAB), although tumor oxygen demand was raised, i.e. the Michaelis-Menten metabolic rate of oxygen consumption M_0 in tumorous tissue was assumed to be four times higher compared to normal tissue (s. Table 1).

Figs 9D, 10D and 11B are in qualitative agreement with clinical data (s. Fig 8), apart from missing simulated data above the lower bounds of Y. This discrepancy might be explained by partial volume effects. Implicitly our simulations assume the spherical tumor to consist of a homogeneous distribution of viable tumor cells, apart from its vasculature, thus assuming homogeneity with respect to oxygen consumption. However, breast tumors of patients may

contain necrotic regions or partial volumes consisting of viable tumor cells and normal breast cells. In either case the effective oxygen demand is reduced leading to higher tissue blood oxygen saturations Y at constant tissue hemoglobin concentration c_{Hb}.

Tumor blood flow rates outweigh increased oxygen demand

Clinical data on metabolic rate of oxygen consumption of tumors are scarce. Our choice of $M_0(tumor) = 14.8 \ \mu lO_2/ml/min$ corresponds to simulated metabolic rates MRO_2 in tumors to be about 12 $\mu lO_2/ml/min$ (s. Table 4), consistent with the high end of oxygen metabolic rates reported for human xeno-transplanted breast cancers in animal tumor models [82]. Considerably higher oxygen consumption rates ($M_0 = 33.4 \pm 8.3 \ \mu lO_2/ml/min$) of human breast carcinoma cells (MDA-MB-468) were recently reported based on in-vitro measurements of oxygen flux above a monolayer of the tumor cells [83]. Assuming a M-M consumption rate of $M_0 = 24.6 \ \mu lO_2/ml/min$ raised the simulated tissue metabolic rate of oxygen consumption to 18.6 $\mu l O_2/ml/min$ (BASE), yet did not change the situation, i.e. tissue blood oxygen saturation Y of tumors was simulated to be above normal (s. Panels A and B in Fig A in S2 Fig). Likewise, simulated tissue blood oxygen saturation Y of tumors (case METAB) changed only little compared to case BASE (s. Figs 9B and 11A), when the metabolic rate M_0 was randomly selected from a lognormal distribution for each of the 90 growth processes to simulate phenotypical differences between breast cancer patients. We therefore conclude that tissue blood oxygen saturation Y of breast tumors below normal (Fig 7B) is unlikely caused by high metabolic rate of oxygen consumption in tumorous tissue, rather than by insufficient oxygen supply.

Vascular compression is responsible for low tumor oxygen saturation

It follows that the growth processes of tumor vasculature of case BASE (METAB) need to be augmented (case CMPR). Our method to simulate tumor vasculature had been developed previously based on morphologic data (MVD) of melanomas. It is therefore not surprising that addition of data on tissue blood oxygen saturation Y depending on metabolic characteristics of tumor tissue besides vascular structure and hemodynamics, requires modifications of previously employed models. Tissue blood oxygen saturation Y is (negatively) correlated with blood oxygen extraction fraction $OEF = MRO_2/rJ_{in}$, where rJ_{in} is the oxygen influx per unit volume of tissue. In simulations, tumor oxygen extraction fraction can be increased and hence tissue blood oxygen saturation Y lowered by compressing vessels, thus restricting oxygen influx, while keeping tissue metabolic rate of oxygen consumption MRO_2 (approximately) constant. Therefore, we tentatively assume that blood vessels are compressed during tumor growth by solid pressure, known to be elevated in solid tumors [9, 11], caused by proliferating tumor cells and modifications of the tumor extracellular matrix, e.g. by increased deposition of hyaluronan [96]. Previously, compression of intratumoral vessels was observed in an animal model, attributed to proliferating tumor cells [10]. Presently, the precise mechanisms are still under debate by which extravascular pressure compresses tumor vessels [78, 79].

For simplicity, CMPR assumes the same radius reduction factor ξ_{cpr} for all vessel segments, where ξ_{cpr} is randomly selected for each of the 90 tumor growth processes. Case CMPR shows tumor blood oxygen saturation Y to fall above and below normal (Fig 10B), consistent with the clinical data. Qualitatively speaking, for a sufficiently small radius reduction factor ξ_{cpr} selected, vessel segments whose radii fell above the maximal dilatation radius $r^{(max)} = 14 \ \mu m$ (CMPR) at the start of the tumor growth process will most likely end up to be narrower compared to case BASE, whereas radii of smaller vessel segments ($r < r^{(max)}$) will be comparable for both scenarios at the end of the growth process, since the higher maximal dilatation radius of case CMPR compensates for vessel segment compression. It follows that oxygen supply by high caliber

vessels threading the tumor center (s. Figs 5D and 6) is reduced, causing Y to fall below case BASE. On the other hand for a radius reduction factor ξ_{cpr} close to 1, tissue blood saturation Y of high caliber vessel segments will be comparable for cases BASE and CMPR, explaining the difference between Figs 9B and 10B. Likewise, compared to case BASE/METAB, compression of vessels with radii larger than $r^{(max)}$ contribute to the reduction of the ensemble averages of perfusion rBF and scaled perfusion rBF_{scaled} by 30% and 35%, respectively (case CMPR, s. Table 3).

Fig 10E and 10F illustrate that Y_{tum} generally decreases with decreasing factor ξ_{cpr}, simulating increasing vascular compression by solid stress and with decreasing average vascular radius r. Although we cannot rule out other biological processes that may cause radial extent of tumor blood vessels to shrink we take clinical data with $Y_{tum}/Y_{norm} < 1$ to be indicative of vascular compression. Based on data from optical mammography [22] one might expect that tumors with $Y_{tum} < Y_{norm}$ have vascular networks with morphological characteristics that are very different from tumors with $Y_{tum} > Y_{norm}$. However, our results suggest that similar vascular network morphologies and similar compartmentalization cover a wide range of values for Y_{tum} above and below Y_{norm}, in good agreement with clinical data. Since compression of blood vessels will impede chemotherapy we conclude that tumors with oxy-to total hemoglobin concentration below normal are less likely to respond to chemotherapy. Such behavior was recently reported for neo-adjuvant chemotherapy of locally advanced breast tumors [47].

Oxygen extraction and vascular surface density

Fig 12D and 12F correlate oxygen extraction fraction OEF with perfusion rBF for normal and tumorous tissue, respectively. A comparison of Fig 12E and 12F illustrates implicitly the negative correlation of tissue blood oxygenation Y and oxygen extraction fraction OEF for tumorous tissue (CMPR). Such a correlation is also seen for normal tissue. As a matter of fact, for normal tissue, the sum $OEF + Y$ is only slightly larger than 1, being rather independent of perfusion. Since metabolic rate of oxygen consumption MRO_2 is essentially an input in either case and oxygen concentration c_{in} of feeding vessels is nearly constant, Fig 12D and 12F show a hyperbolic dependence of $OEF = MRO_2/c_{in}/rBF$ on perfusion rBF.

Fig 13 relates vascular geometric properties of normal and tumorous (case CMPR) tissue that are not easily amenable to clinical measurements. As expected, vascular surface density S_D increases with increasing volume density rBV, both for normal (Fig 13A) and tumorous (Fig 13B) tissue. Since vascular volume density is higher in tumorous tissue compared to normal tissue (s. Fig 10A), the same applies to vascular surface density (s. Fig 13C). In contrast, vascular surface to volume ratios S_D/rBV decrease with increasing rBV in either case, probably due to the presence of larger vessels at higher fractional blood volumes (Fig 13D and 13E), yet vascular surface to volume ratios of tumors may fall above or below normal (Fig 13F), depending on whether or not the increase in tumor surface density over that of normal tissue outweighs the corresponding increase in tumor volume density over normal.

Limitations

Although we explained salient features of the clinically observed correlations of hemoglobin concentration and tissue blood oxygen saturation between tumorous and corresponding normal breast tissue (inter-network correlations) as well as the dependence of tissue blood oxygenation on hemoglobin concentration for normal breast tissue and tumors (intra-network correlations) our model has important limitations.

Our computational method presently based on a uniform grid has limited accuracy due to poor convergence with lattice spacing h. Optimal convergence of the solution of elliptic partial

differential equations with Dirac source terms can be achieved by adaptive meshes, concentrating discretization points near the source contributions [97]. In future, adaptive meshes should be used to improve the accuracy of our method.

The small size of the spherical tumors embedded in the simulation domain make a comparison of simulated data with clinical results uncertain, notably for perfusion. Also, the vascular structure of cm sized tumors might be different from the mm-sized tumors that were simulated. Apart from its vasculature, we implicitly assumed the growing spherical tumor to be homogeneous. However, in real tumors, viable, oxygen consuming, tumor cells are concentrated near blood vessels, whereas necrotic regions which hardly, if at all, consume O_2 occur in regions void of vessels. This heterogeneity affects tissue PO2 distributions and therefore likely also tissue blood oxygen saturation Y.

The reduction of tumor vessels radii during the growth process by the same, randomly selected factor is the simplest way to account for compression by solid stress. In effect, this method decreases the radii of vessels where r is larger than the maximal radius $r^{(max)}$ reached by circumferential dilatation. Furthermore, reducing $r^{(max)}$ leads to skewed balance between microvessel density MVD and regional blood volume rBV which we currently consider as adequate. However, rather than a reduction of vessel radii, local pinch-offs of vessels are more likely to occur [12], restricting or obstructing RBC flow and thus delivery of oxygen, yet not changing significantly vascular volume density. Furthermore, only stationary solutions of perfusion were sought, although it is well known that blood flow in capillaries may be chaotic.

If possible anatomical information should be used to generate realistic geometries of feeding arteries (arterioles) and draining veins (venules), rather than arbitrarily creating geometric patterns of root nodes as in this paper. Following [98] a possible remedy to this problem might be to exclude root node geometries that result in unrealistic values of biophysical variables, e.g. unreasonably low or high perfusion rates. Furthermore, probability distributions associated with the clinical data may allow to select the most probable root node geometries.

Conclusions

We have taken a first step to elucidate the relationship between vascular morphology, vascular oxygen concentration and oxygen delivery to tumor and host tissue, thus trying to solve an ill-posed inverse problem, namely to deduce morphological information on vascular networks from clinical coarse grained data. To this end, we related data on tissue hemoglobin concentrations and tissue blood oxygen saturations of breast cancers and surrounding host tissue to synthetic, algorithmically generated tumor blood vessel networks and networks of surrounding normal tissue, by simulating intravascular and extravascular distributions of partial oxygen pressure. Our simulations suggest that elevated fractional volume of blood vessels in breast tumors is likely the result of vascular dilatation, in spite of a drastic reduction of the number of vessels by regression and collapse. Considerable data scatter in simulated quantities, e.g. tumor tissue hemoglobin concentration and tissue blood oxygenation are related to vascular variance of initial blood vessel networks and qualitatively explain the scatter of clinical data of the patient cohort. Furthermore, breast tumors with tissue blood oxygenation above normal are likely associated with high tumor blood flow caused by high-caliber blood vessels penetrating into the tumor. Tissue blood oxygen saturation Y in tumors that is below normal could only be achieved by a reduction of the radii of high-caliber blood vessels, emulating compression of blood vessels caused by intra-tumoral solid stress. Factors contributing to low saturations Y are the reduction in blood flow, increasing the fractional oxygen extraction, and secondly, the associated reduction in vascular volume by which the blood oxygen saturation is weighted. Our simulations provide a possible explanation for tissue blood oxygenation in tumors below

PLOS | ONE   Computation of Tumor Oxygenation with Application to Breast Cancer

normal at baseline reported to be indicative of poorer prognosis for neoadjuvant chemotherapy. We expect our model to find applications to data analysis of PET, MRI, biomedical optics and hybrid techniques such as photoacoustics, probing tissue vascularization and oxygenation.

Supporting Information

S1 Appendix. Model details and validation. Details on the derivation of the transvascular oxygen mass transfer coefficient γ are given, simulation results are compared with literature references, estimating the accuracy of our method, and finally the blood pressure at inlets and outlets $p^{(BC)}(r)$ is defined.
(PDF)

S2 Appendix. Explicit Formulas for Relevant Biophysical Quantities. The simulation of tumor growth and oxygen PO2 distributions in blood and tissue yields vascular flow rates q_v, hematocrit H_v, oxygen partial pressure P at discrete points on vessel axes, and tissue partial oxygen pressure P_t. In this section explicit formulas of other derived biophysical quantities are provided.
(PDF)

S3 Appendix. Regional Blood Volume of Confined Perfect Binary Trees. In this section we derive an approximative relation between the number of root nodes and the regional blood volume, provided that the total number of vessels is held constant. Here we assume that all vascular trees are perfect binary trees.
(PDF)

S4 Appendix. Further details on comparison between simulated and literature biophysical data. In support of our model we further discuss simulated data listed in Tables 3 and 4 in some detail, comparing our results with clinical data, data obtained from animal models and theoretical data available in the literature.
(PDF)

S1 Fig. Tissue PO2 distributions at constant vascular blood oxygenation. We compare the results of our oxygen model (cf. Fig 5C, case CMPR, root node geometry RC9) with predictions of a simplified model using a constant intravascular oxygen concentration.
(PDF)

S2 Fig. Data for doubled parameter value of maximal O$_2$ consumption rate M_0. Correlations of volume (Y) and length (S) weighted blood oxygen saturations at increased metabolic rate of tissue oxygen consumption are compared with case BASE.
(PDF)

Author Contributions

Conceived and designed the experiments: MW.

Performed the experiments: MW TF.

Analyzed the data: MW TF.

Wrote the paper: MW H. Rinneberg TF H. Rieger.

Suggested the scientific problem, contributed to writing and critical review: H. Rinneberg H. Rieger.

References

1. Folkman J. Tumor angiogenesis: therapeutic implications. N Engl J Med. 1971 Nov; 285(21):1182–1186. doi: 10.1056/NEJM197111182852108 PMID: 4938153

2. Nagy JA, Chang SH, Dvorak AM, Dvorak HF. Why are tumour blood vessels abnormal and why is it important to know? Br J Cancer. 2009 Mar; 100(6):865–869. doi: 10.1038/sj.bjc.6604929 PMID: 19240721

3. Carmeliet P, Jain R. Angiogenesis in cancer and other diseases. Nature. 2000 Sep; 407:249–257. doi: 10.1038/35025220 PMID: 11001068

4. Dewhirst MW, Cao Y, Moeller B. Cycling hypoxia and free radicals regulate angiogenesis and radio-therapy response. Nat Rev Cancer. 2008 Jun; 8(6):425–437. doi: 10.1038/nrc2397 PMID: 18500244

5. Jain RK. Normalization of tumor vasculature: an emerging concept in antiangiogenic therapy. Science. 2005 Jan; 307(5706):58–62. doi: 10.1126/science.1104819 PMID: 15637262

6. Neri D, Bicknell R. Tumour vascular targeting. Nat Rev Cancer. 2005 Jun; 5(6):436–446. doi: 10.1038/nrc1627 PMID: 15928674

7. Stamatelos SK, Kim E, Pathak AP, Popel AS. A bioimage informatics based reconstruction of breast tumor microvasculature with computational blood flow predictions. Microvasc Res. 2014 Jan; 91:8–21. doi: 10.1016/j.mvr.2013.12.003 PMID: 24342178

8. Mankoff DA, Dunnwald LK, Gralow JR, Ellis GK, Charlop A, Lawton TJ, et al. Blood flow and metabolism in locally advanced breast cancer: relationship to response to therapy. J Nucl Med. 2002 Apr; 43(4):500–509. Available from: http://jnm.snmjournals.org/content/43/4/500.abstract PMID: 11937594

9. Chauhan VP, Stylianopoulos T, Boucher Y, Jain RK. Delivery of molecular and nanoscale medicine to tumors: transport barriers and strategies. Annu Rev Chem Biomol Eng. 2011; 2(1):281–298. doi: 10.1146/annurev-chembioeng-061010-114300 PMID: 22432620

10. Padera TP, Stoll BR, Tooredman JB, Capen D, di Tomaso E, Jain RK. Pathology: cancer cells compress intratumour vessels. Nature. 2004 Feb; 427(6976):695. doi: 10.1038/427695a PMID: 14973470

11. Stylianopoulos T, Martin JD, Chauhan VP, Jain SR, Diop-Frimpong B, Bardeesy N, et al. Causes, consequences, and remedies for growth-induced solid stress in murine and human tumors. Proc Natl Acad Sci USA. 2012 Sep; 109(38):15101–15108. doi: 10.1073/pnas.1213353109 PMID: 22932871

12. Brown JM, Wilson WR. Exploiting tumour hypoxia in cancer treatment. Nat Rev Cancer. 2004 Jun; 4(6):437–447. doi: 10.1038/nrc1367 PMID: 15170446

13. Harris AL. Hypoxia–a key regulatory factor in tumour growth. Nat Rev Cancer. 2002 Jan; 2(1):38–47. doi: 10.1038/nrc704 PMID: 11902584

14. Vaupel P, Schlenger K, Knoop C, Hockel M. Oxygenation of human tumors: Evaluation of tissue oxygen distribution in breast cancers by computerized O2 tension measurements. Cancer Research. 1991 Jun; 51(12):3316–3322. PMID: 2040005

15. Fleming IN, Manavaki R, Blower PJ, West C, Williams KJ, Harris AL, et al. Imaging tumour hypoxia with positron emission tomography. Br J Cancer. 2015 Jan; 112(2):238–250. doi: 10.1038/bjc.2014.610 PMID: 25514380

16. Christen T, Bolar DS, Zaharchuk G. Imaging brain oxygenation with MRI using blood oxygenation approaches: methods, validation, and clinical applications. AJNR Am J Neuroradiol. 2013 Jun-Jul; 34(6):1113–1123. doi: 10.3174/ajnr.A3070 PMID: 22859287

17. An H, Liu Q, Eldeniz C, Lin W. Absolute oxygenation metabolism measurements using magnetic resonance imaging. Open Neuroimag J. 2011; 5:120–135. Suppl. 1–M8: . doi: 10.2174/1874440001105010120 PMID: 22276084

18. Taroni P. Diffuse optical imaging and spectroscopy of the breast: a brief outline of history and perspectives. Photochem Photobiol Sci. 2012 Feb; 11(2):241–250. doi: 10.1039/C1PP05230F PMID: 22094324

19. Grosenick D, Moesta KT, Möller M, Mucke J, Wabnitz H, Gebauer B, et al. Time-domain scanning optical mammography: I. Recording and assessment of mammograms of 154 patients. Phys Med Biol. 2005 Jun; 50(11):2429–2449. doi: 10.1088/0031-9155/50/11/001 PMID: 15901947

20. Taroni P, Torricelli A, Spinelli L, Pifferi A, Arpaia F, Danesini G, et al. Time-resolved optical mammography between 637 and 985 nm: clinical study on the detection and identification of breast lesions. Phys Med Biol. 2005 Jun; 50(11):2469–2488. doi: 10.1088/0031-9155/50/11/003 PMID: 15901949

21. Choe R, Konecky SD, Corlu A, Lee K, Durduran T, Busch DR, et al. Differentiation of benign and malignant breast tumors by in-vivo three-dimensional parallel-plate diffuse optical tomography. J Biomed Opt. 2009 Mar-Apr; 14(2):024020. doi: 10.1117/1.3103325 PMID: 19405750

PLOS | ONE   Computation of Tumor Oxygenation with Application to Breast Cancer

22. Grosenick D, Wabnitz H, Moesta KT, Mucke J, Schlag PM, Rinneberg H. Time-domain scanning optical mammography: II. Optical properties and tissue parameters of 87 carcinomas. Phys Med Biol. 2005 Jun; 50(11):2451–2468. doi: 10.1088/0031-9155/50/11/002 PMID: 15901948

23. Spinelli L, Torricelli A, Pifferi A, Taroni P, Danesini G, Cubeddu R. Characterization of female breast lesions from multi-wavelength time-resolved optical mammography. Phys Med Biol. 2005 Jun; 50 (11):2489–2502. doi: 10.1088/0031-9155/50/11/004 PMID: 15901950

24. Quarto G, Spinelli L, Pifferi A, Torricelli A, Cubeddu R, Abbate F, et al. Estimate of tissue composition in malignant and benign breast lesions by time-domain optical mammography. Biomed Opt Express. 2014 Sept; 5(10):3684–3698. doi: 10.1364/BOE.5.003684 PMID: 25360382

25. Anderson PG, Kainerstorfer JM, Sassaroli A, Krishnamurthy N, Homer MJ, Graham RA, et al. Broad-band Optical Mammography: Chromophore Concentration and Hemoglobin Saturation Contrast in Breast Cancer. PLOS ONE. 2015 Mar; 10(3):e0117322. Available from: http://journals.plos.org/plosone/article?id=10.1371/journal.pone.0117322 doi: 10.1371/journal.pone.0117322 PMID: 25781469

26. Ntziachristos V, Yodh AG, Schnall MD, Chance B. MRI-Guided Diffuse Optical Spectroscopy of Malignant and Benign Breast Lesions. Neoplasia (New York, NY). 2002 Jul; 4(4):347–354. Available from: http://www.ncbi.nlm.nih.gov/pmc/articles/PMC1661680/ doi: 10.1038/sj.neo.7900244

27. Rieger H, Welter M. Integrative models of vascular remodeling during tumor growth: Integrative models of vascular remodeling. Wiley Interdisciplinary Reviews: Systems Biology and Medicine. 2015 May; 7 (3):113–129. Available from: http://doi.wiley.com/10.1002/wsbm.1295 doi: 10.1002/wsbm.1295 PMID: 25808551

28. Welter M, Rieger H. Interstitial fluid flow and drug delivery in vascularized tumors: a computational model. PLoS ONE. 2013; 8(8):e70395. doi: 10.1371/journal.pone.0070395 PMID: 23940570

29. Krogh A. The number and distribution of capillaries in muscles with calculations of the oxygen pressure head necessary for supplying the tissue. J Physiol (Lond). 1919 May; 52(6):409–415. doi: 10.1113/jphysiol.1919.sp001839

30. Goldman D. Theoretical models of microvascular oxygen transport to tissue. Microcirculation. 2008 Nov; 15(8):795–811. doi: 10.1080/10739680801938289 PMID: 18608981

31. Da su A, Toma-Da su I, Karlsson M. Theoretical simulation of tumour oxygenation and results from acute and chronic hypoxia. Phys Med Biol. 2003 Sep; 48(17):2829–2842. doi: 10.1088/0031-9155/48/17/307

32. Espinoza I, Peschke P, Karger CP. A model to simulate the oxygen distribution in hypoxic tumors for different vascular architectures. Med Phys. 2013 Aug; 40(8):081703. doi: 10.1118/1.4812431 PMID: 23927300

33. Kelly CJ, Brady M. A model to simulate tumour oxygenation and dynamic [18F]-Fmiso PET data. Phys Med Biol. 2006 Nov; 51(22):5859–5873. doi: 10.1088/0031-9155/51/22/009 PMID: 17068369

34. Mönnich D, Troost EG, Kaanders JH, Oyen WJ, Alber M, Thorwarth D. Modelling and simulation of [18F]fluoromisonidazole dynamics based on histology-derived microvessel maps. Phys Med Biol. 2011 Apr; 56(7):2045–2057. doi: 10.1088/0031-9155/56/7/009 PMID: 21386142

35. Skeldon AC, Chaffey G, Lloyd DJ, Mohan V, Bradley DA, Nisbet A. Modelling and detecting tumour oxygenation levels. PLoS ONE. 2012; 7(6):e38597. doi: 10.1371/journal.pone.0038597 PMID: 22761687

36. Lagerlöf JH, Kindblom J, Bernhardt P. The impact of including spatially longitudinal heterogeneities of vessel oxygen content and vascular fraction in 3D tumor oxygenation models on predicted radiation sensitivity. Med Phys. 2014 Apr; 41(4):044101. doi: 10.1118/1.4866887

37. Kirkpatrick JP, Brizel DM, Dewhirst MW. A mathematical model of tumor oxygen and glucose mass transport and metabolism with complex reaction kinetics. Radiat Res. 2003 Mar; 159(3):336–344. doi: 10.1667/0033-7587(2003)159%5B0336:AMMOTO%5D2.0.CO;2 PMID: 12600236

38. Goldman D, Popel AS. Computational modeling of oxygen transport from complex capillary networks. Relation to the microcirculation physiome. Adv Exp Med Biol. 1999; 471:555–563. doi: 10.1007/978-1-4615-4717-4_65 PMID: 10659189

39. Fraser GM, Goldman D, Ellis CG. Comparison of generated parallel capillary arrays to three-dimensional reconstructed capillary networks in modeling oxygen transport in discrete microvascular volumes. Microcirculation. 2013 Nov; 20(8):748–763. doi: 10.1111/micc.12075 PMID: 23841679

40. Hsu R, Secomb TW. A Green's function method for analysis of oxygen delivery to tissue by microvascular networks. Mathematical Biosciences. 1989; 96(1):61–78. doi: 10.1016/0025-5564(89)90083-7 PMID: 2520192

94

41. Secomb TW, Hsu R, Park EYH, Dewhirst MW. Green's Function Methods for Analysis of Oxygen Delivery to Tissue by Microvascular Networks. Annals of Biomedical Engineering. 2004 Nov; 32(11):1519–1529. doi: 10.1114/B:ABME.0000049036.08817.44 PMID: 15636112

42. Safaeian N, Sellier M, David T. A computational model of hemodynamic parameters in cortical capillary networks. J Theor Biol. 2011 Feb; 271(1):145–156. doi: 10.1016/j.jtbi.2010.11.038 PMID: 21130099

43. Safaeian N, David T. A computational model of oxygen transport in the cerebrocapillary levels for normal and pathologic brain function. J Cereb Blood Flow Metab. 2013 Oct; 33(10):1633–1641. doi: 10.1038/jcbfm.2013.119 PMID: 23921901

44. Beard DA. Computational framework for generating transport models from databases of microvascular anatomy. Ann Biomed Eng. 2001 Oct; 29(10):837–843. doi: 10.1114/1.1408920 PMID: 11764314

45. Walocha JA, Litwin JA, Miodoński AJ. Vascular system of intramural leiomyomata revealed by corrosion casting and scanning electron microscopy. Hum Reprod. 2003 May; 18(5):1088–1093. doi: 10.1093/humrep/deg213 PMID: 12721189

46. Less J, Skalak T, Sevick E, Jain R. Microvascular network architecture in a mammary carcinoma. In: Steiner R, Weisz P, Langer R, editors. Angiogenesis. vol. 61 of Experientia Supplementum. Birkhäuser Basel; 1992. p. 74–80.

47. Ueda S, Roblyer D, Cerussi A, Durkin A, Leproux A, Santoro Y, et al. Baseline tumor oxygen saturation correlates with a pathologic complete response in breast cancer patients undergoing neoadjuvant chemotherapy. Cancer Res. 2012 Sep; 72(17):4318–4328. doi: 10.1158/0008-5472.CAN-12-0056 PMID: 22777823

48. Kim E, Stamatelos S, Cebulla J, Bhujwalla ZM, Popel AS, Pathak AP. Multiscale imaging and computational modeling of blood flow in the tumor vasculature. Ann Biomed Eng. 2012 Nov; 40(11):2425–2441. doi: 10.1007/s10439-012-0585-5 PMID: 22565817

49. Kim E, Cebulla J, Ward BD, Rhie K, Zhang J, Pathak AP. Assessing breast cancer angiogenesis in vivo: which susceptibility contrast MRI biomarkers are relevant? Magn Reson Med. 2013 Oct; 70(4):1106–1116. doi: 10.1002/mrm.24530 PMID: 23225578

50. Welter M, Bartha K, Rieger H. Emergent vascular network inhomogeneities and resulting blood flow patterns in a growing tumor. J Theor Biol. 2008 Jan; 250(2):257–280. doi: 10.1016/j.jtbi.2007.09.031 PMID: 17996256

51. Bartha K, Rieger H. Vascular network remodeling via vessel cooption, regression and growth in tumors. J Theor Biol. 2006 Aug; 241(4):903–918. doi: 10.1016/j.jtbi.2006.01.022 PMID: 16545398

52. Lee DS, Rieger H, Bartha K. Flow correlated percolation during vascular remodeling in growing tumors. Physical Review Letters. 2006; 96(5):058104–1–058104–4. doi: 10.1103/PhysRevLett.96.058104

53. Welter M, Bartha K, Rieger H. Vascular remodelling of an arterio-venous blood vessel network during solid tumour growth. J Theor Biol. 2009 Aug; 259(3):405–422. doi: 10.1016/j.jtbi.2009.04.005 PMID: 19371750

54. Welter M, Rieger H. Physical determinants of vascular network remodeling during tumor growth. Eur Phys J E Soft Matter. 2010 Oct; 33(2):149–163. doi: 10.1140/epje/i2010-10611-6 PMID: 20607341

55. Gödde R, Kurz H. Structural and Biophysical Simulation of Angiogenesis and Vascular Remodeling. Developmental Dynamics. 2001 Apr; 220(4):387–401. doi: 10.1002/dvdy.1118 PMID: 11307171

56. Döme B, Paku S, Somlai B, Tímár J. Vascularization of cutaneous melanoma involves vessel co-option and has clinical significance. The Journal of Pathology. 2002 Jul; 197(3):355–362. doi: 10.1002/path.1124 PMID: 12115882

57. Holash J, Maisonpierre PC, Compton D, Boland P, Alexander CR, Zagzag D, et al. Vessel Cooption, Regression, and Growth in Tumors Mediated by Angiopoietins and VEGF. Science. 1999 Jun; 284(5422):1994–1998. doi: 10.1126/science.284.5422.1994 PMID: 10373119

58. Moschandreou TE, Ellis CG, Goldman D. Influence of tissue metabolism and capillary oxygen supply on arteriolar oxygen transport: a computational model. Math Biosci. 2011 Jul; 232(1):1–10. doi: 10.1016/j.mbs.2011.03.010 PMID: 21439980

59. Zubieta-Calleja G, Paulev PE. 15. In: New Human Physiology. Paulev-Zubieta; 2015.

60. Pittman RN. Regulation of tissue oxygenation. In: Colloquium Series on Integrated Systems Physiology: From Molecule to Function. vol. 3. Morgan & Claypool Life Sciences; 2011. p. 1–100.

61. Kesmarky G, Kenyeres P, Rabai M, Toth K. Plasma viscosity: a forgotten variable. Clin Hemorheol Microcirc. 2008; 39(1-4):243–246. PMID: 18503132

62. Yaseen MA, Srinivasan VJ, Sakadzic S, Radhakrishnan H, Gorczynska I, Wu W, et al. Microvascular oxygen tension and flow measurements in rodent cerebral cortex during baseline conditions and functional activation. J Cereb Blood Flow Metab. 2011 Apr; 31(4):1051–1063. doi: 10.1038/jcbfm.2010.227 PMID: 21179069

95

63. Jain RK. Transport of molecules, particles, and cells in solid tumors. Annu Rev Biomed Eng. 1999; 1 (1):241–263. doi: 10.1146/annurev.bioeng.1.1.241 PMID: 11701489

64. Leu AJ, Berk DA, Yuan F, Jain RK. Flow velocity in the superficial lymphatic network of the mouse tail. Am J Physiol. 1994 Oct; 267(4 Pt 2):H1507–1513. PMID: 7943396

65. Chary SR, Jain RK. Direct measurement of interstitial convection and diffusion of albumin in normal and neoplastic tissues by fluorescence photobleaching. Proc Natl Acad Sci USA. 1989 Jul; 86:5385–5389. doi: 10.1073/pnas.86.14.5385 PMID: 2748592

66. Dafni H, Israely T, Bhujwalla ZM, Benjamin LE, Neeman M. Overexpression of vascular endothelial growth factor 165 drives peritumor interstitial convection and induces lymphatic drain: magnetic resonance imaging, confocal microscopy, and histological tracking of triple-labeled albumin. Cancer Res. 2002 Nov; 62(22):6731–6739. Available from: http://cancerres.aacrjournals.org/content/62/22/6731.abstract PMID: 12438274

67. Safaeian, N. Computational Modelling of Capillaries in Neuro-vascular Coupling. University of Canterbury; 2012.

68. Coppola G and Caro C. Oxygen mass transfer in a model three-dimensional artery. Journal of The Royal Society Interface. 2008 Sept; 5(26):1067–1075. doi: 10.1098/rsif.2007.1338

69. Hellums JD, Nair PK, Huang NS, Ohshima N. Simulation of intraluminal gas transport processes in the microcirculation. Ann Biomed Eng. 1996 Jan-Feb; 24(1):1–24. PMID: 8669708

70. Nair PK, Huang NS, Hellums JD, Olson JS. A simple model for prediction of oxygen transport rates by flowing blood in large capillaries. Microvasc Res. 1990 Mar; 39(2):203–211. doi: 10.1016/0026-2862 (90)90070-8 PMID: 2352490

71. Pries A, Secomb T, Gaehtgens P, Gross J. Blood flow in microvascular networks. Experiments and simulation. Circulation Research. 1990 Oct; 67(4):826–834. doi: 10.1161/01.RES.67.4.826 PMID: 2208609

72. Heroux MA, Bartlett RA, Howle VE, Hoekstra RJ, Hu JJ, Kolda TG, et al. An overview of the Trilinos project. ACM Transactions on Mathematical Software. 2005 Sep; 31(3):397–423. doi: 10.1145/1089014.1089021

73. Pries AR, Secomb TW, Gessner T, Sperandio MB, Gross JF, Gaehtgens P. Resistance to blood flow in microvessels in vivo. Circ Res. 1994 Nov; 75(5):904–915. doi: 10.1161/01.RES.75.5.904 PMID: 7923637

74. Thomas H Cormen RLR Charles E Leiserson, Stein C. 22.3. In: Introduction to Algorithms, third edition. The MIT Press; 2009.

75. LeVeque RJ. Finite difference methods for ordinary and partial differential equations—steady-state and time-dependent problems. SIAM; 2007.

76. Knabner P, L A. Numerik partieller Differentialgleichungen. Springer Verlag; 2000.

77. Grimes DR, Kelly C, Bloch K, Partridge M. A method for estimating the oxygen consumption rate in multicellular tumour spheroids. J R Soc Interface. 2014 Jan; 11(92):20131124. doi: 10.1098/rsif.2013.1124 PMID: 24430128

78. Chauhan VP, Boucher Y, Ferrone CR, Roberge S, Martin JD, Stylianopoulos T, et al. Compression of pancreatic tumor blood vessels by hyaluronan is caused by solid stress and not interstitial fluid pressure. Cancer Cell. 2014 Jul; 26(1):14–15. doi: 10.1016/j.ccr.2014.06.003 PMID: 25026209

79. DelGiorno KE, Carlson MA, Osgood R, Provenzano PP, Brockenbough JS, Thompson CB, et al. Response to Chauhan et al.: interstitial pressure and vascular collapse in pancreas cancer-fluids and solids, measurement and meaning. Cancer Cell. 2014 Jul; 26(1):16–17. doi: 10.1016/j.ccr.2014.06.004 PMID: 25026210

80. Stylianopoulos T, Martin JD, Snuderl M, Mpekris F, Jain SR, Jain RK. Coevolution of solid stress and interstitial fluid pressure in tumors during progression: implications for vascular collapse. Cancer Res. 2013 Jul; 73(13):3833–3841. doi: 10.1158/0008-5472.CAN-12-4521 PMID: 23633490

81. Griffon-Etienne G, Boucher Y, Brekken C, Suit HD, Jain RK. Taxane-induced apoptosis decompresses blood vessels and lowers interstitial fluid pressure in solid tumors: clinical implications. Cancer Res. 1999 Aug; 59(15):3776–3782. Available from: http://cancerres.aacrjournals.org/content/59/15/3776.abstract PMID: 10446995

82. Kallinowski F, Schlenger KH, Runkel S, Kloes M, Stohrer M, Okunieff P, et al. Blood flow, metabolism, cellular microenvironment, and growth rate of human tumor xenografts. Cancer Res. 1989 Jul; 49 (14):3759–3764. Available from: http://cancerres.aacrjournals.org/content/49/14/3759.abstract PMID: 2736517

83. Grimes DR, Kannan P, McIntyre A, Kavanagh A, Siddiky A, Wigfield S, et al. The Role of Oxygen in Avascular Tumor Growth. PLOS ONE. 2016 Apr; 11(4):e0153692. Available from: http://journals.plos.org/plosone/article?id=10.1371/journal.pone.0153692 doi: 10.1371/journal.pone.0153692 PMID: 27088720

84. Viacava P, Naccarato AG, Bocci G, Fanelli G, Aretini P, Lonobile A, et al. Angiogenesis and VEGF expression in pre-invasive lesions of the human breast. J Pathol. 2004 Oct; 204(2):140–146. doi: 10.1002/path.1626 PMID: 15376259

85. Dhakal HP, Bassarova A, Naume B, Synnestvedt M, Borgen E, Kaaresen R, et al. Breast carcinoma vascularity: a comparison of manual microvessel count and Chalkley count. Histol Histopathol. 2009 Aug; 24(8):1049–1059. PMID: 19554512

86. Fernandez-Guinea O, Alvarez-Cofino A, Eiro N, Gonzalez LO, del Casar JM, Fernandez-Garcia B, et al. Low microvascular density at the tumor center is related to the expression of metalloproteases and their inhibitors and with the occurrence of distant metastasis in breast carcinomas. Int J Clin Oncol. 2013 Aug; 18(4):629–640. doi: 10.1007/s10147-012-0428-2 PMID: 22688161

87. Beaney RP. Positron emission tomography in the study of human tumors. Semin Nucl Med. 1984 Oct; 14(4):324–341. doi: 10.1016/S0001-2998(84)80006-9 PMID: 6387916

88. Wilson CB, Lammertsma AA, McKenzie CG, Sikora K, Jones T. Measurements of blood flow and exchanging water space in breast tumors using positron emission tomography: a rapid and noninvasive dynamic method. Cancer Res. 1992 Mar; 52(6):1592–1597. Available from: http://cancerres.aacrjournals.org/content/52/6/1592.abstract PMID: 1540969

89. Carp SA, Selb J, Fang Q, Moore R, Kopans DB, Rafferty E, et al. Dynamic functional and mechanical response of breast tissue to compression. Opt Express. 2008 Sep; 16(20):16064–16078. doi: 10.1364/OE.16.016064 PMID: 18825246

90. Kallinowski F, Schlenger KH, Kloes M, Stohrer M, Vaupel P. Tumor blood flow: the principal modulator of oxidative and glycolytic metabolism, and of the metabolic micromilieu of human tumor xenografts in vivo. Int J Cancer. 1989 Aug; 44(2):266–272. doi: 10.1002/ijc.2910440214 PMID: 2759732

91. Marieb EN, Hoehn K. Human Anatomy & Physiology. Pearson; 2013.

92. Sharan M, Vovenko EP, Vadapalli A, Popel AS, Pittman RN. Experimental and theoretical studies of oxygen gradients in rat pial microvessels. J Cereb Blood Flow Metab. 2008 Sep; 28(9):1597–1604. doi: 10.1038/jcbfm.2008.51 PMID: 18506196

93. Ito H, Kanno I, Kato C, Sasaki T, Ishii K, Ouchi Y, et al. Database of normal human cerebral blood flow, cerebral blood volume, cerebral oxygen extraction fraction and cerebral metabolic rate of oxygen measured by positron emission tomography with 15O-labelled carbon dioxide or water, carbon monoxide and oxygen: a multicentre study in Japan. Eur J Nucl Med Mol Imaging. 2004 May; 31(5):635–643. PMID: 14730405

94. Hartmann P, Mirtolouei R, Untersberger S, Ziegler W, Hermann Z, Richtig E, et al. Non-invasive imaging of tissue PO2 in malignant melanoma of the skin. Melanoma Res. 2006 Dec; 16(6):479–486. doi: 10.1097/01.cmr.0000222605.03675.1d PMID: 17119448

95. Ito M, Yang DJ, Mawlawi O, Mendez R, Oh CS, Azhdarinia A, et al. {PET} and Planar Imaging of Tumor Hypoxia With Labeled Metronidazole. Academic Radiology. 2006 May; 13(5):598–609. doi: 10.1016/j.acra.2006.01.007 PMID: 16627201

96. Provenzano PP, Cuevas C, Chang AE, Goel VK, Von Hoff DD, Hingorani SR. Enzymatic targeting of the stroma ablates physical barriers to treatment of pancreatic ductal adenocarcinoma. Cancer Cell. 2012 Mar; 21(3):418–429. doi: 10.1016/j.ccr.2012.01.007 PMID: 22439937

97. D'Angelo C. Finite Element Approximation of Elliptic Problems with Dirac Measure Terms in Weighted Spaces: Applications to One- and Three-dimensional Coupled Problems. SIAM Journal on Numerical Analysis. 2012; 50(1):194–215. doi: 10.1137/100813853

98. Sourbron SP, Buckley DL. Tracer kinetic modelling in MRI: estimating perfusion and capillary permeability. Phys Med Biol. 2012 Jan; 57(2):1–33. doi: 10.1088/0031-9155/57/2/R1

3.1.2   Supplemental Material

S1 Appendix

Model details and validation

Transvascular oxygen mass transfer coefficient

We base the transvascular mass transfer coefficient γ on experimental and theoretical data [1, 2] for the Nusselt number which is related to γ by

$$\gamma = \frac{D_p \alpha_p}{2r} Nu, \tag{1}$$

where r is the vessel radius, and D_p and α_p are the diffusion coefficient and solubility of oxygen in blood plasma, respectively. As seen in Figure A, we use a phenomenological fit function which approximately describes the literature data [1, 2] for Nusselt numbers (assuming a blood oxygen saturation of 90%). The form of this function is

$$Nu(r) = p_2(1 - \exp(-r/p_1)), \tag{2}$$

with parameters p_2 and p_1. A best fit gives $p_1 = 8 \ \mu m$ and $p_2 = 4.7$. This is a good approximation for small radii $r < 100\mu m$. For very large radii of several mm, which are not relevant here, we expect this approximation to fail because then a vessels may be considered as a large reservoir of oxygen, where the total transvascular flux is dominantly determined by the vessel surface area. Hence we expect Nu to become proportional to r for $r \gg p_1$ so that r cancels out of the flux density of extravasated oxygen $j_{tv} = D_p \alpha_p Nu/2r(P - P_t)$.
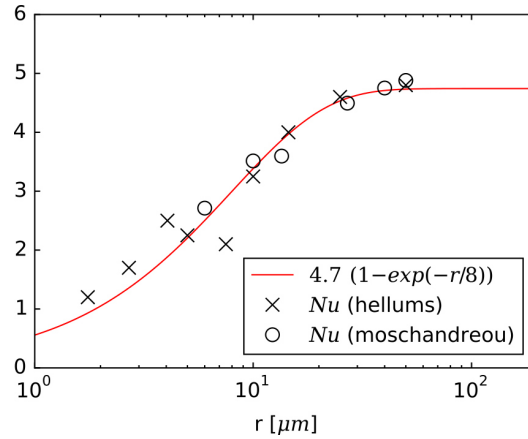
Figure A. Nusselt numbers: The dimensionless Nusselt number Nu describes the oxygen flux through the vessel wall in proportion to the difference between the average intravascular PO2 and the PO2 at the wall. $Nu(hellums)$ and $Nu(moschandreou)$ denote experimental [1] and theoretical data [2, Fig. 6], assuming a blood oxygen saturation of $S \approx 0.9$. The red curve is a best fit to the data.

Validation and comparison with literature data

To validate our model we considered the variation of intravascular PO2 distributions in systems comprising a single vascular tube which is embedded in a block of a medium through which oxygen can diffuse. We considered several cases with a tube length of $4 \ mm$ and various radii, and compared these cases with literature data [2, 3] obtained from precise calculations with detailed models. In general we obtain fair agreement. For comparison Figure B shows blood oxygen saturations S at the end of the tube depending on tube radius r.

Details of the considered configurations are given in the following. The theoretical model of Ref. [2] incorporates a multi-layered vascular tube as source of oxygen and a surrounding infinite

1

tissue with a homogeneous background representing oxygen release from the capillary plexus. We augmented the tissue diffusion equation (15, s. main text) accordingly by adding the source term $\kappa - P_{t,i}\kappa/P^*$, where $\kappa = 0.625 mmHg$ and $\kappa/P^* = 30$. Other parameter which are already present in our model were readily adopted. The flow rate q poses an exception since it was not provided directly by Ref. [2]. We determined it according to [2, (A6)] using the velocity profile coefficients in the appendix. The simulation box was made large enough for the radial P_t profile to assume the asymptotic value ($42\ mmHg$) determined by κ and M_0. [3] considered a configuration where a vascular tube is surrounded by a block of rubber which is in contact with air at a specific oxygen partial pressure. Two model variants exist. One situation where oxygen rich blood releases oxygen to the rubber block [3, Fig. 2] and another where oxygen depleted blood takes up oxygen [3, Fig. 3] from it. In the former case the PO2 of the air is kept at $160\ mmHg$ and the blood PO2 at the inlet is 0. Vice versa for the former case. In either case, gas exchange happens through the surrounding rubber block. We accounted for this situation by Dirichlet boundary conditions and by setting the consumption rate $M_0 = 0$. The faces perpendicular to the longitudinal axis are imposed with no-flux conditions. The system size is set according to the reported half-thickness of the block as $4\ mm \times 80\ \mu m \times 80\ \mu m$. Computation were performed with a grid resolution of $h = 20\ \mu m$. The maximal relative error of the saturation obtained at the end of some tube $S(x = 4mm)$ amounts to approximately 16%.

Additionally, we compared our model with other numerical simulation methods using small vascular networks. [4] recently published the software that produced the results for the theoretical studies [5, 6] using a Green's function method. Using software provided by Ref. [4] we were limited to small networks confined within volumes of ca. $0.1\ mm^3$ due to the computational cost of the Green's function method. Exemplary simulation results can be seen in Figure C. Obtained PO2 distributions are in good agreement with results obtained by our method. We estimate a local worst case difference in the intravascular PO2, P, of 30%, and an average difference relative to the mean of P of ca. 16%.

Poor convergence of the solution with the grid constant h is a significant source of error in our method. Convergence tests with respect to the grid constant h show sublinear convergence as shown in Fig D where we plotted vascular and tissue oxygen partial pressures in a single vascular tube for different grid constants. After an initial settling length, the oxygen partial pressure behind the inlet is underestimated by an approximately constant offset, depending on h. The difference between the on-axis value of blood and tissue PO2 remains approximately spatially constant. Relative errors from the extrapolated true solution therefore start rather small behind the inlet (approx. 3%) and increase to 13% at the end. The reason for poor convergence is the singular nature of the oxygen source term (18) in the tissue oxygen diffusion equation , i.e. the use of the Dirac-δ function. D'Angelo [7] obtained better convergence by using locally refined meshes. Although it is a very challenging task, steps along those lines could be undertaken to improve numerical accuracy.

It is possible to arrive at inconsistent solutions when the iteration of (20) and (21) has not sufficiently converged. Then the amount of oxygen extracted from the network is not the same as the amount consumed by tissue. Hence, in order to check for conservation of mass we determined the total transvascular oxygen flux J_{tv}, the total consumption $J_{cons} = \int_\Omega M(P_t)\boldsymbol{dx}$ and considered the error $e_{tv} = (J_{tv} - J_{cons})/J_{tv}$. We also checked for mass conservation errors in the vasculature due to the numerical integration of P and determined $e_v = (J_{in} - J_{out} - J_{tv})/J_{in}$, where J_{in} and J_{out} are the influx and efflux through root nodes. We found both errors to be less than 1% at the point where further iteration does not change the solution any more.

2
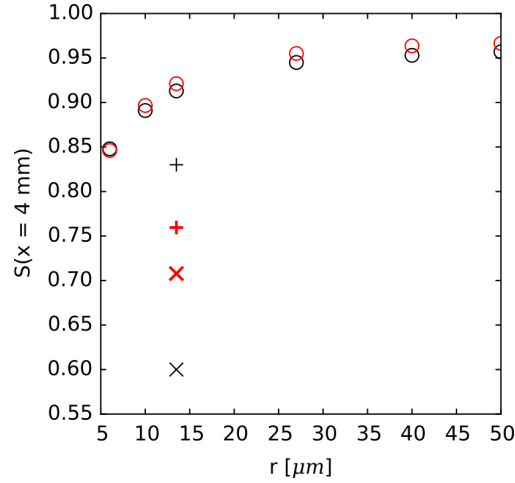
Figure B. Comparison of blood oxygen saturations at ends of vascular tubes: We considered a single $4\ mm$ long vascular tube embedded in a passive medium through which oxygen can diffuse. We computed the blood oxygen saturation S at the end of the vascular tube $x = 4\ mm$ (red) under various conditions (see text), such as varying vascular radii r, which is plotted here. Literature data of more sophisticated capillary models for equivalent cases [2, Fig. 4] ($\circ$), [3, Fig. 2] ($\times$), and [3, Fig. 3] ($+$) are shown as black symbols.
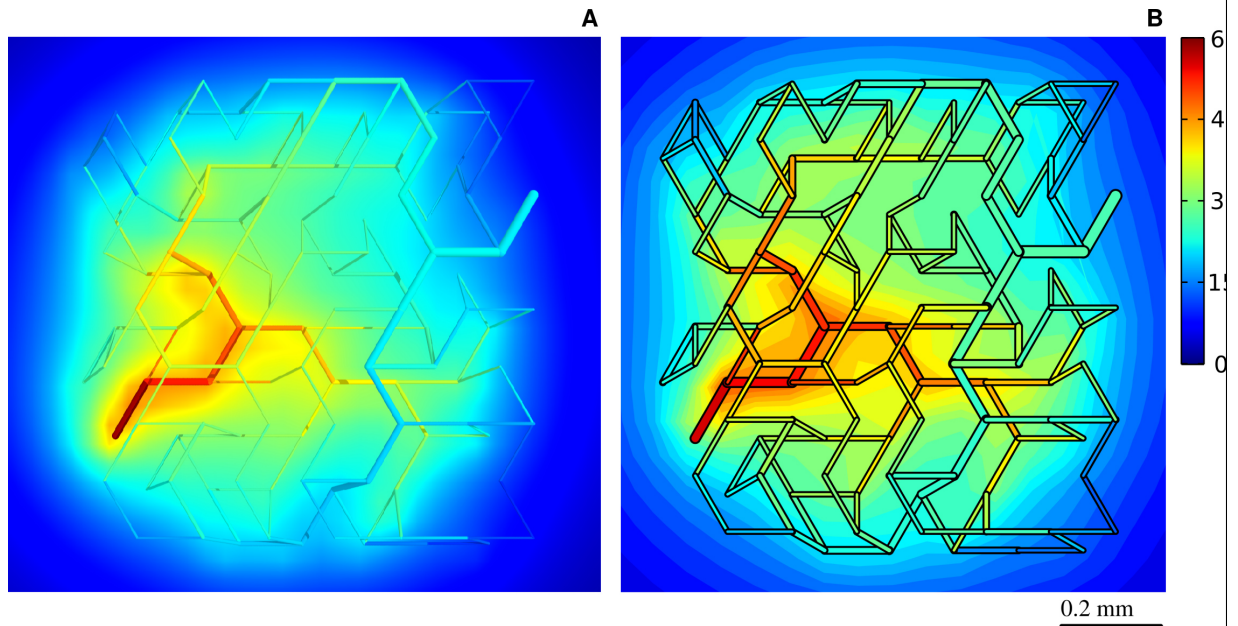
Figure C. Comparison with Green's function method: (A) shows the oxygen partial pressure PO2 distribution produced by our program. (B) shows the distribution produced by the software by [4]. The solution of vascular PO2 distribution P is layered on top of a slice through the tissue oxygen PO2 distribution P_t. The input to both programs was a small artificial network, identical parameters, and a spacing of tissue points of $h = 40\ \mu m$. However, boundary conditions for the tissue PO2 diffusion equations could not be matched. Therefore we extended the simulation box beyond the displayed region by $1\ mm$ on every side. The colorscale for P and P_t is given in $mmHg$.

3
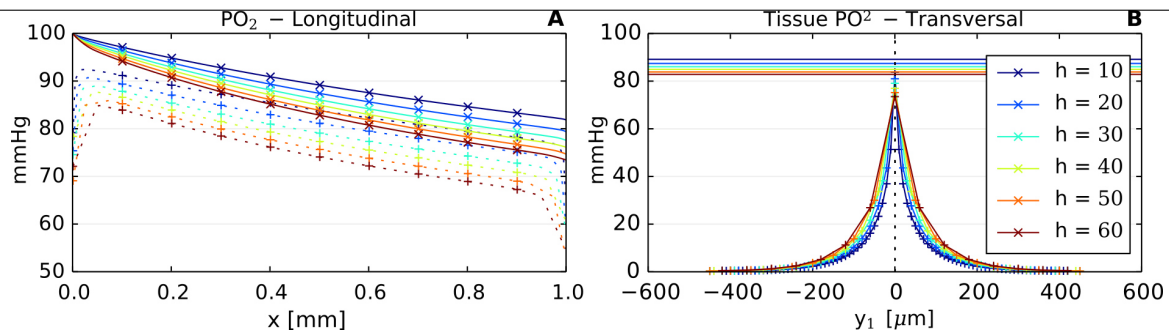
Figure D. Convergence test w.r.t. grid constant h. We consider a small simulation volume with a single vessel of length $1\ mm$ inside. Vascular (P, crosses) and tissue (P_t, pluses) oxygen partial pressure PO2 distributions are shown. The development of P and P_t (dotted line) along the vessel center axis is displayed in (A). In (B) we plotted the transversal profile of P_t, i.e. perpendicular to the vessel axis along the spatial coordinate y_1 at a point half way between the ends of the vessel. The horizontal lines indicate the vascular PO2 at this point. For smaller h the curves lie somewhat further apart, indicating sub-linear convergence, i.e. if the error to the true solution was linear in h we would observe a constant spacing between curves.

Blood Pressure Radius Relation

Blood flow boundary conditions of our model are such that the blood pressure is set to fixed numbers $p^{(BC)}$ for the solution for nodal pressures. Since blood pressure correlates well with vascular radius r, we let $p^{(BC)}$ be given as function of r and the type of vessel (arterial or venous). We first fit a curve to blood pressure data of rat mesentery [8]. Then we scaled the curve (adjusting $A1$ and $A2$) so that physiological blood pressures [9, Fig. 19.6] are obtain in venules and arterioles, thus obtaining for the blood pressure boundary condition

$$p^{(BC)}(r) = [A2 + (A1 - A2)/(1 + \exp((r' - r_0)/\Delta r))], \qquad (3)$$

where $r' = r$ for a vein, else $-r$, and $A1 = 89\ mmHg$, $A2 = 18\ mmHg$, $r_0 = -21\mu m$, $\Delta r = 16\mu m$.

References

[1] Hellums JD, Nair PK, Huang NS, Ohshima N. Simulation of intraluminal gas transport processes in the microcirculation. Ann Biomed Eng. 1996 Jan-Feb;24(1):1–24. doi:10.1007/bf02770991.

[2] Moschandreou TE, Ellis CG, Goldman D. Influence of tissue metabolism and capillary oxygen supply on arteriolar oxygen transport: a computational model. Math Biosci. 2011 Jul;232(1):1–10. doi:10.1016/j.mbs.2011.03.010.

[3] Nair PK, Huang NS, Hellums JD, Olson JS. A simple model for prediction of oxygen transport rates by flowing blood in large capillaries. Microvasc Res. 1990 Mar;39(2):203–211. doi:10.1016/0026-2862(90)90070-8.

[4] Secomb TW; 2014. Available from: http://www.physiology.arizona.edu/people/secomb/greens.

[5] Secomb TW, Hsu R, Park EYH, Dewhirst MW. Green's Function Methods for Analysis of Oxygen Delivery to Tissue by Microvascular Networks. Annals of Biomedical Engineering. 2004 Nov;32(11):1519–1529. doi:10.1114/b:abme.0000049036.08817.44.

[6] Safaeian, N . Computational Modelling of Capillaries in Neuro-vascular Coupling. University of Canterbury; 2012. doi:10092/8038.

4

CHAPTER 3. ORIGINAL PUBLICATIONS

3.1. COMPUTATIONAL MODEL FOR TUMOR OXYGENATION APPLIED TO CLINICAL DATA ON BREAST TUMOR HEMOGLOBIN CONCENTRATIONS SUGGESTS VASCULAR DILATION AND COMPRESSION

[7] D'Angelo C. Finite Element Approximation of Elliptic Problems with Dirac Measure Terms in Weighted Spaces: Applications to One- and Three-dimensional Coupled Problems. SIAM Journal on Numerical Analysis. 2012;50(1):194–215. doi:10.1137/100813853.

[8] Pries AR, Secomb TW, Gaehtgens P. Design principles of vascular beds. Circulation Research. 1995;77(1017-1022). doi:10.1161/01.res.77.5.1017.

[9] Marieb EN, Hoehn K. Human Anatomy & Physiology. Pearson; 2013.

5

S2 Appendix

Explicit Formulas for Relevant Biophysical Quantities

After vascular networks of normal tissue and tumor were constructed, distributions of hematocrit in vascular networks and oxygen concentrations in vascular networks and tissue are calculated, yielding for each vessel segment $v \in \mathbb{V}$ e.g. radius r_v , length l_v, hematocrit H_v, blood flow q_v, blood oxygen saturation $S_v(0)$ and oxygen concentration $c_v(0)$ at vessel entrance as well as average blood oxygen saturation S_v. Using this information, the following averages are calculated, pertaining to the tissue volume Ω.

Length density :

$$L_D = \frac{1}{|\Omega|} \sum_{v \in \mathbb{V}} l_v, \tag{1}$$

taken as measure for microvessel density MVD.

Regional blood volume (vascular volume density) :

$$rBV = \frac{1}{|\Omega|} \sum_{v \in \mathbb{V}} \pi r_v^2 l_v \tag{2}$$

Vascular surface density :

$$S_D = \frac{1}{|\Omega|} \sum_{v \in \mathbb{V}} 2\pi r_v l_v. \tag{3}$$

Regional blood flow (perfusion) :

$$rBF = \frac{1}{|\Omega|} \sum_{v \in \mathbb{I} \cap \partial\Omega} q_v = \frac{1}{|\Omega|} \sum_{v \in \mathbb{O} \cap \partial\Omega} q_v, \tag{4}$$

where $\mathbb{I} \cap \mathbb{V}$ ($\mathbb{O} \cap \mathbb{V}$) denote set of all vessel segments penetrating surface $\partial\Omega$ with blood flow pointing inwards (outwards).

Tissue hemoglobin concentration :

$$c_{Hb} = MCHC \cdot rRBCV = \frac{MCHC}{|\Omega|} \sum_{v \in \mathbb{V}} \pi r_v^2 l_v H_v \tag{5}$$

with mean corpuscular hemoglobin concentration $MCHC$, regional RBC volume $rRBCV$.

Tissue oxyhemoglobin concentration :

$$c_{HbO} = \frac{MCHC}{|\Omega|} \sum_{v \in \mathbb{V}} \pi r_v^2 l_v H_v \frac{1}{l_v} \int_v S_v(x) dx \tag{6}$$

and an analogous expression for the tissue deoxyhemoglobin concentration c_{HbD}, replacing $\frac{1}{l_v} \int_v S_v(x)dx$ by $1 - \frac{1}{l_v} \int_v S_v(x)dx$.

Tissue blood oxygen saturation :

$$Y = \frac{c_{HbO}}{c_{Hb}} = \sum_{v \in \mathbb{V}} \left\{ \frac{\pi r_v^2 H_v l_v}{\sum_{u \in \mathbb{V}} \pi r_u^2 l_u H_u} \frac{1}{l_v} \int_v S_v(x) dx \right\}, \tag{7}$$

where Y is the RBC-volume-weighted average of blood oxygen saturation taken over all vessel segments.

1

Length-weighted average blood oxygen saturation :

$$\langle S \rangle = \sum_{v \in \mathbb{V}} \frac{l_v}{\sum_{u \in \mathbb{V}} l_u} \frac{1}{l_v} \int_v S_v(x) dx \tag{8}$$

Average partial oxygen pressure in blood :

$$\langle P \rangle = \sum_{v \in \mathbb{V}} \frac{l_v}{\sum_u l_u} \frac{1}{l_v} \int_v P(x) dx, \tag{9}$$

where the average concentration of dissolved oxygen in blood is given by $\bar{c}_p = \alpha_p \langle P \rangle$.

Average tissue partial oxygen pressure :

$$P_t = \frac{1}{|\Omega|} \int_\Omega P_t(\boldsymbol{x}) d^3 x, \tag{10}$$

where the average oxygen concentration in tissue is given by $\bar{c}_t = \alpha_t \langle P_t \rangle$.

Metabolic rate of oxygen consumption :

$$MRO_2 = \frac{1}{|\Omega|} \int_\Omega M(P_t(\boldsymbol{x})) d^3 x, \tag{11}$$

where M is the Michaelis-Menten relation (17).

Total transvascular oxygen flux :

$$J_{tv} = \sum_{v \in \mathbb{V}} 2\pi r_v \gamma(r_v) \int_v \{ P(x) - P_t(x) \} dx, \tag{12}$$

and corresponding regional transvascular oxygen flux $rJ_{tv} = J_{tv}/|\Omega| = MRO_2$.

Average transvascular oxygen flux density :

$$\langle j_{tv} \rangle = \frac{1}{\sum_{u \in \mathbb{V}} l_u} \sum_{v \in \mathbb{V}} \gamma(r_v) \int_v \{ P(x) - P_t(x) \} dx, \tag{13}$$

i.e. the average transvascular oxygen flux density is the length weighted average over the mean oxygen flux density of all vessel segments; note that $S_D \langle j_{tv} \rangle \neq \frac{J_{tv}}{|\Omega|} = MRO_2$.

Oxygen flux entering vascular network :

$$J_{in} = \sum_{v \in \mathbb{I} \cap \partial\Omega} q_v \{ c_0 H_v S_{in,v} + \alpha_p P_{in,v} \}, \tag{14}$$

with $P_{in,v} = P_v^{(BC)}$ and $S_{in,v}$ given by the Hill equation. The corresponding regional influx is $rJ_{in} = J_{in}/|\Omega|$.

Oxygen flux leaving vascular network :

$$J_{out} = \sum_{v \in \mathbb{O} \cap \partial\Omega} q_v \{ c_0 H_v S_{out,v} + \alpha_p P_{out,v} \} \tag{15}$$

Oxygen extraction fraction :

$$OEF = \frac{J_{in} - J_{out}}{J_{in}} = MRO_2/rJ_{in}. \tag{16}$$

2

S3 Appendix

Regional Blood Volume of Confined Perfect Binary Trees

In this section we derive an approximative relation between the number of root nodes R and the regional blood volume rBV, provided that the total number of vessels M is held constant, i.e. all vascular trees are confined to the simulation box Ω and adhere to a fixed vascular density. Naturally R is also the number of trees. We assume that all vascular trees are perfect binary trees, i.e. tree levels from $k = 0$ at the top to $k = n-1$ at capillary (leaf) level have the maximum number of vessels 2^k. Furthermore we assume that trees are equal in the number of vessels (connections) N. Hence $M = N \cdot R$ is split to equal parts between trees. There is no distinction between arterial and venous trees. For given number of levels (depth) n, a tree has $N = \sum_{k=0}^{n-1} 2^k$ connections. This is a geometric series for which holds in general

$$\sum_{k=0}^{n-1} q^k = \frac{q^n - 1}{q - 1}, \tag{1}$$

for some q. N can therefore be written as $N = 2^n - 1$, from which we obtain the depth

$$n = \log_2(N + 1), \tag{2}$$

Let further the radii at a bifurcation be given by Murray's law, i.e. $r_c^\alpha = r_a^\alpha + r_b^\alpha$. Since a and b are the same, we have $r_c = 2^{1/\alpha} r_{a=b}$, or in relation to the tree level k, we have the radius at level k

$$r_k = 2^{(n-1-k)/\alpha} r_{n-1}, \tag{3}$$

where r_{n-1} is the capillary radius. Now let's estimate the volume of the tree TV, provided equal vessel lengths l. By summing over tree levels we obtain

$$TV = l\pi \sum_{k=0}^{n-1} 2^k r_k^2, \tag{4}$$

since each level has 2^k vessels of radius r_k. Replacing r_k by Eq.(3) we obtain

$$TV = \pi r_{n-1}^2 l \cdot 2^{(n-1)2/\alpha} \sum_{k=0}^{n-1} 2^{k(1-2/\alpha)}. \tag{5}$$

This is again a geometric series which is rewritten with the help of Eq.(1) and $q = 2^{1-\frac{2}{\alpha}}$ to remove the sum. Furthermore without loss of generality we set $\pi r_{n-1}^2 l = 1$. After some basic algebra, the result is

$$TV = \frac{2^n - 2^{(2/\alpha)n}}{2 - 2^{2/\alpha}} \tag{6}$$

$$= \frac{(N+1) - (N+1)^{2/\alpha}}{2 - 2^{2/\alpha}}, \tag{7}$$

where in the second line we further used that $2^n = N + 1$. Now to satisfy the constraint that the total number of vessels taken over all trees is constant M, we substitute $N = M/R$, using the number of trees R. For brevity we set the volume of the simulation box $|\Omega| = 1$ without loss of generality. Thus we obtain the total regional volume of all trees rBV

$$rBV = \frac{TV R}{|\Omega|} \tag{8}$$

$$= M \frac{1 + \frac{R}{M} - \frac{R}{M}(\frac{M}{R} + 1)^{2/\alpha}}{2 - 2^{2/\alpha}}. \tag{9}$$

The denominator $2 - 2^{2/\alpha}$ is a positive increasing function of α that vanishes for $\alpha = 2$ and which asymptotically approaches 1 for $\alpha \to \infty$. It can be shown that the nominator is a decreasing

1

function in R, which is well approximated for small $R/M \ll 1$ by $1 - (R/M)^{(1-2/\alpha)}$. In the edge case where $\alpha = 2$ we still obtain a decreasing function by calculating the limit of $\alpha \to 2$ for Eq.(6). In that case it is logarithmic with $rBV = \frac{1}{2}(R + M)\log_2(M/R + 1)$.

Murrays α determines how much parent vessel radii grow at bifurcations. In the limit of $\alpha \to \infty$, Murrays law selects the radius of the thicker child vessel as the radius of the parent vessel. This means all radii become equal, and indeed $rBV(\alpha \to \infty) = M$ is obtained from Eq.(9). As we would intuitively expect, the dependence on R is eliminated. For realistic $2 \le \alpha \le 3$, the dependence on R cannot be removed. Moreover we can consider the case where all vessels are root vessels, i.e. $R = M$. Then again $rBV = M$ is obtained, which is clear since then again all vessels have equal radii. In actual simulations the assumption of perfect and equally sized trees does not hold, i.e. frequently, small branches are generated. Moreover, even if all lattice boundary sites are occupied with root nodes, only a small fraction of them grow to vascular trees of significant size. Most of them regress to a single starting node without any connections. Despite that, we observe a clear trend of decreasing rBV with increasing R.

2

S4 Appendix

Further details on comparison between simulated and literature biophysical data (see Tables 3 and 4)

In support of our model we further discuss simulated data listed in Tables 3 and 4 in some detail, comparing our results with clinical data, data obtained from animal models and theoretical data available in the literature.

Microvessel density MVD

The microvessel density MVD is measured microscopically by counting the number of microvessels per area of a tissue microscopic slide. The MVD is a quantity not easy to simulate. Therefore we take the simulated length density L_D, i.e. the total length of the vascular network divided by the tissue volume as measure for MVD (s. S2 Appendix). This definition yields the correct dimension and is identical to the number of vessels per cross-sectional area in case of a Krogh-like arrangement of parallel vessels. However, when comparing experimental MVD data and simulated length densities L_D it should be kept in mind that both parameters are not identical. In a large portion of the experimental literature on breast tumors, the MVD is obtained from well vascularized areas, so called hot-spots. Dhakal et al. [1] reported densities between 15-348 mm^{-2} with a mean of 88 mm^{-2}. Hot-spots are predominantly found near the tumor rim, but apparently not exclusively. Fernandez-Guinea et al. [2] reported somewhat lower MVD values of 0-157 mm^{-2} from breast tumor centers with a median of 20 mm^{-2}. Stamatelos et al [3] reconstructed the vasculature of a tumor of volume $280\,mm^3$ of a human breast cancer animal model and these authors report an average length density L_D of $21\,mm^{-2}$. However, spatial heterogeneity of the vasculature length density varied considerably within the experimental tumor investigated, ranging from about $9\,mm^{-2}$ up to $101\,mm^{-2}$. We obtain a whole tumor average of $133 \pm 18\,mm^{-2}$ (case CMPR, s. Table 3) which includes a significant contribution of the rim. The prediction of the MVD of the central part of the tumor agrees with the data of [2]. Microvessel density MVD of normal breast tissue is reproduced accurately.

Regional vessel volume rBV

The regional vessel volume rBV denotes the volume fraction of tissue occupied by vessels, i.e. vascular volume density (s. S2 Appendix). Using clinical data on hemoglobin concentrations of normal breast tissue ($c_{Hb} = 17.3 \pm 6.2\ \mu mol/l$ [4]), and of tumors ($c_{Hb} = 53 \pm 32\ \mu mol/l$ [4]), we estimated the vascular volume fraction. Tissue hemoglobin concentration c_{Hb} is the product of mean corpuscular hemoglobin concentration ($MCHC$) and regional RBC volume $rRBCV$ (s. S2 Appendix). Assuming hematocrit $H = 0.45$ to be homogeneously distributed within the vascular network, tissue hemoglobin concentration is given by $c_{Hb} = MCHC \cdot H \cdot rBV = c_{Hb,blood} \cdot rBV$, where $c_{Hb,blood}$ is the hemoglobin concentration in whole blood. Using $64.5 kg/mol$ for the hemoglobin molar mass and assuming for the hemoglobin concentration in blood $c_{Hb,blood} = 14 g/dl$ (women, normal range: $12 - 16\ g/dl$), we estimate $rBV = 0.008 \pm 0.003$ (normal breast tissue) and $rBV = 0.024 \pm 0.015$ (breast tumors). Results on hemoglobin concentration of normal breast tissue and breast tumors obtained by a number of groups using optical mammography scatter by about a factor of two [4], resulting in an upper limit of $rBV = 0.016$ for normal breast tissue and a range of $rBV = 0.01$–0.06 for breast tumors. Stamatelos et al [3] report an average of tumor vessel volume density of 0.007 and rBV to vary within the tumor of the human breast cancer model from 0.002 up to 0.032. Beaney [5] obtained distinctly larger rBV estimates for human breast tissue ($rBV = 0.034$) and human breast tumors ($rBV = 0.043$), derived from PET measurements using the steady state $^{15}O_2$ inhalation technique. Note, however, that the rBV values reported by Beaney [5] for breast tumors, have to be considered as unreliable since the compartment model used to analyze the PET data is inaccurate for heterogeneous tissue [6]. For comparison, in normal human brain regional blood volume was determined from PET measurements to be $rBV = 0.038 \pm 0.007$ [7]. Using MRI and a brain tumor animal model yielded $rBV = 0.026 \pm 0.003$ (normal brain tissue) and $rBV = 0.053 \pm 0.006$ (brain tumor) [8]. Our simulation results on regional vessel volume of normal breast tissue and breast tumors (case CMPR) agree with clinical data derived from optical

1

CHAPTER 3. ORIGINAL PUBLICATIONS

3.1. COMPUTATIONAL MODEL FOR TUMOR OXYGENATION APPLIED TO CLINICAL DATA ON BREAST TUMOR HEMOGLOBIN CONCENTRATIONS SUGGESTS VASCULAR DILATION AND COMPRESSION

mammography. Furthermore, rBV of breast tumors (case CMPR) falls within the range of volume densities reported in [3] for the animal breast cancer model. In addition, for normal breast tissue, we deduce a venous fraction of the total blood volume fraction $vrBV/rBV = 68\%$ in fair agreement with MRI data of normal human brain (77%) [9]. Because the classification of vessel segments of the tumor vasculature into arterioles, capillaries and venules no longer applies, the venous fractional blood volume is meaningless in case of tumors.

Vessel surface to vessel volume

Besides vascular surface density S_D, Table 3 lists the vessel surface density to vessel volume density ratio S_D/rBV. For a single vessel segment vessel surface to vessel volume scales as $1/r$. Although this result will no longer be exactly applicable for the ratio of vessel surface density to vessel volume density, we expect this ratio to decrease with increasing average vessel radius. For tumor vasculature (case CMPR) we find $S_D/rBV = 0.27\ \mu m^{-1}$ close to the simulated value for normal breast tissue ($S_D/rBV = 0.29\ \mu m^{-1}$). This modest decrease is ultimately explained by the low maximal dilation radius $r^{(max)} = 14\ \mu m$, leading to an average vascular radius of $r = 5.2\ \mu m$ (case CMPR), only $2\ \mu m$ above the average radius of initial networks. A contributing factor is the peripheral plexus of thin and densely packed vessel (high S_D/rBV), part of which is included in the tumor volume. Stamatelos et al [3] reported a surface to volume ratio of $S_D/rBV = 0.17\ \mu m^{-1}$ for a human breast tumor animal model together with an average (median) vessel radius of $r = 9.2\ \mu m$.

Perfusion

Dynamical PET measurements ($^{15}O_2$) on 37 breast cancer patients yielded $rBF = 0.06\ ml/g/min$ (mean, normal tissue, range $0.03-0.17\ ml/g/min$) and $rBF = 0.32 ml/g/min$ (mean, tumor, range $0.08 - 0.9\ ml/g/min$) [10]. Nearly the same results were reported in [11]. Volumes of human breast cancers imaged range from one to several cm^3, typically. On the other hand, the range of simulated regional blood flow $rBF = q_{sph,tum}/|\Omega_{sph}|$ of the small ($0.014\ cm^3$) spherical tumor amounts to $0.13 - 7.5 ml/g/min$, with a mean $1.25 ml/g/min$ (case CMPR) being higher by about a factor of 4 compared to the clinical results (s. Table 3). We attributed the discrepancy between simulated perfusion and clinical data to the considerable difference in tumor volumes. Indeed, a general decrease of perfusion with increasing tumor mass was seen previously for human breast cancer xenografts. Perfusion ranged from $0.5\ ml/g/min$ at $m_{tum} = 0.4\ g$ down to $0.025\ ml/g/min$ at $m_{tum} = 8\ g$ [12] . For eliminating the dependence of simulated perfusion on tumor volume, Table 3 lists the scaled perfusion $rBF_{scaled} = rBF_{norm} \cdot q_{sph,tum}(t = 600h)/q_{sph,norm}(t = 0)$. Mean simulated scaled perfusion rBF_{scaled} (case CMPR) is lower by about a factor of 2 compared to the clinical results, possibly overestimating size dependence of tumor perfusion. Our results for normal breast tissue (range: $0.032 - 0.064 ml/ml/min$) agree well with clinical data.

Wall shear stress

Simulated wall shear stress of normal vasculature falls within the range of shear stresses measured for human conjunctival arterioles, capillaries and venoles [13, 14]. Simulated shear stresses of the tumor model variants are consistent with shear stresses reported by Stamatelos et al [3] for a human breast cancer animal model.

Tissue oxygen partial pressures

The global ensemble average of simulated PO2 of normal tissue and tumor tissue amounts to $36 \pm 6\ mmHg$ and $29 \pm 13\ mmHg$, respectively (s. Table 4). Polarographic PO2 measurements at a large number of sites in normal breast tissue and breast tumors of 15 patients yielded median PO2 values of $65\ mmHg$ and $30\ mmHg$, respectively [12]. The simulated PO2 value of tumor tissue (case CMPR) reproduces the clinical result exactly, the coincidence possibly being fortuitous, considering the skewed histogram of measured partial oxygen pressures [12]. Since the distribution of measured partial oxygen pressures in normal breast tissue is rather broad, simulated and measured tissue partial oxygen pressures in normal tissue can be considered to agree.

2

Metabolic rate of oxygen consumption

Our model assumes tissue metabolic rate of oxygen consumption to follow a Michaelis-Menten relation and takes the maximal rate M_0 and half-pressure P_{M50} as input. In particular, maximal rate M_0 in tumor tissue was assumed to be four times larger than in normal breast tissue, whereas half-pressure P_{M50} of normal breast tissue was adopted to be twice that of breast cancers (s. Table 1). Since (average) partial oxygen pressures in normal and tumorous breast tissue were simulated to be considerably higher than the assumed half-pressures P_{M50}, the simulated metabolic rates $MRO_2 = 3.25\ \mu lO_2/ml/min$ (normal tissue) and $MRO_2 = 12.1\ \mu lO_2/ml/min$ (breast tumor, case CMPR) are essentially determined by the adopted parameter M_0 of the Michaelis-Menten relation. From PET measurements based on the steady-state $^{15}O_2$ inhalation technique, Beaney [5] reported $MRO_2 = 4.5\ \mu lO_2/ml/min$ and $MRO_2 = 6.6\ \mu lO_2/ml/min$ for normal breast tissue and breast tumors, respectively. The latter value had been challenged because of tumor inhomogeneity [6]. Recently, a considerably higher metabolic rate of oxygen consumption $M_0 = 40.6 \pm 7.8\ \mu l\ O_2/ml/min$ was reported of viable multicellular human colorectal carcinoma spheroids, taken as in-vitro tumor model [15]. In addition, measurements of oxygen flux above a monolayer of cancer cells in culture medium yielded metabolic rates M_0 from $21\ \mu l\ O_2/ml/min$ up to $52\ \mu l\ O_2/ml/min$ for various human cancer cells, with $M_0 = 33.4 \pm 8.3\ \mu l\ O_2/ml/min$ for human breast cancer cells MDAMB- 468 [16]. For comparison we note that for normal human brain PET measurements yielded $CMRO_2 = 33 \pm 5\ \mu l\ O_2/ml/min$ [7].

Oxygen extraction fraction

Average blood oxygen saturation is (negatively) correlated with oxygen extraction fraction $OEF = J_{tv}/J_{in} = (J_{in} - J_{out})/J_{in} = MRO_2/rJ_{in}$, where J_{tv} is the total transvascular oxygen flux into tissue, in $J_{in}(J_{out})$ the total oxygen influx (efflux) into the vasculature (leaving the vasculature) of the tissue volume and rJ_{in} is the oxygen influx per unit volume of tissue considered. For the whole simulation box, J_{in} and J_{out} are determined by summing oxygen flux qc over all root arteries or veins, respectively. For the tumor, we sum qc over vessels penetrating the tumor surface with a flow direction into or out of the tumor. For normal breast tissue and breast tumors (case CMPR) we obtain the result $OEF = 0.34 \pm 0.1$ and $OEF = 0.11 \pm 0.09$, respectively. Oxygen extraction data on normal breast tissue and breast tumors are scarce in the literature. Beaney [5] reported the oxygen extraction fraction of normal breast tissue to be $OEF = 0.65 \pm 0.1$. This result seems to be rather high considering the oxygen extraction of normal human brain measured by PET to be $OEF = 0.44 \pm 0.06$ [7].

Using the steady state $^{15}O_2$ inhalation technique almost the same oxygen extraction fractions were measured for breast tumors ($OEF = 0.23 \pm 0.08$, [5]) and brain tumors ($OEF = 0.22 \pm 0.04$, [17]), however the same reservations remain concerning inadequate data analysis because of tissue heterogeneity. Our simulations predict for breast tumors (case CMPR) oxygen extraction fractions of $OEF = 0.11 \pm 0.09$, an estimate likely to be too low. Since $MRO_2 = \epsilon \cdot c_{Hb,blood} S_{in} \cdot rBF \cdot OEF$, where ϵ is the Hüfner factor and S_{in} the arterial blood oxygenation of the vessels penetrating the surface of the spherical tumor, overestimation of the tumor regional blood flow will cause an underestimation of the oxygen extraction fraction OEF, since the metabolic rate of oxygen consumption is essentially fixed by the input parameters of the model. Conversely, estimates of scaled perfusion are probably too low, overestimating the dependence of perfusion on tumor volume. Therefore, corresponding oxygen extraction fractions of breast tumors are probably on the high side ($OEF = 0.66$, CMPR). In addition, Table 4 lists the oxygen influx J_{in} and average transvascular oxygen flux density j_{tv}, where we write j_{tv} informally for the average over the network length (s. S2 Appendix).

Tissue blood oxygen saturation

Vessel segments contribute to tissue hemoglobin concentration c_{Hb} (tissue oxyhemoglobin concentration c_{HbO}) according to their blood hemoglobin concentration, (blood oxyhemoglobin concentration) weighted by their fractional volume. In order to simulate c_{HbO} for each vessel segment its average blood oxygenation has to be known. Simulated tissue blood oxygen saturation $Y = c_{HbO}/c_{Hb}$ agree well with clinical data.

3

References

[1] Dhakal HP, Bassarova A, Naume B, Synnestvedt M, Borgen E, Kaaresen R, et al. Breast carcinoma vascularity: a comparison of manual microvessel count and Chalkley count. Histol Histopathol. 2009 Aug;24(8):1049–1059.

[2] Fernandez-Guinea O, Alvarez-Cofino A, Eiro N, Gonzalez LO, del Casar JM, Fernandez-Garcia B, et al. Low microvascular density at the tumor center is related to the expression of metalloproteases and their inhibitors and with the occurrence of distant metastasis in breast carcinomas. Int J Clin Oncol. 2013 Aug;18(4):629–640. doi:10.1007/s10147-012-0428-2.

[3] Stamatelos SK, Kim E, Pathak AP, Popel AS. A bioimage informatics based reconstruction of breast tumor microvasculature with computational blood flow predictions. Microvasc Res. 2014 Jan;91:8–21. doi:10.1016/j.mvr.2013.12.003.

[4] Grosenick D, Wabnitz H, Moesta KT, Mucke J, Schlag PM, Rinneberg H. Time-domain scanning optical mammography: II. Optical properties and tissue parameters of 87 carcinomas. Phys Med Biol. 2005 Jun;50(11):2451–2468. doi:10.1088/0031-9155/50/11/002.

[5] Beaney RP. Positron emission tomography in the study of human tumors. Semin Nucl Med. 1984 Oct;14(4):324–341. doi:10.1016/s0001-2998(84)80006-9.

[6] Lammertsma AA, Jones T. Low oxygen extraction fraction in tumours measured with the oxygen-15 steady state technique: effect of tissue heterogeneity. The British Journal of Radiology. 1992;65(776):697–700. doi:10.1259/0007-1285-65-776-697.

[7] Ito H, Kanno I, Kato C, Sasaki T, Ishii K, Ouchi Y, et al. Database of normal human cerebral blood flow, cerebral blood volume, cerebral oxygen extraction fraction and cerebral metabolic rate of oxygen measured by positron emission tomography with 15O-labelled carbon dioxide or water, carbon monoxide and oxygen: a multicentre study in Japan. Eur J Nucl Med Mol Imaging. 2004 May;31(5):635–643. doi:10.1007/s00259-003-1430-8.

[8] Christen T, Lemasson B, Pannetier N, Farion R, Remy C, Zaharchuk G, et al. Is T2* enough to assess oxygenation? Quantitative blood oxygen level-dependent analysis in brain tumor. Radiology. 2012 Feb;262(2):495–502. doi:10.1148/radiol.11110518.

[9] An H, Lin W. Cerebral venous and arterial blood volumes can be estimated separately in humans using magnetic resonance imaging. Magn Reson Med. 2002 Oct;48(4):583–588. doi:10.1002/mrm.10257.

[10] Mankoff DA, Dunnwald LK, Gralow JR, Ellis GK, Charlop A, Lawton TJ, et al. Blood flow and metabolism in locally advanced breast cancer: relationship to response to therapy. J Nucl Med. 2002 Apr;43(4):500–509. Available from: http://jnm.snmjournals.org/content/43/4/500.abstract.

[11] Wilson CB, Lammertsma AA, McKenzie CG, Sikora K, Jones T. Measurements of blood flow and exchanging water space in breast tumors using positron emission tomography: a rapid and noninvasive dynamic method. Cancer Res. 1992 Mar;52(6):1592–1597. Available from: http://cancerres.aacrjournals.org/content/52/6/1592.abstract.

[12] Vaupel P, Schienger K, Knoop C, Hockel M. Oxygenation of human tumors: Evaluation of tissue oxygen distribution in breast cancers by computerized O2 tension measurements. Cancer Research. 1991 Jun;51(12):3316–3322.

[13] Koutsiaris AG, Tachmitzi SV, Batis N. Wall shear stress quantification in the human conjunctival pre-capillary arterioles in vivo. Microvasc Res. 2013 Jan;85:34–39. doi:10.1016/j.mvr.2012.11.003.

[14] Koutsiaris AG, Tachmitzi SV, Batis N, Kotoula MG, Karabatsas CH, Tsironi E, et al. Volume flow and wall shear stress quantification in the human conjunctival capillaries and post-capillary venules in vivo. Biorheology. 2007;44(5-6):375–386. Available from: http://content.iospress.com/articles/biorheology/bir470.

4

[15] Grimes DR, Kelly C, Bloch K, Partridge M. A method for estimating the oxygen consumption rate in multicellular tumour spheroids. J R Soc Interface. 2014 Jan;11(92):20131124. doi:10.1098/rsif.2013.1124.

[16] Grimes DR, Kannan P, McIntyre A, Kavanagh A, Siddiky A, Wigfield S, et al. The Role of Oxygen in Avascular Tumor Growth. PLOS ONE. 2016 Apr;11(4):e0153692. Available from: http://journals.plos.org/plosone/article?id=10.1371/journal.pone.0153692. doi:10.1371/journal.pone.0153692.

[17] Leenders KL. PET: blood flow and oxygen consumption in brain tumors. J Neurooncol. 1994;22(3):269–273. doi:10.1007/bf01052932.

5

S1 Figure

Tissue PO2 distributions at constant vascular blood oxygenation

For some applications, such as models of tumor growth, it might be sufficient to implement a simplified model of oxygenation where the intravascular PO2 is a constant input parameter to the model. Results obtained from such a model are presented in the following. To this end we modified our present model, omitting the propagation of oxygen losses through the vascular network, and instead setting the oxygen partial pressure P to a constant. A map of the resulting oxygen distribution is shown here in Fig. A, where we set $P = 39\ mmHg$, equal to the mean intravascular PO2 taken over initial ($t = 0$) networks of the simulated cohort as it is obtained from the full model. An obvious qualitative difference is the absence of long ranged P_t variations in normal tissue. Instead, fine grained fluctuations in-between neighboring vessels are much more apparent. As expected, the P_t level along the surviving tumor vessels is nearly constant so that the P_t distribution can approximately be described by a function of the distance to the closest vessel alone. The neglect of varying intravascular PO2, leads to overestimation of P_t in the peripheral region (cf. Fig. 5 C). Naturally, this simplified model implies constant tissue oxygen saturation Y, and thus does not allow to analyze experimental data on blood oxygen saturation in normal and tumorous tissue.
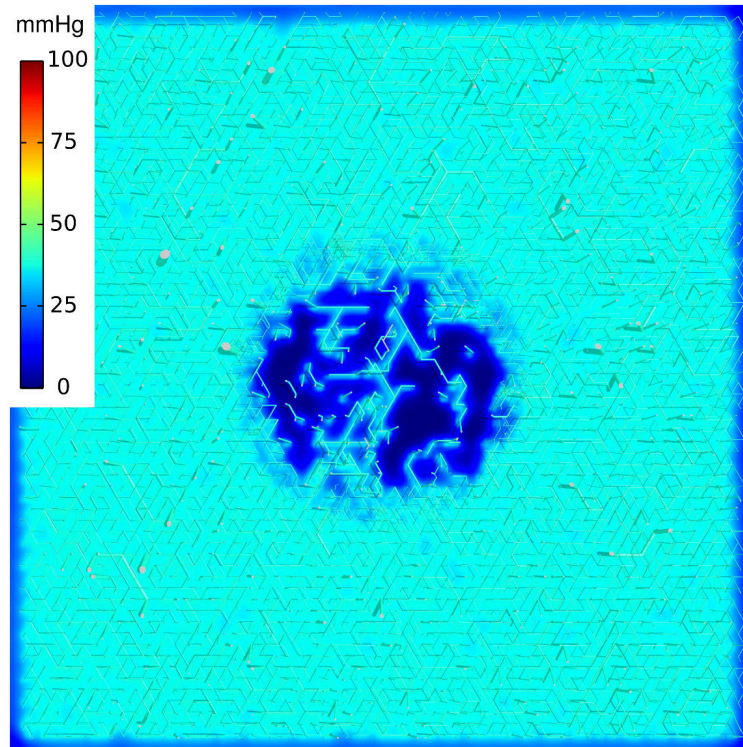
Figure A. Tissue oxygen distribution at constant vascular PO2: This figure shows a visualization of the network depicted in Fig 5 C,D but with blood PO2 held constant.

1

S2 Figure

Base (M_0 = 14.8 µl O2 / ml /min)
(MRO_2 = 12.5 µl O2 / ml /min)
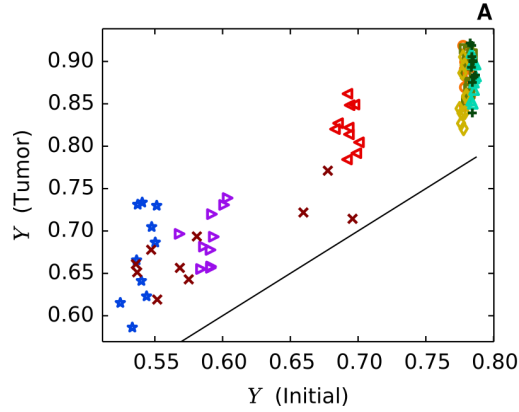
Base (M_0 = 24.6 µl O2 / ml /min)
(MRO_2 = 18.4 µl O2 / ml /min)
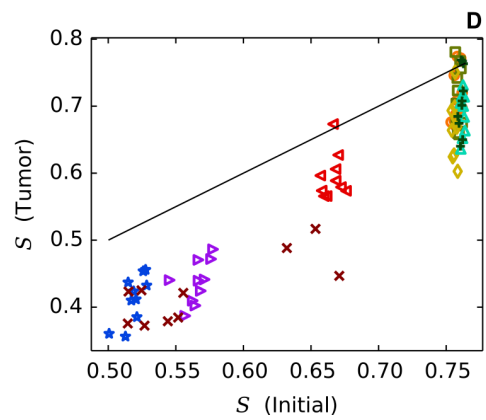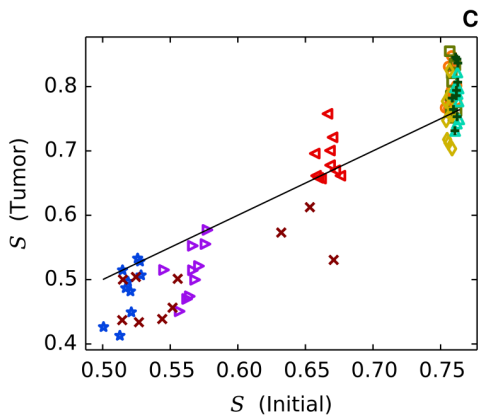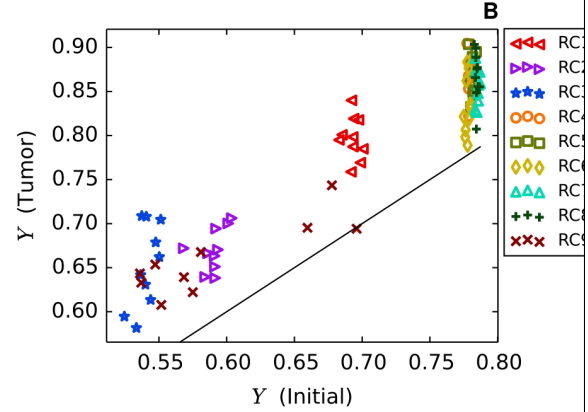
Figure A. Correlations of tissue blood oxygenation Y and length weighted blood oxygen saturation S for two assumed Michaelis-Menten metabolic rates of oxygen consumption M_0 (case BASE): Tissue blood oxygen saturation of tumors versus host tissue (A) and length-weighted blood oxygen saturation S of tumors versus host tissue (C) at $M_0 = 14.8\,\mu l\ O_2/ml/min$ (case BASE); right column: tissue blood oxygen saturation of tumors versus host tissue (B) and length-weighted blood oxygen saturation S of tumors versus host tissue (D) at elevated $M_0 = 24.6\,\mu l\ O_2/ml/min$; the color code to identify root node geometry is the same as in Fig 9.

1

3.2 Tumorcode - A framework to simulate vascularized tumors

Reprinted with permission from Springer Nature: The European Physical Journal E - Soft Matter Tumorcode by Thierry Fredrich, Michael Welter and Heiko Rieger copyright 2018 (see appendix G).

3.2.1 Main Manuscript

**THE EUROPEAN
PHYSICAL JOURNAL E**

Tips and Tricks

Tumorcode⋆

A framework to simulate vascularized tumors

Thierry Fredrich[1,a], Michael Welter[2], and Heiko Rieger[1,b]

[1] Theoretical Physics and Center for Biophysics (ZBP), Saarland University, Saarbrücken, Germany
[2] TruPhysics GmbH, Nobelstraße 15, 70569 Stuttgart, Germany

Abstract. During the past years our group published several articles using computer simulations to address the complex interaction of tumors and the vasculature as underlying transport network. Advances in imaging and lab techniques pushed *in vitro* research of tumor spheroids forward and animal models as well as clinical studies provided more insights to single processes taking part in tumor growth, however, an overall picture is still missing. Computer simulations are a non-invasive option to cumulate current knowledge and form a quasi *in vivo* system. In our software, several known models were assembled into a multi-scale approach which allows to study length scales relevant for clinical applications. We release our code to the public domain, together with a detailed description of the implementation and several examples, with the hope of usage and futher development by the community. A justification for the included algorithms and the biological models was obtained in previous publications, here we summarize the technical aspects following the workflow of a typical simulation procedure.

1 Introduction

Vascular networks play an important role in therapy and progression of cancer. In particular their formation and modifications are a special feature of most malignant tumors [1]. In the case of solid tumors, the growth of cancer cells is facilitated by the diffusion of nutrients within the vicinity of the cells. Growing beyond the average diffusion length of nutrients, tumors adopt new strategies to acquire nutrients. By transforming the present blood vessels, the tumor exploits them for his own purposes. The full complexity of this process is not yet understood.

Since the vasculature transports drugs to cancer cells, this transformation is certainly of interest for chemotherapy, and also radio therapy is known to be dependent on the oxygen level inside the tissue which is again dependent on the vessel morphology and vessel wall properties. The complex dependence of solute transport or solute distribution and spatial arrangement of the blood vessels is therefore of great importance in every cancer therapy.

Obtaining experimental or clinical data of sufficiently high resolution to reconstruct vascular networks is by itself a hard task [2]. To overcome the lack of data, *in silico* modeling of vasculature is done by various authors. In [3]

an off-lattice, agent-based model is used to successfully construct vascular structures of around 1 mm in size. Others also focus on the extra cellular matrix [4], but most studies focusing on structural aspects neglect blood transport inside the vessels which is essential for clinical applications. Well-established models consider the blood flow but are restricted to two dimensions [5] and only a few are done in 3D [6]. Apart from blood vessel network construction, the growth of tumors is of key interest.

The implementation strategies for tumor growth fall into two categories. First: discrete, particle-based approaches where each cancerous cell is modeled individually [7]. Naturally this takes considerable computational efforts providing greater details on the cell level. Second: models where the tumor is described by continuous equations, reaching dimensions relevant for diagnostics [8]. Nevertheless, it is mostly neglected that tumors in patients or animal models grow within well-vascularized environments which means the original or initial network is not adequately represented.

Another problem in the field is that the code is maintained and used by corresponding groups only, rather than sharing implementations which would simply save time. Repositories for open source code are well known in computer science and started to become useful in life science as well [9, 10].

To create blood vessel networks, we use a lattice-based attempt which discretizes the angular freedom and enables us to explore large scales. To the best of our knowledge there is no other software constructing synthetic arterio-

---

venous blood vessel networks on macroscopic tissue volumes in 3 dimension matching topological, morphological and hydrodynamic properties observed in real samples. Our multi-scale approach describes tumor growth by partial differential equations and thus it is possible to simulate system sizes of the order of centimeters.

Subsequently, the interpretation of clinical studies, animal models and testing of hypotheses on biological processes is feasible. Our approach allows us to study topological and functional aspects at the same time which is relevant for therapeutics.

Since the understanding of malignant tumors is of great interest in the life science community and *in silico* experiments are an extension of traditional biological techniques, we make our code, together with a detailed user manual, available to the public.

2 Design and implementation

Like modern implementations we reassemble two most distinct aspects. On the one hand, we use *python* together with the *scipy* packages for an easy and straightforward scripting of scientific problems. On the other hand, computationally expensive tasks are delegated to a core written in *C++* for performance reasons. Following up, a pythonic interface to this core has been created with the help of *Boost.Python*. We decided to use the "*hdf5*"-file format [11] to store data since it is highly scaleable and supported by both programming languages used.

2.1 Computational core

Standard *C++* coding is used where the comments follow the *doxygen* notation enabling the user to retrieve information about dependences and inheritance within the object-oriented kernel. Instructions on how to create the documentation can be found in the subfolder "*doc*".

Examples for demanding main applications are: 1) calculating the hydro- and hemodynamics and 2) solving partial differential equations. Both problems reduce to solving systems of sparse linear equations which we do by the *Trilinos* package [12].

2.1.1 Hydro- and hemodynamics

Before determining hydro- and hemodynamics of the network, the topology itself is created by the vesselgenerator (see folder "*src/common/vesselgen*"). The idea follows a 3-dimensional generalization of the algorithm presented in [13]. An example output can be found in fig. 1 and a complete description of the algorithm is provided in [2], sect. 2.1. We summarize the basic steps as follows: First, arterial and venous root nodes are placed on a lattice and blood pressure or blood flow rate is assigned. The phenomenological formula, eq. (3) in `https://doi.org/10.1371/journal.pone.0161267.s001`, is well suited for this task. Next, segments are appended at random until arterial and venous trees meet. Fixing the radii of the capillaries, Murray's law allows us
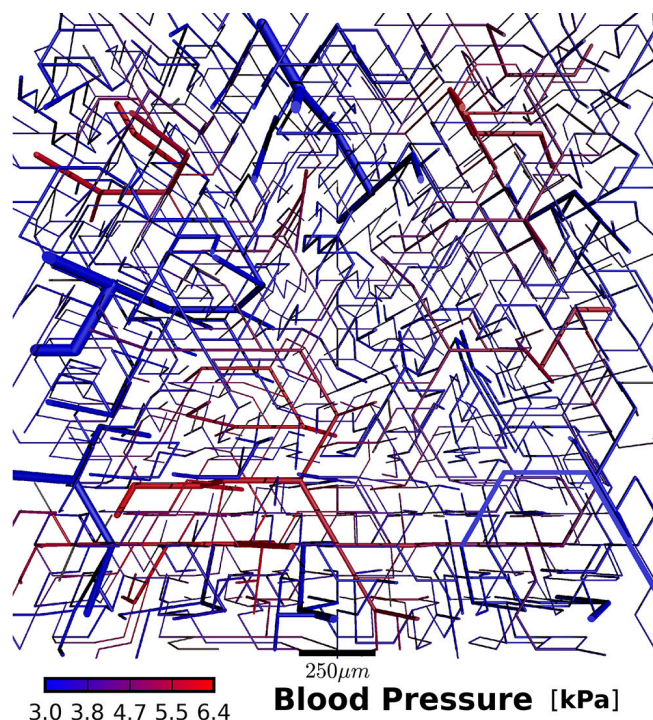
Fig. 1. Rendering of blood vessel network. The rendering of the blood vessel network created in `suppl-file4` is shown. Instructions on how to obtain such images from the software are explained in `suppl-file8`. Blood pressure is color-coded in kPa and a scale bar of $250\,\mu$m is present. A slice throughout the whole 3D cube is displayed in the figure.

to determine the radii of all mother vessels up to the root node level. Once the radii are known, we assume mass conservation at each vertex to get a matrix equation analogous to a Kirchhoff circuit in electrodynamics. Solving this sparse matrix equation provides blood pressure values and blood flow rates for every vessel. Subsequently, the formula for laminar flow allows to calculate the shear force acting on the wall. In a last step, the total shear force is optimized in a Monte Carlo manner which requires to solve the sparse matrix equation frequently. Capillaries are deleted and inserted as long as the total shear force is minimized and the spatial distribution of capillaries is maximized. At the end of the construction step we take the Fåhræus-Lindqvist and phase separation effect into account.

2.1.2 Tumor growth

The bulk tissue tumor model is based on a framework developed in [8], where the tissue is described as a mixture of various components. Our implementation includes normal, tumor and necrotic phases. The levelset-method is used to distinguish the different phases and defines the interface between them. Assuming incompressibility, one can describe the composition in terms of volume fractions which leads to a system of partial differential equations of diffusion-convection-reaction type for each phase. Introducing a regular cubic lattice for bulk tissue allows
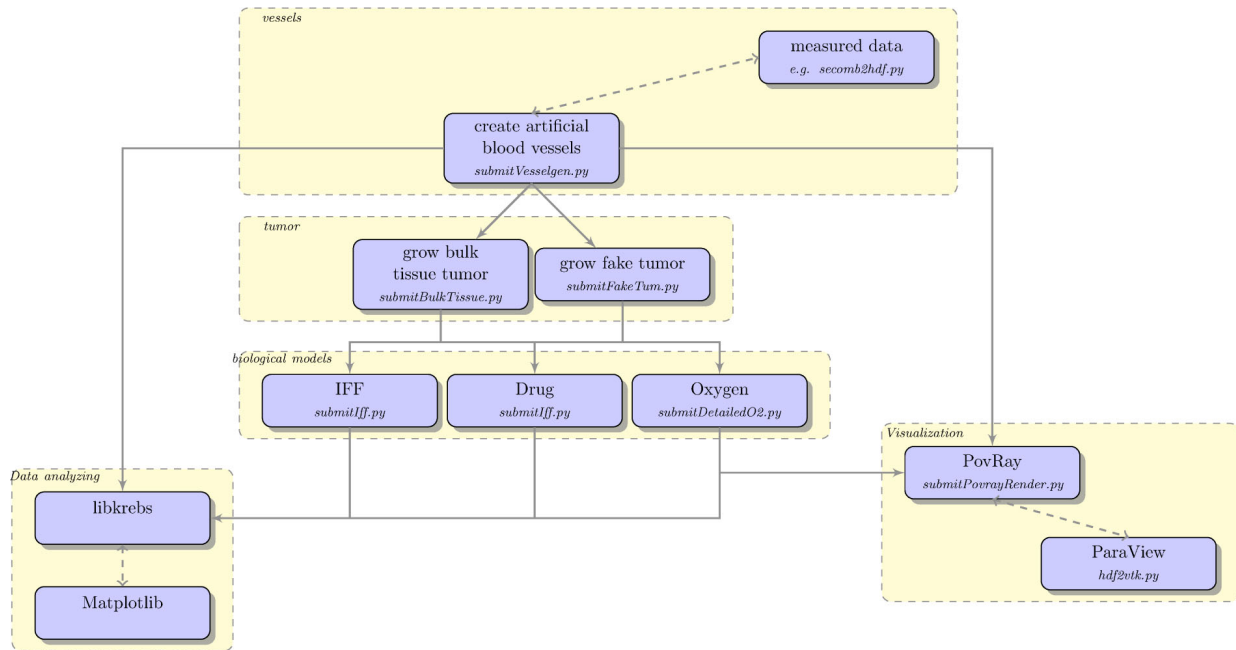
Fig. 2. Workflow of *tumorcode*. Dotted lines indicate that connected modules can be interchanged. The straight arrows must be followed in the direction indicated by the arrow head.

to solve these equations by Finite Difference techniques. Consequently, the numerical resolution of the *tumorcode* is governed by the lattice constant chosen. The number of grid points and vessels is limited by the provided hardware memory. Note that the bulk tissue and vascular network coexist in the same space, however, on different lattices. To fully utilize the modern computing equipment we parallelized our code with the shared memory API of OpenMP. More details about this methodology could be found in the well-written article [14].

For explorative studies, a fake tumor calculation which neglects the full dynamics of the cells and represents a tumor as spherically expanding mass of cells at a constant speed is implemented. Still the remodeling of the vasculature via vessel cooption, regression, and growth takes place.

2.1.3 Finite elements method

In [15] we showed that the equation for the vascular oxygen distribution together with the diffusion equation for the tissue form a complicated nonlinear system of equations with the partial pressure values of oxygen as unknowns. For the longitudinal transport a bisection search is used to gather the partial oxygen pressure values within each vessel. Constructing consistent expressions for the transvascular exchange of oxygen across the vessel lumen was a challenging task, but enabled us to use the exchange as source or sink for the diffusion equation of the tissue oxygen field. Standard Galerkin methods were used to translate the task of solving the diffusion equation into solving sparse linear equations. To this end, the algebraic multigrid methods implemented in *Trilinos* were appropriate. Alternating the solver for vascular oxygen transport and the solver for the partial oxygen pressure of the tissue results in a stable self-consistent equilibrium oxygen distribution.

2.2 Python API

After successful installation, the main tools can be found in the "*bin*" folder. Note that the Input Interface is written in *python* and that necessary parameters are also stored as python dictionaries (see folder "*py/krebsjobs/parameters*").

tumorcode is ready to use on computing clusters equipped with a queuing system. To remember the fact that the computation will be submitted to a queuing system, the name of the simulation programs start with *submit*. Currently we support "*PBS (Portable Batch System)*" and "*Slurm Workload Manager*". Job details such as expected runtime and allocated memory could be provided as optional command line arguments. If no supported queuing system is present or the flag (*–q-local*) is invoked, the computation runs on the local machine. Possible command line arguments and their structure are illustrated to the user by running the main programs with the help flag (*-h*). Each submit scripts expect the user to supply at least the name of a parameter set as command line argument.

How the single calculations are invoked and executed is presented in the supplementary material (`suppl-file4`–`suppl-file8`).

3 Workflow

The following subsections track a typical workflow corresponding to the yellow frames in fig. 2, where we visualize the procedure.
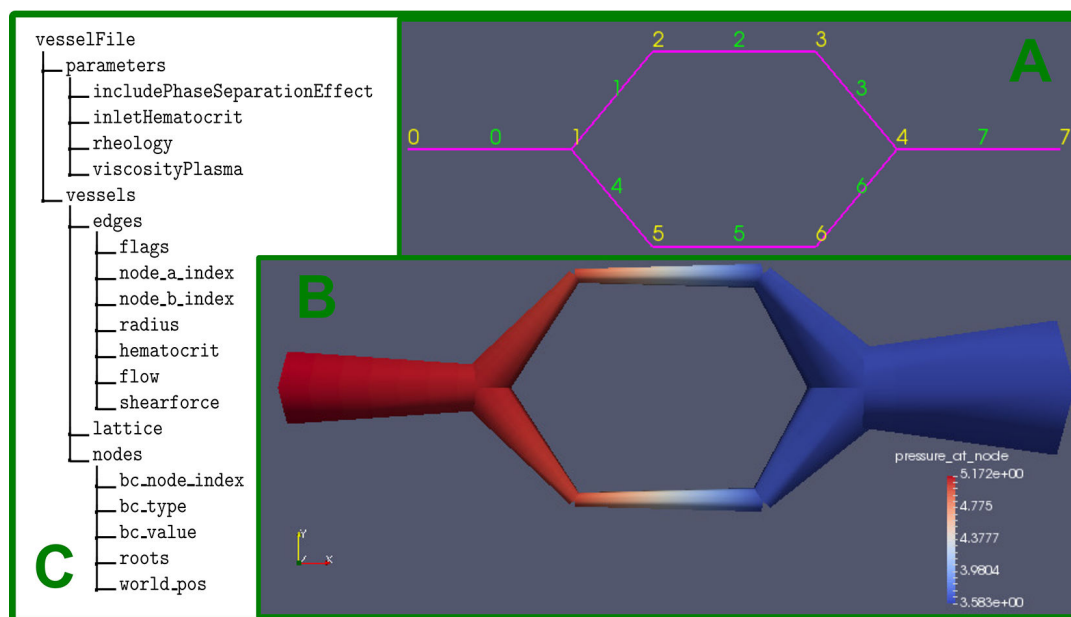
Fig. 3. Illustration of vessel data structure. This minimal example contains 3 arteries, 3 veins and 2 capillaries. Inset A: the topological structure given by labels of the node points in yellow and the label of the edges in green. Inset B: morphology calculated by tumorcode, note the size radii of the vessels and the color-code due to the pressure given in kPa. Inset C: structure of the *"hdf5"*-file containing the vessel structure.

3.1 Vessels

In general, one starts by creating synthetic blood vessels which serve as host and transport network (see 2.1.1). Another possibility is to provide measured input data. A transformation from the published data in [16] to the structure used by our software is described in the file *"py/krebs/adaption/apj2hdf.py"*. To elaborate the characteristic structure of a vessel file, a minimal working example is created where 3 arteries, 3 veins and 2 capillaries form a loop. In principal, each vessel is defined as an edge linking two nodes. Details can be obtained from fig. 3 as well as from the source stored in *"py/tests/simpleVesselConfig.py"*. The hemodynamic and morphological data calculated throughout the creation process as described in sect. 2.1.1 is stored for each vessel within the "edges" directory, *e.g.*, flow, radius and hematocrit. Further, the parameters used to calculate the hemodynamics, as specified by the *"-p"* flag, are written into the sub-folder "parameters". The arrangement of root nodes accross the lattice is specified by the type (*"-t"*) flag. The choice between 0 and 8 corresponds to one of the distribution shown in `https://doi.org/10.1371/journal.pone.0161267.g003`. The flag (*"–twoD"*) is of particular interest here. If selected, the creation process is restricted to a plane. All other programs are in full 3D.

3.2 Tumor

Once vessels are constructed or read from experimental data, the workflow continues to the tumor stage where
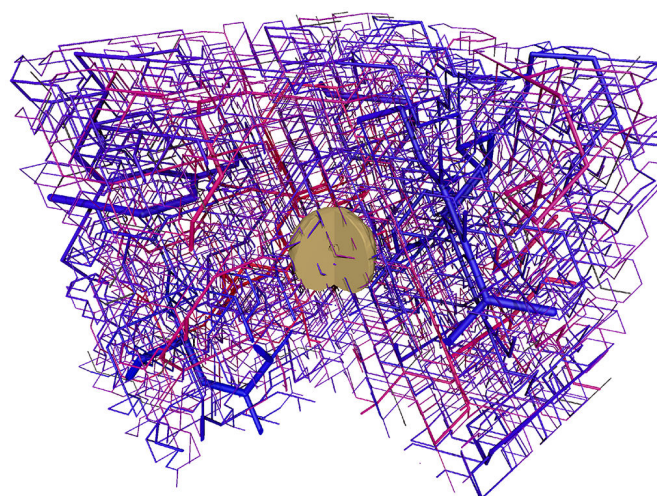
Fig. 4. Rendering of a bulk tissue tumor simulation. `suppl-file5` explains how to obtain this image. The camera position "pie" is chosen in order to see the tumor inside the cube. The vessel network is the same as shown in fig. 1.

the simulation of either a fake tumor or a bulk tissue tumor can be started. *"submitBulkTissue"* runs simulations using the algorithm from the core discussed in sect. 2.1.2 and *"submitFakeTum"* includes the discussed simplifications. Both types of tumor simulation need a parameter set and a *"hdf5"*-file containing proper vessels as command line input. When running, these simulations output their current configuration at time intervals as specified by the parameters. The groups in the output file are named out0000, out0001, etc. Figure 4 shows a snapshot of the simulation carried out in the `suppl-file5`.

3.3 Biological models

After the tumor stage, a "*hdf5*"-file containing time snapshots of either tumor simulation should be present. To invoke one of the biological models, the time point needs to be passed as additional argument. Therefore one needs to provide the name of a parameter set, the tumor file and the name of the time point. Note that time points are labeled consecutively by out0000, out0001 etc.

"*submitIff*" allows you to calculate distributions of the interstitial fluid flow and corresponding advection maps of drugs. Valid parameter sets can be found in "*/krebsjobs/parameters/parameterSetsIff.py*". The subdictionary "iff" adjusts the interstitial fluid while the "ift" sub-dictionary adjusts the treatment of the tumor by the chemotherapy. Currently, we provide 2 administration protocol:

– DF_INJECT_MODE_EXP decreases the drug within the bloodstream in an exponential fashion. We correlate this with the injection of a single bolus decaying in the bloodstream.
– DF_INJECT_MODE_JUMP lets the level of drug within the blood stream jump from a constant value to zero. This mimics permanent infusion of a drug.

Varying the diffusion constant of the drug and its vessel wall permeability allows to screen for different modalities (see `suppl-file6` and refererences therein).

Secondly, an elaborated model of blood and tissue oxygenation was developed [15]. Similarly to "*submitIff*", "*submitDetailedO2*" needs a parameter set, a tumor simulation and a specified time point as input.

3.4 Analyzing and visualization

Finally, we offer a large number of scripts that we use to analyze raw simulation data.

Like the simulations, our analysis programs are hybrids between *C++* and *python*. Since the datasets can become quite large in filesize and take a long time to be processed, most evaluation programs are equipped with datacache, *i.e.*, the results of certain costly computations are saved to disk and loaded from there next time the execution is called with the same arguments. This facilitates the iterative development, at least to some degree, without recomputation.

In order to use state-of-the-art visualization techniques, we export datasets created with *tumorcode* in 2 different data formats as demonstrated in `suppl-file8`. *ParaView* allows an elaborated inspection of the vessel network structure. It offers interactive viewing and basic statistics on medium size systems, depending on your machines RAM. To render even the largest systems, we follow the ray trace approach of *POV-Ray*. Similar to *ParaView*, we offer a wrapper which converts vessel, tumor, oxygen and drug datasets to *POV-Ray* scene files, and run *POV-Ray* automatically in succession. Images of this kind are depicted in our latest publications [15,17].

4 Applications

As an illustration of the capabilities of *tumorcode*, we designed the supplemental examples (`suppl-file4`, `suppl-file5`, `suppl-file6`, `suppl-file7` and `suppl-file8`) within the realm of the two studies already published. However doing the same, we scaled the simulation in the examples to be smaller and quickly reproducible. On a standard desktop PC (Intel i7, 2×8 GB RAM) they are executed within minutes.

For details on the exact setup we refer to [15,17].

4.1 Blood vessels and tumor morphology

In silico modeling features the opportunity to measure structural and dynamical quantities at the same time. Simple averages of, *e.g.*, flow, radii and vessel volume are implemented straightforward in our software. Additionally, we can average data over spherical surfaces to mimic various experimental measurements. A profound inspection of a bulk tissue tumor simulation on a large scale could be found in [17], fig. 3. There the graphs display microvessel density (MVD), vessel radius, cell velocity, oxygen, wall thickness and wall shear stress where the time course of tumor growth is visualized by different colors. The level set method allows to localize the distance of the tumor-tissue interface which is used as ordinate for the cited plots. Within that framework it is easy to define the "inside" and "outside" of a tumor and focus on the differences.

Distinct experimental techniques such as MRI, micro-CT or xenografts are available to access morphological data of tumor tissue as well. But comparable data obtained from animal models usually requires the immolation of an animal per time point. Therefore such studies are heavily biases by inter-subject variation. Recently, we used this framework to create networks matching the morphology of a swine animal model. In `suppl-file4`, we create a dataset of this kind and present the analysis.

4.2 IFF and drug distribution

To measure IFF and the related interstitial fluid pressure (IFP) *in vivo* is an especially hard task even with modern measurement methods. Regarding the medical aspects, special interest is drawn to the vasculature as source for therapeutics and nutrients. A solid understanding of IFF and IFP is also crucial for fighting cancer since an elevated IFP is believed to pose a barrier to drug delivery and oxygenation. The resulting hypoxia leads to inefficacy of drugs and radiation. For this type of simulation we consider the IFP as driving force of the flow, *i.e.* via Darcy's law. Differences between IFP, blood pressure and the fluid pressure within lymphatics drive transvascular fluxes according to Starling's equation. We solve the stationary case leading to a Poisson equation for the pressure.

Ensuing the determination of IFF, solute transport into tissue can be simulated. If specified by parameters (see `suppl-file6`), the mass balance equation for solutes is integrated numerically based on the calculated flow,
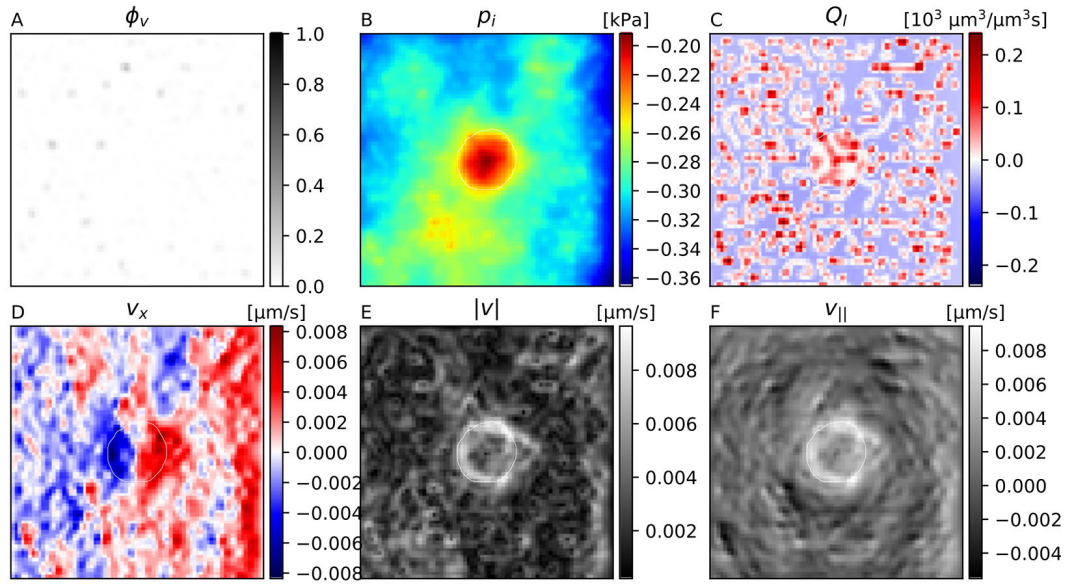
Fig. 5. Snapshots of interstitial fluid flow quantities. (A) Vessel volume fraction, (B) IFP, (C) fluid source term, (D) x-component of the IF velocity, (E) magnitude of the IF velocity, (F) projection of IF velocity in outward direction. The plots were generated from 2d slices through the center of the simulation result obtained in `suppl-file6`. The contour line indicates the boundary of the viable tumor mass. The internal regions consist of necrotic tissue, while the outer area is normal host tissue.
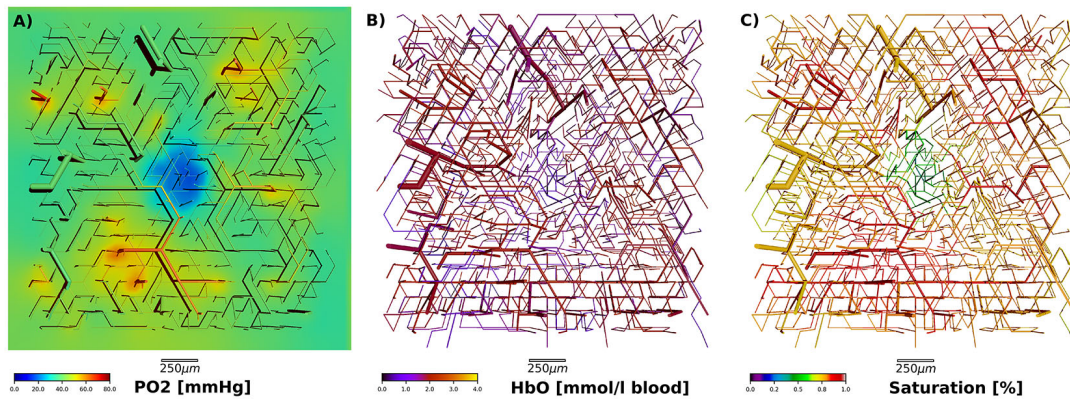
Fig. 6. Overview of detailed oxygen simulation. (A) Partial oxygen pressure within vessels and surrounding tissue. Note the hypoxic core in the center where the tumor grows. (B) Amount of oxygenated hemoglobin within the vessels. For illustration purposes the tissue is not depicted. (C) Blood oxygen saturation within the vessels. Note that all three figures show the same blood vessel network. See `suppl-file7` for construction details.

diffusion coefficients, rate constants, etc. For an exemplary overview of such quantities, see fig. 5. Quantitatively these agree well with the results obtained by simulating larger systems where the administration of doxorubicin was included (see [17], figs. 4, 7). Notably, our results obtained by these simulations suggest that despite of an IFP plateau within the tumor, IFF does not cease and still allows for substantial convective transport which was in contradiction to the view at that time. Furthermore we varied numerous parameters and the administration protocol emulating clinical studies which would be extensive and lengthy in practice.

4.3 Detailed oxygen distribution

We augmented the model of oxygen transport such that intravascular variation of the oxygen content along vessel center lines is taken into account. Moreover a varying hematocrit based on the (Red Blood Cell) phase separation effect (see [18] and sections "Hydro- and hemodynamics", "Finite elements method") has been implemented. Since most oxygen is transported through the body while bound to the RBCs, the hematocrit distribution is the physical key to the oxygen transport. Together with the unbound oxygen within the blood, we implemented a coarse-grained model of oxygen concentration along the direction of blood flow which causes tissue oxygenation. An example of this type of simulations is presented in `suppl-file7`. Here we show the visualization of the simulation results as fig. 6.

The focus of the published study was to simulate tissue total hemoglobin concentrations cHb and tissue blood oxygen saturation Y of tumors and host tissue and compare the results with clinical data on breast tumors and

surrounding normal breast tissue obtained from a cohort of 87 breast cancer patients using optical mammograph. Following the workflow of *tumorcode* we began by constructing 90 distinct host vasculatures followed by the growth of fake tumors. Using the detailed oxygen simulation, we showed that the redirection of the hematocrit during the tumor growth is accompanied by changes in flow rates and identified this as key element of the modulation in blood oxygen saturation. In contrast, the fact that vascular dilatation leads to an elevated tumor oxygen saturation is not intuitive but confirmed by our simulations. Strikingly, we found evidence that different types of initial vascular configurations are correlated to the variance of tissue hemoglobin concentration, tissue blood oxygen saturation and perfusion which raises biological insight.

5 Conclusion

This manuscript describes the software used to draw conclusions about elevated interstitial fluid pressure, drug and oxygen distribution in previous publications. All simulations are based on constructing synthetic arterio-venous blood vessel networks on macroscopic tissue volumes matching topological, morphological and hydrodynamic properties observed in real samples. To the best of our knowledge there is no comparable software for this task.

Development, implementation and debugging of software is tedious, and distracts from biological or medical aspects. By varying the parameters in our simulation framework, we allow everybody to tackle its own questions within the realm of this software. Further, we allow everybody to reproduce the experiments we carried out so far, as it is required by good scientific practice. We share the source-code under open source license at `https://github.com/thierry3000/tumorcode`.

Despite the code is platform independent, successful compilation and usage as described in this article is restricted to Unix-based systems at the moment. If required, support for different operating systems is feasible. Likewise, implementing a graphical user interface as extension of our module-based code is straightforward and could serve other researchers in life science with less background in computer science. Following the direction towards a common code base in the field, we hope this article and mainly the examples in the supplementary material help to overcome technical struggles. In the future, merging tumorcode with other codes may be an option.

Currently, the drug as well as the detailed oxygen distribution is calculated at time snapshots of the tumor growth process only. To engage pharmacodynamics and improve predictions, correlating the time points could be considered in the future. Also additional features relevant for clinics like, pH, ATP consumption or formation of metastasis could be included. The questions in the broad field of cancer research are immense.

Author contribution statement

HR proposed the scientific problem and supervised the research project. MW implemented the kernel modules. TF wrote and revised the manuscript, provided the supplementary material, maintains the source code.

Supplementary material

`suppl-file1.zip`: *Data created in the examples*. We add an archive of all data produced in `suppl-file4`–`suppl-file8`.

`suppl-file2.mov`: *Blood vessel network creation process*. To illustrate the process of network creation, we show an example in fast motion. The resulting dataset is quite big and therefore all intermediate stages are omitted. The complete source used to construct the data for the movie can be found in the file *povrayRenderVesselgeneratorDbg.py* for references.

`suppl-file3.avi`: *3D model of tumor-induced angiogenesis*. To illustrate the tumor model we show a video of the dynamical growth process.

`suppl-file4.pdf`: *Blood vessel network creation*. In this supplementary example we create an artificial blood vessel network using *submitVesselgeneration* and show some measurement tools. The algorithmically description is documented in [2].

`suppl-file5.pdf`: *Tumor growth*. In this supplementary example we grow tumors on the previous created artificial blood vessel networks and show how to invoke some quantifications.

`suppl-file6.pdf`: *Interstitial fluid flow and drug transport*. Providing a tumor simulation, we describe here how interstitial fluid pressure and drug distributions could be calculated and visualized. These simulation where used for the publication [17].

`suppl-file7.pdf`: *Detailed oxygen distribution*. Providing a tumor simulation, we calculate the detailed oxygen distribution as described in [15] and run the scripts in order to analyze those oxygen distribution.

`suppl-file8.pdf`: *Visualization tools*. Using the data created in previous examples, we show how the simulation results can be visualized using your tools facilitated by Povray and ParaView.

References

1. Peter Carmeliet, Rakesh K. Jain, Nature **407**, 249 (2000).
2. Heiko Rieger, Thierry Fredrich, Michael Welter, Eur. Phys. J. Plus **131**, 31 (2016).
3. Holger Perfahl, Barry D. Hughes, Toms Alarcn, Philip K. Maini, Mark C. Lloyd, Matthias Reuss, Helen M. Byrne, J. Theor. Biol. **414**, 254 (2017).
4. Roeland M.H. Merks, Erica D. Perryn, Abbas Shirinifard, James A. Glazier, PLoS Comput. Biol. **4**, e1000163 (2008).

5. A.R.A. Anderson, M.A.J. Chaplain, Bull. Math. Biol. **60**, 857 (1998).

6. Paul Macklin, Steven McDougall, Alexander R.A. Anderson, Mark A.J. Chaplain, Vittorio Cristini, John Lowengrub, J. Math. Biol. **58**, 765 (2009).

7. Edoardo Milotti, Roberto Chignola, PLoS ONE **5**, e13942 (2010).

8. Luigi Preziosi, Andrea Tosin, J. Math. Biol. **58**, 625 (2008).

9. James Grogan, Anthony J. Connor, Bostjan Markelc, Ruth J. Muschel, Philip K. Maini, Helen M. Byrne, Joe M. Pitt-Francis, *Microvessel Chaste: An Open Library for Spatial Modelling of Vascularized Tissues*, bioRxiv 105692, `https://doi.org/10.1101/105692` (2017).

10. Abbas Shirinifard, J. Scott Gens, Benjamin L. Zaitlen, Nikodem J. Popawski, Maciej Swat, James A. Glazier, PLoS ONE **4**, e7190 (2009).

11. The HDF Group, Hierarchical Data Format, version 5, 1997.

12. Michael Heroux, Roscoe Bartlett, Vicki Howle Robert Hoekstra, Jonathan Hu, Tamara Kolda, Richard Lehoucq, Kevin Long, Roger Pawlowski, Eric Phipps, Andrew Salinger, Heidi Thornquist, Ray Tuminaro, James Willenbring, Alan Williams, *An Overview of Trilinos*, Technical Report SAND2003-2927 (Sandia National Laboratories, 2003).

13. Ralf Gödde, Haymo Kurz, Dev. Dyn. **220**, 387 (2001).

14. Cosmina S. Hogea, Bruce T. Murray, James A. Sethian, J. Math. Biol. **53**, 86 (2006).

15. Michael Welter, Thierry Fredrich, Herbert Rinneberg, Heiko Rieger, PLoS ONE **11**, e0161267 (2016).

16. A.R. Pries, B. Reglin, T.W. Secomb, Am. J. Physiol. - Heart Circul. Physiol. **284**, H2204 (2003).

17. Michael Welter, Heiko Rieger, PLoS ONE **8**, e70395 (2013).

18. A.R. Pries, T.W. Secomb, P. Gaehtgens, J.F. Gross, Circul. Res. **67**, 826 (1990).

3.2.2 Supplemental Material

3.2.2.1 Supplemental 1-3

The supplemental material 1-3 is in electronic from only.
Supplemental 1 is a snapshot of your repository at time of publication
(available for download at: https://static-content.springer.com/esm/
art%3A10.1140%2Fepje%2Fi2018-11659-x/MediaObjects/10189_2018_11659_MOESM1_ESM.zip)
Supplemental 2 is a video illustrating the vessel network construction algorithm.
(available for download at: https://static-content.springer.com/esm/
art%3A10.1140%2Fepje%2Fi2018-11659-x/MediaObjects/10189_2018_11659_MOESM2_ESM.mov)
Supplemental 3 is a video illustrating a bulk tissue tumor simulation including a necrotic core.
(available for download at: https://static-content.springer.com/esm/
art%3A10.1140%2Fepje%2Fi2018-11659-x/MediaObjects/10189_2018_11659_MOESM3_ESM.avi) Supplemental 4-8 are in written form and reprinted in the following:

3.2.2.2 Supplemental 4: Vessel Network Generation

In this supplementary example we create an artificial blood vessel network using *submitVesselgeneration* and show some measurement tools. The algorithmically description is documented in [1].

Usage

Entering

```
submitVesselgeneration −h
```

in your console should print possible options as seen in Listing 1.

Listing 1: Console options for *submitVesselgeneration*

```
usage: submitVesselgeneration [−h] [−t TYPE [TYPE ...]] [−p VESSELPARAMSET]
                              [−w WIDTH_CUBE] [−−twoD] [−i ITER_H]
                              [−e ENSEMBLE_SIZE]

Compute an artificial blood vessel network.

optional arguments:
  −h, −−help            show this help message and exit
  −t TYPE [TYPE ...], −−type TYPE [TYPE ...]
                        Type of root node configurations, range from 0 to 8
  −p VESSELPARAMSET, −−VesselParamSet VESSELPARAMSET
                        specify Parameterset for creation, possible configs
                        are found in /krebsjobs/parameters/vesselGenParams.py
  −w WIDTH_CUBE, −−width_cube WIDTH_CUBE
                        Size of vesselcube you want to create
  −−twoD                Creates only 2D network, default is 3D
  −i ITER_H, −−iter_h ITER_H
                        Number of hieracial iterations
  −e ENSEMBLE_SIZE, −−ensemble_size ENSEMBLE_SIZE
                        Number of realizations
```

We will create systems of type 8 which means that the inlets (arterious roots) and the outlets (venous drains) are randomly distributed around a cube with length $2000\mu m$. Different types are shown here. One hierarchal iteration step is applied and in total 5 different realizations are created. The default parameters used in this example are illustrated in Fig 1. The command is:

```
submitVesselgeneration −t 8 −p default −w 2000 −i 1 −e 5
```

In about 10 minutes this will create the files *vessels-default-typeI-15x19L130-sample00.h5* to *vessels-default-typeI-15x19L130-sample04.h5* which we could analyze now.

Analyzing

One of the main tools to extract information about a vessel network is

```
python2 /your/install/path/py/krebs/plotVessels.py −h
```

This call lists the following options

```
usage: plotVessels.py [−h] [−O] [−T] [−a] [−s]
                      [vesselFileNames [vesselFileNames ...]] grp_pattern

Plot/ Analyze infos about vessel network.

positional arguments:
  vesselFileNames       Vessel file to calculate
  grp_pattern           Where to find the vessel group in the file

optional arguments:
  −h, −−help            show this help message and exit
  −O, −−with−o2         look at detailed o2 data
  −T, −−only_two_root   flag to change the considered types
  −a, −−with_all_types  take all types
  −s, −−singel_type
```

1

```
default (parameterset name)
├── tip_radius_arterial = 2.5
├── tip_radius_capi = 2.5
├── tip_radius_vein = 3.8
├── murray_alpha_vein = 3
├── murray_alpha_artery = 3
├── scale = 130
├── max_sprout_radius_artery = 8
├── max_sprout_radius_vein = 8
├── calcflow
    ├── viscosityPlasma = 1.2e-6
    ├── rheology = 'RheologySecomb2005'
    ├── inletHematocrit = 0.37
    ├── includePhaseSeparationEffect = True
```

Figure 1: Structure of a vessel creation parameters as stored in *vessel-GenParams.py*.

By default the group where a vessel network is stored is labeled 'vessels'. In order to analyze the bunch of created vessel networks we hand the files together with group to the plot program.

```
python2 /your/install/path/py/krebs/plotVessels.py \
vessels−default−typeI−15x19L130−sample00.h5  vessels
```

This will create a file called *vessels-default-typeI-15x19L130-sample00.pdf* where the results are stored. The instructions to visualize such a data set are could be found in an other example.

References

[1] Rieger H, Fredrich T, Welter M. Physics of the tumor vasculature: Theory and experiment. Eur Phys J Plus. 2016;131(2):31. doi:10.1140/epjp/i2016-16031-9.

2

Supplemental 5: Bulk Tumor Simulation

In this supplementary example we grow tumors on the previous created artificial blood vessel networks and show how to invoke some quantifications. In principal there are two programs starting tumor simulations, *submitBulkTissue* [1] and *submitFakeTum* [2] where the API works the same for both. The difference is that *submitBulkTissue* exploits our full tumor model also mimicking cells in contrast to *submitFakeTum* where the dynamic of the cells is just and expanding sphere with constant speed set by the parameters.

Usage

Entering

```
submitBulkTissue −h
```

or

```
submitFakeTum −h
```

in your console should print possible options as seen in Listing 1.

Listing 1: Console options for *submitBulkTissue*

```
usage: submitBulkTissue [−h] [−n]
                        tumParamSet [vesselFileNames [vesselFileNames ...]]

Compute BulkTissue tumor. Either with or without vessels

positional arguments:
  tumParamSet      Valid configuration are found in
                   /py/krebsjobs/parameters/fakeTumorParams.py
  vesselFileNames  Vessel file to calculate

optional arguments:
  −h, −−help       show this help message and exit
  −n, −−no_vessel  compute the continuum model of tumor cells, no vessels
                   needed for that
```

We chose the parameter setting *defaultconfig_bulktissue* and provide a vessel network file created in previous examples by typing:

```
submitBulkTissue defaultconfig_bulktissue \
vessels−default−typeI−15x19L130−sample00.h5
```

It takes a desktop PC about 20 minutes to execute the simulation where the file *tumBulkdefaulttypeIsample00defaultconfig_bulktissue.h5* with the structure as depicted in 1 is created which we are going to analyze in the following.

Analyzing

Oxygen

To extract so informations about the oxygen content your can use

```
python2 \
/your/install/path/py/krebs/analyzeTissueOxygen.py −h
```

we run

```
python2 \
/your/install/path/py/krebs/analyzeTissueOxygen.py \
tumBulk−default−typeI−sample00−defaultconfig_bulktissue.h5
```

1

```
tumBulk-default-typeI-sample00-defaultconfig_bulktissue.h5
  field_ld
  parameters
  out0000 ......................................timeframe of simulation
  out0001
     fieldGf ........................ growth factor conc. at timepoint
     fieldOxy ............................. oxygen conc. at timepoint
     vessel_volume_fraction
     tumor ............................................tumor data
     vessels ..........................................vessel data
        edges
        lattice
        nodes
  out0002
  out0003
  out0004
  out0005
```

Figure 1: Structure of bulk tissue tumor file as stored in *tumBulk-default-typeI-sample00-defaultconfig_bulktissue.h5*. Exemplary a single time frame is zoomed in.

Fractal dimension

The fractal dimension are calculated by

```
python2 \
/your/install/path/py/krebs/fractaldim.py −h
```

This program comes with 2 modes. First, without any arguments we calculate the fractal dimensions by box counting. This could also be done on cluster computers. We run

```
python2 \
/your/install/path/py/krebs/fractaldim.py \
tumBulk−default−typeI−sample00−defaultconfig_bulktissue.h5 \
out0005
```

After calculating you created a file called *fractaldim_tumBulk-default-typeI-sample00-defaultconfig_bulktissue.h5*. Using the plot flag, you can now plot your data by

```
python2 \
/your/install/path/py/krebs/fractaldim.py −−plot \
fractaldim_tumBulk−default−typeI−sample00−defaultconfig_bulktissue.h5 \
out0005
```

Morphological data

Some morphological data is sampled by

```
python2 \
/your/install/path/py/krebs/analyzeVesselsBulkTumor.py −h
```

2

References

[1] Welter M, Rieger H. Interstitial Fluid Flow and Drug Delivery in Vascularized Tumors: A Computational Model. PLoS ONE. 2013;8(8):e70395. doi:10.1371/journal.pone.0070395.

[2] Welter M, Fredrich T, Rinneberg H, Rieger H. Computational Model for Tumor Oxygenation Applied to Clinical Data on Breast Tumor Hemoglobin Concentrations Suggests Vascular Dilatation and Compression. PLOS ONE. 2016;11(8):e0161267. doi:10.1371/journal.pone.0161267.

3

Supplemental 6: Interstitial Fluid Flow Simulation

```
iff_default (parameterset name)
 │__ field_ld
 │__ iff ...........results of the IFF simulation
 │__ measurements
 │__ out0000
 │__ out0001 ......timeframe of drug-simulation
 │__ out0002
 │__ out0003
 │__ out0004
 │__ parameters
      │__ iff ....................related to IFF
      │__ ift ...................related to drug
```

Figure 1: Structure of IFF simulation file as result of *submitIff*.

Providing a tumor simulation, we describe here how interstitial fluid pressure and drug distributions could be calculated and visualized. These simulation where used for the publication [1].

Usage

Entering

```
submitiff −h
```

in your console should print possible options as seen in Listing 1.

Listing 1: Console options for *submitIff*

```
usage: submitIff [−h]
                 Iffparams [tumorFileNames [tumorFileNames ...]] grp_pattern

Compute IFF distributions and drugs analyze them.

positional arguments:
  Iffparams       choose the parameter for the simulation, possible configs
                  are found in /krebsjobs/parameters/parameterSetsIff.py
  tumorFileNames  tumor files to calculate
  grp_pattern     Where to find the tumor. Usually this is somthing with out∗

optional arguments:
  −h, −−help      show this help message and exit
```

We will simulate IFF for bulk tumors created in previous examples (*tumBulk-default-typeI-sample00-defaultconfig_bulktissue.h5*). From the parameters we choose the 'iff_default' where the evolution of the drugs is only calculated for 0.5 hours which is doable in about 2 minutes. See the parameter 'out_times' for this.

```
submitIff iff_default \
tumBulk−default−typeI−sample00−defaultconfig_bulktissue.h5 \
out0005
```

Upon   a   successful   run   the   file *iff_default_ulk-default-typeI-sample00-defaultconfig_bulktissue.h5* with structure as depicted in Fig 1 will be created.

1

Analyzing

IFF

One of the main tools to extract information about an IFF simulation file is

```
python2 /your/install/path/py/krebs/plotIff.py −h
```

We run

```
python2 /your/install/path/py/krebs/plotIff.py \
iff_default_ulk −default −typeI−sample00−defaultconfig_bulktissue.
```

This gives a detailed analysis on the iterstitial fluid pressure and flow which was calculated. Integral plots as well as radial averages are calculated and shown in diagrams. Further a 2D histograms on the dataset is shown as image.

Drug

Quantitative informations on the evolution of drugs within the blood and the interstial volume could be drawn with the help of

```
python2 /your/install/path/py/krebs/plotDrug.py −h
```

We run

```
python2 /your/install/path/py/krebs/plotDrug.py \
iff_default_ulk −default −typeI−sample00−defaultconfig_bulktissue.
```

References

[1] Welter M, Rieger H. Interstitial Fluid Flow and Drug Delivery in Vascularized Tumors: A Computational Model. PLoS ONE. 2013;8(8):e70395. doi:10.1371/journal.pone.0070395.

2

Supplemental 7: Detailed Oxygen Simulation

```
o2_tumBulk-default (filename)
 ┣━po2
 ┃   ┣━out0005
 ┃   ┣━field_ld
 ┃   ┣━iterations
 ┃   ┣━parameters
 ┃   ┣━samples_and_fluxes
 ┃   ┣━p2field ........................... O2 tissue field
 ┃   ┣━po2vessels .......................... O2 in vessels
 ┗━recomputed_flow ............. flow computed before O2
```

Figure 1:   Structure of DetailedO2 simulation file as result of *submitDetailedO2*.

Providing a tumor simulation, we calculate the detailed oxygen distribution as described in [1] and run the scripts in order to analyze those oxygen distribution.

Usage

Entering

```
submitDetailedO2 −h
```

in your console should print possible options as seen in Listing 1.

Listing 1: Console options for *submitDetailed*

```
usage: submitDetailedO2 [−h] [−a] [−r] [−−systemsize SYSTEMSIZE]
                        o2params [vesselFileNames [vesselFileNames ...]]
                        grp_pattern

Compute po2 distributions and analyze them. In normal mode it takes arguments:
parameter set name, filenames, h5 group pattern. In analysis mode −a, it takes
arguments: filenames, h5 group pattern.

positional arguments:
  o2params                   choose the parameter for the simulation. found at
                             /py/krebsjobs/parameters/parameterSetsO2.py
  vesselFileNames            Vessel file to calculate
  grp_pattern                Where to find the vessel group in the file

optional arguments:
  −h, −−help                 show this help message and exit
  −a, −−analyze              loop through all files analyze data and make plot
  −r, −−render               launch rendering of overview images
  −−systemsize SYSTEMSIZE
                             num threads = 1 * systemsize, memory = 2 Gb *
                             systemsize (for o2 computation; analysis uses
                             different scaling (see source)
```

We will simulate the detailed oxygen distribution for bulk tumors created in previous examples (here *tumBulk-default-typeI-sample00-defaultconfig_bulktissue.h5*. From the parameters we choose the 'default_o2'.

```
submitDetailedO2 default_o2 \
tumBulk−default−typeI−sample00−defaultconfig_bulktissue.h5 \
out0005
```

Upon   a   successful   run   the   file *o2_tumBulk-default-typeI-sample00-defaultconfig_bulktissue_default_o2.h5* with structure as depicted in Fig 1 will be created.

1

Analyzing

In principal most of our evaluation scripts focus on averaging multiple runs of a single parameter set to get some statistics. However, in the scope of this example we restrict the application to a single file only due to the computational efforts.

The script which draws conclusions about perufsion, tissue oxygen saturation etc. is *plotVessels.py* together with the flag *-O* indication the calculation of the detailed oxygen quantities.

```
python2 /your/install/path/py/krebs/plotVessels.py −h
```

Running

```
python2 /your/install/path/py/krebs/plotVessels.py −O \
o2_tumBulk−default−typeI−sample00−defaultconfig_bulktissue_default_o2.h5 \
po2/out0005
```

This creates a pdf containing necessary informations.

References

[1] Welter M, Fredrich T, Rinneberg H, Rieger H. Computational Model for Tumor Oxygenation Applied to Clinical Data on Breast Tumor Hemoglobin Concentrations Suggests Vascular Dilatation and Compression. PLOS ONE. 2016;11(8):e0161267. doi:10.1371/journal.pone.0161267.

2

Supplemental 8: Visualization

Using the data created in previous examples, we show how the simulation results can be visualized using your tools facilitated by Povray and ParaView.

Povray

Entering

```
submitPovrayRender −h
```

in your console should print possible options as seen in Listing 1. There are quite some options here for adjusting the graphical representation. Note that you can also store and load these settings from the file *povrayRenderSettings.py* as it is done in your other scripts. In order to not track every graphic setting ever made, we decided not to include the file *povrayRenderSettings.py* in the repository. However we provide a template called *povrayRenderSettingsTemplate.py*.

Listing 1: Console options for *submitPovrayRender*

```
usage: submitPovrayRender [−h] [−p POVPARAMSSET] [−d DATALIST] [−f]
                          [−−filterradiushighpass FILTERRADIUSHIGHPASS]
                          [−−filterradiuslowpass FILTERRADIUSLOWPASS]
                          [−−overlay] [−−dpi DPI] [−−format FORMAT] [−c CAM]
                          [−u] [−a] [−−fontcolor FONTCOLOR]
                          [−−temp_file_dir TEMP_FILE_DIR] [−−keep_files]
                          [−−assumed_gamma ASSUMED_GAMMA]
                          [−−background BACKGROUND]
                          [−−ambient_color AMBIENT_COLOR] [−−res RES]
                          [−−num_threads NUM_THREADS] [−−out_alpha]
                          [−−cam_distance_multiplier CAM_DISTANCE_MULTIPLIER]
                          [−−colored_slice COLORED_SLICE]
                          [−−not_render_volume] [−−not_render_vessels]
                          vesselFileNames [vesselFileNames ...] grp_pattern

Povray wrapper

positional arguments:
  vesselFileNames
  grp_pattern

optional arguments:
  −h, −−help            show this help message and exit
  −p POVPARAMSSET, −−povParamsSet POVPARAMSSET
                        use parameters found in povrayRenderSettings.py
                        (default: None)
  −d DATALIST, −−data DATALIST
                        which data (pressure, flow, shearforce, hematocrit) as
                        comma separated list (default: ['pressure'])
  −f, −−filter−uncirculated
                        filter uncirculated vessels (default: False)
  −−filterradiushighpass FILTERRADIUSHIGHPASS
                        filter vessels from tree above this value (default:
                        −1.0)
  −−filterradiuslowpass FILTERRADIUSLOWPASS
                        filter vessels from tree below this value (default:
                        −1.0)
  −−overlay             decide if mpl overlay is created (default: True)
  −−dpi DPI             dpi for the rendering (default: 300.0)
  −−format FORMAT       output format of image (default: png)
  −c CAM, −−cam CAM     camera mode: topdown, pie, topdown_slice (default:
                        topdown_slice)
  −u, −−plot_auc        for area under curve, we have only a single timepoint
                        (default: False)
  −a, −−auto_colorscale
                        (default: False)
  −−fontcolor FONTCOLOR
                        fontcolor in overlay, use mpl style colors (default:
                        black)
  −−temp_file_dir TEMP_FILE_DIR
                        dir for temp povray scene (default: None)
  −−keep_files          keep tmp file? (default: False)
  −−assumed_gamma ASSUMED_GAMMA
                        (default: 1.0)
  −−background BACKGROUND
                        (default: 1.0)
  −−ambient_color AMBIENT_COLOR
                        (default: (0.1, 0, 0))
  −−res RES             (default: (1024, 1024))
  −−num_threads NUM_THREADS
                        (default: 7)
  −−out_alpha           (default: False)
  −−cam_distance_multiplier CAM_DISTANCE_MULTIPLIER
                        (default: 1.0)
  −−colored_slice COLORED_SLICE
                        (default: True)
  −−not_render_volume   For combined images (default: False)
  −−not_render_vessels  For combined images (default: False)
```

1

This program automatically recognizes the type of file your entered. Depending your input, different subroutines to render vessels, tumors, IFF or detailed oxygen datasets are called. We provide examples for all.

Vessels

We begin by visualizing a vessel network.

```
submitPovrayRender \
vessels−default−typeI−15x19L130−sample00.h5 vessels
```

creates the file *vessels-default-typeI-15x19L130-sample00_vessels_pressure.png* which is also show in main document. The *-d, –data* flag allows you to switch the data which is colorcoded on the vessels e.g.

```
submitPovrayRender \
vessels−default−typeI−15x19L130−sample00.h5 vessels \
−d flow , shearforce
```

will create renderings of the flow or the shearforce. The figure shown in the main document was created by

```
submitPovrayRender \
vessels−default−typeI−15x19L130−sample00.h5 vessels \
−p 'figure_plos_vessels '
```

Tumors

We create a rendering of the tumor simulation at time point *out0005* from the file *tumBulk-default-typeI-sample00-defaultconfig_bulktissue.h5*.

```
submitPovrayRender \
tumBulk−default−typeI−sample00−defaultconfig_bulktissue.h5 \
out0005
```

Upon a successful run the image *tumBulk-default-typeI-sample00-defaultconfig_bulktissue-out0005.png_slice.png* should be present. To illustrate the camera option (*-c, –cam*), we run an other example with

```
submitPovrayRender \
tumBulk−default−typeI−sample00−defaultconfig_bulktissue.h5 \
out0005 \
−c pie
```

The figure shown in the main document was created by

```
submitPovrayRender \
tumBulk−default−typeI−sample00−defaultconfig_bulktissue.h5 \
out0005 \
−p 'figure_plos_tumor '
```

Detailed Oxygen

Of course these datasets can also be visualized. We run

```
submitPovrayRender \
o2_tumBulk−default−typeI−sample00−defaultconfig_bulktissue_default_o2.h5 \
po2/out0005
```

2

Note here the *–render_volume* and *–render_vessels* option which allows you to visualize datasets with and without the vessels in the same plane.

```
submitPovrayRender \
o2_tumBulk-default-typeI-sample00-defaultconfig_bulktissue_default_o2.h5 \
po2/out0005 \
--not_render_vessels
```

IFF

Analogously we run here

```
submitPovrayRender \
iff_default_ulk-default-typeI-sample00-defaultconfig_bulktissue.h5 \
out0004
```

ParaView

To export our file format to paraView, we exploit the script

```
python2 /your/install/path/py/krebs/hdf2vtk.py -h
```

Vessels

For example, here with the lately produced vessels

```
python2 /your/install/path/py/krebs/hdf2vtk.py \
vessels-default-typeI-15x19L130-sample00.h5 vessels
```

creating the file *vessels-default-typeI-15x19L130-sample00-vessels.vtk* which is readable by paraView.

Tumor

Here, with tumor file.

```
python2 /your/install/path/py/krebs/hdf2vtk.py \
tumBulk-default-typeI-sample00-defaultconfig_bulktissue.h5 \
out0005 \
```

This creates input files for paraView. One for the vessels and one for the field. When you load these sets into your paraView, make sure to change representation style to something meaningful e.g. "Points".

3.3 Fine-grained simulations of the microenvironment of vascularized tumours

3.3.1 Main Manuscript

OPEN

Fine-grained simulations of the microenvironment of vascularized tumours

Thierry Fredrich [iD] [1], Heiko Rieger[1], Roberto Chignola [iD] [2] & Edoardo Milotti [iD] [3]

One of many important features of the tumour microenvironment is that it is a place of active Darwinian selection where different tumour clones become adapted to the variety of ecological niches that make up the microenvironment. These evolutionary processes turn the microenvironment into a powerful source of tumour heterogeneity and contribute to the development of drug resistance in cancer. Here, we describe a computational tool to study the ecology of the microenvironment and report results about the ecology of the tumour microenvironment and its evolutionary dynamics.

The tumour microenvironment is characterized by large chemical gradients and contains a mixture of normal and tumour cells. The presence of high gradients favours the formation of different ecological niches which can become an important source of tumour heterogeneity[1–6].

The actual size of the niches is quite small, as it is mostly determined by the structure of the scaffold of capillary vessels that envelope and feed the tumour mass. This structure is highly irregular, with a chaotic blood vessel network, a missing lymphatic network, elevated acidity, poor oxygenation, and high interstitial fluid pressure. The distance between blood vessels may be as large as a few hundred μm, and the regions in between them can become highly hypoxic[4].

The fine-graininess and the large spatial variability are essential features in the formation of the ecological niches and they must belong to any mathematical model that aims to explain tumour heterogeneity as the result of Darwinian selection driven by the local environment. The importance of the microenvironment is widely recognized, and several researchers have tackled the problem of its description and understanding from the computational point of view, e.g.[7–13], and the reviews[14,15].

The studies, however, mainly focus on the biochemical, cellular and biophysical properties of the tumour microenvironment and not on its active role in providing varied evolutionary paths to genetic variants of the tumour cells. As it has already been pointed out[16,17], the adaptive evolution of tumour clones (central concept of Darwinian dynamics) is driven by the formation of new environmental niches. Many practical difficulties limit the experimental study of the adaptation process, while computer simulations can shed light — albeit in a limited way — on the dynamics of many steps like the convergent evolution of different genotypes to the same phenotype, and the selective loss of specific cell functions.

Simulations of avascular solid tumours show that the microenvironment of these small cell aggregates is formed by rather homogeneous niches with smooth gradients of oxygen, of other nutrients, waste molecules and cell viability[18]. After the angiogenic transition, however, the microenvironment differentiates in unpredictable ways. To identify underlying processes and provide reasoning, we have developed a computational model that is a tool to understand the fine-grained features of a simplified tumour microenvironment, i.e. of a microenvironment that contains only tumour cells and blood vessels. This is a rather strong simplifying assumption, since experimental observations show that in addition to tumour cells the microenvironment contains several other important cell types such as stromal and immune cells. We wish to stress that this assumption is a necessary compromise, because no computer model can presently describe the huge biological complexity of the tumour microenvironment and capture its growth at appropriate spatial and temporal resolutions.

Our computational model combines two different simulation programs, namely, a lattice-free simulation of small avascular solid tumours and a lattice-based simulation of the blood vessels dynamics in solid tumours. As we discuss below, both models have been individually validated with experimental data, and here we provide

[1]Center for Biophysics & FB Theoretical Physics, Saarland University, Saarbrücken, 66123, Germany. [2]Universita degli Studi di Verona, Department of Biotechnology, Verona, 37134, Italy. [3]University of Trieste, Department of Physics, Trieste, 34127, Italy. Correspondence and requests for materials should be addressed to T.F. (email: thierry@lusi.uni-sb.de)

1
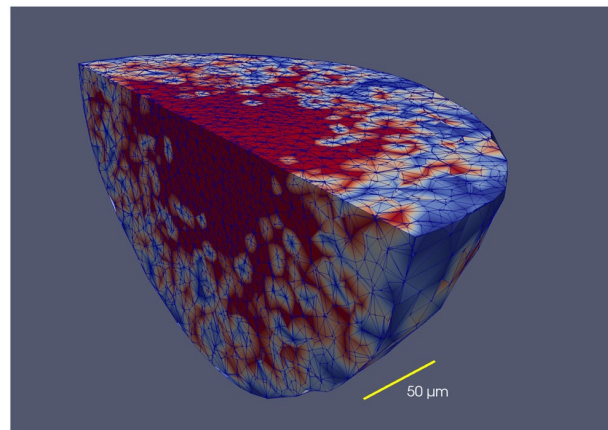
Figure 1. Distribution of cell phases in a tumour spheroid (avascular *in vitro* tumour) simulated with VBL. The figure shows a clipped spheroid, to display the cell phases in the inside of the spheroid. The colors represent different cell phases, and in this example it is only important to note that the necrotic regions are red. Note that there is no clear cut boundary between the proliferating part of the necrotic core. The triangulation used by VBL is also shown. This simulated tumour spheroid comprises almost 24000 cells.
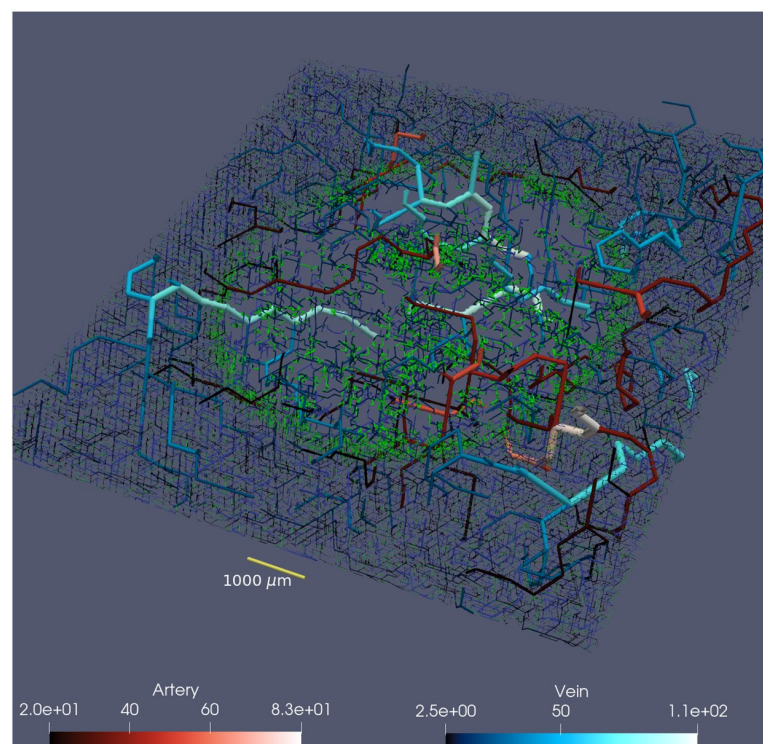
Figure 2. 500 μm thick slice trough tumour vasculature of 1 cm lateral size. For 3D illustration we extent vessels with radius bigger than 20 μm for another 750 μm above and below the slice. According to the lower panels: arteries are displayed in varying reddish color and veins in varying blueish color (unit is also μm). Capillaries and young vessel are shown in green.

a first validation of the combined model by correctly reproducing the relevant observed gradients of tumour oxygenation and other biochemical and biological features. Next, we use the combined model to explore how the tumour microenvironment takes shape in small solid tumours at the transition from the avascular to the vascular growth phases, the so-called angiogenic switch[19]. We follow the complex dynamics of this process in detail and in real time and show that, already at these early stages of tumour development, the diversity of environmental niches is high enough to promote adaptive evolution of tumour variants.
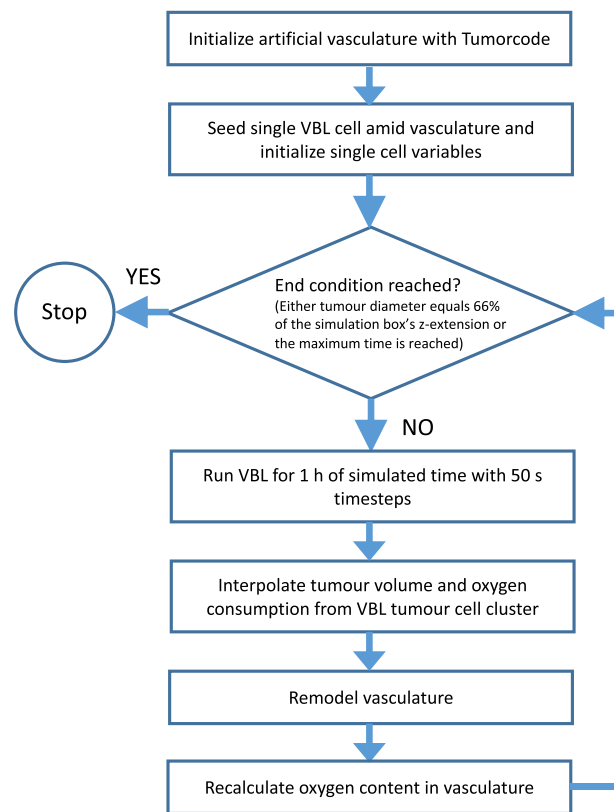
Figure 3. Flowchart of combined VBL and Tumorcode simulation.
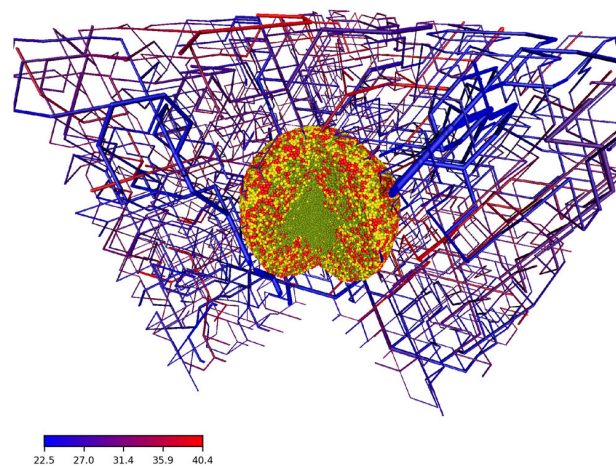
Figure 4. Artificial blood vessel network containing a tumour after 23 simulated days past the initial seeding. For visualization we removed a quarter of the system. The color code in the bottom left corresponds to the blood pressure at a given vessel segment. Cells are colored by their cell phase. Red: phases G1m and G1p; yellow: phases S, G2 and M; light green: dead cells.

Brief Outline of "Virtual Biology Lab" (VBL) and Tumorcode

In this section we give a short description of the two programs that have been merged. The present account is very brief as both programs have been described in detail in past papers (for VBL, see[18,20–23], for Tumorcode, see[24–26]).

VBL. VBL is a lattice-free, cell-based program that can simulate both: the growth and proliferation of disperse cells and of more complex, avascular cell clusters (tumour spheroids). It contains a detailed simulation of the metabolic activity of each cell including discrete events at the individual cell level (for instance: mitochondrial

144
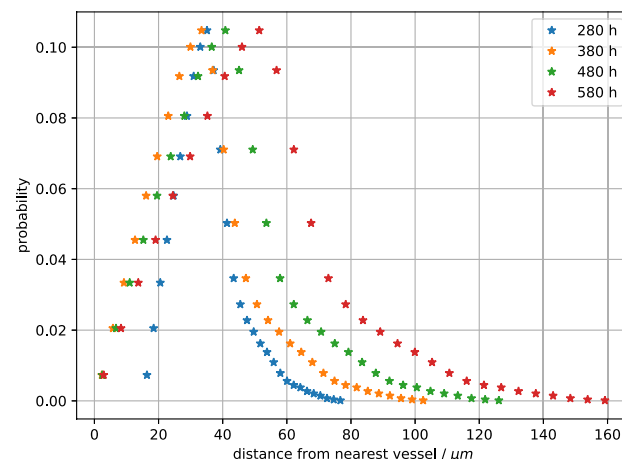
Figure 5. Empirical distribution of the distance to the closest vessel for all cells in the developing tumour. The snapshots are taken at simulated times 280 hours, 380 hours, 480 hours and 580 hours past the initial seed. Colors represent the different simulation times.

partitioning at mitosis), and has the potential to activate phenotypic differentiation. More specifically, the model has the following features:

- The model of human tumor cells includes both- the internal biochemical processes and a phenomenological description of the biomechanics of cells.
- Spatially, each cell is a two-compartment structure, the inside of the cell and the adjacent extracellular environment or intercellular space; this is important to handle simple diffusion and facilitated diffusion across the cell membrane at the same time.
- Discrete events are simulated and interleaved between successive deterministic steps; the random nature of some of them contributes to the stochasticity of the simulation as a whole.
- Each cell is characterized by its own phenotype which means that a specific set of parameters is linked to an individual cell.
- Enzyme activity is modulated both by pO_2 concentration and by pH.
- Weighting of molecular paths and cellular mechanisms is possible.
- The program simulates dispersed tumor cells and cell clusters (tumor spheroids) including the intercellular space.
- The surrounding environment is an integral part of the simulation.

The numerical methods used in VBL have been described elsewhere[27], here we only mention that although the simulation is lattice-free, continuum processes are actually discretized on the continually-variable irregular lattice defined by the Delaunay triangulation[28] based on the cells' centres which also defines the proximity relations among cells that are necessary to compute the cell-cell forces. We find that the computational geometry library CGAL (https://www.cgal.org)[29] is an easy tool that offers necessary triangulation features amended by the possibility to calculate alpha shapes. This is necessary to define the surface or contact zone of the spheroid with the environment. It is important to note that the simulation spans many orders of magnitude in time which makes the large system of differential equations describing the deterministic part of the program extremely stiff. Therefore we solve the equations by means of implicit integration methods, that allow for comparatively large time steps (of the order of 1–10 s in terms of simulated time)[30].

Figure 1 shows an example of a tumour spheroid simulated by VBL. As we have shown in the past, the main metabolic, morphologic and kinetic parameters are correctly reproduced both for isolated cells and for cells grown as three- dimensional clusters[21,27].

Tumorcode. While cell-cell interactions like in VBL naturally produce nearly spherical structures, modelling the growth of blood vessels moves the complexity of the simulation one step higher to the level of tissue morphogenesis. The list of models is long. For an appropriate discussion of the existing models for tumor vasculature see[31].

Solid tumours grow in originally healthy tissue featuring a normal vasculature build up by a hierarchically organized arterio-venous blood vessel network that is then dynamically modified by the growing tumor. An integrative modeling approach thus has to address two issues: first, it has to find an appropriate representation of the original vasculature of the host tissue; and second, the dynamics of the given blood vessel network has to be defined, which includes the insertion of new vessels via angiogenesis as well as the removal of existing vessels (old and new) via vessel regression, and the modification of existing vessels via dilation, constriction or occlusion. Moreover, the network carries a blood flow and transports and emits oxygen, nutrients and drugs, which has to be represented, too. Various modeling approaches have been presented in the past (for a review see e.g.[24,31,32]), here
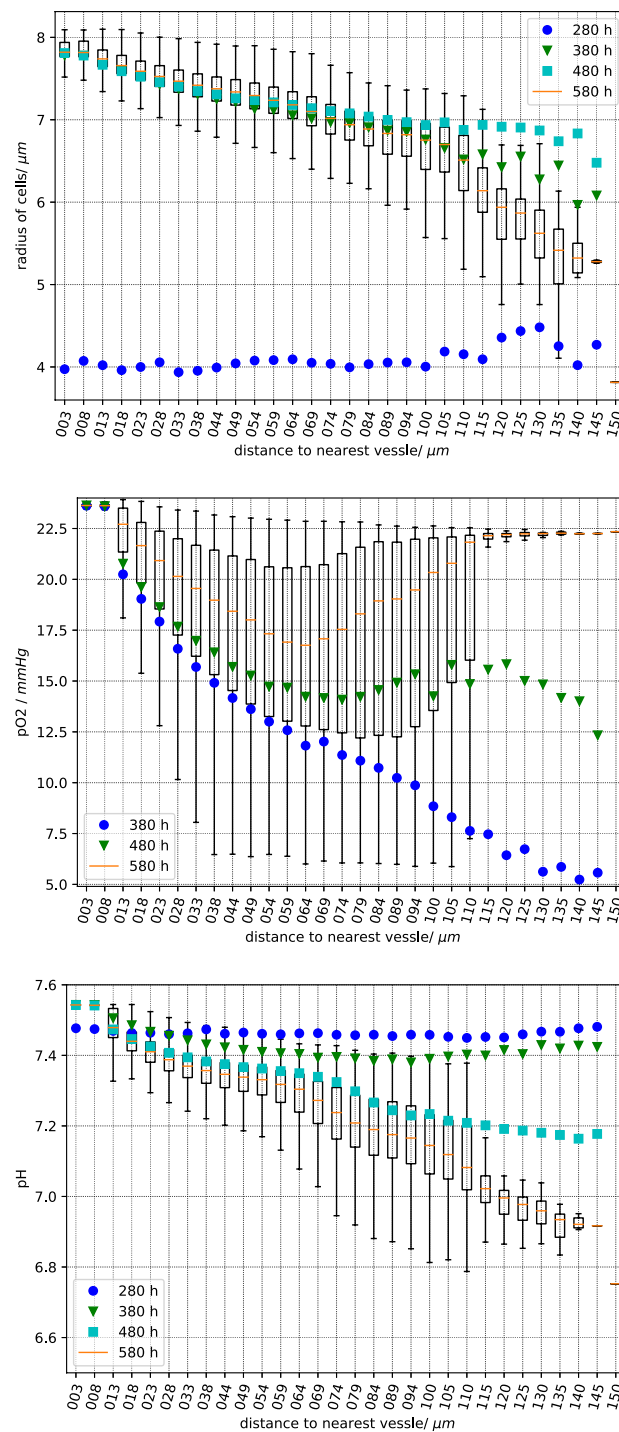
Figure 6. Sampled cell quantities vs. the distance to the nearest vessel. Top panel: cell radius, center panel: partial oxygen pressure, bottom panel: extracellular pH. Each box plot has been obtained using the values in cells at a given distance from the nearest vessel as indicated by the abscissa. As usual, the vertical error bars ("whiskers") represent the lower and upper quartile. The data is sampled 280, 380, 480 and 580 hours past the initial seeding. For better clarity, we omit the complete boxes for the time points 280, 380 and 480 and plot only the mean value in different colors.

we use the simulation framework Tumorcode described in[25], which does not only create artificial arterio-venous blood vessel networks representing the healthy initial vasculature, but includes vascular remodeling during solid tumour growth by angiogenesis, vessel dilation, regression and collapse. The created networks were tested against

146
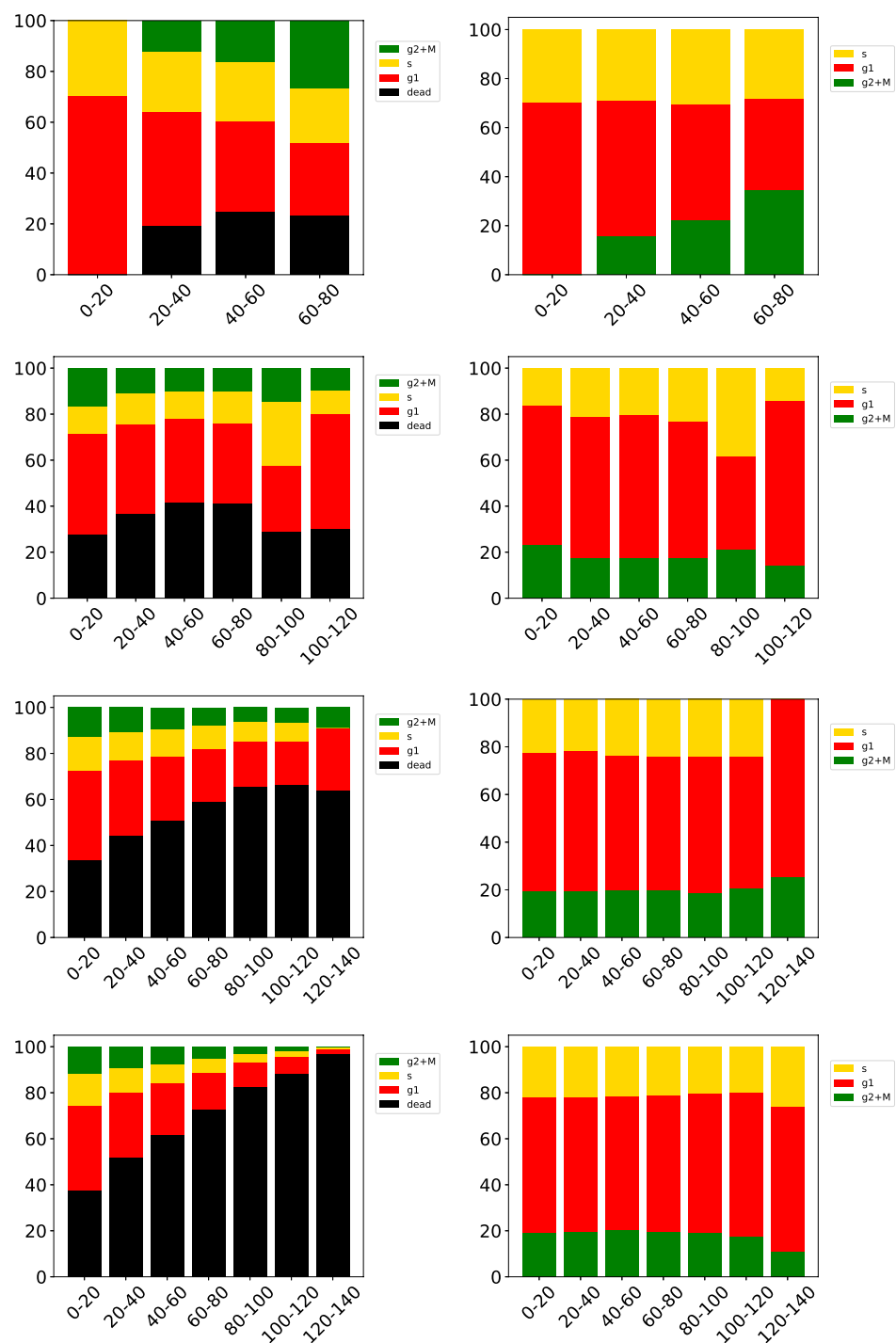
Figure 7. Distribution of the cell phases at different distances from the closest blood vessel. From top row to bottom row the data is take after 280, 380, 480, 580 hours past this inital seed. The left panels show the number of cells in the corresponding phase relative to the total number of current cells. G1m and G1p in red, S in yellow, G2 and M in green and dead cells in black. In the right panels we consider only alive cells. The abscissa is the distance to the nearest vessel.

experimental data and successfully reproduced: 1) morphology and flow characteristics[33,34], 2) interstitial fluid flow and pressure[35], and 3) tissue oxygenation[26] for both, healthy and tumour tissue.

Again, here is a short list of its main features of Tumorcode:
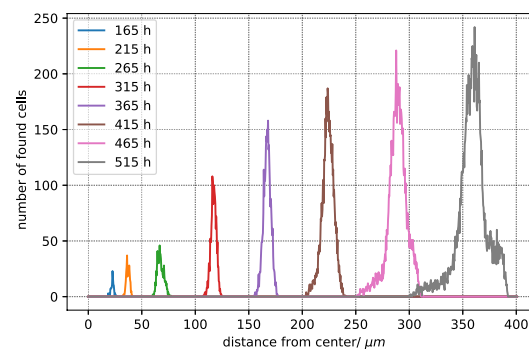
Figure 8. Distribution of distance from tumour centroid to cells in contact with the environment (normal tissue). The colors indicate the different sampling times past the inital seeding. The bin size is $30\,\mu$m.
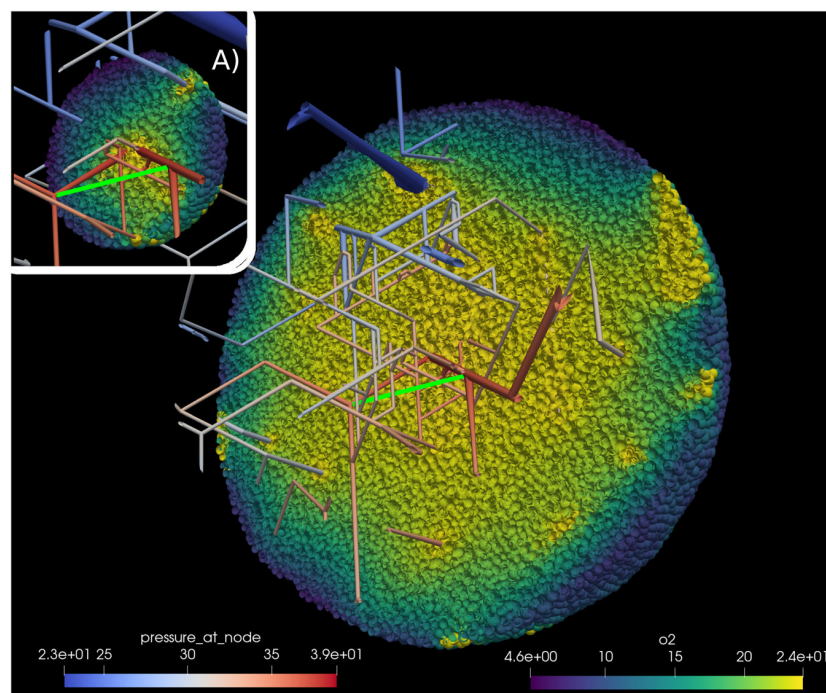
Figure 9. Sampling the partial oxygen pressure pO_2 along lines between blood vessels. We sampled along the line joining two blood vessels (bright green). Inset (**A**) shows the simulation state 350 hours past initial seeding; the main image shows the state after 527 hours. Note the additional vessel due to angiogenesis. The scale marked "pressure_at_node" refers to the pO_2 value at vessel nodes in mmHg. The scale marked "o2" referes to the value of pO_2 inside cells. See also Supplemental Material for more information.

- Hemodynamics includes the phase separation effect (Fåhræus-Lindqvist effect) and different rheologies.
- Concentrations in the surrounding environment are computed according to a continuum model, i.e., according to a set of partial differential equations discretized by finite elements method solved with the Trilinos C++ library (https://trilinos.org)[36].
- Angiogenesis, i.e., the addition of new segments, is driven by the VGEF gradient and is partly stochastic[24].
- As the tumour grows, the vasculature and the blood flows change, and the modified shear stress leads to *blood vessel dilation* or to *blood vessel collapse*[24].
- A low local VGEF growth factor concentration produces *blood vessel regression*[24].
- The program computes the interaction with surrounding tissues to compute the extraction of oxygen and nutrients from blood vessels.
- The program returns blood flow, oxygen concentration, metabolite concentration, etc, in blood vessels and surrounding tissues.
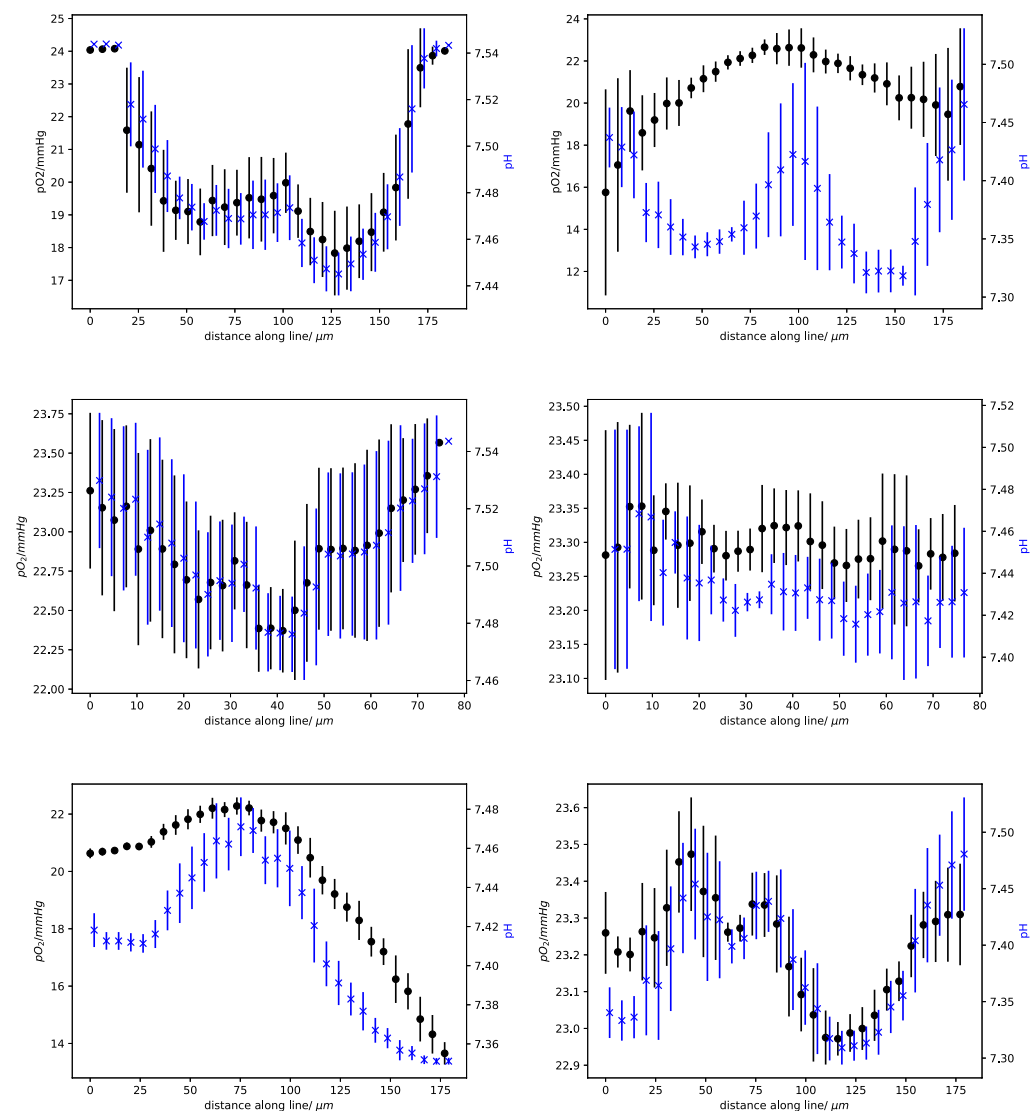
Figure 10. Data for the three measured lines. Each row corresponds to one specific line. The left column represents data taken at 350 hours of simulated time, and the right column at 495 hours past the initial tumour seeding. Each panel shows the sampled partial oxygen pressure (pO$_2$) in black (left hand y-axis) and the pH in blue (right hand y-axis). To improve visibility, the data points of pO$_2$ and pH are shifted against each other by 2 μm. Each line was sampled by 30 points within a sphere of radius 10 μm. The vertical lines represent the standard deviation.

- The blood vessel hematocrit acts as source for oxygen dissolved in tissue and the tissue simultaneously consumes the oxygen. In[26] we explain how the coupled set of non linear differential equations is solved to obtain the oxygen partial pressure for each blood vessel segment.

Figure 2 shows an example of a tumour vasculature simulated by Tumorcode. You can clearly distinguish the vasculature inside the tumour from the surrounding healthy tissue. Note the difference in length scale when comparing Figs 1 and 2, and the fact that the tumour is a continuous structure (governed by reaction-diffusion equations[25]) in Tumorcode. In contrast to VBL, it cannot describe the evolutionary features of the microenvironment at the single cell level.

The Merging of the Two Programs

To merge the two programs into one, we had to match the spatial structures of the two programs. The cells are not confined to a lattice however the diffusion processes in VBL are calculated by means of a disordered Delaunay triangulation which is not permanent and has a variable size, as cells position change at each time step while the cells grow and proliferate. The situation is almost the reverse in Tumorcode where blood vessel segments belong to an FCC lattice and the continous space is discretized by a cubic lattice to solve the partial differential
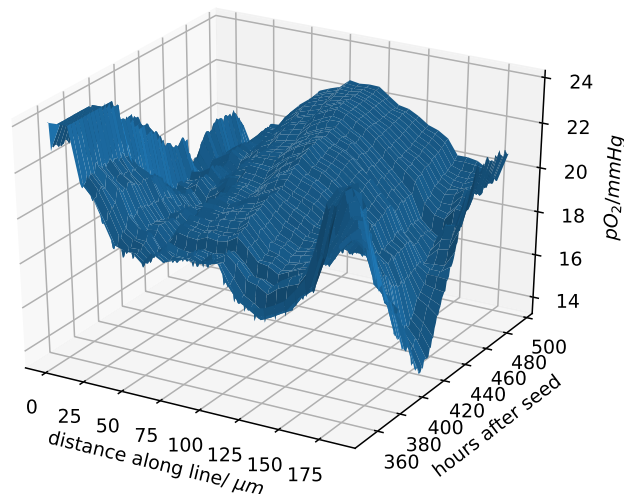
Figure 11. Change of pO_2 due to the blood vessel dynamics. This data extends those in the first row of Fig. 10. In contrast to Fig. 10, we show all intermediate time points in this plot.

equations. We interpolated cell properties from the cells position to the surrounding nodes of the cubic lattice (compare Fig. 3). In particular, the Tumorcode requires an oxygen consumption field and each cell is considered as point- like source of growth factor. Once the growth factor field exceeds the threshold, the vessel remodelling of Tumorcode starts.

We estimate that the accurate calculation of any substance concentration for a given cell requires $\mathcal{O}(N_C N_{BV})$ number of operations, where N_C is the number of cells and N_{BV} is the number of blood vessels segments. Since both N_C and N_{BV} easily exceed 10^6 in the smallest-sized biologically relevant simulation runs, $\mathcal{O}(N_C N_{BV}) \sim 10^{12}$ per time step, making the simulations utterly unmanageable. To reduce the computational complexity, we take into account that only the nearest blood vessels actually contribute to the inputs and outputs of the different molecules in the vicinity of a given cell trimming the large number of cell-blood vessel pairs to $\mathcal{O}(N_C)$. Moreover, the timesteps to follow cell biochemistry are of order $1–10\,s$ while biological relevant timesteps for vascular remodelling are in the order of hours. Therefore we introduce two different time steps to avoid a huge number of useless sweeps over the blood vessel network (compare Fig. 3).

Development of the Microenvironment in Small Solid Tumours

With the program described before, we studied selected aspects of the tumour microenvironment. To this end, we carried out simulation runs with three different tumour seeds: 1. at the center of a blood vessel network, 2. close to an arterial bifurcation, 3. close to a venous bifurcation. The details of each simulation are reported in the Supplemental Material. Here we display the results in a way that allows an easy comparison with measurements[37,38].

As expected, the seeding is important in the very first steps of tumour growth: a seed close to blood vessels leads to fast growth and to a quick remodelling of the blood vessel network; for seeds far from blood vessels, the initial growth is slower and the subsequent initial development of the tumor microenvironment differs slightly.

Seed at the center of a blood vessel network. The computational approach provides an easy access to information that is hard to obtain with experiments and allows multiple ways of visualization (compare Fig. 4). Here we take advantage of the information about the distance to the nearest blood vessel for every cell. We start with the distribution which is a defining feature of the microenvironment, as larger distances mean less oxygen and nutrients, and therefore starvation and death for many tumour cells. In Fig. 5 we see how the distribution changes while the tumour grows. The distribution at the early stage (280 hours past seeding) ranges from 0 to $80\,\mu m$ ensuring a optimal oxygenation to all cells and gets distorted until it covers a range of up to $160\,\mu m$ at a later stage (580 hours past seeding) where cells not receive a sufficient input of oxygen and nutrients.

Intuitively the increase in the mean of cell-blood vessel distances leads to a decrease of available oxygen and nutrients, and to an increase of lactate ions and to a lower pH. Since the cell-blood vessel distance is known, we can display space-time data on the distributions of cell radii, pO_2 and pH (Fig. 6) - the data confirms the intuition. We uploaded two videos where we visualize pO_2 (`fredrich:po2:2018`) and pH (`fredrich:pH:2018`) during the complete of the growth processes.

Finally, the changes in the microenvironment stretch the cell proliferation period and therefore modifies the cell cycle distribution as seen in Fig. 7 where we can follow the formation of a necrotic core. At the beginning (280 hours past initial seed) the relative amount of cells in the different phases varies with the distance from the nearest vessel. Surprisingly this relative amount stays almost constant after the establishment of different niches. Compare with Fig. 4 were we show the cell phase distribution in a more pictorial way. Even in such a

small tumour we observe the initial development of necrotic regions which characterizes the development of the tumour microenvironment.

Actual tumours have irregular shapes, while the cells in VBL are not polarized, and when grown in uniform environments produce nearly spherical shapes. In the presented case the blood vessel network drives the growth in specific directions and we expect a marked deviation from sphericity already with small simulated tumours. Ideally, in a spherical tumour all cells on the surface have the same distance to the centroid. We find that the distribution of distances from the spheroid's surface to the centroid a) broadens and b) deviates from symmetric form as the tumour grows (Fig. 8) which is a clear indication of the deformation of the cell cluster and of its deviation from sphericity.

Seed close to an arterial or venous bifurcation. Helminger *et al.*[38] measured the partial oxygen pressure and pH within different tumours. To compare our simulations with their experimental results, we seeded the initial tumour cell close to bifurcations, both arterial and venous, and sampled the cells along different lines (for details see Supplemental Material). Figure 9 is meant to illustrates the sampling procedure while we show data for a early and a late simulation state in Fig. 10.

It is interesting to note that the left panel in first row in Fig. 10 shows a dip in both pO_2 and pH approximately midway between the two blood vessels. The right panel in the same row, taken at a later time, shows a maximum at roughly the same position because a new blood vessel sprouted into the intervening space. A detailed view of this dynamic change is shown in Fig. 11, where the mean of the pO_2 data is plotted for all intermediate time points as the new blood vessel grows.

Conclusions

As explained in the introduction, the study of the ecology of the tumour microenvironment at the angiogenic switch is the primary motivation for the work described in this paper and for the development of the presented complex software tool. Indeed, the Figs 10 and 11 display a surprisingly large spatial and temporal variability already in a very small vascularized tumour. In particular, Fig. 11 shows a continually changing and rugged landscape: this means that the niche diversity is large, and consequently that there is a high evolutionary pressure, and a high probability that the microenvironment selects different tumour clones even in small tumours. This is important in view of the long time required for tumour growth, as it has been estimated that a tumour requires about 10 years to reach a size of 1 cm[39]. According to the *clonal selection hypothesis* new and aggressive tumour clones develop through Darwinian selection during this extended growth time[39,40]. The results discussed in this paper lend further credibility to the *clonal selection hypothesis*, and in our future studies we plan to demonstrate the spatial and temporal variations of different clone populations in this very complex tumour microenvironment. In order to highlight common and diverse evolutionary pathways in different cancers, we also plan to explore the adaptive evolution of cell clones in different microenvironments mimicking different organs or tissue types to reproduce the distinguishing features of selected tumour types.

Finally, we note that the molecular mechanisms that promote genotypic changes in tumour clones are well known and understood, but genotypic variability is only one feature of cancer's evolutionary landscape. The other important feature is the variability of the environment that supervenes the genome and drives evolution itself, and with our computational tool we can start to explore its Darwinian dynamics[16].

Data Availability

We uploaded the full simulation raw data to zenodo with following digital object identifiers: https://doi.org/10.5281/zenodo.2541688, https://doi.org/10.5281/zenodo.2541655, https://doi.org/10.5281/zenodo.2541678, https://doi.org/10.5281/zenodo.2541667.

Code Availability

All source code containing the used parameters is distributed with this article as Supplementary Material and hosted at GitHub https://github.com/thierry3000/tumorcode.

References

1. Anderson, A. R. A., Weaver, A. M., Cummings, P. T. & Quaranta, V. Tumor morphology and phenotypic evolution driven by selective pressure from the microenvironment. *Cell* **127**, 905–15, https://doi.org/10.1016/j.cell.2006.09.042 (2006).
2. Sprouffske, K., Merlo, L. M., Gerrish, P. J., Maley, C. C. & Sniegowski, P. D. Cancer in Light of Experimental Evolution. *Current Biology* **22**, R762–R771, https://doi.org/10.1016/j.cub.2012.06.065 (2012).
3. Beerenwinkel, N., Greenman, C. D. & Lagergren, J. Computational Cancer Biology: An Evolutionary Perspective. *PLoS Comput Biol* **12**, e1004717, https://doi.org/10.1371/journal.pcbi.1004717 (2016).
4. Yuan, Y. Spatial Heterogeneity in the Tumor Microenvironment. *Cold Spring Harb Perspect Med* **6**, https://doi.org/10.1101/cshperspect.a026583 (2016).
5. Basanta, D. & Anderson, A. R. A. Homeostasis Back and Forth: An Ecoevolutionary Perspective of Cancer. *Cold Spring Harb Perspect Med* **7**, https://doi.org/10.1101/cshperspect.a028332 (2017).
6. Gatenby, R. & Brown, J. The Evolution and Ecology of Resistance in Cancer Therapy. *Cold Spring Harb Perspect Med* **8**, https://doi.org/10.1101/cshperspect.a033415 (2018).
7. Shirinifard, A. *et al.* 3d Multi-Cell Simulation of Tumor Growth and Angiogenesis. *PLoS One* **4**, e7190, https://doi.org/10.1371/journal.pone.0007190 (2009).
8. Tang, L. *et al.* Computational Modeling of 3d Tumor Growth and Angiogenesis for Chemotherapy Evaluation. *PLoS One* **9**, e83962, https://doi.org/10.1371/journal.pone.0083962 (2014).
9. Grogan, J. A. *et al.* Microvessel Chaste: An Open Library for Spatial Modeling of Vascularized Tissues. *Biophysical Journal* **112**, 1767–1772, https://doi.org/10.1016/j.bpj.2017.03.036 (2017).
10. Xu, J., Vilanova, G. & Gomez, H. A Mathematical Model Coupling Tumor Growth and Angiogenesis. *PLoS One* **11**, e0149422, https://doi.org/10.1371/journal.pone.0149422 (2016).

11. Vilanova, G., Colominas, I. & Gomez, H. A mathematical model of tumour angiogenesis: growth, regression and regrowth. *J R Soc Interface* **14**, https://doi.org/10.1098/rsif.2016.0918 (2017).
12. Zhao, G. *et al*. Three-dimensional model of metastatic tumor angiogenesis in response to anti-angiogenic factor angiostatin. *J. Mech. Med. Biol.* **17**, 1750094, https://doi.org/10.1142/S0219519417500944 (2017).
13. Zheng, X., Wise, S. M. & Cristini, V. Nonlinear simulation of tumor necrosis, neo-vascularization and tissue invasion via an adaptive finite-element/level-set method. *Bull. Math. Biol.* **67**, 211, https://doi.org/10.1016/j.bulm.2004.08.001 (2005).
14. Rejniak, K. A. (ed.) *Systems Biology of Tumor Microenvironment: Quantitative Modeling and Simulations*. Advances in Experimental Medicine and Biology (Springer International Publishing, 2016).
15. Deisboeck, T. S., Wang, Z., Macklin, P. & Cristini, V. Multiscale Cancer Modeling. *Annual Review of Biomedical Engineering* **13**, 127–155, https://doi.org/10.1146/annurev-bioeng-071910-124729 (2011).
16. Gatenby, R. A., Gillies, R. J. & Brown, J. S. Of cancer and cavefish. *Nat Rev Cancer* **11**, 237–238 (2011).
17. Gatenby, R. A., Cunningham, J. J. & Brown, J. S. Evolutionary triage governs fitness in driver and passenger mutations and suggests targeting never mutations. *Nat Commun* **5**, 5499, https://doi.org/10.1038/ncomms6499 (2014).
18. Milotti, E. & Chignola, R. Emergent properties of tumor microenvironment in a real-life model of multicell tumor spheroids. *PLoS One* **5**, e13942 (2010).
19. Bergers, G. & Benjamin, L. E. Tumorigenesis and the angiogenic switch. *Nature Reviews Cancer* **3**, 401, https://doi.org/10.1038/nrc1093 (2003).
20. Chignola, R. & Milotti, E. Bridging the gap between the micro-and the macro-world of tumors. *AIP Advances* **2**, 011204 (2012).
21. Chignola, R., Sega, M., Stella, S., Vyshemirsky, V. & Milotti, E. From single-cell dynamics to scaling laws in oncology. *Biophysical Reviews and Letters* **9**, 273–284 (2014).
22. Milotti, E., Vyshemirsky, V., Sega, M. & Chignola, R. Interplay between distribution of live cells and growth dynamics of solid tumours. *Scientific Reports* **2**, 990 (2012).
23. Stella, S., Chignola, R. & Milotti, E. Competing computational approaches to reaction-diffusion equations in clusters of cells. In *Journal of Physics: Conference Series*, vol. 490, 012129 (IOP Publishing, 2014).
24. Rieger, H., Fredrich, T. & Welter, M. Physics of the tumor vasculature: Theory and experiment. *Eur. Phys. J. Plus* **131**, 31, https://doi.org/10.1140/epjp/i2016-16031-9 (2016).
25. Fredrich, T., Welter, M. & Rieger, H. Tumorcode. *Eur. Phys. J. E* **41**, 55, https://doi.org/10.1140/epje/i2018-11659-x (2018).
26. Welter, M., Fredrich, T., Rinneberg, H. & Rieger, H. Computational model for tumor oxygenation applied to clinical data on breast tumor hemoglobin concentrations suggests vascular dilatation and compression. *PLoS One* **11**, e0161267, https://doi.org/10.1371/journal.pone.0161267 (2016).
27. Chignola, R., Del Fabbro, A., Farina, M. & Milotti, E. Computational challenges of tumor spheroid modeling. *Journal of bioinformatics and computational biology* **9**, 559–577 (2011).
28. De Berg, M., Van Kreveld, M., Overmars, M. & Schwarzkopf, O. C. *Computational geometry* (Springer, 2000).
29. The CGAL Project. *CGAL User and Reference Manual*, 4.13 edn. (CGAL Editorial Board, 2018).
30. Milotti, E., Del Fabbro, A. & Chignola, R. Numerical integration methods for large-scale biophysical simulations. *Computer Physics Communications* **180**, 2166–2174 (2009).
31. Rieger, H. & Welter, M. Integrative models of vascular remodeling during tumor growth. *Wiley Interdiscip Rev Syst Biol Med* **7**, 113–29, https://doi.org/10.1002/wsbm.1295 (2015).
32. Welter, M. & Rieger, H. Computer simulations of the tumor vasculature: Applications to interstitial fluid flow, drug delivery, and oxygen supply. *Adv Exp Med Biol* **936**, 31–72, https://doi.org/10.1007/978-3-319-42023-3_3 (2016).
33. Welter, M., Bartha, K. & Rieger, H. Vascular remodelling of an arterio-venous blood vessel network during solid tumour growth. *Journal of Theoretical Biology* **259**, 405–422, https://doi.org/10.1016/j.jtbi.2009.04.005 (2009).
34. Welter, M. & Rieger, H. Physical determinants of vascular network remodeling during tumor growth. *Eur. Phys. J. E* **33**, 149–163, https://doi.org/10.1140/epje/i2010-10611-6 (2010).
35. Welter, M. & Rieger, H. Interstitial fluid flow and drug delivery in vascularized tumors: a computational model. *PLoS One* **8**, e70395, https://doi.org/10.1371/journal.pone.0070395 (2013).
36. Heroux, M. A. *et al*. An overview of the Trilinos project. *ACM Transactions on Mathematical Software* **31**, 397–423, https://doi.org/10.1145/1089014.1089021 (2005).
37. Yano, S. *et al*. Spatial-temporal fucci imaging of each cell in a tumor demonstrates locational dependence of cell cycle dynamics and chemoresponsiveness. *Cell Cycle* **13**, 2110–9, https://doi.org/10.4161/cc.29156 (2014).
38. Helmlinger, G., Yuan, F., Dellian, M. & Jain, R. K. Interstitial pH and pO2 gradients in solid tumors *in vivo*: High-resolution measurements reveal a lack of correlation. *Nature Medicine* **3**, 177–182, https://doi.org/10.1038/nm0297-177 (1997).
39. Talmadge, J. E. Clonal selection of metastasis within the life history of a tumor. *Cancer research* **67**, 11471–11475 (2007).
40. Arneth, B. Comparison of Burnet's clonal selection theory with tumor cell-clone development. *Theranostics* **8**, 3392 (2018).

Acknowledgements

Author Contributions

T.F.: conducted simulations, analyzed data, drafted results part of manuscript; E.M.: suggested scientific problem, added VBL to public domain, drafted other sections; T.F. and E.M.: designed an interface for VBL and Tumorcode, optimized parameters; R.C.: helped with biological aspects and parameter tuning; H.R.: developed Tumorcode program, supervised T.F. All authors approve the content and reviewed the manuscript.

Additional Information

Supplementary information accompanies this paper at https://doi.org/10.1038/s41598-019-48252-8.

Competing Interests: The authors declare no competing interests.

Publisher's note: Springer Nature remains neutral with regard to jurisdictional claims in published maps and institutional affiliations.

www.nature.com/scientificreports/

3.3.2 Supplemental Material

3.3.2.1 Supplemental 1: Simulation details

Supplementary text for "Fine-grained simulations of the microenvironment of vascularized tumours"

Thierry Fredrich[1,*], Heiko Rieger[1], Roberto Chignola[2], and Edoardo Milotti[3]

[1]Center for Biophysics & FB Theoretical Physics, Saarland University, Saarbrücken, 66123, Germany
[2]Universita degli Studi di Verona, Department of Biotechnology, Verona, 37134, Italy
[3]University of Trieste, Department of Physics,Trieste, 34127, Italy
[*]thierry@lusi.uni-sb.de

ABSTRACT

In this little supplementary file to the main manuscript we elaborate on the implementation, hardware and simulation details.

1 Introduction

All source code and parameters to reproduce our simulations are publicly available at GitHub

VBL   : https://github.com/thierry3000/VBL
Tumorcode : https://github.com/thierry3000/tumorcode

and distributed with this supplemental material. For the VBL parameters, see the subfolder `parameters` and for Tumorcode parameters, see the subfolder `py/krebsjobs/parameters` within their sources.

 The initial vasculature was created with the Tumorcode program[1] `submitVesselgeneration` and the following arguments: `-p default -t 8 -w 1500 -i 1` , see command line help (`-h` option) for their explanation. The resulted initial vasculature comprises a lattice with a constant of 130 μm and a total size of (1690 μm x 2080 μm x 1820 μm). For the cancerous modifications, this is subdivided by a factor of 10 such that the tumor vasculature's lattice constant is 13 μm . Note that the subdivision of a face centered cubic lattice is again a face centered lattice which is an essential feature of our lattice based simulation. As reported in[2,3], the vessel network is superimposed by regular cubic grid taking care of the continuum equations. We chose a constant of 30 μm .

 We chose VBL to operate with a time step of 50 seconds while the minimal time step in Tumorcode is one hour, so the time scales from VBL and Tumorcode are sufficiently different to interleave the two programs. To this end, the VBL software was redesigned with the submodule or library approach in mind that allows single calls execution a complete procedure.

1.1 Finding the nearest vessel
Finding the nearest vessel for every cell is nearly impossible from measured datasets. For our in silico system this is straightforward.

 For every vessel, we compute its center of mass and hand it to the ANN library (https://www.cs.umd.edu/~mount/ANN/)[4]. The library uses a special storage structure allowing a quick read out of the nearest neighbors for a given query point which is the cell's position in our case.

1.2 Variation of initial seed
In the main document, we report simulations with 3 different tumor seeding positions: one in the center of the simulation domain, one next to an arterial bifurcation and one next to a venous bifurcation. All other parameters stay the same.

 For the seeds next to the bifurcation, we report measurements along 3 different lines. For simplification, we label them here as follows:

case Ap a parallel line along an arterial bifurcation

case Vp a parallel line along a venous bifurcation

case Vo an orthogonal line in between an venous bifurcation

1

case	sampling line start	sampling line end	seeding point	taken time step
Ap	(195,356.5, -424.5)	(195,506.6,-318.4)	(240, 400, -310)	350,495
Vp	(349,157,-350)	(344,185,-281)	(360, 180, -310)	350,495
Vo	(350, 248,-327)	(327, 78,-281)	(360, 180, -310)	350,495

Table 1. Detailed position of sampled lines.

2 Computing the oxygen content

VBL outputs the amount of oxygen carried per cell in piko gramm (pg). Knowing the cells volume from the radius and the solubility of oxygen, the partial pressure is calculated and used in all our analysis. For the oxygen solubility within the cell we use the value reported in[5].

$$\alpha = 0.003 \frac{\text{ml O2}}{\text{cm}^3 \text{ mmHg}}$$

3 Videos

To highlight the temporal evolution, we visualized the simulation were the spheroid was seeded in the center by means of 2 videos. Each frame is rendered by Tumorcode which provides a direct call to POV-Ray (http://www.povray.org/). The successive images were combined into to movie of 20 frames per second by the ffmpeg tool (http://www.ffmpeg.org/). The movies show the initial vasculature colored by their blood pressure (left color bar) and cut open in a pie like fashion which allows a better view on the developing spheroid in the center. In the file (https://figshare.com/articles/VBL_tumor_PO2/7406180) the cells are color code due to their value of oxygen partial pressure (right colorbar). Note that we can observe the hypoxic rim by pure eye. In the second file (https://figshare.com/articles/VBL_tumor_pH/7406183) , the cells are color coded by their value of pH . The formation of the regions with different values of pH is observed in the presented microenvironment.

4 Hardware

We used nodes of a linux cluster with 28 cores and 128GB memory. The runtime varied from 4 to 6 weeks. This is expected, because of the large number of random events.

References

1. Fredrich, T., Welter, M. & Rieger, H. Tumorcode. *Eur. Phys. J. E* **41**, 55, DOI: 10.1140/epje/i2018-11659-x (2018).

2. Welter, M., Fredrich, T., Rinneberg, H. & Rieger, H. Computational model for tumor oxygenation applied to clinical data on breast tumor hemoglobin concentrations suggests vascular dilatation and compression. *PLoS One* **11**, e0161267, DOI: 10.1371/journal.pone.0161267 (2016).

3. Welter, M. & Rieger, H. Interstitial fluid flow and drug delivery in vascularized tumors: a computational model. *PLoS One* **8**, e70395, DOI: 10.1371/journal.pone.0070395 (2013).

4. Arya, S., Mount, D. M., Netanyahu, N. S., Silverman, R. & Wu, A. Y. An optimal algorithm for approximate nearest neighbor searching fixed dimensions. *Journal of the ACM* **45**, 891–923, DOI: 10.1145/293347.293348 (1998).

5. Pittman, R. N. *Oxygen Transport* (Morgan & Claypool Life Sciences, 2011).

3.3.2.2 Supplemental 2-3

Supplement 2 and 3 contain source code that is only available in digital form. Supplement 2 contains the files of the Virtual Biology Lab (VBL) code
(https://static-content.springer.com/esm/art%3A10.1038%2Fs41598-019-48252-8/MediaObjects/41598_2019_48252_MOESM2_ESM.zip)
and supplement 3 contains the files of Tumorcode
(https://static-content.springer.com/esm/art%3A10.1038%2Fs41598-019-48252-8/MediaObjects/41598_2019_48252_MOESM3_ESM.zip)
with which the reported simulations where conducted.

3.4 Dynamic vessel adaptation in synthetic arteriovenous networks

Reprinted with permission from Elevier: Journal of Theoretical Biology, Dynamic vessel adaptation in synthetic arteriovenous networks by Thierry Fredrich, Michael Welter and Heiko Rieger copyright 2019.

3.4.1 Main Manuscript

Dynamic vessel adaptation in synthetic arteriovenous networks

Thierry Fredrich*, Michael Welter, Heiko Rieger

Saarland University, Center for Biophysics & Dept. Theoretical Physics, Saarbrücken 66123, Germany

ARTICLE INFO

ABSTRACT

Blood vessel networks of living organisms continuously adapt their structure under the influence of hemodynamic and metabolic stimuli. For a fixed vessel arrangement, blood flow characteristics still depend crucially on the morphology of each vessel. Vessel diameters adapt dynamically according to internal and external stimuli: Endothelial wall shear stress, intravascular pressure, flow-dependent metabolic stimuli, and electrical stimuli conducted from distal to proximal segments along vascular walls. Pries et al. formulated a theoretical model involving these four local stimuli to simulate long-term changes of vessel diameters during structural adaption of microvascular networks. Here we apply this vessel adaptation algorithm to synthetic arteriovenous blood vessel networks generated by our simulation framework "Tumorcode". We fixed the free model parameters by an optimization method combined with the requirement of homogeneous flow in the capillary bed. We find that the local blood volume, surface to volume ratio and branching ratio differs from networks with radii fulfilling Murray's law exactly to networks with radii obtained by the adaptation algorithm although their relation is close to Murray's law.

© 2019 Elsevier Ltd. All rights reserved.

1. Introduction

Life depends crucially on the efficiency of transport networks and therefore it is essential to understand how they are functioning and why they are efficient (Banavar et al., 1999). In particular, the vasculature of all mammalians demonstrates how nature efficiently transports and distributes nutrients at minimal costs.

Cecil Murray observed blood vessel networks in 1926 and proposed a formula describing observations on the thickness of the branches (Murray, 1926). In his theoretical derivation of the formula, he considered two energies with opposed dependency on the vessel radius r: the energy required to drive the flow and the energy required to maintain the metabolic demands of the surrounding tissue. To drive the flow, the system needs to overcome the viscous drag that is proportional to $1/r^4$ in case of Hagen–Poiseuille flow and to maintain the metabolic demands, a constant volume of "fresh" blood is required in a first approximation. By minimizing the sum of these two energies, he found that the sum of the cubes of the daughter vessel's radii equals the cube of a parent vessel's radius. In case of a simple junction with one mother vessel of radius r_c and two daughter vessels of radius r_a and r_b, this reduces to:

$$r_c^3 = r_a^3 + r_b^3 \tag{1}$$

Since his assumptions are rather general, they hold true for the respiratory system of animals and insects, xylem in plants and diverse other kinds of transport networks as well (Stephenson et al., 2015). Murray's law is based on an optimality criterion and suggests the intriguing question how the vasculature of living organisms achieves this optimality? The blood vessel wall is formed by endothelial cells with a surrounding layer of smooth muscle cells. Because the muscular layer adjusts the vessel caliber continuously during growth, maturation, in response to exercise, wound healing and diseases, the vasculature is non-stationary with regulatory mechanisms that are still under investigation. While the vascular reactions to shear stress have been known for a long time (Thoma, 1893; Wetterdal, 1920), recent studies showed that: 1) The shear stress is linked to the local intravascular pressure (Pries Axel R. et al., 1995); 2) the vascular diameter is controlled by the metabolic needs of the tissue (local oxygen partial pressure, metabolic signaling substances) (Adair et al., 1990; Berne, 1964; Berne et al., 1983; Björnberg et al., 1989) and the metabolites remaining in blood after the exchange (Ellsworth, 2004); 3) electrical signals are conducted along the blood vessel wall by endothelial and smooth muscle cells via gap junctions (Segal and Duling, 1986; de Wit et al., 2003; Bagher and Segal, 2011) and 4) in case of hypertension, the vasculature switches to inward remodeling (Jacobsen et al., 2003; Pries and Secomb, 2008).

Beginning in 1995, Pries Axel R. et al. (1995) published a series of papers (Pries et al., 1998; 2001; 2003; Pries and Secomb, 2008; Pries et al., 2009) where they constructed a feedback loop between the discussed mechanisms and the blood vessel radii. Provided the resulting radius adaption dynamics leads to a stable state, this algorithm determines the blood vessel radii of a given network topology, in particular the relation between mother and daughter vessel radii at each junction without referring to Murray's law.

In this manuscript we explore the application of the adaptation algorithm to in silico arteriovenous networks and analyze the emerging vessel radii and blood flow characteristics. Initially, the networks created by our in-house simulation framework Tumor-code (Fredrich et al., 2018) are consistent with Murray's law. The vessel adaptation algorithm modifies each single vessel radius and we analyze the resulting distribution of radii. After validating our implementation by comparison with existing data in Section 3.1, we optimize the free model parameters for a fixed vessel network in Section 3.2 with respect to a maximally homogeneous blood flow in the capillary bed. In Section 3.3, we compare the distribution of radii from the initial networks with the one emerging after the application of the vessel adaptation algorithm to them.

2. Methods

2.1. The adaptation algorithm

Pries et al. (1998) presented a theoretical model to simulate vessel radii of arteriovenous networks. They constructed a feedback loop between the spatial position of the vessels (topology) and their biological functions including hydrodynamics, shear stress and metabolism of the surrounding tissue. For an elaborated review and some applications of the model see Secomb et al. (2012). In the following, we describe the vessel adaptation algorithm of Pries et al. (1998).

Considering a vessel of radius r during a time step Δt, its adaption or change $\Delta r = S_{tot} \, r \, \Delta t$ is proportional to the sum of five signals $S_{tot} = \sum_{i=1}^{5} S_i$ which are defined below.

S_1 - *Shear stress.* Based on the correlation between wall shear stress and vessel radius, the adaptation algorithm reduces the vessel radius whenever the wall shear stress (τ_w) falls below $1 \, \text{dyn/cm}^2 = 10^{-4}$ kPa and extends the radius otherwise, i.e:

$$S_1 = \log_{10}(\tau_w) \tag{2}$$

S_2 - *Blood pressure.* Pries Axel R. et al. (1995) studied the interaction of the transmural pressure P and the wall shear stress τ_e

Table 1
Parameters of the adaptation model. The values in the right column are used in Pries et al. (1998).

Signal	Free	Fixed
S_3	k_m	Q_{ref} = 40 nl/min
S_4	k_c	L = 1500 μm,
		S_0 = 40
S_5	k_s	

proposing a "pressure-shear" hypothesis

$$\tau_e(P) = 100 - 86 \exp\left(-5000\{\log_{10}[\log_{10}(P)]\}^{5.4}\right) \tag{3}$$

The functional form of the shear-pressure dependency is sigmoidally increasing from 14 dyn/cm^2 for pressures of 10 mmHg–100 dyn/cm^2 for pressures at 90 mmHg (Eq. (3)). With this

$$S_2 = -\log_{10}[\tau_e(P)] \tag{4}$$

S_3 - *Metabolic demand.* Similar to the idea of Murray (see Section 1 Introduction), the metabolic demand needs to be maintained at all times. Since oxygen is transported as cargo by the red blood cells (RBC), a constant volume flow of RBCs is required to sustain a constant oxygen supply. Given the volume flow of blood Q with hematocrit H, the volume flow of RBCs is HQ and maintained at a reference value Q_{ref} by the metabolic signal S_3.

$$S_3 = k_m \log_{10}\left(\frac{Q_{ref}}{HQ} + 1\right) \tag{5}$$

The definition of S_3 results in a strictly positive signal where the amplitude increases stronger for vessels with a lower flow rate ($HQ < Q_{ref}$) compared to vessels with a higher flow rate ($HQ > Q_{ref}$) than the reference flow Q_{ref}. In contrast to the biologically motivated reference flow, k_m is an unknown model parameter (compare Table 1).

S_4 - *Topological position.* S_4 is sensitive to the position of the vessel within the entire network structure. The signal propagates from the capillary bed to the most upstream vessel in the arterial branch and to the most downstream vessel in the venous branch. While the downstream propagation of metabolic waste to the draining vein is reasonable, the upstream signaling is less obvious, but recent studies confirmed that vessels communicate via electrical signals within their endothelial layer (Segal and Duling, 1986; de Wit et al., 2003; Bagher and Segal, 2011). In principle the algorithm works with arbitrary number of vessels per intersection. For simplicity, we limit the discussion to Y-shaped intersections (Fig. 1) where a vessel c has two downstream connections (to vessel a of length x_a and to vessel b of length x_b) in an arterial branch and two feeding vessels (vessel a of length x_a and vessel b of
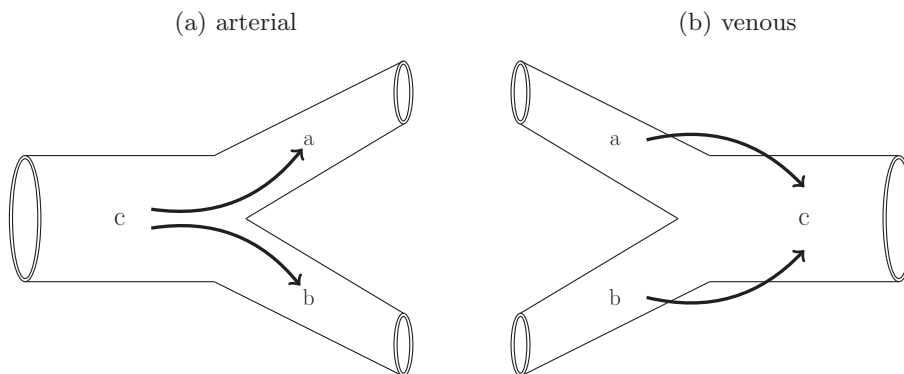

(a) arterial   (b) venous

Fig. 1. Recursive propagation of the conducted signal at a vessel junction. Left: Arterial case. Right venous case. Arrows indicate the direction of information propagation. See Eq. (6).

length x_b) in a venous branch. The conducted or topological signal is calculated in a recursive fashion by the weighted sum of the metabolic signals (S_3) along the direction of information propagation (Eq. (6)). The weighting factor is proportional to the exponential of the normalized length of the vessel segments ($\frac{x_a}{L}$ and $\frac{x_b}{L}$).

$$S_{4,c} = S_{3,a} + S_{3,b} + S_{4,a} \exp\left(-x_a/L\right) + S_{4,b} \exp\left(-x_b/L\right) \tag{6}$$

Since the recursive summation might result in excessive values, the signal is damped by a reference value S_0 such that the complete conducted signal for a single vessel becomes:

$$S_4 = k_c \frac{S_{4,c}}{S_{4,c} + S_0} \tag{7}$$

Note that the constant k_c, the reference value S_0 and the normalization length L are unknown model parameters (compare Table 1).

S_5 - *Shrinking tendency.* The introduction of a strictly positive metabolic (S_3) and conducted signal (S_4) necessitates a negative counterbalance. Its biological motivation is the tension in the endothelial layer which leads to a contraction of the vessel radius in the absence of all other signals. In the formula of the adaptation model this is embedded by subtracting a overall constant k_s.

$$S_5 = -k_s \tag{8}$$

2.2. The artificial blood vessel networks.

We construct artificial 3D arteriovenous networks by means of our simulation framework Tumorcode (Fredrich et al., 2018). We report the complete methodology in Rieger et al. (2016) and summarize only the main steps here. First, at least one arterial and one venous root node have to be distributed in space and assigned with a hydrodynamic boundary condition (either a blood pressure value or a flow rate) before straight or Y- shape elements are appended until the arterial and venous branch merge by the capillaries. Second, the position of the capillaries within the volume is optimized towards a homogeneous capillary volume density using a hierarchical iteration scheme. For the scope of this paper, we consider only a root node configuration (RC) where one artery is opposite to one vein on the same axis (Fig. 2, compare also RC5 in Fig. 4 of Welter et al., 2016) and a single hierarchical iteration. Since the construction algorithm in the Tumorcode fixes the radii of all capillaries (2.5 μm in presented case) and determines the radii of all intermittent vessels between root nodes and capillaries by Murray's law, all radii at the intersections fulfill Murray's law by construction. Therefore we label them **M-networks** in contrast to the **A-networks** which obtain their vessel radii by applying the adaptation algorithm to the **M-networks**.
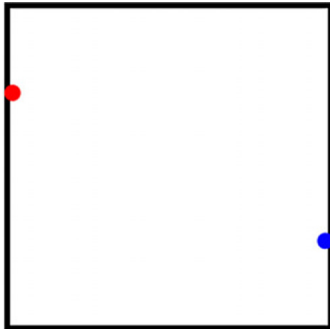
Fig. 2. Schematic root node configuration (RC) for construction the arteriovenous networks. Red (left): arterial root, blue (right): venous root.

2.3. Parameter optimization

Inspecting Section 2.1, we count six unknown model parameters as summarized in Table 1. Considering the additional hydrodynamic boundary condition at the two root nodes, we end up with 8 degrees of freedom for the model. To find the unknown parameters, we presume that a properly working vasculature requires a homogeneous flow inside the capillary bed to maintain the nutrient exchange and apply a computational optimization technique where the variance of the volume blood flow inside all capillaries ($Q_{capillaries}$) is used as cost function

$$f = Var(Q_{capillaries}) \tag{9}$$

We used particle swarm optimization (PSO) (Kennedy and Eberhart, 1995) to minimize the cost function f defined in Eq. (9). Although there is no guarantee to find the best solution, PSO finds at least a "robust" solution i.e. a solution that is robust against varying the initial conditions. In our case, the initial conditions are the values of the parameters k_m, k_c and k_s. During the PSO, we vary these parameters in the range of 0.5–4.0 for each fixed set of hydrodynamic boundary conditions. The hydrodynamic boundary conditions are the arterial inlet flow and the venous outlet pressure which we also varied in a systematic way (see supplemental text).

The numerical values of $Q_{ref} = 40$ nl/min, $L = 1500$ μm and $S_0 = 20$ were kept fix at the values reported in Pries et al. (1998).

All exact numbers, computational details and the implementation are reported in a supplemental text to this manuscript.

2.4. Definition of biophysical quantities

Given a blood vessel network inside a volume V that consists of N tubes with radii r_i and lengths l_i, two quantities of interest are the regional blood volume (rBV) and the surface to volume ratio (s2v).

2.4.1. Regional Blood Volume (rBV)
The regional blood volume measures the percentage of blood within the volume.

$$rBV = \frac{\sum_{i=1}^{N} \pi r_i^2 l_i}{V} \tag{10}$$

2.4.2. Surface to volume ratio (s2v)
The surface to volume ratio measures the ratio between the surface of an object and the volume included by this surface. Since nutrient exchange happens across the vessel surface, the exchange is proportional to the surface and therefore the s2v is an interesting quantity.

$$s2v = \frac{1}{N} \sum_{i=1}^{N} \frac{2\pi r_i l_i}{\pi r_i^2 l_i} \tag{11}$$

3. Results

3.1. Reproducing available data

We applied our implementation of the adaptation algorithm to a experimentally determined rat mesentery network. Since the hydrodynamic boundary conditions were measured, we incorporated them accordingly. The same procedure was done in Pries et al. (1998) (Network I). Unfortunately, the used time step Δt is not documented. We used $\Delta t = 0.1$ and the other adaptation parameters in Table 2. To verify our implementation, we reproduced two figures comparing the shear stress, vessel diameters, and the adaptation signals S_1, S_2, S_3 and S_4 before and after application of the algorithm.
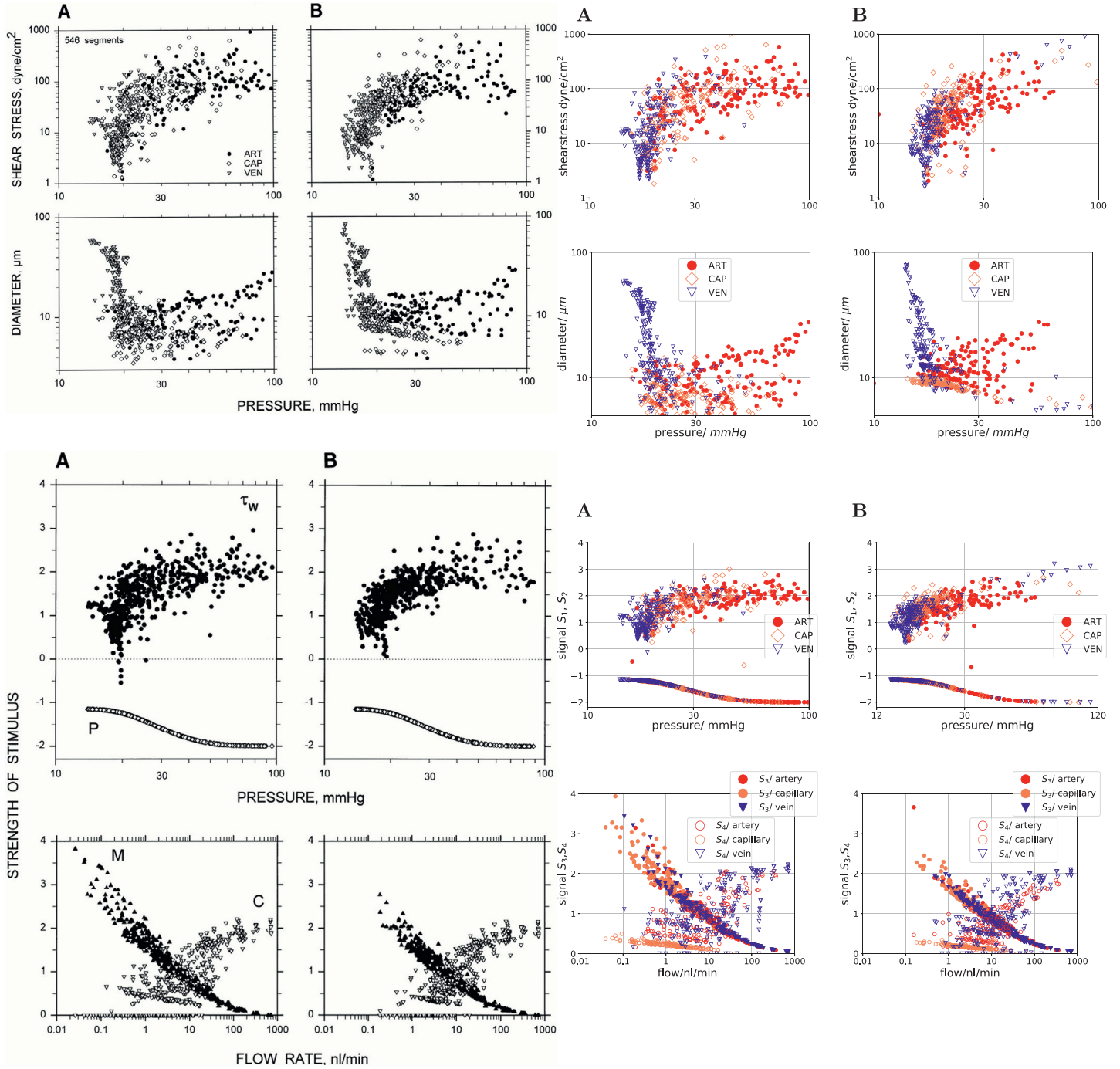
Fig. 3. Left column (black and white): reprint of Fig. 4 and 5 from Pries et al. (1998) with permission. Right column (colored): reproduced by our implementation/ software. (A): Values obtained with experimentally determined vessel diameters, (B): values obtained by simulated vessel adaptation. Top and second from top row: Distribution of shear stress and diameter for a rat mesentery network with 546 segments (162 arterioles, 167 capillaries and 217 venules). Hemodynamic parameters were calculated using the network flow model based on measured network morphology and topology. Last before bottom row: hydrodynamic stimuli derived from shear stress (τ_w) and blood pressure (P) are plotted as functions of pressure. Last row: the metabolic (M) and conducted stimuli (C) are plotted as functions of flow rate, to show functional dependence of these stimuli. (For interpretation of the references to colour in this figure legend, the reader is referred to the web version of this article.)

Table 2
Parameters used to adapt vessel radii of rat mesentery network with Tumorcode. Parameter labeled by * is not shown in Pries et al. (1998).

k_c	k_m	k_s	Q_{ref}	S_0	Δt	L
2.74	0.83	1.79	40 nl/min	20	0.1*	1500 μm

Due to the lack of quantitative data in Pries et al. (1998) we cannot compare directly, but our figures are in qualitative agreement with the original (Fig. 3). For the hydrodynamics (top row and second from top row of Fig. 3), we observe that the shear

stress saturates with increasing blood pressure (top row) and the diameter varies for veins in a broader range than for the arteries with the same pressure (second row). The adaptation tends to increase the radius of the capillaries (coral labeled points in rightmost image of second row). For the distribution of the adaptation signals S_1 and S_2 (last before bottom row of Fig. 3), we find vessels in the adapted network with a higher blood pressure than 100 mmHg and therefore we extended the pressure axis (x-axis) to 120 mmHg. For the distribution of the adaptation signals S_3 and S_4 (bottom row of Fig. 3), we find that adaptation shifts the spectrum towards increased flow. In agreement with model assumptions,

161
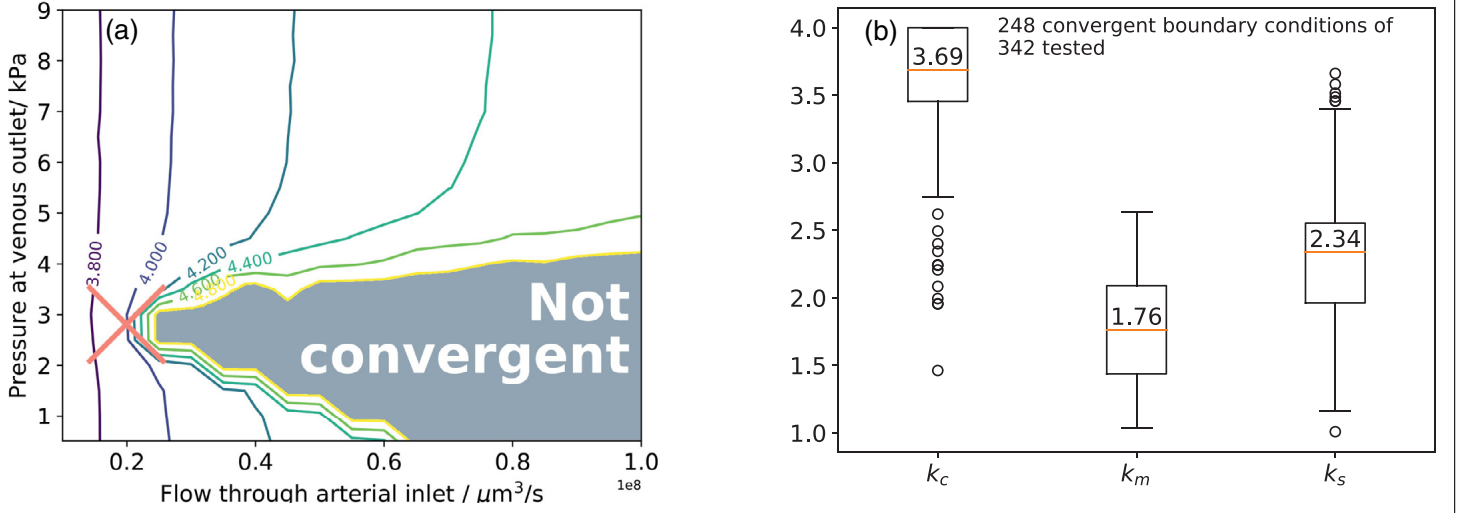
Fig. 4. Results of the particle swarm optimization (PSO). (a) Contour plot of the logarithm of the cost function f (Eq. 9) used for the PSO. x-axis: flow boundary condition at the arterial inlet. y-axis: pressure boundary condition at the venous outlet. The cross shows the boundary conditions used in Section 3.3; (b) Distribution of optimized choice for k_m, k_c and k_s. Only the convergent hydrodynamic boundary conditions are considered. The median value is write above the corresponding line.
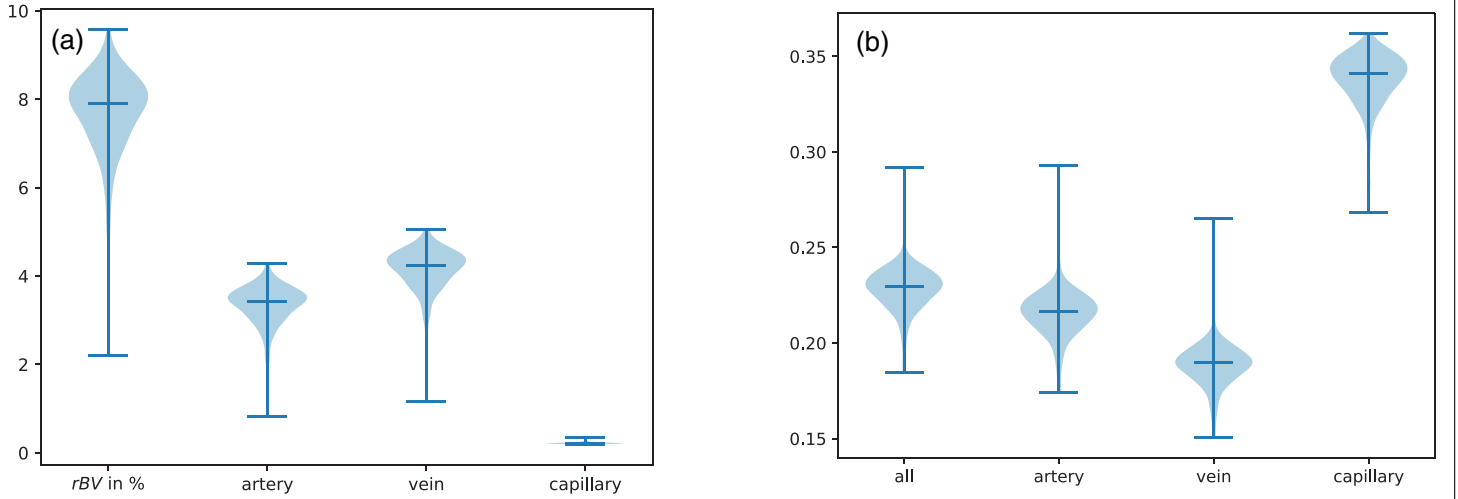
Fig. 5. Biophysical variables influenced by the adaptation algorithm. Distribution is obtained from a single configuration of vessels in space (Section 3.2), but different radii distributions obtained during particle swarm optimization. We considered the 248 convergent boundary conditions here. (a) Distribution of regional blood volume (rBV); (b) Distribution of surface to volume ratio ($s2v$) in 1/µm.

the metabolic signal/ demand (S_3) is higher for low flow segments and the conducted signal (S_4) increases for segments with higher flow that are more up or downstream respectively.

3.2. Single topology, varying boundary conditions

As already discussed in Pries et al. (1998), there are two possible outcomes when applying the adaptation scheme in a repeated manner: either one reaches a steady state where the changes of radii become arbitrary small with each iteration or the radii changes increase to unrealistic values which also implies unrealistic values for pressure and flow, and are not further consider.

In the remaining, we switch from the rat mesentery network to synthetic arteriovenous networks constructed by Tumorcode. We start with a single fixed topology and apply the optimization procedure described in Section 2.3. Thereby we identified the hydrodynamic boundary conditions and parameters that result in convergence of the adaptation algorithm with the fixed network topology (see Fig. 4(a)) and achieved an optimal homogeneity in the blood flow of the capillaries. Interestingly, the distribution of

optimization parameters (Fig. 4(b)) indicates the same relation between the parameters ($k_m < k_s < k_c$) as found by Pries et al. in their three samples of rat mesentery networks (Pries et al., 1998).

To estimate the biological relevance of the optimized networks, we analyze two biophysical variables (Section 2.4): The regional blood volume (Fig. 5(a)) and the surface to volume ratio (Fig. 5(b)). The total regional blood volume varies within a physiological regime from 2% up to 10% (left column in Fig. 5(a)). To estimate the contributions from arteries, capillaries and veins to the total rBV, we segmented them in Fig. 5(a).

The results for the surface to volume ratio are shown in similar fashion (Fig. 5(b)). As expected, the surface to volume ratio is highest for small capillaries, smaller for arteries and the smallest for the large veins.

3.3. Varying topology, fixed boundary conditions

In contrast to the previous section, we now 1) keep the hydrodynamic boundary conditions and adaptation parameters fixed and 2) vary the topological arrangement of the vessels i.e. we
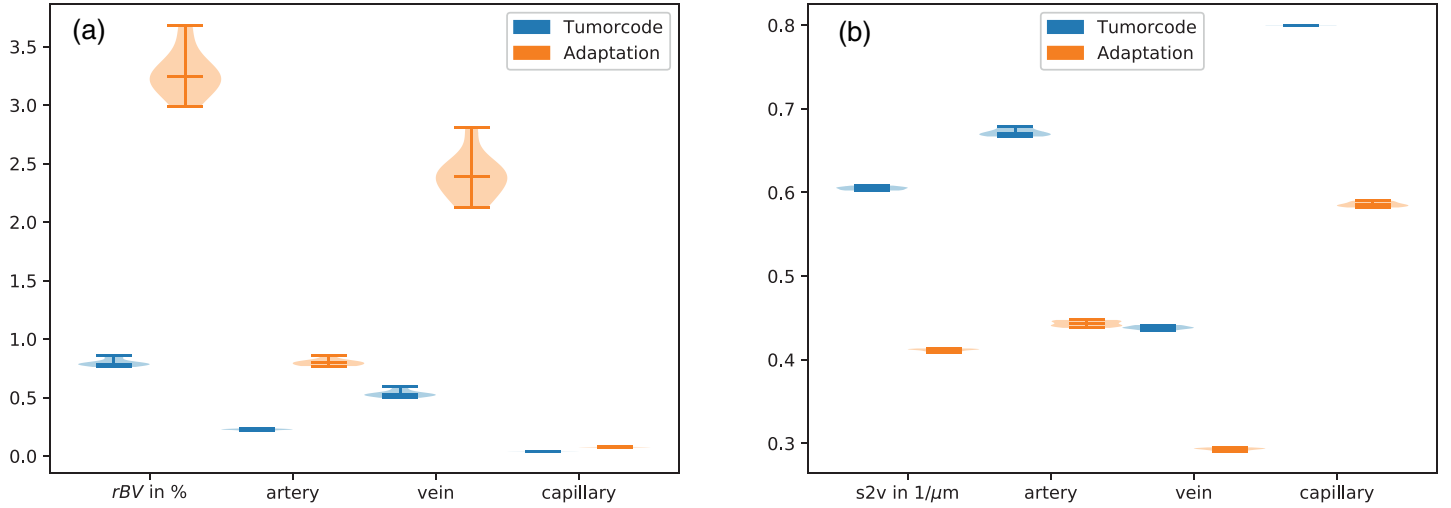
Fig. 6. Biophysical variables influenced by the adaptation algorithm. Distribution is taken from 10 different arrangements of vessels in space with radii obtained by 1) construction by Tumorcode (blue) and 2) application of the adaptation algorithm with a fixed set of parameters (Table 2, orange). (a) Distribution of regional blood volume (*rBV*); (b) Distribution of surface to volume ratio (*s2v*) in 1/μm. (For interpretation of the references to colour in this figure legend, the reader is referred to the web version of this article.)

Table 3
Mean value and standard error of the mean for rBV and s2v averaged over the 10 considered networks.

		All types	Artery	Vein	Capillary
rBV	Tumorcode	0.80 ± 0.03	0.227 ± 0.006	0.532 ± 0.03	0.039 ± 0.001
	Adaptation	3.3 ± 0.2	0.80 ± 0.03	2.4 ± 0.2	0.076 ± 0.003
s2v	Tumorcode	0.605 ± 0.002	0.672 ± 0.004	0.439 ± 0.002	0.8^{*}
	Adaptation	0.412 ± 0.001	0.443 ± 0.003	0.293 ± 0.002	0.586 ± 0.003

* Note that the radius of a capillary is fixed in synthetic networks constructed by Tumorcode. Data also visualized in Fig. 6.

grow different networks with same root node configuration. Based on the results of the PSO (red cross in Fig. 4(a)), we decided to use a pressure of 2.8 kPa at venous outlet and a volume flow rate of $2 \cdot 10^7$ μm^3/s at the arterial inlet to create 10 independent realizations of arteriovenous networks (**M-networks**) of lateral size 1500 μm (see Section 2.2).

3.3.1. Biophysical quantities

We apply the adaptation algorithm with the parameter set listed in Table 2 to the 10 samples. Hence we constructed 10 **A-networks** which we compare regarding their regional blood volume rBV (Fig. 6(a)) and their surface to volume ratio s2v (Fig. 6(b)) to the **M-networks** (numerical values listed in Table 3).

For the **A-networks**, the overall rBV is more than 4 times higher than for the **M-networks** (left column of Fig. 6(a)). In each case, the contribution of the veins to the rBV is the highest (66% for Tumorcode and 72% for Adaptation). For the **M-networks**, the overall s2v ratio is about 1.5 times higher than for the **A-networks** (left column of Fig. 6(b)). The s2v is highest at the capillary bed followed by the arteries and the veins.

The observed behavior follows from the hierarchical structure of the vascular network. Considering a fixed volume and vessels with fixed segment length (as in our case), the s2v scales proportional to the inverse of the radius and the rBV scales proportional to the vessel radius squared (Section 2.4). Since capillaries are smaller than arteries and veins in a hierarchical structure, the s2v increases and the rBV decreases when going from the upper (artery, vein) to the lower level (capillary), as observed.

Essentially, the **M-networks** feature systematically smaller vessel radii increasing the s2v ratio at the cost of higher flow resistance.

3.3.2. Adaptation signals

Similar to Fig. 3, we plot: a) The hydrodynamic characteristics (top and next to top row in Fig. 7), b) the hydrodynamic signal (last before bottom row in Fig. 7), and c) the conducted and metabolic signals (bottom row in Fig. 7) for one representative of the **A-networks** in Fig. 7. For the other nine networks, the plots look qualitatively similar.

Before adaptation, there is no correlation between the wall shear stress and the pressure, and since the signal S_1 (positive values of last before bottom row) depends only on the logarithm of the shear stress, there is also no functional dependence of S_1 on the pressure. After the adaptation however, the dependence of the shear stress and the signal S_1 on the pressure becomes more pronounced (right column of Fig. 7): Veins approach a plateau with increasing pressure and the arteries with decreasing pressure. For the shear stress, the plateau is between 50–100 dyn/cm^2 and for the signal S_1 around 2. The diameter depends on the pressure as expected for our networks: starting with the vessels of the smallest diameter (the capillaries), the diameter increases as we raise the pressure along the arterial branch and decrease the pressure along the venous branch (second row of Fig. 7). The negative values in the last before bottom row of Fig. 7 present the signal S_2 (Eq. 4). Here we notice that the values for S_2 are more restricted for veins (between -1.2 and -1.7) than for arteries (between -1.1 and -2.0). The metabolic and conducted signal (bottom row of Fig. 7) shift their maximum / minimum from 0.01 nl/min to increased flows at about 1 nl/min.

3.3.3. Visual inspection

Although the distribution of radii changes from the **M-networks** (bottom left of Fig. 8) to **A-networks** (bottom right
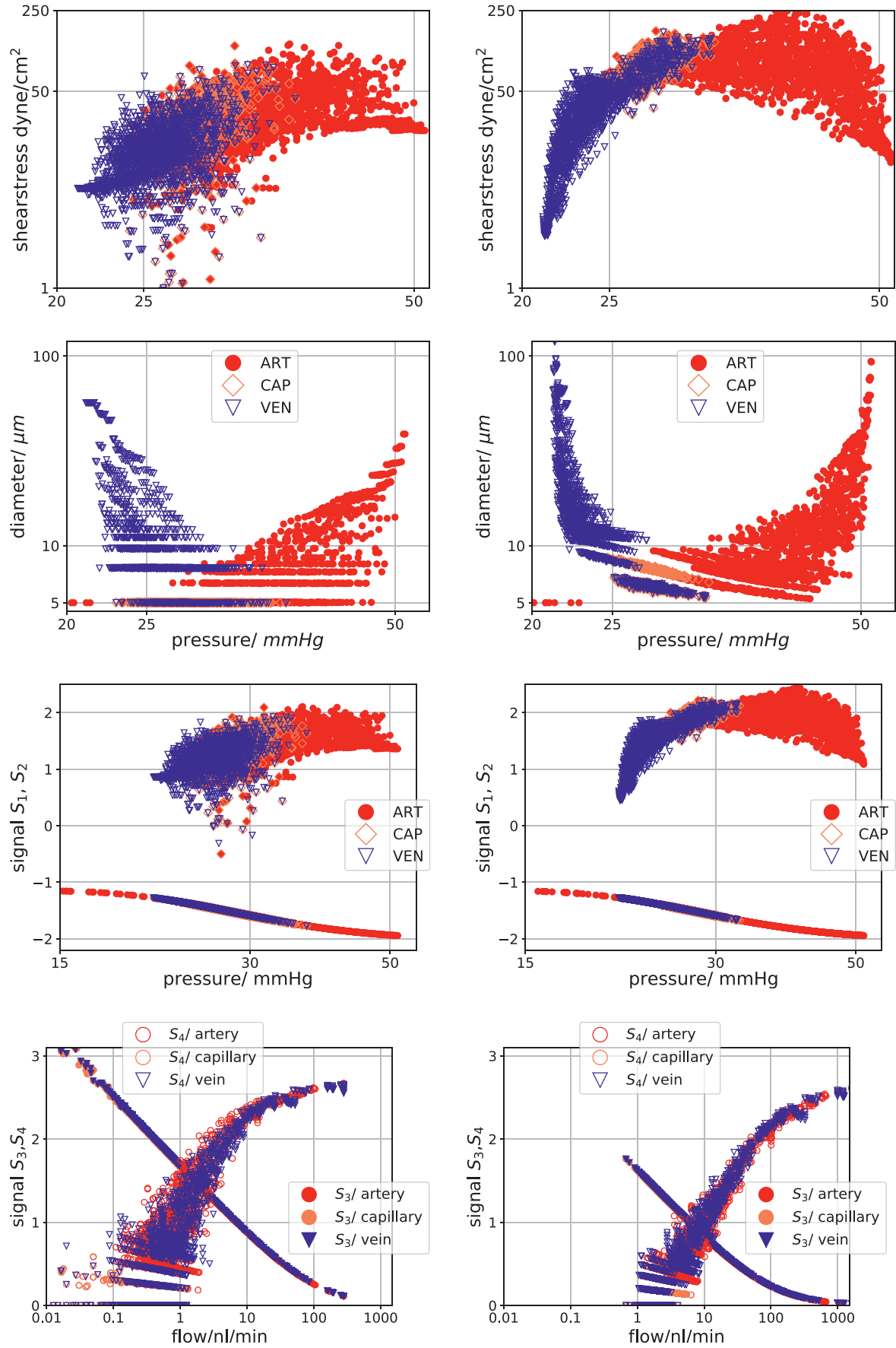
Fig. 7. The characteristics for a single arteriovenous network. Left column: Without adaptation. Right column: convergent adaptation with parameters listed in Table 2. A graphical representation of this particular network is shown in Fig. 8. From top to bottom we compare the shear stress, the vessel diameter, the hydrodynamic signals (S_1 and S_2 of Section 2.1) and the metabolic and conducted signal (S_3 and S_4 of Section 2.1). (For interpretation of the references to colour in this figure legend, the reader is referred to the web version of this article.)
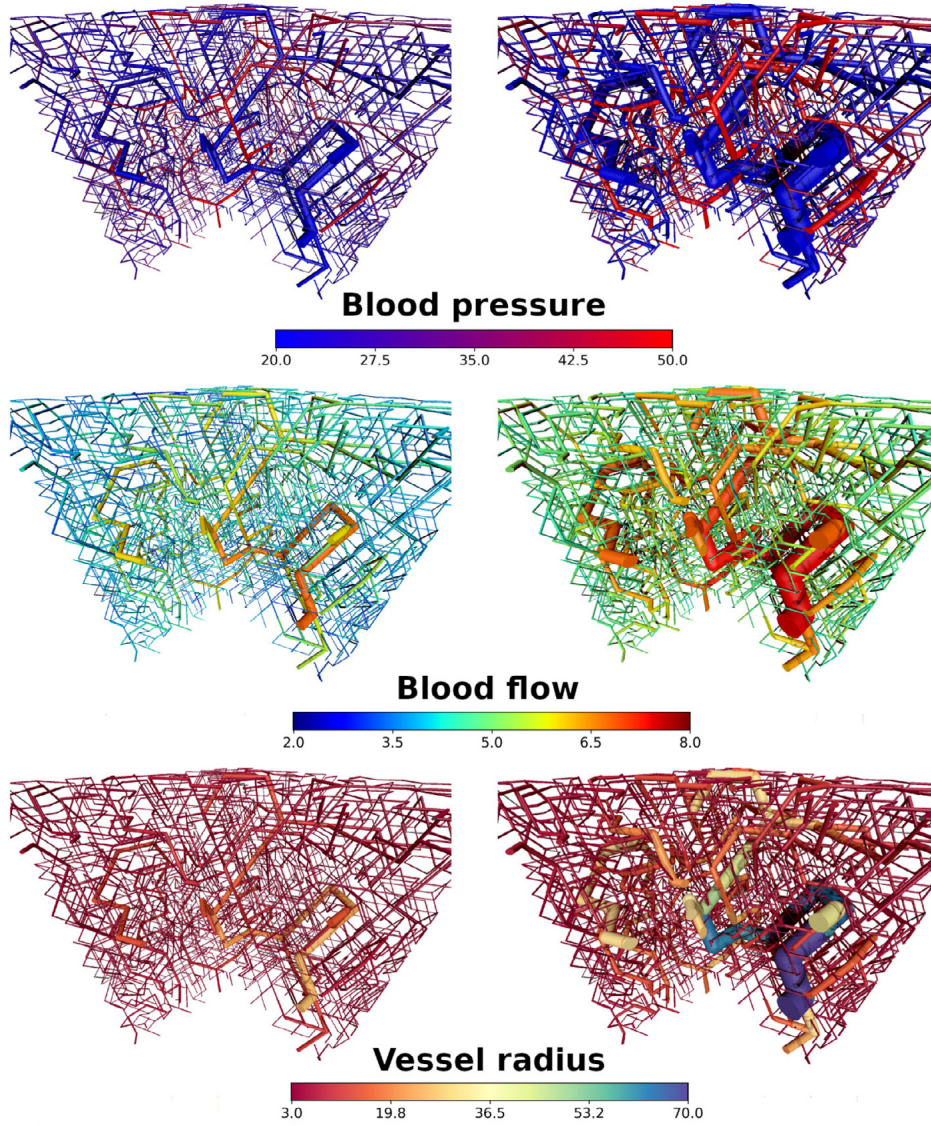
Fig. 8. Color coded vessel properties for one representative of the ensemble of synthetic arteriovenous networks. Left column: radii distribution from Tumorcode (Murray's law). Right column: Radii distribution after adaptation. From top to bottom: Pressure in mmHg, volume flow (logarithmic scale) in μm³/s, radius in μm. (For interpretation of the references to colour in this figure legend, the reader is referred to the web version of this article.)

column of Fig. 8), the distribution of the blood pressure does not change because of the fixed boundary conditions (colors of top row in Fig. 8). The shear force is proportional to the flow and therefore the distribution of the shear force looks similar to the distribution of flow as show in the center row of Fig. 8. In the bottom row of Fig. 8, we colored the vessel by their radii to highlight changes of the vessel radii by the adaptation algorithm.

Finally, Fig. 9 shows data that is only available in the adaptation case (metabolic signal and conducted signal). In agreement with model assumptions, the metabolic signal is highest at the thin capillaries and the conducted signal is highest at the most distal points.

3.4. Murray's law

The networks created by Tumorcode fulfill Murray's law by construction (Section 2.2). Here we check for a single network (shown in Fig. 8) whether it still fulfills Murray's law after the application of the adaptation algorithm.

In Fig. 10 we plot for each bifurcation the cubic root of the sum of daughter vessel radii cube against the radius of the mother vessel. If the mother and daughter vessel radii would fulfill Murray's

law, the data points would lie on the straight line, which they do remarkably closely. Applying Murray's law locally at each bifurcation in large networks results in a complicated dependence of the vessel radius on the global vessel arrangement. Nevertheless the distribution of the differences between the radii of two daughter vessels in **M-networks** displays characteristic features like discrete peaks at specific difference values, as shown in Fig. 11. This can be understood as follows: since the network construction algorithm of Tumorcode uses a fixed capillary radius and a discrete vessel length (on a lattice), repeated application of Murray's law leads more often to the same proportions at an intersection. To illustrate this, we use a hypothetical capillary bed as shown in Fig. 12. For the bifurcations b_1, b_2 and b_3 (Fig. 12), we calculate the quantity used in the histogram shown in Fig. 11: The differences of the daughter vessel radii normalized by the mother vessel radius.

b_1	b_2	b_3
$\frac{2.5\mu m - 2.5\mu m}{3.15\mu m} = 0.0$	$\frac{3.15\mu m - 2.5\mu m}{3.61\mu m} = 0.18$	$\frac{3.61\mu m - 2.5\mu m}{3.97\mu m} = 0.28$

The three highest peaks of the histogram are located around the calculated values (0.0, 0.18 and 0.28).
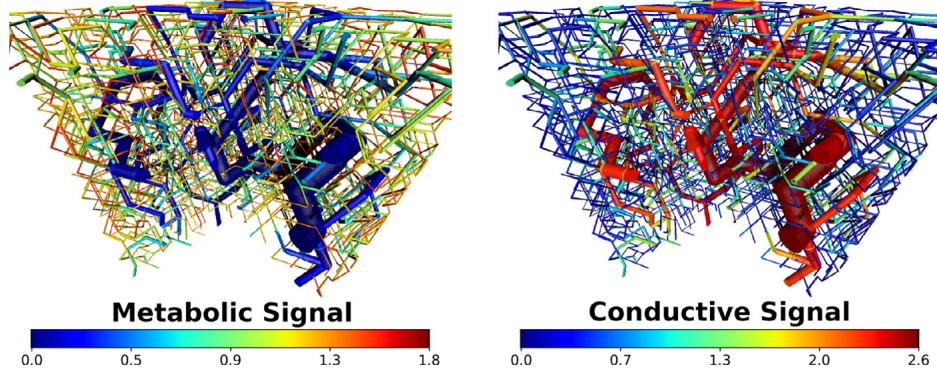
Fig. 9. Adaptation signals (Section 2.1) for one representative of the ensemble of synthetic arteriovenous networks. Left column: Metabolic signal (S_3) Right column: conducted signal (S_4). (For interpretation of the references to colour in this figure legend, the reader is referred to the web version of this article.)
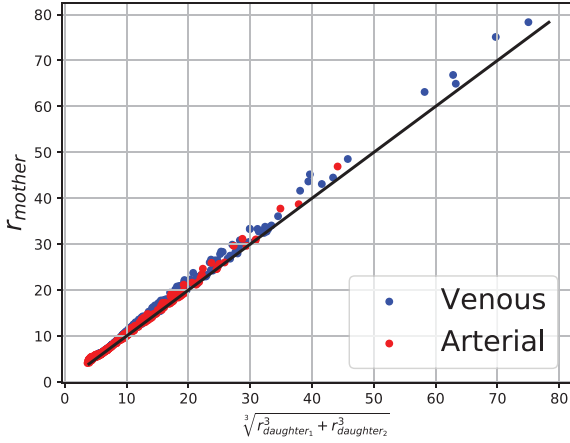
Fig. 10. The black diagonal represents Murray's law for $\alpha = 3$. The data points are taken from the A-network shown in Fig. 8 in the right column. Blue dots are venous intersections (431) and red dots are arterial intersections (475). (For interpretation of the references to colour in this figure legend, the reader is referred to the web version of this article.)

On the other hand, the distribution of the differences between the radii of daughter vessels in **A-networks** is much smoother and lacks discrete peaks. The adaptation algorithm adjusts each vessel radius and removes the initial vessel radii discretization, resulting

in a radii distribution in **A-networks** that differs significantly from **M-networks**. The more remarkable is the observation that the radii still obey Murray's law very closely.

4. Discussion

We compared arteriovenous networks constructed by the Tumorcode (**M-networks**, radii obey Murray's law by construction) with networks having the same topology, but with vessel radii obtained by the adaptation algorithm (**A-networks**).

The most interesting result is that structural adaptation leads to a network that differs significantly from one generated by strict application of Murray's law, yet the adapted network satisfies Murray's law quite closely. Small but systematic deviations from Murray's law at each bifurcation level (compare Fig. 10) accumulate over subsequent levels and result in generally larger vessel radii in **A-networks** compared to **M-networks** and consequently in global differences in regional blood flow (rBV) and surface to volume ratio (s2v). A quantitative analysis of rBV (Fig. 5(a), 6(a) and Table 3) and s2v (Fig. 5(b), 6(b) and Table 3) confirms that the **A-networks** carry more blood while the **M-networks** show a higher surface to volume ratio — especially at the capillary level — at the expense of an elevated flow resistance.

Moreover, the adaptation algorithm smoothens the distribution of the differences of the radii of the two daughter vessels at each

(a) Tumorcode
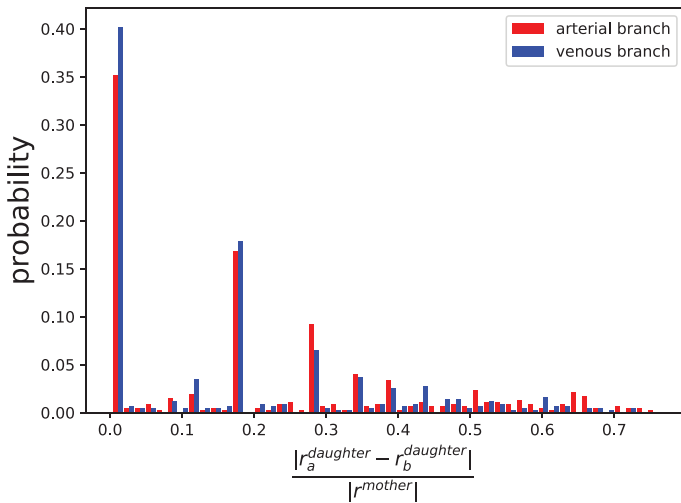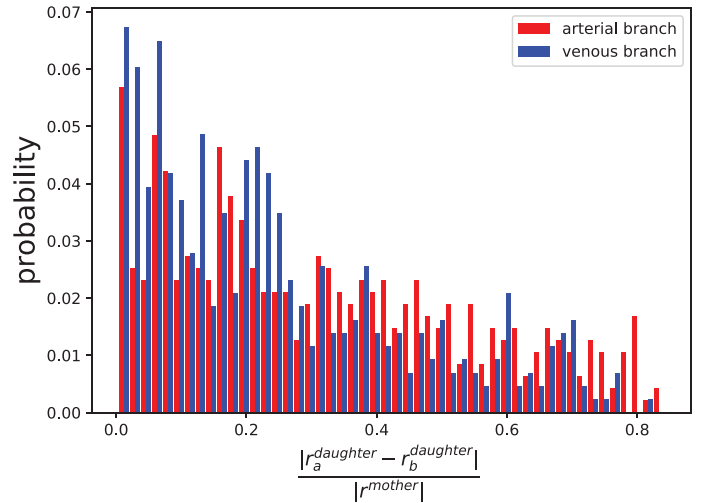
(b) Adaptation

Fig. 11. Normalized distribution of differences between two daughter vessels at a Y- shaped intersection. The used topology is the same for both cases and shown in Fig. 8. Left column: before adaptation (vessel radii fulfilling Murray's law by construction in Tumorcode). Right column: same topology as left column but vessel radii adapted with parameter set listed in Table 2. (For interpretation of the references to colour in this figure legend, the reader is referred to the web version of this article.)
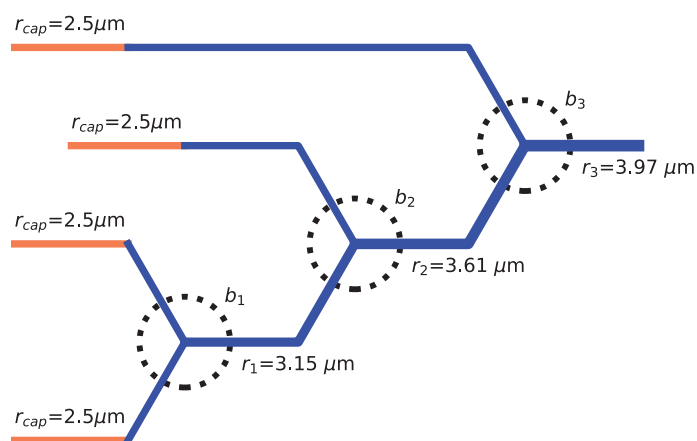
Fig. 12. Schematic view on capillary bed as constructed by the Tumorcode Software. The vessels indicated in coral are capillaries with radius r_{cap}=2.5 μm. At bifurcation b_1, b_2 and b_3 the upstream vessel radii r_1, r_2 and r_3 are calculate by Murray's law with exponent 3. (For interpretation of the references to colour in this figure legend, the reader is referred to the web version of this article.)

bifurcation. This observation demonstrates that for a given network topology more than one radii distribution can fulfill Murray's law, at least very closely. The reproduction of Murray's law by structural adaptation is particularly remarkable since the algorithm produces radii variation due to signals involving chemical energy (metabolic signal), the tension of endothelial layer (shrinking tendency) and non-local contributions (conducted signal). It is interesting to find a relation close to Murray's law although drag and flow are not directly used in the adaptation model. Instead, our choice of the objective function in the optimization procedure (Section 2.3) is based on a requirement for optimal homogenization of the capillary flow. Among several other objective functions, we found that minimizing the overall variance of the capillary flow achieves convergence of the adaptation algorithm for our synthetic arteriovenous networks.

It would be interesting to study structural adaptation in the case of pathological networks such as blood vessel networks modified by a growing tumor (Carmeliet and Jain, 2000), involving angiogenesis, vessel regression and collapse. We tried to include the adaptation algorithm into our model of tumor vascularization (Welter and Rieger, 2010; Rieger et al., 2016; Welter et al., 2016), implemented in Tumorcode (Fredrich et al., 2018). Using a convergent set of adaptation parameters for a given arteriovenous network (as analyzed in this manuscript), the convergence was not achieved when the network topology is subsequently altered during tumor growth. The potential reasons for the failure of convergence are analyzed in a supplemental text. A successful application of the adaptation algorithm in the presence of vascular remodeling was reported in Secomb et al. (2013): Angiogenesis combined with vascular pruning based on low oxygen saturation resulted in stable radii distributions. The application of structural adaptation amended by angiogenesis and pruning to vascular remodeling in growing tumors is topic of future research. So far, there seems to be no consensus in the field how to include structural adaptation into vascular tumor growth. The discussion of the stability of networks with low generation shunts in the appendix of Pries et al. (1998) proves that the adaptation algorithm cannot be stable without the conducted signal. However, some mathematical models of vascularized tumor growth include vessel radius adaptation (McDougall et al., 2006), but no conducted signal, although it is an integral component of the structural adaptation theory, at least in the non-cancerous setting.

The signals introduced by the adaptation algorithm are based on biological relevant processes which provide an input for mathematical modeling. Currently the signals are modeled with parameters (compare Table 1), but in the future the variations in endothelial cell membrane potential along a vessel or its metabolic uptake might become experimentally measurable fixing the free parameters of the adaptation model used here.

5. Data availability

We support open science by sharing our software and the created raw data at www.zenodo.org.

5.1. Software

A developer version of the Tumorcode software tool (Fredrich et al., 2018) is hosted at www.github.com/thierry3000/tumorcode. For the presented manuscript, we worked with the Pre-release v1.1.0-alpha.1 (Adaptation) version of the code which we also archived (Fredrich and DaWelter, 2019).

5.2. Data

We store the results of executed simulations, the used settings and parameters, the network topologies and the images in a single compressed archive (Fredrich, 2019).

Supplementary material

Supplementary material associated with this article can be found, in the online version, at doi:10.1016/j.jtbi.2019.109989.

References

Adair, T.H., Gay, W.J., Montani, J.P., 1990. Growth regulation of the vascular system: evidence for a metabolic hypothesis. Am. J. Physiol.-Regul. Integr. Compar. Physiol. 259 (3), R393–R404. doi:10.1152/ajpregu.1990.259.3.R393.

Bagher, P., Segal, S.S., 2011. Regulation of blood flow in the microcirculation: role of conducted vasodilation. Acta physiologica (Oxford, England) 202 (3), 271–284. doi:10.1111/j.1748-1716.2010.02244.x.

Banavar, J.R., Maritan, A., Rinaldo, A., 1999. Size and form in efficient transportation networks. Nature 399 (6732), 130–132. doi:10.1038/20144.

Berne, R.M., 1964. Metabolic regulation of blood flow. Circul. Res. 15, SUPPL:261–268.

Berne, R.M., Knabb, R.M., Ely, S.W., Rubio, R., 1983. Adenosine in the local regulation of blood flow: a brief overview. Feder. Proc. 42 (15), 3136–3142.

Björnberg, J., Maspers, M., Mellander, S., 1989. Metabolic control of large-bore arterial resistance vessels, arterioles, and veins in cat skeletal muscle during exercise. Acta Physiologica Scandinavica 135 (2), 83–94. doi:10.1111/j.1748-1716.1989.tb08555.x.

Carmeliet, P., Jain, R.K., 2000. Angiogenesis in cancer and other diseases. Nature 407 (6801), 249. doi:10.1038/35025220.

Ellsworth, M.L., 2004. Red blood cell–derived ATP as a regulator of skeletal muscle perfusion. Med. Sci. Sports Exer. 36 (1), 35. doi:10.1249/01.MSS.0000106284.80300.B2.

Fredrich, T., 2019. Dynamic vessel adaptation in synthetic arteriovenous networks. Technical Report. Zenodo doi:10.5281/zenodo.2710926.

Fredrich, T., DaWelter, 2019. thierry3000/tumorcode: adaptation. doi:10.5281/zenodo.2710460.

Fredrich, T., Welter, M., Rieger, H., 2018. Tumorcode. Eur. Phys. J. E 41 (4), 55. doi:10.1140/epje/i2018-11659-x.

Jacobsen, J.C.B., Gustafsson, F., Holstein-Rathlou, N.-H., 2003. A model of physical factors in the structural adaptation of microvascular networks in normotension and hypertension. Physiol. Meas. 24 (4), 891–912. doi:10.1088/0967-3334/24/4/007.

Kennedy, J., Eberhart, R., 1995. Particle swarm optimization. In: Proceedings of ICNN'95 - International Conference on Neural Networks, 4, pp. 1942–1948 vol.4. doi:10.1109/ICNN.1995.488968.

McDougall, S.R., Anderson, A.R.A., Chaplin, M.A.J., 2006. Mathematical modelling of dynamic adaptive tumour-induced angiogenesis: clinical implications and therapeutic targeting strategies. J. Theoret. Biol. 241 (3), 564–589. doi:10.1016/j.jtbi.2005.12.022.

Murray, C.D., 1926. The physiological principle of minimum work. Proc. Natl. Acad. Sci.United States Am. 12 (5), 299–304.

Pries, A.R., Cornelissen, A.J.M., Sloot, A.A., Hinkeldey, M., Dreher, M.R., Höpfner, M., Dewhirst, M.W., Secomb, T.W., 2009. Structural adaptation and heterogeneity of normal and tumor microvascular networks. PLoS Comput. Biol. 5 (5), e1000394. doi:10.1371/journal.pcbi.1000394.

Pries, A.R., Reglin, B., Secomb, T.W., 2001. Structural adaptation of microvascular networks: functional roles of adaptive responses. Am. J. Physiol. 281 (3), H1015–H1025.

Pries, A.R., Reglin, B., Secomb, T.W., 2003. Structural response of microcirculatory networks to changes in demand: information transfer by shear stress. Am. J. Physiol. 284 (6), H2204–H2212. doi:10.1152/ajpheart.00757.2002.

Pries, A.R., Secomb, T.W., 2008. Modeling structural adaptation of microcirculation. Microcirculation (New York, N.Y. : 1994) 15 (8), 753–764. doi:10.1080/10739680802229076.

Pries, A.R., Secomb, T.W., Gaehtgens, P., 1998. Structural adaptation and stability of microvascular networks: theory and simulations. Am. J. Physiol. 275 (2), H349–H360.

Pries Axel, R., Secomb Timothy, W., Peter, G., 1995. Design principles of vascular beds. Circul. Res. 77 (5), 1017–1023. doi:10.1161/01.RES.77.5.1017.

Rieger, H., Fredrich, T., Welter, M., 2016. Physics of the tumor vasculature: theory and experiment. Eur. Phys. J. Plus 131 (2), 31. doi:10.1140/epjp/i2016-16031-9.

Secomb, T.W., Alberding, J.P., Hsu, R., Dewhirst, M.W., Pries, A.R., 2013. Angiogenesis: an adaptive dynamic biological patterning problem. PLoS Comput. Biol. 9 (3), e1002983. doi:10.1371/journal.pcbi.1002983.

Secomb, T.W., Dewhirst, M.W., Pries, A.R., 2012. Structural adaptation of normal and tumour vascular networks. BasicClin. Pharmacol. Toxicol. 110 (1), 63–69. doi:10.1111/j.1742-7843.2011.00815.x.

Segal, S.S., Duling, B.R., 1986. Flow control among microvessels coordinated by intercellular conduction. Science 234 (4778), 868–870. doi:10.1126/science.3775368.

Stephenson, D., Patronis, A., Holland, D.M., Lockerby, D.A., 2015. Generalizing murray's law: an optimization principle for fluidic networks of arbitrary shape and scale. J. Appl. Phys. 118 (17), 174302. doi:10.1063/1.4935288.

Thoma, R.A., 1893. Untersuchungen über die Histogenese und Histomechanik des Gefäss-systems, von Dr R. Thoma, ... F. Enke, Stuttgart. OCLC: 458283924

Welter, M., Fredrich, T., Rinneberg, H., Rieger, H., 2016. Computational model for tumor oxygenation applied to clinical data on breast tumor hemoglobin concentrations suggests vascular dilatation and compression. PLOS ONE 11 (8), e0161267. doi:10.1371/journal.pone.0161267.

Welter, M., Rieger, H., 2010. Physical determinants of vascular network remodeling during tumor growth. Eur. Phys. J. E 33 (2), 149–163. doi:10.1140/epje/i2010-10611-6.

Wetterdal, P., 1920. Beiträge zur Morphologie des Gefässsystems: Die Entwickelung der Gefässe in der Brustflosse bei Squalus Acanthias nebst Bemerkungen über die Entwickelung der Arterien der vorderen Extremitäten im Allgemeinen. J.F. Bergmann-Verlag München.

de Wit, C., Roos, F., Bolz, S.-S., Pohl, U., 2003. Lack of vascular connexin 40 is associated with hypertension and irregular arteriolar vasomotion. Physiol. Genomics 13 (2), 169–177. doi:10.1152/physiolgenomics.00169.2002.

3.4.2 Supplemental Material

Supplemental material for main text: "Dynamic vessel adaptation in synthetic arteriovenous networks"

Thierry Fredrich[a,*], Michael Welter[b], Heiko Rieger[a]

[a]*Saarland University, Campus E2.6, 66123 Saarbrücken, Germany*
[b]*TruPhysics GmbH, Seyfferstraße 34, 70197 Stuttgart, Germany*

*Corresponding author
Email address:* `thierry@lusi.uni-sb.de` (Thierry Fredrich)
URL: `https://www.github.com/thierry3000` (Thierry Fredrich),
`http://www.uni-saarland.de/fak7/rieger/index.html` (Heiko Rieger)

1. Details of the particle swarm optimization used in 3.1 "Single topology, varying boundary conditions"

Our aim was to use deap (Distributed Evolutionary Algorithms in Python) to spread the evaluation of multiple vessel adaptations with different boundary conditions and algorithm parameters across multiple processors.

1.1. Required Software

We used the Intel Parallel Studio XE 2018 with its compiler to achieve fast hardware execution times. The intel python bindings (IntelPython) were used consistently with Tumorcode. We had to install *libzmq* and the python bindings from source. We used SCOOP (Scalable COncurrent Operations in Python) which is nice module to distribute computational task from heterogeneous grids to supercomputers. In our case we used a small beowulf cluster (64 Nodes with up to 28 cores) hosted by the theoretical physics department of Saarland University. Apart from the aforementioned software the cluster runs operationg system Gentoo linux hardened SLURM queuing system.

1.2. Particle swarm optimization

We conducted Particle swarm optimization with the deap software based on their example in the documentation. Our source code is available on GitHub at: https://github.com/thierry3000/tumorcode. (py/krebs/adaption).

All optimizations listed in table 1 were conducted with a population of 320 individuals and 10 generations of mutation. We used 20 Nodes with 16 cores each to have 320 independent tasks. For the discussion presented in the main article, we evaluated the PSO with the parameter set value_list_14 however we performed more optimizations. All successful runs could be downloaded at: [1].

2

name	#boundary conditions	flow/10^7 μm^3/s	pressure/ kPa
value_list_11	160	1-9	3.5-4.5
value_list_12	160	1-9	3.5-4.5
value_list_13	864	1- 90	1.8-4.5
value_list_14	342	0.5-10	0.5-9.5

Table 1: Datasets resulting from successful PSO (downloadable at:). All optimizations were conducted with a population of 320 individuals and 10 generations of mutation.

2. Application to cancerous networks

The adaptation algorithm accounts for the modification of radii in blood vessel networks without topological modifications. In solid tumors, topological modifications are an essential part of the growth procedure and therefore considered in our simulation framework [2]. In [3], we simulated the oxygen distribution in breast carcinoma and found that an additional vessel dilation is required to obtain oxygen distributions in agreement with the clinical measurements. We conjectured that the adaptation algorithm could possibly provide a physiological mechanism for this vessel dilation. Indeed we observe the expected behaviour in a minimal example (figure 1): the high metabolic demand ($HQ < Q_{\text{ref}}$) of the vessels created by angiogenesis increases the radii during adaptation (see zoom in the upper right of figure 1). The new tumor vessels couple two previously uncoupled branches and thereby raise the topological signal in the connected branches as intended by the adaptation algorithm (see value of main inlet and outlet in bottom right of figure 1).

Although this works in this simplified example, we found that such modifications destabilize the convergence of the adaptation algorithm when occuring in a repeated manner or at multiple locations at the same time as it happens our simulations of tumor growth in large arteriovenous systems.

3
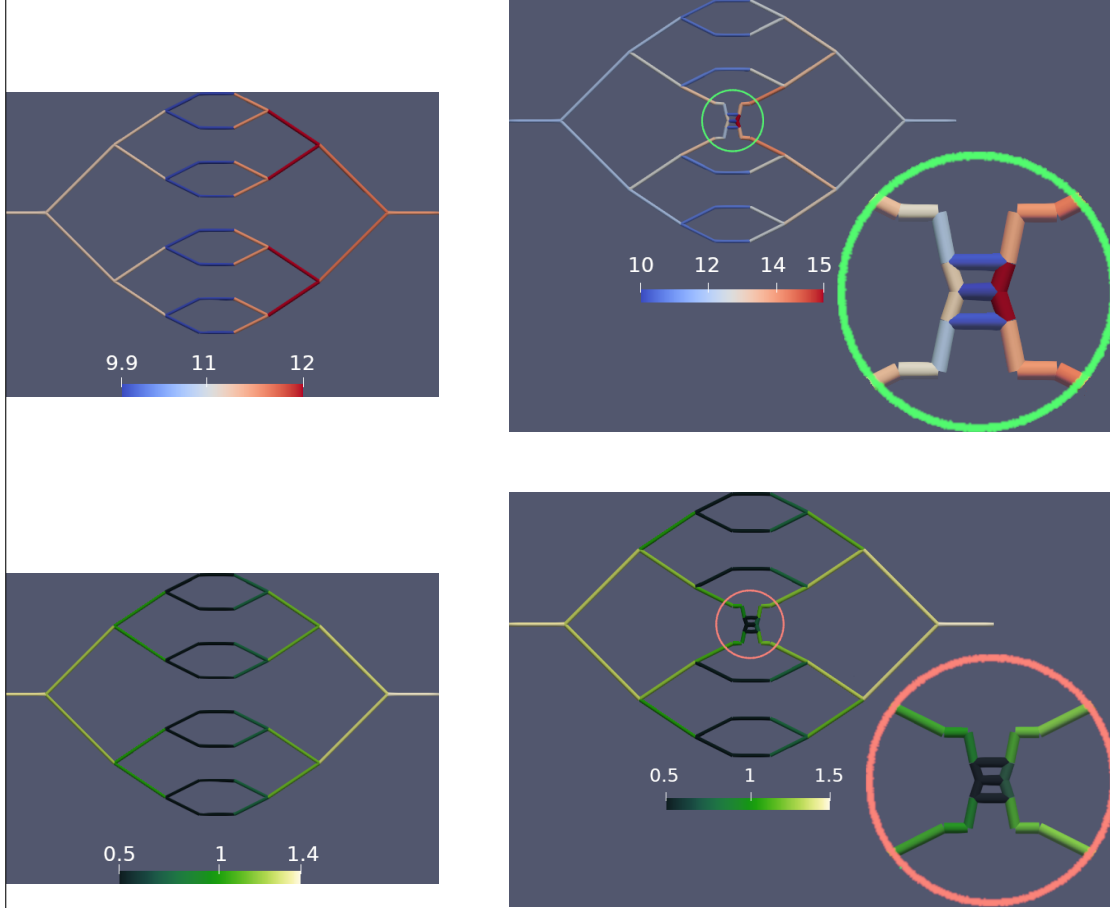
Figure 1: Critial behaviour during angiogenesis. We constructed a minimal example consisting of four closed capillary loops which is representative for the situation larger arteriovenous networks. Left column: w/o tumor, right column: slightly remodelled situation by angiogenesis during tumor growth with zoom into the critical area. Top row: vessels color-coded by their vessel radius. Bottom row: vessels color-coded by their value of the conducted signal. The complete example with the topology, the boundary conditions and the adaptation parameters is documented in the source code distributed with this manuscript or on GitHub at https://github.com/thierry3000/tumorcode (py/krebs/adaption/testAdaption.py)

4

References

[1] T. Fredrich, Dynamic vessel adaptation in synthetic arteriovenous networks, Tech. rep., Zenodo (May 2019). `doi:10.5281/zenodo.2710926`. URL `https://zenodo.org/record/2710926#.XNqrY6F8KV4`

[2] T. Fredrich, M. Welter, H. Rieger, Tumorcode, The European Physical Journal E 41 (4) (2018) 55 (Apr. 2018). `doi:10.1140/epje/i2018-11659-x`. URL `https://doi.org/10.1140/epje/i2018-11659-x`

[3] M. Welter, T. Fredrich, H. Rinneberg, H. Rieger, Computational Model for Tumor Oxygenation Applied to Clinical Data on Breast Tumor Hemoglobin Concentrations Suggests Vascular Dilatation and Compression, PLOS ONE 11 (8) (2016) e0161267 (Aug. 2016). `doi:10.1371/journal.pone.0161267`. URL `http://journals.plos.org/plosone/article?id=10.1371/journal.pone.0161267`

5

Chapter 4

Demarcation from the coauthors

Required by the regulations (see appendix A on page 199), I provide the written confirmation of my contributions to [1, 2, 3, 4] (reprinted in chapter 3) by all of my coauthors.

Contents

4.1 Prof. Dr. Dr. h.c. Heiko Rieger

Demarcation from Scientific Work of Thierry Fredrich (TF)

With my signature I (Prof. Dr. Dr. h.c. Heiko Rieger) confirm the following statements:

- I supervised TF during all steps of his PhD studies;
- Dr. Michael Welter (MW) conceived and designed the experiments reported in [1];
- TF assisted MW in implementing and performing the experiments reported in [1]. In particular TF compared the main numerical method to another available software at that time contributing Figure C in the supplemental material "S1 Appendix" of [1];
- TF revised the manuscript of [1] jointly with all the coauthors;
- Prof. Dr. Herbert Rinneberg and me suggested the scientific problem of [1]
- TF conceived and wrote the manuscript of [2] which was successively revised by all the coauthors;
- MW conceived the kernel modules reported in [2];
- I supervised the research project underlying [2];
- TF provided the supplemental material to [2] and maintained the source code;
- TF wrote the results part of [3];
- Prof. Dr. Edoardo Milotti (EM) wrote the other parts of [3];
- [3] was successively revised by all the coauthors including myself;
- TF and EM jointly designed an interface for the Virtual Biology Lab (VBL) and the Tumorcode software;
- TF and EM jointly optimized the parameters of the simulations reported in [3];
- TF conceptualized, conducted and analyzed the computational studies reported in [3] resulting in the figures and the movies;
- I designed the principles of Tumorcode;
- MW and TF developed the Tumorcode software;
- EM suggested the scientific problem of [3] and added the VBL software to the public domain;
- Prof. Dr. Roberto Chignola helped with biological aspects and assisted in parameter tuning of the combined simulation reported in [3];
- MW suggested the scientific problem of [4];
- TF conceived and conducted the numerical studies reported in [4];
- TF wrote the manuscript of [4] which was successively revised by all the coauthors;

12.11.2019

Date   Signature

References

[1] M. Welter, T. Fredrich, H. Rinneberg, and H. Rieger, "Computational Model for Tumor Oxygenation Applied to Clinical Data on Breast Tumor Hemoglobin Concentrations Suggests Vascular Dilatation and Compression," *PLOS ONE*, vol. 11, no. 8, p. e0161267, Aug. 2016. [Online]. Available: https://journals.plos.org/plosone/article?id=10.1371/journal.pone.0161267

[2] T. Fredrich, M. Welter, and H. Rieger, "Tumorcode," *The European Physical Journal E*, vol. 41, no. 4, p. 55, Apr. 2018. [Online]. Available: https://doi.org/10.1140/epje/i2018-11659-x

[3] T. Fredrich, H. Rieger, R. Chignola, and E. Milotti, "Fine-grained simulations of the microenvironment of vascularized tumours," *Scientific Reports*, vol. 9, no. 1, pp. 1–12, Aug. 2019. [Online]. Available: https://www.nature.com/articles/s41598-019-48252-8

[4] T. Fredrich, M. Welter, and H. Rieger, "Dynamic vessel adaptation in synthetic arteriovenous networks," *Journal of Theoretical Biology*, vol. 483, p. 109989, Dec. 2019. [Online]. Available: http://www.sciencedirect.com/science/article/pii/S0022519319303406

4.2 Dr. Michael Welter

Demarcation from Scientific Work of Thierry Fredrich (TF)

With my signature I (Dr. Michael Welter) confirm the following statements:

- I conceived and designed the experiments reported in [1];

- TF assisted me in implementing and performing the experiments reported in [1]. In particular TF compared the main numerical method to another available software at that time contributing Figure C in the supplemental material "S1 Appendix" of [1];

- TF revised the manuscript of [1] jointly with all the coauthors;

- Prof. Dr. Herbert Rinneberg and Prof. Dr. Dr. h.c. Heiko Rieger suggested the scientific problem of [1]

- TF conceived and wrote the manuscript of [2] which was successively revised by all the coauthors;

- I conceived the kernel modules reported in [2];

- Prof. Dr. Dr. h.c. Heiko Rieger supervised the research project underlying [2];

- TF provided the supplemental material to [2] and maintained the source code;

- I suggested the scientific idea of [4];

- TF conceived and conducted the numerical studies reported in [4];

- TF wrote the manuscript of [4] which was successively revised by all the coauthors;

- I developed the Tumorcode software in collaboration with TF who maintains the software since I left the project in 2015;

12.11.2019

_____
Date

_____
Signature

References

[1] M. Welter, T. Fredrich, H. Rinneberg, and H. Rieger, "Computational Model for Tumor Oxygenation Applied to Clinical Data on Breast Tumor Hemoglobin Concentrations Suggests Vascular Dilatation and Compression," *PLOS ONE*, vol. 11, no. 8, p. e0161267, Aug. 2016. [Online]. Available: https://journals.plos.org/plosone/article?id=10.1371/journal.pone.0161267

[2] T. Fredrich, M. Welter, and H. Rieger, "Tumorcode," *The European Physical Journal E*, vol. 41, no. 4, p. 55, Apr. 2018. [Online]. Available: https://doi.org/10.1140/epje/i2018-11659-x

[3] T. Fredrich, H. Rieger, R. Chignola, and E. Milotti, "Fine-grained simulations of the microenvironment of vascularized tumours," *Scientific Reports*, vol. 9, no. 1, pp. 1–12, Aug. 2019. [Online]. Available: https://www.nature.com/articles/s41598-019-48252-8

[4] T. Fredrich, M. Welter, and H. Rieger, "Dynamic vessel adaptation in synthetic arteriovenous networks," *Journal of Theoretical Biology*, vol. 483, p. 109989, Dec. 2019. [Online]. Available: http://www.sciencedirect.com/science/article/pii/S0022519319303406
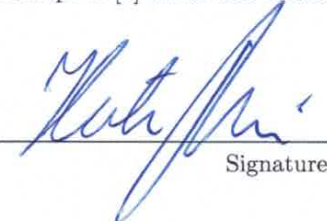
4.3 Prof. Dr. Herbert Rinneberg

Demarcation from Scientific Work of Thierry Fredrich (TF)

With my signature I (Prof. Dr. Herbert Rinneberg) confirm the following statements regarding [1]:

- Dr. Michael Welter conceived and designed the reported experiments;

- TF assisted Michael Welter in implementing and performing the reported experiments. In particular TF compared the main numerical method to another available software at that time contributing Figure C in the supplemental material "S1 Appendix" of [1];

- TF revised the manuscript jointly with all the coauthors;

- Prof. Dr. Dr. h.c. Heiko Rieger and me suggested the scientific problem of [1]

26. 11. 2019   Prof. Dr. Herbert

Date   Signature

References

[1] M. Welter, T. Fredrich, H. Rinneberg, and H. Rieger, "Computational Model for Tumor Oxygenation Applied to Clinical Data on Breast Tumor Hemoglobin Concentrations Suggests Vascular Dilatation and Compression," *PLOS ONE*, vol. 11, no. 8, p. e0161267, Aug. 2016. [Online]. Available: https://journals.plos.org/plosone/article?id=10.1371/journal.pone.0161267

[2] T. Fredrich, M. Welter, and H. Rieger, "Tumorcode," *The European Physical Journal E*, vol. 41, no. 4, p. 55, Apr. 2018. [Online]. Available: https://doi.org/10.1140/epje/i2018-11659-x

[3] T. Fredrich, H. Rieger, R. Chignola, and E. Milotti, "Fine-grained simulations of the microenvironment of vascularized tumours," *Scientific Reports*, vol. 9, no. 1, pp. 1–12, Aug. 2019. [Online]. Available: https://www.nature.com/articles/s41598-019-48252-8

[4] T. Fredrich, M. Welter, and H. Rieger, "Dynamic vessel adaptation in synthetic arteriovenous networks," *Journal of Theoretical Biology*, vol. 483, p. 109989, Dec. 2019. [Online]. Available: http://www.sciencedirect.com/science/article/pii/S0022519319303406

4.4 Prof. Dr. Edoardo Milotti

Demarcation from Scientific Work of Thierry Fredrich (TF)

With my signature I (Prof. Dr. Edoardo Milotti) confirm the following statements regarding [3]:

- Thierry Fredrich wrote the results part;

- I wrote the other parts;

- [3] was successively revised by all the coauthors including myself;

- Thierry Fredrich and me designed jointly an interface for the Virtual Biology Lab (VBL) and the Tumorcode software;

- Thierry Fredrich implemented the interface;

- Thierry Fredrich and me optimized the parameters of the combined simulation jointly;

- Thierry Fredrich conceptualized, conducted and analyzed the reported computational studies resulting in the figures and the movies;

- Prof. Dr. Dr. h.c. Heiko Rieger designed the principles of Tumorcode and supervised TF;

- Dr. Michael Welter and TF developed the Tumorcode software;

- I suggested the scientific problem and added the VBL software to the public domain;

- Prof. Dr. Roberto Chignola helped with biological aspects and assisted in parameter tuning of the combined simulation;

14/11/2019

| Date | Signature |

References

[1] M. Welter, T. Fredrich, H. Rinneberg, and H. Rieger, "Computational Model for Tumor Oxygenation Applied to Clinical Data on Breast Tumor Hemoglobin Concentrations Suggests Vascular Dilatation and Compression," *PLOS ONE*, vol. 11, no. 8, p. e0161267, Aug. 2016. [Online]. Available: https://journals.plos.org/plosone/article?id=10.1371/journal.pone.0161267

[2] T. Fredrich, M. Welter, and H. Rieger, "Tumorcode," *The European Physical Journal E*, vol. 41, no. 4, p. 55, Apr. 2018. [Online]. Available: https://doi.org/10.1140/epje/i2018-11659-x

[3] T. Fredrich, H. Rieger, R. Chignola, and E. Milotti, "Fine-grained simulations of the microenvironment of vascularized tumours," *Scientific Reports*, vol. 9, no. 1, pp. 1–12, Aug. 2019. [Online]. Available: https://www.nature.com/articles/s41598-019-48252-8

[4] T. Fredrich, M. Welter, and H. Rieger, "Dynamic vessel adaptation in synthetic arteriovenous networks," *Journal of Theoretical Biology*, vol. 483, p. 109989, Dec. 2019. [Online]. Available: http://www.sciencedirect.com/science/article/pii/S0022519319303406

4.5   Prof. Dr. Roberto Chignola

Demarcation from Scientific Work of Thierry Fredrich (TF)

With my signature I (Prof. Dr. Roberto Chignola) confirm the following statements regarding [3]:

- Thierry Fredrich wrote the results part;

- Prof. Dr. Edoardo Milotti (EM) wrote the other parts;

- [3] was successively revised by all the coauthors including myself;

- Thierry Fredrich and EM jointly designed an interface for the Virtual Biology Lab (VBL) and the Tumorcode software;

- Thierry Fredrich implemented the interface;

- Thierry Fredrich and EM jointly optimized the parameters of the combined simulation;

- Thierry Fredrich conceptualized, conducted and analyzed the reported computational studies resulting in the figures and the movies;

- Prof. Dr. Dr. h.c. Heiko Rieger designed the principles of Tumorcode and supervised TF;

- Dr. Michael Welter and TF developed the Tumorcode software;

- EM suggested the scientific problem and added the VBL software to the public domain;

- I helped with biological aspects and assisted in parameter tuning of the combined simulation;

November 11, 2019

Date   Signature

References

[1] M. Welter, T. Fredrich, H. Rinneberg, and H. Rieger, "Computational Model for Tumor Oxygenation Applied to Clinical Data on Breast Tumor Hemoglobin Concentrations Suggests Vascular Dilatation and Compression," *PLOS ONE*, vol. 11, no. 8, p. e0161267, Aug. 2016. [Online]. Available: https://journals.plos.org/plosone/article?id=10.1371/journal.pone.0161267

[2] T. Fredrich, M. Welter, and H. Rieger, "Tumorcode," *The European Physical Journal E*, vol. 41, no. 4, p. 55, Apr. 2018. [Online]. Available: https://doi.org/10.1140/epje/i2018-11659-x

[3] T. Fredrich, H. Rieger, R. Chignola, and E. Milotti, "Fine-grained simulations of the microenvironment of vascularized tumours," *Scientific Reports*, vol. 9, no. 1, pp. 1–12, Aug. 2019. [Online]. Available: https://www.nature.com/articles/s41598-019-48252-8

[4] T. Fredrich, M. Welter, and H. Rieger, "Dynamic vessel adaptation in synthetic arteriovenous networks," *Journal of Theoretical Biology*, vol. 483, p. 109989, Dec. 2019. [Online]. Available: http://www.sciencedirect.com/science/article/pii/S0022519319303406

List of Figures

Bibliography

[1] M. Welter, T. Fredrich, H. Rinneberg, and H. Rieger, "Computational Model for Tumor Oxygenation Applied to Clinical Data on Breast Tumor Hemoglobin Concentrations Suggests Vascular Dilatation and Compression," *PLOS ONE*, vol. 11, no. 8, p. e0161267, Aug. 2016. [Online]. Available: https://journals.plos.org/plosone/article?id=10.1371/journal.pone.0161267

[2] T. Fredrich, M. Welter, and H. Rieger, "Tumorcode," *The European Physical Journal E*, vol. 41, no. 4, p. 55, Apr. 2018. [Online]. Available: https://doi.org/10.1140/epje/i2018-11659-x

[3] T. Fredrich, H. Rieger, R. Chignola, and E. Milotti, "Fine-grained simulations of the microenvironment of vascularized tumours," *Scientific Reports*, vol. 9, no. 1, pp. 1–12, Aug. 2019. [Online]. Available: https://www.nature.com/articles/s41598-019-48252-8

[4] T. Fredrich, M. Welter, and H. Rieger, "Dynamic vessel adaptation in synthetic arteriovenous networks," *Journal of Theoretical Biol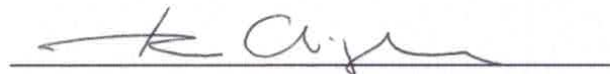ogy*, vol. 483, p. 109989, Dec. 2019. [Online]. Available: http://www.sciencedirect.com/science/article/pii/S0022519319303406

[5] H. Rieger, T. Fredrich, and M. Welter, "Physics of the tumor vasculature: Theory and experiment," *The European Physical Journal Plus*, vol. 131, no. 2, p. 31, Feb. 2016. [Online]. Available: http://link.springer.com/article/10.1140/epjp/i2016-16031-9

[6] "Cancer," Aug. 2019, page Version ID: 912768301. [Online]. Available: https://en.wikipedia.org/w/index.php?title=Cancer&oldid=912768301

[7] D. Hanahan and R. A. Weinberg, "The Hallmarks of Cancer," *Cell*, vol. 100, no. 1, pp. 57–70, Jan. 2000. [Online]. Available: http://www.sciencedirect.com/science/article/pii/S0092867400816839

[8] A. W. Shafer, "Etiology of Leukemia—A Review," *California Medicine*, vol. 104, no. 3, pp. 161–165, Mar. 1966. [Online]. Available: https://www.ncbi.nlm.nih.gov/pmc/articles/PMC1516260/

[9] C. L. Sawyers, C. T. Denny, and O. N. Witte, "Leukemia and the disruption of normal hematopoiesis," *Cell*, vol. 64, no. 2, pp. 337–350, Jan. 1991. [Online]. Available: http://www.sciencedirect.com/science/article/pii/009286749190643D

[10] W. Ladines-Castro, G. Barragán-Ibañez, M. A. Luna-Pérez, A. Santoyo-Sánchez, J. Collazo-Jaloma, E. Mendoza-García, and C. O. Ramos-Peñafiel, "Morphology of leukaemias," *Revista Médica del Hospital General de México*, vol. 79, no. 2, pp. 107–113, Apr. 2016. [Online]. Available: http://www.sciencedirect.com/science/article/pii/S0185106315000724

[11] C. Verdier, J. Etienne, A. Duperray, and L. Preziosi, "Review: Rheological properties of biological materials," *Comptes Rendus Physique*, vol. 10, no. 8, pp. 790–811, Nov. 2009. [Online]. Available: http://www.sciencedirect.com/science/article/pii/S1631070509001492

[12] Mediran, "English: A typical animal cell with labeled organelles." Aug. 2012. [Online]. Available: https://commons.wikimedia.org/wiki/File:Eukaryotic_Cell_(animal).jpg

[13] P. A. Pullarkat, P. A. Fernández, and A. Ott, "Rheological properties of the Eukaryotic cell cytoskeleton," *Physics Reports*, vol. 449, no. 1, pp. 29–53, Sep. 2007. [Online]. Available: http://www.sciencedirect.com/science/article/pii/S0370157307001305

[14] Histidine, "English: By Richard Wheeler (Zephyris) 2006. Schematic representation of the cell cycle. Cytokinesis forms rapidly in the process of the cell cycle." Jan. 2011. [Online]. Available: https://commons.wikimedia.org/wiki/File:Cell_Cycle_2-2.svg

[15] B. Alberts, A. Johnson, J. Lewis, M. Raff, K. Roberts, and P. Walter, *Molecular Biology of the Cell*, 4th ed.   Garland Science, 2002.

[16] "Eukaryotic Cell - Definition, Characteristics, Structure and Examples." [Online]. Available: https://biologydictionary.net/eukaryotic-cell/

[17] A. Sakaue-Sawano, H. Kurokawa, T. Morimura, A. Hanyu, H. Hama, H. Osawa, S. Kashiwagi, K. Fukami, T. Miyata, H. Miyoshi, T. Imamura, M. Ogawa, H. Masai, and A. Miyawaki, "Visualizing Spatiotemporal Dynamics of Multicellular Cell-Cycle Progression," *Cell*, vol. 132, no. 3, pp. 487–498, Feb. 2008. [Online]. Available: http://www.sciencedirect.com/science/article/pii/S0092867408000548

[18] S. Yano, Y. Zhang, S. Miwa, Y. Tome, Y. Hiroshima, F. Uehara, M. Yamamoto, A. Suetsugu, H. Kishimoto, H. Tazawa, M. Zhao, M. Bouvet, T. Fujiwara, and R. M. Hoffman, "Spatial–temporal FUCCI imaging of each cell in a tumor demonstrates locational dependence of cell cycle dynamics and chemoresponsiveness," *Cell Cycle*, vol. 13, no. 13, pp. 2110–2119, Jul. 2014. [Online]. Available: https://doi.org/10.4161/cc.29156

[19] C. A. M. L. Porta and S. Zapperi, "The Physics of Cancer by Caterina A. M. La Porta," Apr. 2017. [Online]. Available: /core/books/physics-of-cancer/A49179C602856C3CDF08C5BC084633F7

[20] M. Abedin and N. King, "Diverse evolutionary paths to cell adhesion," *Trends in cell biology*, vol. 20, no. 12, pp. 734–742, Dec. 2010. [Online]. Available: https://www.ncbi.nlm.nih.gov/pmc/articles/PMC2991404/

[21] P. Tracqui, "Biophysical models of tumour growth," *Reports on Progress in Physics*, vol. 72, no. 5, p. 056701, 2009. [Online]. Available: http://stacks.iop.org/0034-4885/72/i=5/a=056701

[22] G. Lazzari, P. Couvreur, and S. Mura, "Multicellular tumor spheroids: a relevant 3d model for the in vitro preclinical investigation of polymer nanomedicines," *Polymer Chemistry*, vol. 8, no. 34, pp. 4947–4969, Aug. 2017. [Online]. Available: https://pubs.rsc.org/en/content/articlelanding/2017/py/c7py00559h

[23] R. M. Sutherland, J. A. McCredie, and W. R. Inch, "Growth of multicell spheroids in tissue culture as a model of nodular carcinomas," *Journal of the National Cancer Institute*, vol. 46, no. 1, pp. 113–120, Jan. 1971.

[24] R. Sutherland, J. Carlsson, R. Durand, and J. Yuhas, "Spheroids in Cancer Research," *Cancer Research*, vol. 41, no. 7, pp. 2980–2984, Jul. 1981. [Online]. Available: https://cancerres.aacrjournals.org/content/41/7/2980

[25] S. Nath and G. R. Devi, "Three-Dimensional Culture Systems in Cancer Research: Focus on Tumor Spheroid Model," *Pharmacology & therapeutics*, vol. 163, pp. 94–108, Jul. 2016. [Online]. Available: https://www.ncbi.nlm.nih.gov/pmc/articles/PMC4961208/

[26] M. B. Schaaf, A. D. Garg, and P. Agostinis, "Defining the role of the tumor vasculature in antitumor immunity and immunotherapy," *Cell Death & Disease*, vol. 9, no. 2, p. 115, Jan. 2018. [Online]. Available: https://www.nature.com/articles/s41419-017-0061-0

[27] "Circulatory system," Aug. 2019, page Version ID: 911012160. [Online]. Available: https://en.wikipedia.org/w/index.php?title=Circulatory_system&oldid=911012160

[28] J. D. B. Macdougall and M. Mccabe, "Diffusion Coefficient of Oxygen through Tissues," *Nature*, vol. 215, no. 5106, p. 1173, Sep. 1967. [Online]. Available: https://www.nature.com/articles/2151173a0

[29] P. Carmeliet and R. K. Jain, "Angiogenesis in cancer and other diseases," *Nature*, vol. 407, no. 6801, p. 249, Sep. 2000. [Online]. Available: https://www.nature.com/articles/35025220

[30] G. Gompper and D. A. Fedosov, "Modeling microcirculatory blood flow: current state and future perspectives," *Wiley Interdisciplinary Reviews: Systems Biology and Medicine*, vol. 8, no. 2, pp. 157–168, Mar. 2016. [Online]. Available: http://onlinelibrary.wiley.com/doi/10.1002/wsbm.1326/abstract

[31] S. Pillay, H. M. Byrne, and P. K. Maini, "Modeling angiogenesis: A discrete to continuum description," *Physical Review E*, vol. 95, no. 1, p. 012410, Jan. 2017. [Online]. Available: https://link.aps.org/doi/10.1103/PhysRevE.95.012410

[32] G. Bergers and L. E. Benjamin, "Tumorigenesis and the angiogenic switch," *Nature Reviews Cancer*, vol. 3, no. 6, p. 401, Jun. 2003. [Online]. Available: https://www.nature.com/articles/nrc1093

[33] M. De Palma, D. Biziato, and T. V. Petrova, "Microenvironmental regulation of tumour angiogenesis," *Nature Reviews Cancer*, vol. 17, no. 8, pp. 457–474, Aug. 2017. [Online]. Available: https://www.nature.com/articles/nrc.2017.51

[34] M. Welter, "A theoretical model of vascularized tumors : simulation of blood vessel network remodeling, interstitial fluid flow and oxygenation," 2015. [Online]. Available: https://publikationen.sulb.uni-saarland.de/handle/20.500.11880/23261

[35] J. Folkman, "What Is the Evidence That Tumors Are Angiogenesis Dependent?" *JNCI: Journal of the National Cancer Institute*, vol. 82, no. 1, pp. 4–7, Jan. 1990. [Online]. Available: https://academic.oup.com/jnci/article/82/1/4/1035101

[36] "Extracellular fluid - Wikipedia." [Online]. Available: https://en.wikipedia.org/wiki/Extracellular_fluid

[37] M. Welter and H. Rieger, "Interstitial Fluid Flow and Drug Delivery in Vascularized Tumors: A Computational Model," *PLOS ONE*, vol. 8, no. 8, p. e70395, May 2013. [Online]. Available: https://journals.plos.org/plosone/article?id=10.1371/journal.pone.0070395

[38] G. B. West, J. H. Brown, and B. J. Enquist, "A General Model for the Origin of Allometric Scaling Laws in Biology," *Science*, vol. 276, no. 5309, pp. 122–126, Apr. 1997. [Online]. Available: https://science.sciencemag.org/content/276/5309/122

[39] C. D. Murray, "The Physiological Principle of Minimum Work," *Proceedings of the National Academy of Sciences of the United States of America*, vol. 12, no. 5, pp. 299–304, May 1926. [Online]. Available: http://www.ncbi.nlm.nih.gov/pmc/articles/PMC1084544/

[40] J. S. Lowengrub, H. B. Frieboes, F. Jin, Y.-L. Chuang, X. Li, P. Macklin, S. M. Wise, and V. Cristini, "Nonlinear modelling of cancer: bridging the gap between cells and tumours," *Nonlinearity*, vol. 23, no. 1, pp. R1–R9, 2010. [Online]. Available: https://www.ncbi.nlm.nih.gov/pmc/articles/PMC2929802/

[41] R. Araujo, "A history of the study of solid tumour growth: the contribution of mathematical modelling," *Bulletin of Mathematical Biology*, vol. 66, no. 5, pp. 1039–1091, Sep. 2004. [Online]. Available: http://link.springer.com/10.1016/j.bulm.2003.11.002

[42] N. Bellomo, E. De Angelis, and L. Preziosi, "Multiscale Modeling and Mathematical Problems Related to Tumor Evolution and Medical Therapy," 2003. [Online]. Available: https://www.hindawi.com/journals/cmmm/2003/820273/abs/

[43] S. Sanga, J. P. Sinek, H. B. Frieboes, M. Ferrari, J. P. Fruehauf, and V. Cristini, "Mathematical modeling of cancer progression and response to chemotherapy," *Expert Review of Anticancer Therapy*, vol. 6, no. 10, pp. 1361–1376, Oct. 2006. [Online]. Available: https://doi.org/10.1586/14737140.6.10.1361

[44] V. Quaranta, A. M. Weaver, P. T. Cummings, and A. R. A. Anderson, "Mathematical modeling of cancer: The future of prognosis and treatment," *Clinica Chimica Acta*, vol. 357, no. 2, pp. 173–179, Jul. 2005. [Online]. Available: http://www.sciencedirect.com/science/article/pii/S0009898105001944

[45] J. T. Oden, E. A. B. F. Lima, R. C. Almeida, Y. Feng, M. N. Rylander, D. Fuentes, D. Faghihi, M. M. Rahman, M. DeWitt, M. Gadde, and J. C. Zhou, "Toward Predictive Multiscale Modeling of Vascular Tumor Growth," *Archives of Computational Methods in Engineering*, vol. 23, no. 4, pp. 735–779, Dec. 2016. [Online]. Available: https://doi.org/10.1007/s11831-015-9156-x

[46] Karolak Aleksandra, Markov Dmitry A., McCawley Lisa J., and Rejniak Katarzyna A., "Towards personalized computational oncology: from spatial models of tumour spheroids, to organoids, to tissues," *Journal of The Royal Society Interface*, vol. 15, no. 138, p. 20170703, Jan. 2018. [Online]. Available: https://royalsocietypublishing.org/doi/full/10.1098/rsif.2017.0703

[47] J. Metzcar, Y. Wang, R. Heiland, and P. Macklin, "A Review of Cell-Based Computational Modeling in Cancer Biology," *JCO Clinical Cancer Informatics*, no. 3, pp. 1–13, Feb. 2019. [Online]. Available: https://ascopubs.org/doi/full/10.1200/CCI.18.00069

[48] B. Chopard, R. Ouared, A. Deutsch, H. Hatzikirou, and D. Wolf-Gladrow, "Lattice-Gas Cellular Automaton Models for Biology: From Fluids to Cells," *Acta Biotheoretica*, vol. 58, no. 4, pp. 329–340, Dec. 2010. [Online]. Available: https://doi.org/10.1007/s10441-010-9118-5

[49] C. S. Peskin, "The immersed boundary method," *Acta Numerica*, vol. 11, pp. 479–517, Jan. 2002. [Online]. Available: https://www.cambridge.org/core/journals/acta-numerica/article/immersed-boundary-method/95ECDAC5D1824285563270D6DD70DA9A

[50] D. C. Resasco, F. Gao, F. Morgan, I. L. Novak, J. C. Schaff, and B. M. Slepchenko, "Virtual Cell: computational tools for modeling in cell biology," *Wiley Interdisciplinary Reviews. Systems Biology and Medicine*, vol. 4, no. 2, pp. 129–140, Apr. 2012.

[51] C. Gong, O. Milberg, B. Wang, P. Vicini, R. Narwal, L. Roskos, and A. S. Popel, "A computational multiscale agent-based model for simulating spatio-temporal tumour immune response to PD1 and PDL1 inhibition," *Journal of The Royal Society Interface*, vol. 14, no. 134, p. 20170320, Sep. 2017. [Online]. Available: https://royalsocietypublishing.org/doi/10.1098/rsif.2017.0320

[52] R. A. Gatenby, K. Smallbone, P. K. Maini, F. Rose, J. Averill, R. B. Nagle, L. Worrall, and R. J. Gillies, "Cellular adaptations to hypoxia and acidosis during somatic evolution of breast cancer," *British Journal of Cancer*, vol. 97, no. 5, pp. 646–653, Aug. 2007. [Online]. Available: https://www.ncbi.nlm.nih.gov/pmc/articles/PMC2360372/

[53] K. Smallbone, R. A. Gatenby, R. J. Gillies, P. K. Maini, and D. J. Gavaghan, "Metabolic changes during carcinogenesis: Potential impact on invasiveness," *Journal of Theoretical Biology*, vol. 244, no. 4, pp. 703–713, Feb. 2007. [Online]. Available: http://www.sciencedirect.com/science/article/pii/S0022519306004115

[54] S. R. McDougall, A. R. A. Anderson, M. a. J. Chaplain, and J. A. Sherratt, "Mathematical modelling of flow through vascular networks: implications for tumour-induced angiogenesis and chemotherapy strategies," *Bulletin of Mathematical Biology*, vol. 64, no. 4, pp. 673–702, Jul. 2002.

[55] S. R. McDougall, A. R. A. Anderson, and M. A. J. Chaplain, "Mathematical modelling of dynamic adaptive tumour-induced angiogenesis: Clinical implications and therapeutic targeting strategies," *Journal of Theoretical Biology*, vol. 241, no. 3, pp. 564–589, Aug. 2006. [Online]. Available: http://www.sciencedirect.com/science/article/pii/S0022519305005564

[56] A. L. Bauer, T. L. Jackson, and Y. Jiang, "A cell-based model exhibiting branching and anastomosis during tumor-induced angiogenesis," *Biophysical Journal*, vol. 92, no. 9, pp. 3105–3121, May 2007.

[57] Y. Cai, S. Xu, J. Wu, and Q. Long, "Coupled modelling of tumour angiogenesis, tumour growth and blood perfusion," *Journal of Theoretical Biology*, vol. 279, no. 1, pp. 90–101, Jun. 2011. [Online]. Available: http://www.sciencedirect.com/science/article/pii/S0022519311001196

[58] S. E. M. Boas and R. M. H. Merks, "Tip cell overtaking occurs as a side effect of sprouting in computational models of angiogenesis," *BMC systems biology*, vol. 9, p. 86, Nov. 2015.

[59] M. Wu, H. B. Frieboes, S. R. McDougall, M. A. J. Chaplain, V. Cristini, and J. Lowengrub, "The effect of interstitial pressure on tumor growth: coupling with the blood and lymphatic vascular systems," *Journal of Theoretical Biology*, vol. 320, pp. 131–151, Mar. 2013.

[60] A. G. Fletcher, P. J. Murray, and P. K. Maini, "Multiscale modelling of intestinal crypt organization and carcinogenesis," *Mathematical Models and Methods in Applied Sciences*, vol. 25, no. 13, pp. 2563–2585, Jul. 2015. [Online]. Available: https://www.worldscientific.com/doi/abs/10.1142/S0218202515400187

[61] J. Poleszczuk, P. Hahnfeldt, and H. Enderling, "Evolution and Phenotypic Selection of Cancer Stem Cells," *PLOS Computational Biology*, vol. 11, no. 3, p. e1004025, Mar. 2015. [Online]. Available: https://journals.plos.org/ploscompbiol/article?id=10.1371/journal.pcbi.1004025

[62] J. C. L. Alfonso, N. Jagiella, L. Núñez, M. A. Herrero, and D. Drasdo, "Estimating Dose Painting Effects in Radiotherapy: A Mathematical Model," *PLOS ONE*, vol. 9, no. 2, p. e89380, Feb. 2014. [Online]. Available: https://journals.plos.org/plosone/article?id=10.1371/journal.pone.0089380

[63] M. Tektonidis, H. Hatzikirou, A. Chauvière, M. Simon, K. Schaller, and A. Deutsch, "Identification of intrinsic in vitro cellular mechanisms for glioma invasion," *Journal of Theoretical Biology*, vol. 287, pp. 131–147, Oct. 2011. [Online]. Available: http://www.sciencedirect.com/science/article/pii/ S0022519311003626

[64] H. Hatzikirou, D. Basanta, M. Simon, K. Schaller, and A. Deutsch, "'Go or Grow': the key to the emergence of invasion in tumour progression?" *Mathematical Medicine and Biology: A Journal of the IMA*, vol. 29, no. 1, pp. 49–65, Mar. 2012. [Online]. Available: https://academic.oup.com/imammb/article/29/1/49/753882

[65] K. Böttger, H. Hatzikirou, A. Chauviere, and A. Deutsch, "Investigation of the Migration/Proliferation Dichotomy and its Impact on Avascular Glioma Invasion," *Mathematical Modelling of Natural Phenomena*, vol. 7, no. 1, pp. 105–135, 2012. [Online]. Available: https://www.mmnp-journal.org/ articles/mmnp/abs/2012/01/mmnp201271p105/mmnp201271p105.html

[66] J. C. L. Alfonso, K. Talkenberger, M. Seifert, B. Klink, A. Hawkins-Daarud, K. R. Swanson, H. Hatzikirou, and A. Deutsch, "The biology and mathematical modelling of glioma invasion: a review," *Journal of the Royal Society, Interface*, vol. 14, no. 136, 2017.

[67] T. Brabletz, R. Kalluri, M. A. Nieto, and R. A. Weinberg, "EMT in cancer," *Nature Reviews Cancer*, vol. 18, no. 2, pp. 128–134, Feb. 2018. [Online]. Available: https: //www.nature.com/articles/nrc.2017.118

[68] D. Reher, B. Klink, A. Deutsch, and A. Voss-Böhme, "Cell adhesion heterogeneity reinforces tumour cell dissemination: novel insights from a mathematical model," *Biology Direct*, vol. 12, no. 1, p. 18, 2017.

[69] K. A. Rejniak, S. E. Wang, N. S. Bryce, H. Chang, B. Parvin, J. Jourquin, L. Estrada, J. W. Gray, C. L. Arteaga, A. M. Weaver, V. Quaranta, and A. R. A. Anderson, "Linking Changes in Epithelial Morphogenesis to Cancer Mutations Using Computational Modeling," *PLOS Computational Biology*, vol. 6, no. 8, p. e1000900, Aug. 2010. [Online]. Available: https://journals.plos.org/ploscompbiol/article?id=10.1371/journal.pcbi.1000900

[70] A. Ghaffarizadeh, R. Heiland, S. H. Friedman, S. M. Mumenthaler, and P. Macklin, "PhysiCell: An open source physics-based cell simulator for 3-D multicellular systems," *PLOS Computational Biology*, vol. 14, no. 2, p. e1005991, Feb. 2018. [Online]. Available: https://journals.plos.org/ploscompbiol/article?id=10.1371/journal.pcbi.1005991

[71] J. N. Kather, J. Poleszczuk, M. Suarez-Carmona, J. Krisam, P. Charoentong, N. A. Valous, C.-A. Weis, L. Tavernar, F. Leiss, E. Herpel, F. Klupp, A. Ulrich, M. Schneider, A. Marx, D. Jäger, and N. Halama, "In Silico Modeling of Immunotherapy and Stroma-Targeting Therapies in Human Colorectal Cancer," *Cancer Research*, vol. 77, no. 22, pp. 6442–6452, 2017.

[72] A. Vaziri and A. Gopinath, "Cell and biomolecular mechanics *in silico*," *Nature Materials*, vol. 7, no. 1, pp. 15–23, Jan. 2008. [Online]. Available: https://www.nature.com/articles/nmat2040

[73] E. K. Afenya and C. P. Calderón, "Diverse Ideas on the Growth Kinetics of Disseminated Cancer Cells," *Bulletin of Mathematical Biology*, vol. 62, no. 3, pp. 527–542, May 2000. [Online]. Available: http://www.sciencedirect.com/science/article/pii/S0092824099901659

[74] F. Kozusko and M. Bourdeau, "A unified model of sigmoid tumour growth based on cell proliferation and quiescence," *Cell Proliferation*, vol. 40, no. 6, pp. 824–834, 2007. [Online]. Available: https://onlinelibrary.wiley.com/doi/abs/10.1111/j.1365-2184.2007.00474.x

[75] M. Marusic, Z. Bajzer, J. P. Freyer, and S. Vuk-Pavlovic, "Analysis of growth of multicellular tumour spheroids by mathematical models," *Cell Proliferation*, vol. 27, no. 2, pp. 73–94, 1994. [Online]. Available: https://onlinelibrary.wiley.com/doi/abs/10.1111/j.1365-2184.1994.tb01407.x

[76] M. W. Retsky, D. E. Swartzendruber, R. H. Wardwell, and P. D. Bame, "Is Gompertzian or exponential kinetics a valid description of individual human cancer growth?" *Medical Hypotheses*, vol. 33, no. 2, pp. 95–106, Oct. 1990. [Online]. Available: http://www.sciencedirect.com/science/ article/pii/030698779090186I

[77] A. Bethge, U. Schumacher, A. Wree, and G. Wedemann, "Are Metastases from Metastases Clinical Relevant? Computer Modelling of Cancer Spread in a Case of Hepatocellular Carcinoma," *PLOS ONE*, vol. 7, no. 4, p. e35689, Apr. 2012. [Online]. Available: https://journals.plos.org/plosone/article?id=10.1371/journal.pone.0035689

[78] A. Bethge, U. Schumacher, and G. Wedemann, "Simulation of metastatic progression using a computer model including chemotherapy and radiation therapy," *Journal of Biomedical Informatics*, vol. 57, pp. 74–87, Oct. 2015. [Online]. Available: http://www.sciencedirect.com/science/article/pii/S1532046415001513

[79] A. M. Turing, "The chemical basis of morphogenesis," *Philosophical Transactions of the Royal Society of London. Series B, Biological Sciences*, vol. 237, no. 641, pp. 37–72, Aug. 1952. [Online]. Available: https://royalsocietypublishing.org/doi/abs/10.1098/rstb.1952.0012

[80] C. Cosner, "Reaction–Diffusion Equations and Ecological Modeling," in *Tutorials in Mathematical Biosciences IV: Evolution and Ecology*, ser. Lecture Notes in Mathematics, A. Friedman, Ed. Berlin, Heidelberg: Springer Berlin Heidelberg, 2008, pp. 77–115. [Online]. Available: https://doi.org/10.1007/978-3-540-74331-6_3

[81] J. D. Murray, *Mathematical Biology: I. An Introduction*, 3rd ed., ser. Interdisciplinary Applied Mathematics, Mathematical Biology. New York: Springer-Verlag, 2002. [Online]. Available: https://www.springer.com/gp/book/9780387952239

[82] E. J. Crampin, E. A. Gaffney, and P. K. Maini, "Reaction and diffusion on growing domains: Scenarios for robust pattern formation," *Bulletin of Mathematical Biology*, vol. 61, no. 6, pp. 1093–1120, Nov. 1999. [Online]. Available: https://doi.org/10.1006/bulm.1999.0131

[83] S. Lee, T. T. Chen, C. L. Barber, M. C. Jordan, J. Murdock, S. Desai, N. Ferrara, A. Nagy, K. P. Roos, and M. L. Iruela-Arispe, "Autocrine VEGF Signaling Is Required for Vascular Homeostasis," *Cell*, vol. 130, no. 4, pp. 691–703, Aug. 2007. [Online]. Available: http://www.sciencedirect.com/science/article/pii/S0092867407009051

[84] D. Selmeczi, S. Mosler, P. H. Hagedorn, N. B. Larsen, and H. Flyvbjerg, "Cell Motility as Persistent Random Motion: Theories from Experiments," *Biophysical Journal*, vol. 89, no. 2, pp. 912–931, Aug. 2005. [Online]. Available: https://www.ncbi.nlm.nih.gov/pmc/articles/PMC1366641/

[85] A. J. Perumpanani, B. P. Marchant, and J. Norbury, "Traveling Shock Waves Arising in a Model of Malignant Invasion," *SIAM Journal on Applied Mathematics*, vol. 60, no. 2, pp. 463–476, Jan. 2000. [Online]. Available: https://epubs.siam.org/doi/abs/10.1137/S0036139998328034

[86] M. Chaplain, M. Ganesh, and I. Graham, "Spatio-temporal pattern formation on spherical surfaces: numerical simulation and application to solid tumour growth," *Journal of Mathematical Biology*, vol. 42, no. 5, pp. 387–423, May 2001. [Online]. Available: https://doi.org/10.1007/s002850000067

[87] S. C. Ferreira, M. L. Martins, and M. J. Vilela, "Reaction-diffusion model for the growth of avascular tumor," *Physical Review E*, vol. 65, no. 2, p. 021907, Jan. 2002. [Online]. Available: https://link.aps.org/doi/10.1103/PhysRevE.65.021907

[88] A. M. Stein, T. Demuth, D. Mobley, M. Berens, and L. M. Sander, "A Mathematical Model of Glioblastoma Tumor Spheroid Invasion in a Three-Dimensional In Vitro Experiment," *Biophysical Journal*, vol. 92, no. 1, pp. 356–365, Jan. 2007. [Online]. Available: https://www.ncbi.nlm.nih.gov/pmc/articles/PMC1697862/

[89] A. Gerisch and M. A. J. Chaplain, "Mathematical modelling of cancer cell invasion of tissue: Local and non-local models and the effect of adhesion," *Journal of Theoretical Biology*, vol. 250, no. 4, pp. 684–704, Feb. 2008. [Online]. Available: http://www.sciencedirect.com/science/article/pii/S0022519307005097

[90] H. P. Greenspan, "On the growth and stability of cell cultures and solid tumors," *Journal of Theoretical Biology*, vol. 56, no. 1, pp. 229–242, Jan. 1976. [Online]. Available: http://www.sciencedirect.com/science/article/pii/S0022519376800549

[91] H. M. Byrne and M. A. J. Chaplain, "Modelling the role of cell-cell adhesion in the growth and development of carcinomas," *Mathematical and Computer Modelling*, vol. 24, no. 12, pp. 1–17, Dec. 1996. [Online]. Available: http://www.sciencedirect.com/science/article/pii/S0895717796001744

[92] V. Cristini, J. Lowengrub, and Q. Nie, "Nonlinear simulation of tumor growth," *Journal of Mathematical Biology*, vol. 46, no. 3, pp. 191–224, Mar. 2003. [Online]. Available: https://doi.org/10.1007/s00285-002-0174-6

[93] L. Graziano and L. Preziosi, "Mechanics in Tumor Growth," in *Modeling of Biological Materials*, ser. Modeling and Simulation in Science, Engineering and Technology, F. Mollica, L. Preziosi, and K. R. Rajagopal, Eds. Boston, MA: Birkhäuser Boston, 2007, pp. 263–321. [Online]. Available: https://doi.org/10.1007/978-0-8176-4411-6_7

[94] H. Byrne and L. Preziosi, "Modelling solid tumour growth using the theory of mixtures," *Mathematical Medicine and Biology: A Journal of the IMA*, vol. 20, no. 4, pp. 341–366, Dec. 2003. [Online]. Available: https://academic.oup.com/imammb/article/20/4/341/714032

[95] P. Macklin and J. Lowengrub, "Nonlinear simulation of the effect of microenvironment on tumor growth," *Journal of Theoretical Biology*, vol. 245, no. 4, pp. 677–704, Apr. 2007. [Online]. Available: http://www.sciencedirect.com/science/article/pii/S0022519306005649

[96] L. Tang, A. L. v. d. Ven, D. Guo, V. Andasari, V. Cristini, K. C. Li, and X. Zhou, "Computational Modeling of 3d Tumor Growth and Angiogenesis for Chemotherapy Evaluation," *PLOS ONE*, vol. 9, no. 1, p. e83962, Jan. 2014. [Online]. Available: https://journals.plos.org/plosone/article?id=10.1371/journal.pone.0083962

[97] V. Vavourakis, T. Stylianopoulos, and P. A. Wijeratne, "In-silico dynamic analysis of cytotoxic drug administration to solid tumours: Effect of binding affinity and vessel permeability," *PLOS Computational Biology*, vol. 14, no. 10, p. e1006460, Oct. 2018. [Online]. Available: https://journals.plos.org/ploscompbiol/article?id=10.1371/journal.pcbi.1006460

[98] M. Chaplain, S. McDougall, and A. Anderson, "Mathematical Modeling of Tumor-Induced Angiogenesis," *Annual Review of Biomedical Engineering*, vol. 8, no. 1, pp. 233–257, 2006. [Online]. Available: https://doi.org/10.1146/annurev.bioeng.8.061505.095807

[99] L. Preziosi and A. Tosin, "Multiphase modelling of tumour growth and extracellular matrix interaction: mathematical tools and applications," *Journal of Mathematical Biology*, vol. 58, no. 4, p. 625, Oct. 2008. [Online]. Available: https://doi.org/10.1007/s00285-008-0218-7

[100] K. A. Rejniak, Ed., *Systems Biology of Tumor Microenvironment: Quantitative Modeling and Simulations*, ser. Advances in Experimental Medicine and Biology. Springer International Publishing, 2016. [Online]. Available: //www.springer.com/de/book/9783319420219

[101] T. S. Deisboeck, Z. Wang, P. Macklin, and V. Cristini, "Multiscale Cancer Modeling," *Annual Review of Biomedical Engineering*, vol. 13, no. 1, pp. 127–155, 2011. [Online]. Available: https://doi.org/10.1146/annurev-bioeng-071910-124729

[102] P. V. Coveney and P. W. Fowler, "Modelling biological complexity: a physical scientist's perspective," *Journal of The Royal Society Interface*, vol. 2, no. 4, pp. 267–280, Sep. 2005. [Online]. Available: https://royalsocietypublishing.org/doi/full/10.1098/rsif.2005.0045

[103] G. M. Cooper, "The Eukaryotic Cell Cycle," *The Cell: A Molecular Approach. 2nd edition*, 2000. [Online]. Available: https://www.ncbi.nlm.nih.gov/books/NBK9876/

[104] M. H. Zangooei and J. Habibi, "Hybrid multiscale modeling and prediction of cancer cell behavior," *PLOS ONE*, vol. 12, no. 8, p. e0183810, Aug. 2017. [Online]. Available: https://journals.plos.org/plosone/article?id=10.1371/journal.pone.0183810

[105] G. Fischer, *Lineare Algebra*, 11th ed., ser. vieweg studium; Grundkurs Mathematik. Vieweg+Teubner Verlag, 1997. [Online]. Available: https://www.springer.com/gp/book/9783322943415

[106] T. A. Davis, *Direct Methods for Sparse Linear Systems*. Philadelphia: Society for Industrial and Applied Mathematics, Sep. 2006.

[107] H. P. Langtangen and S. Linge, *Finite Difference Computing with PDEs: A Modern Software Approach*, ser. Texts in Computational Science and Engineering. Springer International Publishing, 2017. [Online]. Available: https://www.springer.com/gp/book/9783319554556

[108] R. LeVeque, *Finite Difference Methods for Ordinary and Partial Differential Equations: Steady-State and Time-Dependent Problems (Classics in Applied Mathematics Classics in Applied Mathemat)*. Philadelphia, PA, USA: Society for Industrial and Applied Mathematics, 2007.

[109] J. Strikwerda, *Finite Difference Schemes and Partial Differential Equations*, 2nd ed. Philadelphia: SIAM: Society for Industrial and Applied Mathematics, Nov. 2004.

[110] K. Morgan, "Numerical solution of partial differential equations in science and engineering, L. Lapidus and G. F. Pinder, Wiley-Interscience, New York, 1982, No. of pages: 677. Price: £35.00," *International Journal for Numerical Methods in Engineering*, vol. 19, no. 10, pp. 1580–1580, 1983. [Online]. Available: https://onlinelibrary.wiley.com/doi/abs/10.1002/nme.1620191017

[111] E. Bavier, M. Hoemmen, S. Rajamanickam, and H. Thornquist, "Amesos2 and Belos: Direct and iterative solvers for large sparse linear systems," *Scientific Programming*, vol. 20, pp. 241–255, 2012.

[112] S. Abhyankar, J. Brown, E. M. Constantinescu, D. Ghosh, B. F. Smith, and H. Zhang, "PETSc/TS: A Modern Scalable ODE/DAE Solver Library," *arXiv:1806.01437 [math]*, Jun. 2018, arXiv: 1806.01437. [Online]. Available: http://arxiv.org/abs/1806.01437

[113] S. Balay, S. Abhyankar, M. F. Adams, J. Brown, P. Brune, K. Buschelman, L. Dalcin, A. Dener, V. Eijkhout, W. D. Gropp, D. Karpeyev, D. Kaushik, M. G. Knepley, D. A. May, L. C. McInnes, R. T. Mills, T. Munson, K. Rupp, P. Sanan, B. F. Smith, S. Zampini, H. Zhang, and H. Zhang, "PETSc Users Manual," Argonne National Laboratory, Tech. Rep. ANL-95/11 - Revision 3.12, 2019. [Online]. Available: https://www.mcs.anl.gov/petsc

[114] S. Balay, W. D. Gropp, L. C. McInnes, and B. F. Smith, "Efficient Management of Parallelism in Object Oriented Numerical Software Libraries," in *Modern Software Tools in Scientific Computing*, E. Arge, A. M. Bruaset, and H. P. Langtangen, Eds. Birkhäuser Press, 1997, pp. 163–202.

[115] D. Butler, "Dutch lead European push to flip journals to open access," *Nature News*, vol. 529, no. 7584, p. 13, Jan. 2016. [Online]. Available: http://www.nature.com/news/dutch-lead-european-push-to-flip-journals-to-open-access-1.19111

[116] R. Van Noorden, "Open access: The true cost of science publishing," *Nature News*, vol. 495, no. 7442, p. 426, Mar. 2013. [Online]. Available: http://www.nature.com/news/open-access-the-true-cost-of-science-publishing-1.12676

[117] C. DiBona, S. Ockman, and M. Stone, Eds., *Open Sources: Voices from the Open Source Revolution*, 1st ed. Beijing ; Sebastopol, CA: O'Reilly Media, Jan. 1999.

[118] L. A. Maggio, A. R. Artino Jr, and E. W. Driessen, "Preprints: Facilitating early discovery, access, and feedback," *Perspectives on Medical Education*, vol. 7, no. 5, pp. 287–289, Oct. 2018. [Online]. Available: https://doi.org/10.1007/s40037-018-0451-8

[119] N. Fraser, F. Momeni, P. Mayr, and I. Peters, "The effect of bioRxiv preprints on citations and altmetrics," *bioRxiv*, p. 673665, Jun. 2019. [Online]. Available: https://www.biorxiv.org/content/10.1101/673665v1

[120] M. D. Wilkinson, M. Dumontier, I. J. Aalbersberg, G. Appleton, M. Axton, A. Baak, N. Blomberg, J.-W. Boiten, L. B. da Silva Santos, P. E. Bourne, J. Bouwman, A. J. Brookes, T. Clark, M. Crosas, I. Dillo, O. Dumon, S. Edmunds, C. T. Evelo, R. Finkers, A. Gonzalez-Beltran, A. J. G. Gray, P. Groth, C. Goble, J. S. Grethe, J. Heringa, P. A. C. 't Hoen, R. Hooft, T. Kuhn, R. Kok, J. Kok, S. J. Lusher, M. E. Martone, A. Mons, A. L. Packer, B. Persson, P. Rocca-Serra, M. Roos, R. van Schaik, S.-A. Sansone, E. Schultes, T. Sengstag, T. Slater, G. Strawn, M. A. Swertz, M. Thompson, J. van der Lei, E. van Mulligen, J. Velterop, A. Waagmeester, P. Wittenburg, K. Wolstencroft, J. Zhao, and B. Mons, "The FAIR Guiding Principles for scientific data management and stewardship," *Scientific Data*, vol. 3, p. 160018, Mar. 2016. [Online]. Available: https://www.nature.com/articles/sdata201618

[121] C. Heise, *Von Open Access zu Open Science*. Lüneburg: meson press, 2018.

[122] P. Kraker, D. Leony, W. Reinhardt, and G. Beham, "The case for an open science in technology enhanced learning," *International Journal of Technology Enhanced Learning*, vol. 3, no. 6, pp. 643–654, Jan. 2011. [Online]. Available: https://www.inderscienceonline.com/doi/abs/10.1504/IJTEL.2011.045454

[123] K. Fogel, *Producing Open Source Software: How to Run a Successful Free Software Project*, 2nd ed. O'Reilly Media, Jan. 2017.

[124] P. Macklin, "Key challenges facing data-driven multicellular systems biology," *arXiv:1806.04736 [q-bio]*, Jun. 2018, arXiv: 1806.04736. [Online]. Available: http://arxiv.org/abs/1806.04736

[125] A. Updegrove, N. M. Wilson, J. Merkow, H. Lan, A. L. Marsden, and S. C. Shadden, "SimVascular: An Open Source Pipeline for Cardiovascular Simulation," *Annals of Biomedical Engineering*, vol. 45, no. 3, pp. 525–541, Mar. 2017. [Online]. Available: https://doi.org/10.1007/s10439-016-1762-8

[126] J. Pitt-Francis, P. Pathmanathan, M. O. Bernabeu, R. Bordas, J. Cooper, A. G. Fletcher, G. R. Mirams, P. Murray, J. M. Osborne, A. Walter, S. J. Chapman, A. Garny, I. M. M. van Leeuwen, P. K. Maini, B. Rodríguez, S. L. Waters, J. P. Whiteley, H. M. Byrne, and D. J. Gavaghan, "Chaste: A test-driven approach to software development for biological modelling," *Computer Physics Communications*, vol. 180, no. 12, pp. 2452–2471, Dec. 2009. [Online]. Available: http://www.sciencedirect.com/science/article/pii/S0010465509002604

[127] G. R. Mirams, C. J. Arthurs, M. O. Bernabeu, R. Bordas, J. Cooper, A. Corrias, Y. Davit, S.-J. Dunn, A. G. Fletcher, D. G. Harvey, M. E. Marsh, J. M. Osborne, P. Pathmanathan, J. Pitt-Francis, J. Southern, N. Zemzemi, and D. J. Gavaghan, "Chaste: An Open Source C++ Library for Computational Physiology and Biology," *PLOS Computational Biology*, vol. 9, no. 3, p. e1002970, Mar. 2013. [Online]. Available: https://journals.plos.org/ploscompbiol/article?id=10.1371/journal.pcbi.1002970

[128] J. A. Grogan, A. J. Connor, B. Markelc, R. J. Muschel, P. K. Maini, H. M. Byrne, and J. M. Pitt-Francis, "Microvessel Chaste: An Open Library for Spatial Modeling of Vascularized Tissues," *Biophysical Journal*, vol. 112, no. 9, pp. 1767–1772, May 2017. [Online]. Available: http://www.cell.com/biophysj/abstract/S0006-3495(17)30384-3

[129] M. Woelfle, P. Olliaro, and M. H. Todd, "Open science is a research accelerator," *Nature Chemistry*, vol. 3, pp. 745–748, Sep. 2011. [Online]. Available: https://www.nature.com/articles/nchem.1149

[130] G. Helmlinger, P. A. Netti, H. C. Lichtenbeld, R. J. Melder, and R. K. Jain, "Solid stress inhibits the growth of multicellular tumor spheroids," *Nature Biotechnology*, vol. 15, no. 8, p. 778, Aug. 1997. [Online]. Available: https://www.nature.com/articles/nbt0897-778

[131] T. W. Secomb, R. Hsu, E. Y. H. Park, and M. W. Dewhirst, "Green's Function Methods for Analysis of Oxygen Delivery to Tissue by Microvascular Networks," *Annals of Biomedical Engineering*, vol. 32, no. 11, pp. 1519–1529, Nov. 2004. [Online]. Available: https://doi.org/10.1114/B:ABME.0000049036.08817.44

[132] L. Spinelli, A. Torricelli, A. Pifferi, P. Taroni, G. Danesini, and R. Cubeddu, "Characterization of female breast lesions from multi-wavelength time-resolved optical mammography," *Physics in Medicine and Biology*, vol. 50, no. 11, pp. 2489–2502, May 2005. [Online]. Available: https://doi.org/10.1088%2F0031-9155%2F50%2F11%2F004

[133] D. Grosenick, H. Wabnitz, K. T. Moesta, J. Mucke, P. M. Schlag, and H. Rinneberg, "Time-domain scanning optical mammography: II. Optical properties and tissue parameters of 87 carcinomas," *Physics in Medicine and Biology*, vol. 50, no. 11, p. 2451, Jun. 2005. [Online]. Available: http://iopscience.iop.org/0031-9155/50/11/002

[134] R. Hsu and T. W. Secomb, "A Green's function method for analysis of oxygen delivery to tissue by microvascular networks," *Mathematical Biosciences*, vol. 96, no. 1, pp. 61–78, Sep. 1989. [Online]. Available: http://www.sciencedirect.com/science/article/pii/0025556489900837

[135] D. Goldman, "Theoretical Models of Microvascular Oxygen Transport to Tissue," *Microcirculation (New York, N.Y. : 1994)*, vol. 15, no. 8, pp. 795–811, Nov. 2008. [Online]. Available: http://www.ncbi.nlm.nih.gov/pmc/articles/PMC3057578/

[136] "Fåhræus–Lindqvist effect," Dec. 2018, page Version ID: 873515986. [Online]. Available: https://en.wikipedia.org/w/index.php?title=F%C3%A5hr%C3%A6us%E2%80%93Lindqvist_effect&oldid=873515986

[137] F. Clavica, A. Homsy, L. Jeandupeux, and D. Obrist, "Red blood cell phase separation in symmetric and asymmetric microchannel networks: effect of capillary dilation and inflow velocity," *Scientific Reports*, vol. 6, p. 36763, Nov. 2016. [Online]. Available: https://www.nature.com/articles/srep36763

[138] D.-S. Lee, H. Rieger, and K. Bartha, "Flow Correlated Percolation during Vascular Remodeling in Growing Tumors," *Physical Review Letters*, vol. 96, no. 5, p. 058104, Feb. 2006. [Online]. Available: https://link.aps.org/doi/10.1103/PhysRevLett.96.058104

[139] M. D. Mikrenska and N. K. Petrov, "A sparse matrix scheme for finite elements," *Finite Elements in Analysis and Design*, vol. 11, no. 1, pp. 47–53, May 1992. [Online]. Available: http://www.sciencedirect.com/science/article/pii/0168874X9290028B

[140] A. Prokopenko, C. M. Siefert, J. J. Hu, M. Hoemmen, and A. Klinvex, *Ifpack2 User's Guide*, Jun. 2016.

[141] E. Haines and T. Akenine-Möller, Eds., *Ray Tracing Gems*.   Apress, 2019.

[142] D. Buck and A. Collins, "POV-Ray - The Persistence of Vision Raytracer." [Online]. Available: http://www.povray.org/

[143] J. Ahrens, B. Geveci, and C. Law, "Paraview: An end-user tool for large data visualization," *The visualization handbook*, vol. 717, 2005.

[144] U. Ayachit, *The ParaView Guide (Full Color Version): A Parallel Visualization Application*, paraview 4.3 edition ed.   Los Alamos: Kitware, Incorporated, Jan. 2015.

[145] T. Fredrich, R. Chignola, E. Milotti, and H. Rieger, "VBL tumor pH," Nov. 2018. [Online]. Available: https://figshare.com/articles/VBL_tumor_pH/7406183

[146] ——, "VBL tumor PO2," Nov. 2018. [Online]. Available: https://figshare.com/articles/VBL_tumor_PO2/7406180

[147] E. Milotti and R. Chignola, "Emergent Properties of Tumor Microenvironment in a Real-Life Model of Multicell Tumor Spheroids," *PLOS ONE*, vol. 5, no. 11, p. e13942, Nov. 2010. [Online]. Available: https://journals.plos.org/plosone/article?id=10.1371/journal.pone.0013942

[148] M. Welter and H. Rieger, "Physical determinants of vascular network remodeling during tumor growth," *The European Physical Journal E*, vol. 33, no. 2, pp. 149–163, Oct. 2010. [Online]. Available: https://doi.org/10.1140/epje/i2010-10611-6

[149] J. E. Talmadge, "Clonal Selection of Metastasis within the Life History of a Tumor," *Cancer Research*, vol. 67, no. 24, pp. 11 471–11 475, Dec. 2007. [Online]. Available: https://cancerres.aacrjournals.org/content/67/24/11471

[150] B. Arneth, "Comparison of Burnet's clonal selection theory with tumor cell-clone development," *Theranostics*, vol. 8, no. 12, pp. 3392–3399, 2018. [Online]. Available: http://www.thno.org/v08p3392.htm

[151] R. M. Sutherland, "Cell and environment interactions in tumor microregions: the multicell spheroid model," *Science*, vol. 240, no. 4849, pp. 177–184, Apr. 1988. [Online]. Available: https://science.sciencemag.org/content/240/4849/177

[152] "Revival: Spheroid Culture in Cancer Research (1991)." [Online]. Available: https://www.crcpress.com/Revival-Spheroid-Culture-in-Cancer-Research-1991/Bjerkvig/p/book/9781138561908

[153] R. Chignola, R. Foroni, A. Franceschi, M. Pasti, C. Candiani, C. Anselmi, G. Fracasso, G. Tridente, and M. Colombatti, "Heterogeneous response of individual multicellular tumour spheroids to immunotoxins and ricin toxin." *British Journal of Cancer*, vol. 72, no. 3, pp. 607–614, Sep. 1995. [Online]. Available: https://www.ncbi.nlm.nih.gov/pmc/articles/PMC2033892/

[154] C. D. Bortner and J. A. Cidlowski, "Apoptotic volume decrease and the incredible shrinking cell," Dec. 2002. [Online]. Available: https://www.nature.com/articles/4401126

[155] H. Hertz, "Ueber die Berührung fester elastischer Körper." *Journal für die reine und angewandte Mathematik*, vol. 92, pp. 156–171, 1882. [Online]. Available: http://www.digizeitschriften.de/dms/img/?PID=GDZPPN002158264

[156] A. Sackfield and D. A. Hills, "Some useful results in the classical Hertz contact problem," *The Journal of Strain Analysis for Engineering Design*, vol. 18, no. 2, pp. 101–105, Apr. 1983. [Online]. Available: https://doi.org/10.1243/03093247V182101

[157] A. R. Pries, T. W. Secomb, and P. Gaehtgens, "Structural adaptation and stability of microvascular networks: theory and simulations," *American Journal of Physiology - Heart and Circulatory Physiology*, vol. 275, no. 2, pp. H349–H360, Aug. 1998. [Online]. Available: http://ajpheart.physiology.org/content/275/2/H349

[158] A. R. Pries, B. Reglin, and T. W. Secomb, "Structural response of microcirculatory networks to changes in demand: information transfer by shear stress," *American Journal of Physiology-Heart and Circulatory Physiology*, vol. 284, no. 6, pp. H2204–H2212, Jun. 2003. [Online]. Available: https://www.physiology.org/doi/full/10.1152/ajpheart.00757.2002

[159] M. Welter, K. Bartha, and H. Rieger, "Vascular remodelling of an arterio-venous blood vessel network during solid tumour growth," *Journal of Theoretical Biology*, vol. 259, no. 3, pp. 405–422, Aug. 2009. [Online]. Available: http://www.sciencedirect.com/science/article/pii/S0022519309001635

Appendices

Appendix A

"Leitfaden zur Kumulativen Dissertation in der gültigen Fassung"

Vorläufiger Leitfaden und vorläufige Vorgaben für die Erstellung, Einreichung und Veröffentlichung von kumulativen Dissertationsschriften

Beschluss des Promotionsausschusses vom 06.12.2018

Allgemeine Festlegungen

Für Doktorandinnen und Doktoranden der Naturwissenschaftlich-Technischen Fakultät besteht die Möglichkeit, ihre Doktorarbeit in Form einer kumulativen Dissertationsschrift einzureichen, falls die wesentlichen Ergebnisse bereits in einschlägigen wissenschaftlichen Zeitschriften publiziert worden sind.

Die kumulative Dissertation muss eine ausführliche Darstellung des wissenschaftlichen Kontextes (state of the art) zu Beginn der eigenen Forschung enthalten sowie eine angemessene Würdigung der für die Ergebnisse der Arbeit relevanten Literatur. Weiterhin muss eine Diskussion der erzielten Ergebnisse der gesamten Arbeit gegeben werden. Der innere Zusammenhang und der eigene Anteil an den verwendeten wissenschaftlichen Arbeiten sind in einer erweiterten Zusammenfassung darzulegen.

Das Vorliegen einer kumulativen Dissertation muss im Antrag auf Eröffnung des Promotionsverfahrens angezeigt werden.
Auf die Einreichung einer kumulativen Dissertationsschrift besteht kein Anspruch. In jedem Fall bedarf die Einreichung in kumulierter Form des Einverständnisses der Betreuerin/ des Betreuers. Im Sinne der Transparenz und klaren Absprachen wird die Übereinkunft am besten bereits in der Betreuungsvereinbarung formuliert.

Anforderungen an die einzubindenden Publikationen

- Als Dissertationen können auch mehrere wissenschaftliche Arbeiten anerkannt werden, wenn sie in einem inneren Zusammenhang stehen und in ihrer Gesamtheit den Anforderungen nach §4 Abs. 1 der Promotionsordnung (selbständig erarbeiteter Beitrag zur wissenschaftlichen Forschung; einem Fachgebiet der Fakultät zugehörig) entsprechen. Der innere Zusammenhang und der eigene Anteil an den Arbeiten sind in einer erweiterten Zusammenfassung darzulegen.
- Grundlage müssen sein: insgesamt mindestens drei Originalpublikationen, die nach dem peer-reviewed-Verfahren begutachtet wurden, davon mindestens zwei in Erstautorenschaft. Die dritte Publikation kann auch eine Patentschrift sein.
- Übersichtsartikel zählen nicht als Originalpublikation.
- Der Anteil und die Tätigkeit der Mitautoren/innen muss genau beschrieben werden und diese Beschreibung muss in die Arbeit eingebunden werden. Weiterhin muss dem Promotionsbüro eine entsprechende Beschreibung mit Unterschriften von allen anderen Mitautoren/innen für die Akten übergeben werden.
- Von den Journalen endgültig angenommene Publikationen sind im Hinblick auf kumulative Dissertationsschriften an der Fakultät als äquivalent zu veröffentlichten Originalarbeiten zu behandeln. Dies ist jedoch daran geknüpft, dass bei Eröffnung des Promotionsverfahrens (=Abgabe der Arbeit) der „Letter of acceptance" für den bzw. die noch nicht veröffentlichten Publikation/en beigelegt wird.

Im Rahmen von kumulativen Dissertationsschriften ist eine Arbeit in geteilter Erstautorenschaft grundsätzlich zulässig und wird als eine der zwei mindestens notwendigen Veröffentlichungen als Erstautor/in anerkannt. Bei mehr als einer geteilten Erstautorenschaft ist die Arbeit zusammen mit dem Antrag auf Eröffnung des Promotionsverfahrens dem Promotionsausschuss vorzulegen, der auf Basis der Unterlagen (sowie ggf. unter Hinzuziehung von Experten/innen) jeweils eine Einzelfallentscheidung trifft.

Abgabe der Dissertationsschrift bei Eröffnung des Promotionsverfahrens:

Zur Begutachtung Ihrer Dissertationsschrift muss diese den kompletten Abdruck aller Artikel/ Originalarbeiten enthalten. Da es sich hierbei um eine Prüfungsleistung handelt, die zudem nicht öffentlich gemacht wird, verletzen Sie damit keine Verlagsrechte.

<u>Veröffentlichung der kumulativen Dissertationsschrift:</u>

Gemäß §13 der Promotionsordnung müssen die Bewerberinnen/ Bewerber zur Veröffentlichung der Dissertationsschrift sowohl gedruckte Pflichtexemplare abgeben als auch der Universität das Recht einräumen, die Dissertation in Datennetzen zu vervielfältigen und öffentlich wiederzugeben. Dies beinhaltet die Unterzeichnung eines Veröffentlichungsvertrages.

Bei kumulativen Dissertationen müssen Sie sich daher **rechtzeitig vorab** bei den jeweiligen Verlagen zumindest die **Publikationsrechte für die Verwendung in Ihrer Dissertationsschrift** (inklusive der Online-Version) sichern!!

<u>Wie gehen Sie da vor?</u>
- Kümmern Sie sich um die Klärung dieser Frage **sehr frühzeitig**, auch wenn Sie noch nicht sicher sind, ob Sie kumulativ promovieren werden.
- Schreiben Sie die Verlage an, dass Sie die Publikationsrechte für die Verwendung in Ihrer Dissertationsschrift behalten möchten.
- Einige Verlage haben dazu auf ihren Internetseiten ihre „Policy" veröffentlicht, die sie sich für Ihren Fall bestätigen lassen sollten.
- Prüfen Sie vor Einreichung Ihres Artikels über die Sherpa-Romeo-Datenbank, http://www.sherpa.ac.uk/romeo/index.php, ob der Verlag eine Verwertung in der Dissertation zulässt. Wenn nein, schreiben Sie den Verlag dennoch an, ob es in Ihrem Fall zur Veröffentlichung Ihrer Dissertationsschrift möglich ist.

Wenn Sie die Rechte zur Verwendung der Originalpublikationen in Ihrer Dissertationsschrift erhalten, dürfen und müssen Sie diese sowohl in die gedruckten Pflichtexemplare als auch in die finale elektronische Version einbinden. In der Regel entspricht dann also das Pflichtexemplar dem zur Eröffnung des Promotionsverfahrens eingereichten Exemplar.

Es kann sein, dass die Verlage bestimmte Bedingungen vorgeben, z.B.
- Abweichende Seitenzählung
- Änderung des Layouts (insb. Herausnahme des Verlagslogos)
- Ergänzung eines deutlichen Links auf die Publikation des Verlags (z.B. DOI...).
- Einhaltung von Sperrfristen

In einigen Fällen würden die abgegebenen Pflichtexemplare von der zur Eröffnung des Promotionsverfahrens abgegebenen Version abweichen, so dass diese Änderungen oder eine verzögerte Veröffentlichung der Dissertation vorab schriftlich vom Vorsitzenden des Promotionsausschusses genehmigt werden müssen.

Sollten Sie trotz größter Bemühungen **keine** Genehmigung zur Einbindung der Veröffentlichung/en in Ihre Dissertationsschrift erhalten, müssen Sie für Ihren individuellen Fall schriftlich eine Ausnahmegenehmigung des Vorsitzenden des Promotionsausschusses beantragen, dahingehend, dass die copyright-geschützten Originalpublikationen in den Pflichtexemplaren entfernt werden und anstelle dessen lediglich der DOI und bibliographische Daten, die das Auffinden der Publikation ermöglichen (z.B. Autoren, Titel, Journal, Volume, Issue, Seiten) aufgeführt werden. [1]

<u>ACHTUNG:</u>
Mit Verabschiedung einer überarbeiteten Promotionsordnung, spätestens aber ab dem 01.01.2020 gilt:
Sollten Sie keine Genehmigung zur Einbindung der Veröffentlichung in Ihre Dissertationsschrift erhalten, ist eine kumulative Dissertationsschrift mit dieser Publikation **ausgeschlossen**. Die Dissertationsschrift muss stets den **gesamten Text** der Arbeiten einbinden.

---

[1] Sollten die Verlage Ihnen nicht das Recht einräumen, Ihre Artikel als Teil Ihrer Dissertationsschrift zu veröffentlichen, können Sie auch nicht die Manuskriptform der Artikel nutzen, da die Rechte an dieser inhaltsgleichen Version ebenfalls an die Verlage übertragen sind.

Appendix B

Invited Talks

Snapshot of the ICTP website taken at 11th October 2017. The PhD candidate submitting this dissertation presented in the announced seminar.

Modeling vascular tumors (9 October 2017)   http://indico.ictp.it/event/8401/

The Abdus Salam
**International Centre
for Theoretical Physics**

IAEA

United Nations
Educational, Scientific and
Cultural Organization

Support
✉ qls@ictp.it

Modeling vascular tumors
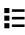
🕐 Starts 9 Oct 2017 14:30   📍 ICTP
Ends 9 Oct 2017 15:30   Common Area, second floor, old SISSA building, via
Central European Time   Beirut

Tumors appear in various types and affect a huge variety of functional aspects. We focus on the stage when the cluster of cancerous cells becomes larger than the average diffusion length of the required nutrients. At this point the tumor starts to modify the surrounding vascular structure of healthy tissue which is a complex and not yet understood process. Since the changes in topology and spatial arrangement of blood vessels and capillaries affect the distribution of interstitial fluid, oxygen, etc. this process is of special interest in order to understand cancer at malignant scales.

We use computer simulations to design artificial blood vessel networks followed by modeling vascular tumor growth. During this talk I will give you a brief overview of our model.

≣ Speaker(s)   Thierry Fredrich - Universität des Saarlandes, Saarbrücken, Germany

Appendix C

Conference/ Workshop Attendance

Deutsche Physikalische Gesellschaft, Spring Meeting 2014, Dresden

Cell Physics 2014, Saarbrücken

Circle Meeting 2015, Amsterdam A computational model of tumor growth based on large scale vascular networks

Deutsche Physikalische Gesellschaft, Spring Meeting 2015, Berlin A computational model of tumor growth based on large scale vascular networks

Physics of Cancer 2015, Leipzig Oxygen supply, Interstitial fluid flow and drug delivery in vascularized tumors: A computational model

StatPhys26 2016, Lyon Computational analysis of tumor oxygenation in vascularized tumors with applications to breast cancer

ECMTB 2016, Nottingham Computational analysis of tumor oxygenation in vascularized tumors with applications to breast cancer

Cell Physcis 2016, Saarbrücken How tumor vessel network morphology determines oxygen concentration

Circle Meeting 2017, Heidelberg Vascular Adaption Dynamics — An old idea considered from a different point of view

Cell Physics 2017, Saarbrücken Vascular Adaption Dynamics — An old idea probed with modern techniques

Mini Symposium Metastasierung 2017, Stralsund

Cuban German Graduate School 2018, Havanna

Circle Meeting 2019, Saarbrücken Fine- grained simulation of the microenvironment of vascularized tumors

Deutsche Physikalische Gesellschaft, Spring Meeting 2019, Regensburg Fine- grained simulation of the microenvironment of vascularized tumors

Cell Physics 2019, Saarbrücken Fine- grained simulation of the microenvironment of vascularized tumors

Appendix D

Teaching

Winterterm 2013/2014 Supervising exercice course on statistical physics.

Summerterm 2014 Supervising exercice course on classical mechanics.

Winterterm 2014/2015 Constructing an exercise for computer physcis course.

Winterterm 2015/2016 Supervising exercice course on statistical physics.

Summerterm 2016 Supervising exercices on quantum mechanics.

Summerterm 2017 managed exercises for computer physics lecture.

Summerterm 2018 Supervising exercices on quantum mechanics.

Winterterm 2018/2019 Introduction to linux OS, C++, scientific python and exercises in computer physics.

Summerterm 2019 Managing and designing exercice courses in advance quantum mechanics

Appendix E

SFB 1027 photo competition

The author of this dissertation contributed with three images to the photo contest anounced by the SFB 1027 in 2018. The contributing images are reprinted in figure E.1, figure E.2 and figure E.3.
The image shown in figure E.1 was awarded to decorate the poster of the "Cell Physics" conference in 2019 (http://www.cell-physics.uni-saarland.de/poster/poster_2019/Cell-Physics-2019-A4.pdf).
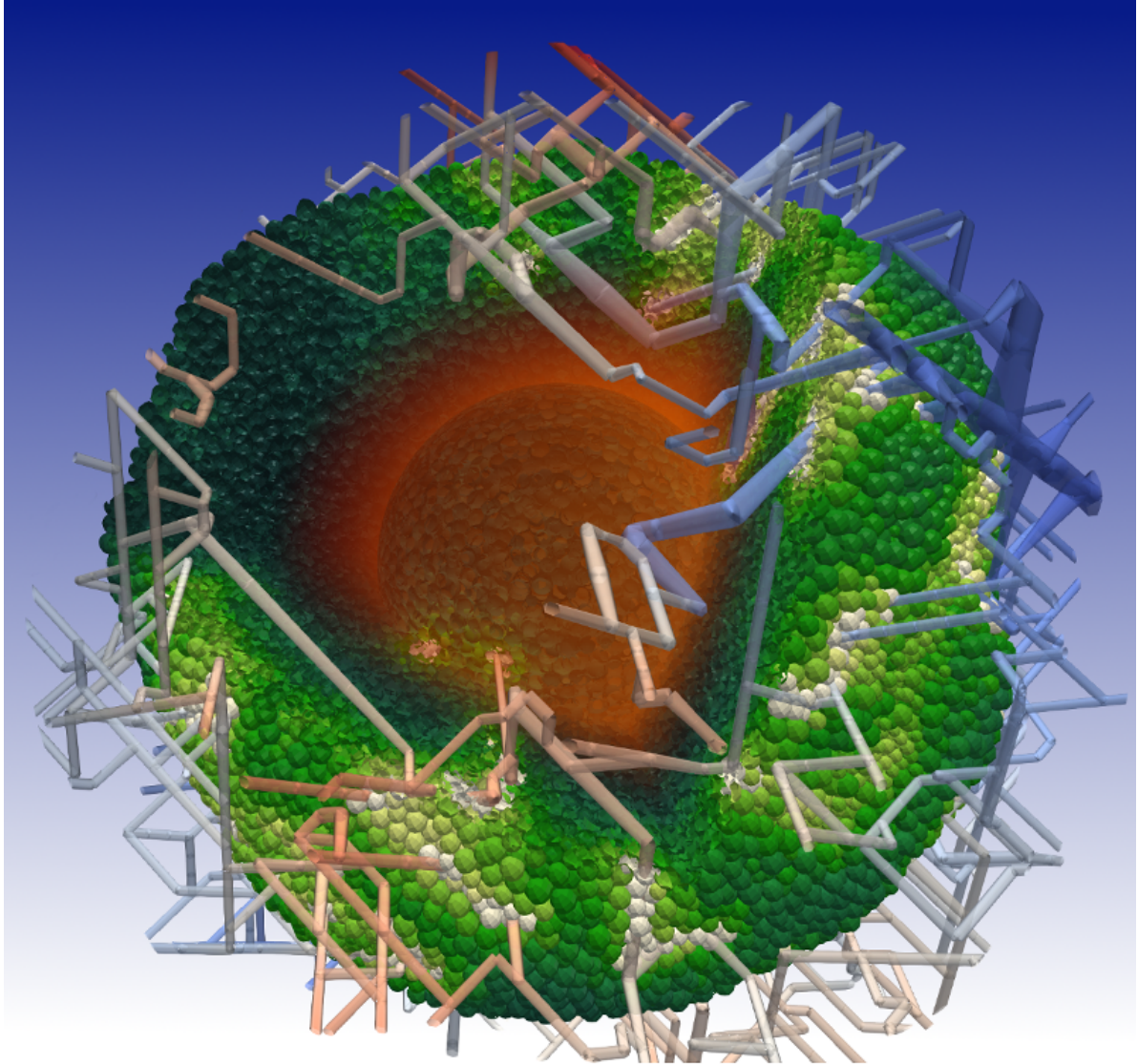
Figure E.1: pH level in vascularized tumor spheroid - vessels are color coded by blood pressure, cells by pH level, the fading orange in the center indicated the amount of vascular endothelial growth factor (VEGF) released by the cells.

A lot of aspects of the SFB 1027 deal with low number of cells. In A3 - physical processes during T cell activation, polarization, and killing - we focus not only on single cells, but also on the complete micro environment required for effective killing which is inherently linked cancer. The presented simulations are a first attempt to combine our vasculature model with cellular information.
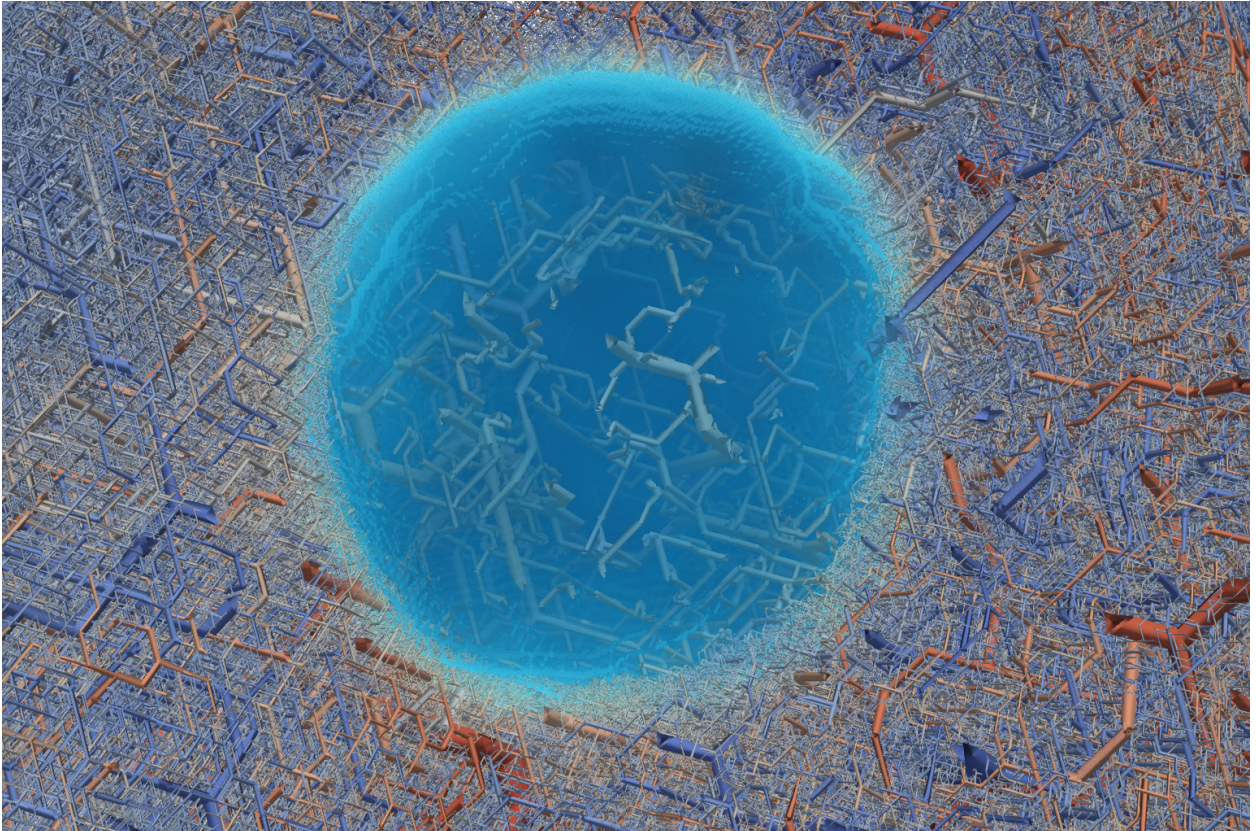
Figure E.2: A tumor modifying the surrounding healthy vasculature. The 3D network is cut to appreciate the tumor in the center. We colored amount of released vascular endothelial growth factor (VEGF) by their value from blue to cyan. The Vessels outside the tumor are depicted by their respective blood pressure from red to blue.

Project A3 deals with biological killing which is dominated by the micro-environment. In our simulations we include the vasculature to understand killing beyond the diffusion limited regime which hallmarks solid tumors in vivo.
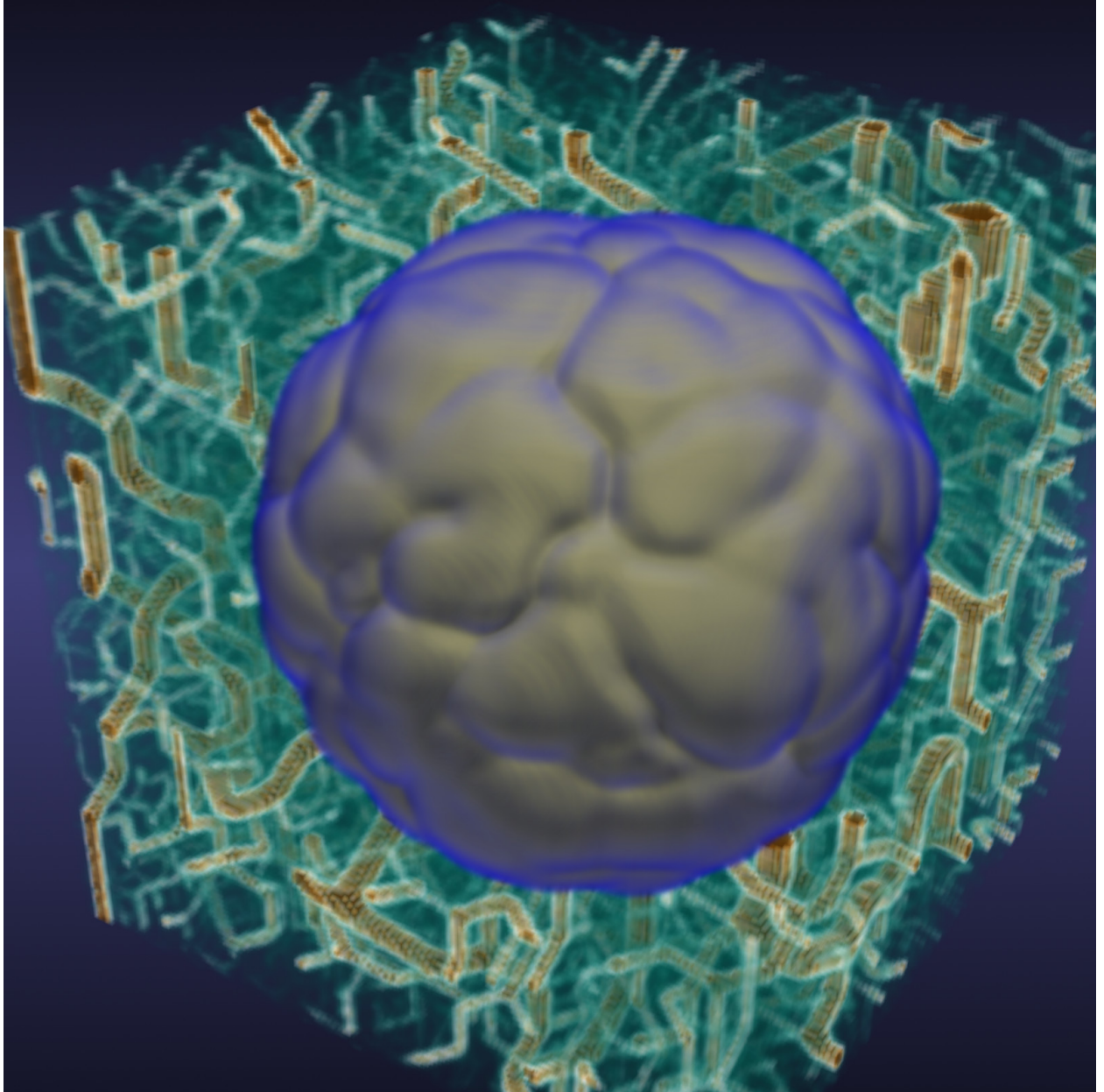
Figure E.3: Vascularized tumor. We display the vasculature as volume fraction occupied by vessels shown from green to brown and the surface as calculated by our simulations.

Project A3 deals with biological killing which is dominated by the micro-environment. In our simulations we include the vasculature to understand killing beyond the diffusion limited regime which hallmarks solid tumors in vivo.

Appendix F

Cover Page of The EPJ E

The author of this dissertation designed the cover page of the The European Physical Journal E Volume 41 / No 4 (April 2018). Available at
https://epje.epj.org/articles/epje/abs/2018/04/contents/10189_0041_004_2018.tif and reprinted with permission (see page 244 of this dissertation) in figure F.1. The image shows a tumor created by the bulk tissue tumor simulation of Tumorcode inside a small vascular network. For more information about the content contact the associated publication reprinted in chapter 3 section 3.2.
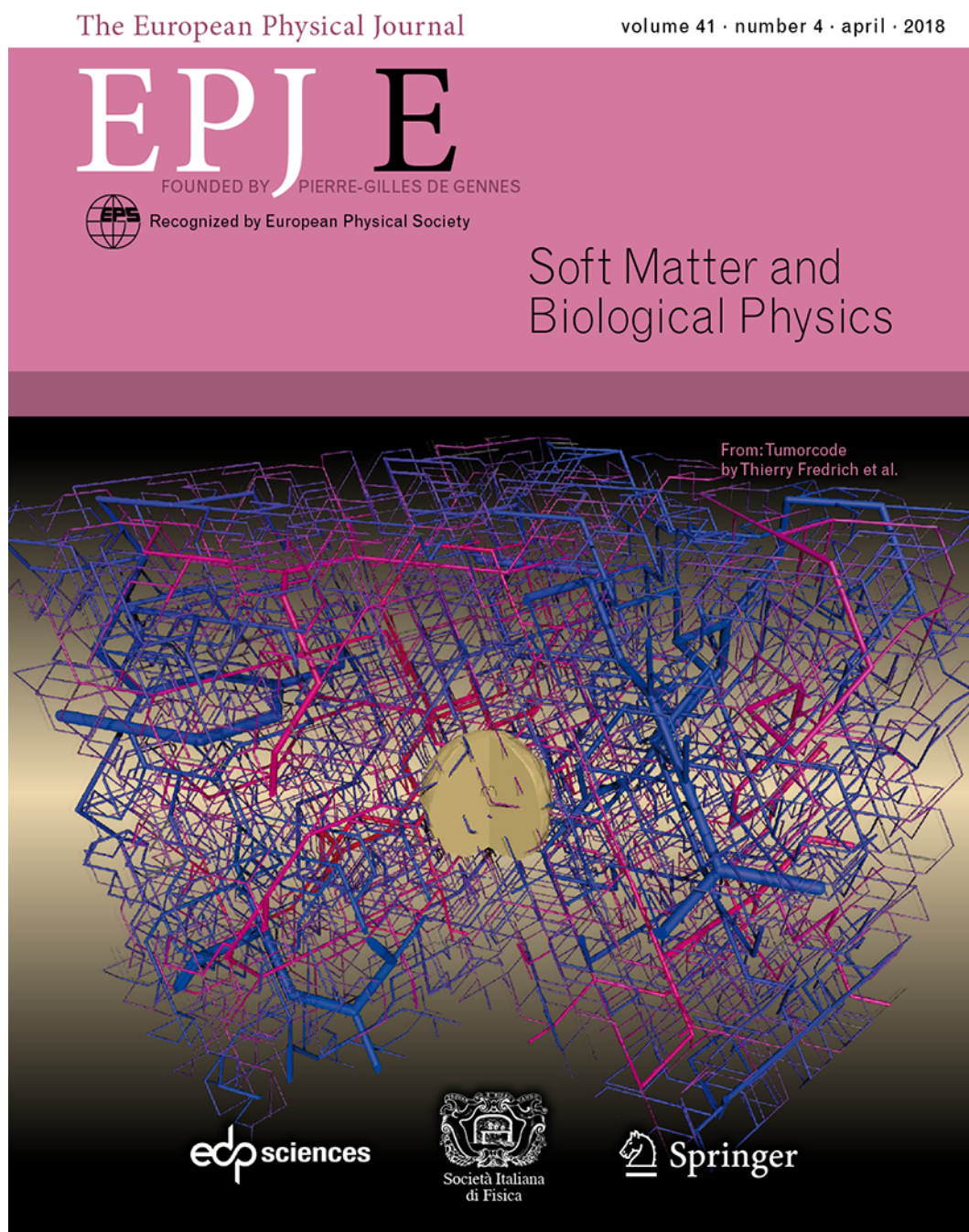
Figure F.1: Cover of The European Physical Journal E Volume 41 / No 4 (April 2018).

Appendix G

Permissions

G.1 Permissions for reprinting [1] and [3]

Creative Commons Legal Code

Attribution 4.0 International

Official translations of this license are available in other languages.

Creative Commons Corporation ("Creative Commons") is not a law firm and does not provide legal services or legal advice. Distribution of Creative Commons public licenses does not create a lawyer-client or other relationship. Creative Commons makes its licenses and related information available on an "as-is" basis. Creative Commons gives no warranties regarding its licenses, any material licensed under their terms and conditions, or any related information. Creative Commons disclaims all liability for damages resulting from their use to the fullest extent possible.

Using Creative Commons Public Licenses

Creative Commons public licenses provide a standard set of terms and conditions that creators and other rights holders may use to share original works of authorship and other material subject to copyright and certain other rights specified in the public license below. The following considerations are for informational purposes only, are not exhaustive, and do not form part of our licenses.

Considerations for licensors: Our public licenses are intended for use by those authorized to give the public permission to use material in ways otherwise restricted by copyright and certain other rights. Our licenses are irrevocable. Licensors should read and understand the terms and conditions of the license they choose before applying it. Licensors should also secure all rights necessary before applying our licenses so that the public can reuse the material as expected. Licensors should clearly mark any material not subject to the license. This includes other CC-licensed material, or material used under an exception or limitation to copyright.

Considerations for the public: By using one of our public licenses, a licensor grants the public permission to use the licensed material under specified terms and conditions. If the licensor's permission is not necessary for any reason–for example, because of any applicable exception or limitation to copyright–then that use is not regulated by the license. Our licenses

grant only permissions under copyright and certain other rights that a licensor has authority to grant. Use of the licensed material may still be restricted for other reasons, including because others have copyright or other rights in the material. A licensor may make special requests, such as asking that all changes be marked or described. Although not required by our licenses, you are encouraged to respect those requests where reasonable.

Creative Commons Attribution 4.0 International Public License

By exercising the Licensed Rights (defined below), You accept and agree to be bound by the terms and conditions of this Creative Commons Attribution 4.0 International Public License ("Public License"). To the extent this Public License may be interpreted as a contract, You are granted the Licensed Rights in consideration of Your acceptance of these terms and conditions, and the Licensor grants You such rights in consideration of benefits the Licensor receives from making the Licensed Material available under these terms and conditions.

Section 1 – Definitions.

a. **Adapted Material** means material subject to Copyright and Similar Rights that is derived from or based upon the Licensed Material and in which the Licensed Material is translated, altered, arranged, transformed, or otherwise modified in a manner requiring permission under the Copyright and Similar Rights held by the Licensor. For purposes of this Public License, where the Licensed Material is a musical work, performance, or sound recording, Adapted Material is always produced where the Licensed Material is synched in timed relation with a moving image.

b. **Adapter's License** means the license You apply to Your Copyright and Similar Rights in Your contributions to Adapted Material in accordance with the terms and conditions of this Public License.

c. **Copyright and Similar Rights** means copyright and/or similar rights closely related to copyright including, without limitation, performance, broadcast, sound recording, and Sui Generis Database Rights, without regard to how the rights are labeled or categorized. For purposes of this Public License, the rights specified in Section 2(b)(1)-(2) are not Copyright and Similar Rights.

d. **Effective Technological Measures** means those measures that, in the absence of proper authority, may not be circumvented under laws fulfilling obligations under Article 11 of the WIPO Copyright Treaty adopted on December 20, 1996, and/or similar international agreements.

e. **Exceptions and Limitations** means fair use, fair dealing, and/or any other exception or limitation to Copyright and Similar Rights that applies to Your use of the Licensed Material.

f. **Licensed Material** means the artistic or literary work, database, or other material to which

the Licensor applied this Public License.

g. **Licensed Rights** means the rights granted to You subject to the terms and conditions of this Public License, which are limited to all Copyright and Similar Rights that apply to Your use of the Licensed Material and that the Licensor has authority to license.

h. **Licensor** means the individual(s) or entity(ies) granting rights under this Public License.

i. **Share** means to provide material to the public by any means or process that requires permission under the Licensed Rights, such as reproduction, public display, public performance, distribution, dissemination, communication, or importation, and to make material available to the public including in ways that members of the public may access the material from a place and at a time individually chosen by them.

j. **Sui Generis Database Rights** means rights other than copyright resulting from Directive 96/9/EC of the European Parliament and of the Council of 11 March 1996 on the legal protection of databases, as amended and/or succeeded, as well as other essentially equivalent rights anywhere in the world.

k. **You** means the individual or entity exercising the Licensed Rights under this Public License. **Your** has a corresponding meaning.

Section 2 – Scope.

a. **License grant**.

  1. Subject to the terms and conditions of this Public License, the Licensor hereby grants You a worldwide, royalty-free, non-sublicensable, non-exclusive, irrevocable license to exercise the Licensed Rights in the Licensed Material to:
      A. reproduce and Share the Licensed Material, in whole or in part; and
      B. produce, reproduce, and Share Adapted Material.

  2. Exceptions and Limitations. For the avoidance of doubt, where Exceptions and Limitations apply to Your use, this Public License does not apply, and You do not need to comply with its terms and conditions.

  3. Term. The term of this Public License is specified in Section 6(a).

  4. Media and formats; technical modifications allowed. The Licensor authorizes You to exercise the Licensed Rights in all media and formats whether now known or hereafter created, and to make technical modifications necessary to do so. The Licensor waives and/or agrees not to assert any right or authority to forbid You from making technical modifications necessary to exercise the Licensed Rights, including technical modifications necessary to circumvent Effective Technological Measures. For purposes of this Public License, simply making modifications authorized by this Section 2(a)(4) never produces Adapted Material.

  5. Downstream recipients.
      A. Offer from the Licensor – Licensed Material. Every recipient of the Licensed

Material automatically receives an offer from the Licensor to exercise the Licensed Rights under the terms and conditions of this Public License.

B. <u>No downstream restrictions</u>. You may not offer or impose any additional or different terms or conditions on, or apply any Effective Technological Measures to, the Licensed Material if doing so restricts exercise of the Licensed Rights by any recipient of the Licensed Material.

6. <u>No endorsement</u>. Nothing in this Public License constitutes or may be construed as permission to assert or imply that You are, or that Your use of the Licensed Material is, connected with, or sponsored, endorsed, or granted official status by, the Licensor or others designated to receive attribution as provided in Section 3(a)(1)(A)(i).

b. **Other rights**.

1. Moral rights, such as the right of integrity, are not licensed under this Public License, nor are publicity, privacy, and/or other similar personality rights; however, to the extent possible, the Licensor waives and/or agrees not to assert any such rights held by the Licensor to the limited extent necessary to allow You to exercise the Licensed Rights, but not otherwise.

2. Patent and trademark rights are not licensed under this Public License.

3. To the extent possible, the Licensor waives any right to collect royalties from You for the exercise of the Licensed Rights, whether directly or through a collecting society under any voluntary or waivable statutory or compulsory licensing scheme. In all other cases the Licensor expressly reserves any right to collect such royalties.

Section 3 – License Conditions.

Your exercise of the Licensed Rights is expressly made subject to the following conditions.

a. **Attribution**.

1. If You Share the Licensed Material (including in modified form), You must:

A. retain the following if it is supplied by the Licensor with the Licensed Material:
   i. identification of the creator(s) of the Licensed Material and any others designated to receive attribution, in any reasonable manner requested by the Licensor (including by pseudonym if designated);
   ii. a copyright notice;
   iii. a notice that refers to this Public License;

iv. a notice that refers to the disclaimer of warranties;

v. a URI or hyperlink to the Licensed Material to the extent reasonably practicable;

B. indicate if You modified the Licensed Material and retain an indication of any previous modifications; and

C. indicate the Licensed Material is licensed under this Public License, and include the text of, or the URI or hyperlink to, this Public License.

2. You may satisfy the conditions in Section 3(a)(1) in any reasonable manner based on the medium, means, and context in which You Share the Licensed Material. For example, it may be reasonable to satisfy the conditions by providing a URI or hyperlink to a resource that includes the required information.

3. If requested by the Licensor, You must remove any of the information required by Section 3(a)(1)(A) to the extent reasonably practicable.

4. If You Share Adapted Material You produce, the Adapter's License You apply must not prevent recipients of the Adapted Material from complying with this Public License.

Section 4 – Sui Generis Database Rights.

Where the Licensed Rights include Sui Generis Database Rights that apply to Your use of the Licensed Material:

a. for the avoidance of doubt, Section 2(a)(1) grants You the right to extract, reuse, reproduce, and Share all or a substantial portion of the contents of the database;

b. if You include all or a substantial portion of the database contents in a database in which You have Sui Generis Database Rights, then the database in which You have Sui Generis Database Rights (but not its individual contents) is Adapted Material; and

c. You must comply with the conditions in Section 3(a) if You Share all or a substantial portion of the contents of the database.

For the avoidance of doubt, this Section 4 supplements and does not replace Your obligations under this Public License where the Licensed Rights include other Copyright and Similar Rights.

Section 5 – Disclaimer of Warranties and Limitation of Liability.

a. **Unless otherwise separately undertaken by the Licensor, to the extent possible, the Licensor offers the Licensed Material as-is and as-available, and makes no representations or warranties of any kind concerning the Licensed Material, whether express, implied, statutory, or other. This includes, without limitation, warranties of title, merchantability, fitness for a particular purpose, non-infringement, absence of latent or other defects, accuracy, or the presence or**

absence of errors, whether or not known or discoverable. Where disclaimers of warranties are not allowed in full or in part, this disclaimer may not apply to You.

b. **To the extent possible, in no event will the Licensor be liable to You on any legal theory (including, without limitation, negligence) or otherwise for any direct, special, indirect, incidental, consequential, punitive, exemplary, or other losses, costs, expenses, or damages arising out of this Public License or use of the Licensed Material, even if the Licensor has been advised of the possibility of such losses, costs, expenses, or damages. Where a limitation of liability is not allowed in full or in part, this limitation may not apply to You.**

c. The disclaimer of warranties and limitation of liability provided above shall be interpreted in a manner that, to the extent possible, most closely approximates an absolute disclaimer and waiver of all liability.

Section 6 – Term and Termination.

a. This Public License applies for the term of the Copyright and Similar Rights licensed here. However, if You fail to comply with this Public License, then Your rights under this Public License terminate automatically.

b. Where Your right to use the Licensed Material has terminated under Section 6(a), it reinstates:

  1. automatically as of the date the violation is cured, provided it is cured within 30 days of Your discovery of the violation; or
  2. upon express reinstatement by the Licensor.

  For the avoidance of doubt, this Section 6(b) does not affect any right the Licensor may have to seek remedies for Your violations of this Public License.

c. For the avoidance of doubt, the Licensor may also offer the Licensed Material under separate terms or conditions or stop distributing the Licensed Material at any time; however, doing so will not terminate this Public License.

d. Sections 1, 5, 6, 7, and 8 survive termination of this Public License.

Section 7 – Other Terms and Conditions.

a. The Licensor shall not be bound by any additional or different terms or conditions communicated by You unless expressly agreed.

b. Any arrangements, understandings, or agreements regarding the Licensed Material not stated herein are separate from and independent of the terms and conditions of this Public License.

Section 8 – Interpretation.

a. For the avoidance of doubt, this Public License does not, and shall not be interpreted to, reduce, limit, restrict, or impose conditions on any use of the Licensed Material that could lawfully be made without permission under this Public License.

b. To the extent possible, if any provision of this Public License is deemed unenforceable, it shall be automatically reformed to the minimum extent necessary to make it enforceable. If the provision cannot be reformed, it shall be severed from this Public License without affecting the enforceability of the remaining terms and conditions.

c. No term or condition of this Public License will be waived and no failure to comply consented to unless expressly agreed to by the Licensor.

d. Nothing in this Public License constitutes or may be interpreted as a limitation upon, or waiver of, any privileges and immunities that apply to the Licensor or You, including from the legal processes of any jurisdiction or authority.

Creative Commons is not a party to its public licenses. Notwithstanding, Creative Commons may elect to apply one of its public licenses to material it publishes and in those instances will be considered the "Licensor." The text of the Creative Commons public licenses is dedicated to the public domain under the CC0 Public Domain Dedication. Except for the limited purpose of indicating that material is shared under a Creative Commons public license or as otherwise permitted by the Creative Commons policies published at creativecommons.org/policies, Creative Commons does not authorize the use of the trademark "Creative Commons" or any other trademark or logo of Creative Commons without its prior written consent including, without limitation, in connection with any unauthorized modifications to any of its public licenses or any other arrangements, understandings, or agreements concerning use of licensed material. For the avoidance of doubt, this paragraph does not form part of the public licenses.

Creative Commons may be contacted at creativecommons.org.

Additional languages available: Bahasa Indonesia, Español, euskara, Deutsch, Español, français, hrvatski, italiano, latviski, Lietuvių, Nederlands, norsk, polski, português, suomeksi, svenska, te reo Māori, Türkçe, čeština, Ελληνικά, русский, українська, العربية, 日本語, 한국어 . Please read the FAQ for more information about official translations.

G.2 Permission for reprinting [2] in section 3.2

SPRINGER NATURE LICENSE **TERMS AND CONDITIONS**	
	Aug 16, 2019

This Agreement between Thierry Fredrich ("You") and Springer Nature ("Springer Nature") consists of your license details and the terms and conditions provided by Springer Nature and Copyright Clearance Center.

License Number	4650661396211
License date	Aug 16, 2019
Licensed Content Publisher	Springer Nature
Licensed Content Publication	The European Physical Journal E - Soft Matter
Licensed Content Title	Tumorcode
Licensed Content Author	Thierry Fredrich, Michael Welter, Heiko Rieger
Licensed Content Date	Jan 1, 2018
Licensed Content Volume	41
Licensed Content Issue	4
Type of Use	Thesis/Dissertation
Requestor type	academic/university or research institute
Format	print and electronic
Portion	full article/chapter
Will you be translating?	no
Circulation/distribution	<501
Author of this Springer Nature content	yes
Title	Computational studies of vascularized tumors
Institution name	Saarland University
Expected presentation date	Jan 2020
Requestor Location	Thierry Fredrich Campus E2.6 -- 4.27 Saarbrücken, 66125 Germany Attn: Thierry Fredrich
Total	0.00 USD
Terms and Conditions	

Springer Nature Customer Service Centre GmbH
Terms and Conditions

This agreement sets out the terms and conditions of the licence (the **Licence**) between you and **Springer Nature Customer Service Centre GmbH** (the **Licensor**). By clicking 'accept' and completing the transaction for the material (**Licensed Material**), you also confirm your acceptance of these terms and conditions.

1. Grant of License

1. 1. The Licensor grants you a personal, non-exclusive, non-transferable, world-wide licence to reproduce the Licensed Material for the purpose specified in your order only. Licences are granted for the specific use requested in the order and for no other use, subject to the conditions below.

1. 2. The Licensor warrants that it has, to the best of its knowledge, the rights to license reuse of the Licensed Material. However, you should ensure that the material you are requesting is original to the Licensor and does not carry the copyright of another entity (as credited in the published version).

1. 3. If the credit line on any part of the material you have requested indicates that it was reprinted or adapted with permission from another source, then you should also seek permission from that source to reuse the material.

2. Scope of Licence

2. 1. You may only use the Licensed Content in the manner and to the extent permitted by these Ts&Cs and any applicable laws.

2. 2. A separate licence may be required for any additional use of the Licensed Material, e.g. where a licence has been purchased for print only use, separate permission must be obtained for electronic re-use. Similarly, a licence is only valid in the language selected and does not apply for editions in other languages unless additional translation rights have been granted separately in the licence. Any content owned by third parties are expressly excluded from the licence.

2. 3. Similarly, rights for additional components such as custom editions and derivatives require additional permission and may be subject to an additional fee. Please apply to Journalpermissions@springernature.com/bookpermissions@springernature.com for these rights.

2. 4. Where permission has been granted **free of charge** for material in print, permission may also be granted for any electronic version of that work, provided that the material is incidental to your work as a whole and that the electronic version is essentially equivalent to, or substitutes for, the print version.

2. 5. An alternative scope of licence may apply to signatories of the STM Permissions Guidelines, as amended from time to time.

3. Duration of Licence

3. 1. A licence for is valid from the date of purchase ('Licence Date') at the end of the relevant period in the below table:

Scope of Licence	Duration of Licence
Post on a website	12 months
Presentations	12 months
Books and journals	Lifetime of the edition in the language purchased

4. Acknowledgement

4. 1. The Licensor's permission must be acknowledged next to the Licenced Material in print. In electronic form, this acknowledgement must be visible at the same time as the figures/tables/illustrations or abstract, and must be hyperlinked to the journal/book's homepage. Our required acknowledgement format is in the Appendix below.

5. Restrictions on use

5. 1. Use of the Licensed Material may be permitted for incidental promotional use and minor editing privileges e.g. minor adaptations of single figures, changes of format, colour and/or style where the adaptation is credited as set out in Appendix 1 below. Any other changes including but not limited to, cropping, adapting, omitting material that affect the meaning, intention or moral rights of the author are strictly prohibited.

5. 2. You must not use any Licensed Material as part of any design or trademark.

5. 3. Licensed Material may be used in Open Access Publications (OAP) before publication by Springer Nature, but any Licensed Material must be removed from OAP sites prior to final publication.

6. Ownership of Rights

6. 1. Licensed Material remains the property of either Licensor or the relevant third party and any rights not explicitly granted herein are expressly reserved.

7. Warranty

IN NO EVENT SHALL LICENSOR BE LIABLE TO YOU OR ANY OTHER PARTY OR ANY OTHER PERSON OR FOR ANY SPECIAL, CONSEQUENTIAL, INCIDENTAL OR INDIRECT DAMAGES, HOWEVER CAUSED, ARISING OUT OF OR IN CONNECTION WITH THE DOWNLOADING, VIEWING OR USE OF THE MATERIALS REGARDLESS OF THE FORM OF ACTION, WHETHER FOR BREACH OF CONTRACT, BREACH OF WARRANTY, TORT, NEGLIGENCE, INFRINGEMENT OR OTHERWISE (INCLUDING, WITHOUT LIMITATION, DAMAGES BASED ON LOSS OF PROFITS, DATA, FILES, USE, BUSINESS OPPORTUNITY OR CLAIMS OF THIRD PARTIES), AND
WHETHER OR NOT THE PARTY HAS BEEN ADVISED OF THE POSSIBILITY OF SUCH DAMAGES. THIS LIMITATION SHALL APPLY NOTWITHSTANDING ANY FAILURE OF ESSENTIAL PURPOSE OF ANY LIMITED REMEDY PROVIDED HEREIN.

8. Limitations

8. 1. ***BOOKS ONLY:***Where **'reuse in a dissertation/thesis'** has been selected the following terms apply: Print rights of the final author's accepted manuscript (for clarity, NOT the published version) for up to 100

copies, electronic rights for use only on a personal website or institutional repository as defined by the Sherpa guideline (www.sherpa.ac.uk/romeo/).

9. Termination and Cancellation

9. 1. Licences will expire after the period shown in Clause 3 (above).

9. 2. Licensee reserves the right to terminate the Licence in the event that payment is not received in full or if there has been a breach of this agreement by you.

<u>Appendix 1 — Acknowledgements:</u>

For Journal Content:
Reprinted by permission from [**the Licensor**]: [**Journal Publisher** (e.g. Nature/Springer/Palgrave)] [**JOURNAL NAME**] [**REFERENCE CITATION** (Article name, Author(s) Name), [**COPYRIGHT**] (year of publication)

For **Advance Online Publication papers:**
Reprinted by permission from [**the Licensor**]: [**Journal Publisher** (e.g. Nature/Springer/Palgrave)] [**JOURNAL NAME**] [**REFERENCE CITATION** (Article name, Author(s) Name), [**COPYRIGHT**] (year of publication), advance online publication, day month year (doi: 10.1038/sj.[JOURNAL ACRONYM].)

For Adaptations/Translations:
Adapted/Translated by permission from [**the Licensor**]: [**Journal Publisher** (e.g. Nature/Springer/Palgrave)] [**JOURNAL NAME**] [**REFERENCE CITATION** (Article name, Author(s) Name), [**COPYRIGHT**] (year of publication)

<u>Note: For any republication from the British Journal of Cancer, the following credit line style applies:</u>

Reprinted/adapted/translated by permission from [**the Licensor**]: on behalf of Cancer Research UK: : [**Journal Publisher** (e.g. Nature/Springer/Palgrave)] [**JOURNAL NAME**] [**REFERENCE CITATION** (Article name, Author(s) Name), [**COPYRIGHT**] (year of publication)

For **Advance Online Publication** papers:
Reprinted by permission from The [**the Licensor**]: on behalf of Cancer Research UK: [**Journal Publisher** (e.g. Nature/Springer /Palgrave)] [**JOURNAL NAME**] [**REFERENCE CITATION** (Article name, Author(s) Name), [**COPYRIGHT**] (year of publication), advance online publication, day month year (doi: 10.1038/sj. [JOURNAL ACRONYM])

For Book content:
Reprinted/adapted by permission from [**the Licensor**]: [**Book Publisher** (e.g. Palgrave Macmillan, Springer etc) [**Book Title**] by [**Book author**(s)] [**COPYRIGHT**] (year of publication)

Other Conditions:

Version   1.2

Questions? customercare@copyright.com or +1-855-239-3415 (toll free in the US) or +1-978-646-2777.

G.3   Permission for reprinting [4] in section 3.4

Creative Commons BY-NC-ND downloaded from https://creativecommons.org/licenses/by-nc-nd/4.0/legalcode at 5th of November 2019.

Creative Commons Legal Code

Attribution-NonCommercial-NoDerivatives 4.0 International

Official translations of this license are available in other languages.

Creative Commons Corporation ("Creative Commons") is not a law firm and does not provide legal services or legal advice. Distribution of Creative Commons public licenses does not create a lawyer-client or other relationship. Creative Commons makes its licenses and related information available on an "as-is" basis. Creative Commons gives no warranties regarding its licenses, any material licensed under their terms and conditions, or any related information. Creative Commons disclaims all liability for damages resulting from their use to the fullest extent possible.

Using Creative Commons Public Licenses

Creative Commons public licenses provide a standard set of terms and conditions that creators and other rights holders may use to share original works of authorship and other material subject to copyright and certain other rights specified in the public license below. The following considerations are for informational purposes only, are not exhaustive, and do not form part of our licenses.

Considerations for licensors: Our public licenses are intended for use by those authorized to give the public permission to use material in ways otherwise restricted by copyright and certain other rights. Our licenses are irrevocable. Licensors should read and understand the terms and conditions of the license they choose before applying it. Licensors should also secure all rights necessary before applying our licenses so that the public can reuse the material as expected. Licensors should clearly mark any material not subject to the license. This includes other CC-licensed material, or material used under an exception or limitation to copyright.

Considerations for the public: By using one of our public licenses, a licensor grants the public permission to use the licensed material under specified terms and conditions. If the licensor's permission is not necessary for any reason–for example, because of any applicable exception or limitation to copyright–then that use is not regulated by the license. Our licenses

grant only permissions under copyright and certain other rights that a licensor has authority to grant. Use of the licensed material may still be restricted for other reasons, including because others have copyright or other rights in the material. A licensor may make special requests, such as asking that all changes be marked or described. Although not required by our licenses, you are encouraged to respect those requests where reasonable.

Creative Commons Attribution-NonCommercial-NoDerivatives 4.0 International Public License

By exercising the Licensed Rights (defined below), You accept and agree to be bound by the terms and conditions of this Creative Commons Attribution-NonCommercial-NoDerivatives 4.0 International Public License ("Public License"). To the extent this Public License may be interpreted as a contract, You are granted the Licensed Rights in consideration of Your acceptance of these terms and conditions, and the Licensor grants You such rights in consideration of benefits the Licensor receives from making the Licensed Material available under these terms and conditions.

Section 1 – Definitions.

a. **Adapted Material** means material subject to Copyright and Similar Rights that is derived from or based upon the Licensed Material and in which the Licensed Material is translated, altered, arranged, transformed, or otherwise modified in a manner requiring permission under the Copyright and Similar Rights held by the Licensor. For purposes of this Public License, where the Licensed Material is a musical work, performance, or sound recording, Adapted Material is always produced where the Licensed Material is synched in timed relation with a moving image.

b. **Copyright and Similar Rights** means copyright and/or similar rights closely related to copyright including, without limitation, performance, broadcast, sound recording, and Sui Generis Database Rights, without regard to how the rights are labeled or categorized. For purposes of this Public License, the rights specified in Section 2(b)(1)-(2) are not Copyright and Similar Rights.

c. **Effective Technological Measures** means those measures that, in the absence of proper authority, may not be circumvented under laws fulfilling obligations under Article 11 of the WIPO Copyright Treaty adopted on December 20, 1996, and/or similar international agreements.

d. **Exceptions and Limitations** means fair use, fair dealing, and/or any other exception or limitation to Copyright and Similar Rights that applies to Your use of the Licensed Material.

e. **Licensed Material** means the artistic or literary work, database, or other material to which the Licensor applied this Public License.

f. **Licensed Rights** means the rights granted to You subject to the terms and conditions of

this Public License, which are limited to all Copyright and Similar Rights that apply to Your use of the Licensed Material and that the Licensor has authority to license.

g. **Licensor** means the individual(s) or entity(ies) granting rights under this Public License.

h. **NonCommercial** means not primarily intended for or directed towards commercial advantage or monetary compensation. For purposes of this Public License, the exchange of the Licensed Material for other material subject to Copyright and Similar Rights by digital file-sharing or similar means is NonCommercial provided there is no payment of monetary compensation in connection with the exchange.

i. **Share** means to provide material to the public by any means or process that requires permission under the Licensed Rights, such as reproduction, public display, public performance, distribution, dissemination, communication, or importation, and to make material available to the public including in ways that members of the public may access the material from a place and at a time individually chosen by them.

j. **Sui Generis Database Rights** means rights other than copyright resulting from Directive 96/9/EC of the European Parliament and of the Council of 11 March 1996 on the legal protection of databases, as amended and/or succeeded, as well as other essentially equivalent rights anywhere in the world.

k. **You** means the individual or entity exercising the Licensed Rights under this Public License. **Your** has a corresponding meaning.

Section 2 – Scope.

a. **License grant**.

    1. Subject to the terms and conditions of this Public License, the Licensor hereby grants You a worldwide, royalty-free, non-sublicensable, non-exclusive, irrevocable license to exercise the Licensed Rights in the Licensed Material to:

        A. reproduce and Share the Licensed Material, in whole or in part, for NonCommercial purposes only; and

        B. produce and reproduce, but not Share, Adapted Material for NonCommercial purposes only.

    2. <u>Exceptions and Limitations</u>. For the avoidance of doubt, where Exceptions and Limitations apply to Your use, this Public License does not apply, and You do not need to comply with its terms and conditions.

    3. <u>Term</u>. The term of this Public License is specified in Section 6(a).

    4. <u>Media and formats; technical modifications allowed</u>. The Licensor authorizes You to exercise the Licensed Rights in all media and formats whether now known or hereafter created, and to make technical modifications necessary to do so. The Licensor waives and/or agrees not to assert any right or authority to forbid You from making technical modifications necessary to exercise the Licensed Rights, including technical

modifications necessary to circumvent Effective Technological Measures. For purposes of this Public License, simply making modifications authorized by this Section 2(a)(4) never produces Adapted Material.

5. <u>Downstream recipients</u>.

    A. <u>Offer from the Licensor – Licensed Material</u>. Every recipient of the Licensed Material automatically receives an offer from the Licensor to exercise the Licensed Rights under the terms and conditions of this Public License.

    B. <u>No downstream restrictions</u>. You may not offer or impose any additional or different terms or conditions on, or apply any Effective Technological Measures to, the Licensed Material if doing so restricts exercise of the Licensed Rights by any recipient of the Licensed Material.

6. <u>No endorsement</u>. Nothing in this Public License constitutes or may be construed as permission to assert or imply that You are, or that Your use of the Licensed Material is, connected with, or sponsored, endorsed, or granted official status by, the Licensor or others designated to receive attribution as provided in Section 3(a)(1)(A)(i).

b. **Other rights**.

1. Moral rights, such as the right of integrity, are not licensed under this Public License, nor are publicity, privacy, and/or other similar personality rights; however, to the extent possible, the Licensor waives and/or agrees not to assert any such rights held by the Licensor to the limited extent necessary to allow You to exercise the Licensed Rights, but not otherwise.

2. Patent and trademark rights are not licensed under this Public License.

3. To the extent possible, the Licensor waives any right to collect royalties from You for the exercise of the Licensed Rights, whether directly or through a collecting society under any voluntary or waivable statutory or compulsory licensing scheme. In all other cases the Licensor expressly reserves any right to collect such royalties, including when the Licensed Material is used other than for NonCommercial purposes.

Section 3 – License Conditions.

Your exercise of the Licensed Rights is expressly made subject to the following conditions.

a. **Attribution**.

1. If You Share the Licensed Material, You must:

A. retain the following if it is supplied by the Licensor with the Licensed Material:

    i. identification of the creator(s) of the Licensed Material and any others designated to receive attribution, in any reasonable manner requested by the Licensor (including by pseudonym if designated);

    ii. a copyright notice;

    iii. a notice that refers to this Public License;

    iv. a notice that refers to the disclaimer of warranties;

    v. a URI or hyperlink to the Licensed Material to the extent reasonably practicable;

B. indicate if You modified the Licensed Material and retain an indication of any previous modifications; and

C. indicate the Licensed Material is licensed under this Public License, and include the text of, or the URI or hyperlink to, this Public License.

For the avoidance of doubt, You do not have permission under this Public License to Share Adapted Material.

2. You may satisfy the conditions in Section 3(a)(1) in any reasonable manner based on the medium, means, and context in which You Share the Licensed Material. For example, it may be reasonable to satisfy the conditions by providing a URI or hyperlink to a resource that includes the required information.

3. If requested by the Licensor, You must remove any of the information required by Section 3(a)(1)(A) to the extent reasonably practicable.

Section 4 – Sui Generis Database Rights.

Where the Licensed Rights include Sui Generis Database Rights that apply to Your use of the Licensed Material:

a. for the avoidance of doubt, Section 2(a)(1) grants You the right to extract, reuse, reproduce, and Share all or a substantial portion of the contents of the database for NonCommercial purposes only and provided You do not Share Adapted Material;

b. if You include all or a substantial portion of the database contents in a database in which You have Sui Generis Database Rights, then the database in which You have Sui Generis Database Rights (but not its individual contents) is Adapted Material; and

c. You must comply with the conditions in Section 3(a) if You Share all or a substantial portion of the contents of the database.

For the avoidance of doubt, this Section 4 supplements and does not replace Your obligations under this Public License where the Licensed Rights include other Copyright and Similar Rights.

Section 5 – Disclaimer of Warranties and Limitation of Liability.

a. Unless otherwise separately undertaken by the Licensor, to the extent possible, the Licensor offers the Licensed Material as-is and as-available, and makes no representations or warranties of any kind concerning the Licensed Material, whether express, implied, statutory, or other. This includes, without limitation, warranties of title, merchantability, fitness for a particular purpose, non-infringement, absence of latent or other defects, accuracy, or the presence or absence of errors, whether or not known or discoverable. Where disclaimers of warranties are not allowed in full or in part, this disclaimer may not apply to You.

b. To the extent possible, in no event will the Licensor be liable to You on any legal theory (including, without limitation, negligence) or otherwise for any direct, special, indirect, incidental, consequential, punitive, exemplary, or other losses, costs, expenses, or damages arising out of this Public License or use of the Licensed Material, even if the Licensor has been advised of the possibility of such losses, costs, expenses, or damages. Where a limitation of liability is not allowed in full or in part, this limitation may not apply to You.

c. The disclaimer of warranties and limitation of liability provided above shall be interpreted in a manner that, to the extent possible, most closely approximates an absolute disclaimer and waiver of all liability.

Section 6 – Term and Termination.

a. This Public License applies for the term of the Copyright and Similar Rights licensed here. However, if You fail to comply with this Public License, then Your rights under this Public License terminate automatically.

b. Where Your right to use the Licensed Material has terminated under Section 6(a), it reinstates:

   1. automatically as of the date the violation is cured, provided it is cured within 30 days of Your discovery of the violation; or
   2. upon express reinstatement by the Licensor.

   For the avoidance of doubt, this Section 6(b) does not affect any right the Licensor may have to seek remedies for Your violations of this Public License.

c. For the avoidance of doubt, the Licensor may also offer the Licensed Material under separate terms or conditions or stop distributing the Licensed Material at any time; however, doing so will not terminate this Public License.

d. Sections 1, 5, 6, 7, and 8 survive termination of this Public License.

Section 7 – Other Terms and Conditions.

a. The Licensor shall not be bound by any additional or different terms or conditions communicated by You unless expressly agreed.

b. Any arrangements, understandings, or agreements regarding the Licensed Material not stated herein are separate from and independent of the terms and conditions of this Public License.

Section 8 – Interpretation.

a. For the avoidance of doubt, this Public License does not, and shall not be interpreted to, reduce, limit, restrict, or impose conditions on any use of the Licensed Material that could lawfully be made without permission under this Public License.

b. To the extent possible, if any provision of this Public License is deemed unenforceable, it shall be automatically reformed to the minimum extent necessary to make it enforceable. If the provision cannot be reformed, it shall be severed from this Public License without affecting the enforceability of the remaining terms and conditions.

c. No term or condition of this Public License will be waived and no failure to comply consented to unless expressly agreed to by the Licensor.

d. Nothing in this Public License constitutes or may be interpreted as a limitation upon, or waiver of, any privileges and immunities that apply to the Licensor or You, including from the legal processes of any jurisdiction or authority.

Creative Commons is not a party to its public licenses. Notwithstanding, Creative Commons may elect to apply one of its public licenses to material it publishes and in those instances will be considered the "Licensor." The text of the Creative Commons public licenses is dedicated to the public domain under the CC0 Public Domain Dedication. Except for the limited purpose of indicating that material is shared under a Creative Commons public license or as otherwise permitted by the Creative Commons policies published at creativecommons.org/policies, Creative Commons does not authorize the use of the trademark "Creative Commons" or any other trademark or logo of Creative Commons without its prior written consent including, without limitation, in connection with any unauthorized modifications to any of its public licenses or any other arrangements, understandings, or agreements concerning use of licensed material. For the avoidance of doubt, this paragraph does not form part of the public licenses.

Creative Commons may be contacted at creativecommons.org.

Additional languages available: Bahasa Indonesia, Español, euskara, Deutsch, Español, français, hrvatski, italiano, latviski, Lietuvių, Nederlands, norsk, polski, português, suomeksi, svenska, te reo Māori, Türkçe, čeština, Ελληνικά, русский, українська, العربية, 日本語, 한국

국어 . Please read the FAQ for more information about official translations.

G.4 Permission to reprint content of figure 2.3

G.4 Permission to reprint content of figure 2.3

SPRINGER NATURE LICENSE **TERMS AND CONDITIONS**	
	Aug 16, 2019

This Agreement between Thierry Fredrich ("You") and Springer Nature ("Springer Nature") consists of your license details and the terms and conditions provided by Springer Nature and Copyright Clearance Center.

License Number	4650660166353
License date	Aug 16, 2019
Licensed Content Publisher	Springer Nature
Licensed Content Publication	The European Physical Journal Plus
Licensed Content Title	Physics of the tumor vasculature: Theory and experiment
Licensed Content Author	Heiko Rieger, Thierry Fredrich, Michael Welter
Licensed Content Date	Jan 1, 2016
Licensed Content Volume	131
Licensed Content Issue	2
Type of Use	Thesis/Dissertation
Requestor type	academic/university or research institute
Format	print and electronic
Portion	figures/tables/illustrations
Number of figures/tables /illustrations	1
Will you be translating?	no
Circulation/distribution	<501
Author of this Springer Nature content	yes
Title	Computational studies of vascularized tumors
Institution name	Saarland University
Expected presentation date	Jan 2020
Portions	Figure 6 page 10
Requestor Location	Thierry Fredrich Campus E2.6 -- 4.27 Saarbrücken, 66125 Germany Attn: Thierry Fredrich
Total	0.00 USD

Springer Nature Customer Service Centre GmbH
Terms and Conditions

This agreement sets out the terms and conditions of the licence (the **Licence**) between you and **Springer Nature Customer Service Centre GmbH** (the **Licensor**). By clicking 'accept' and completing the transaction for the material (**Licensed Material**), you also confirm your acceptance of these terms and conditions.

1. Grant of License

1. 1. The Licensor grants you a personal, non-exclusive, non-transferable, world-wide licence to reproduce the Licensed Material for the purpose specified in your order only. Licences are granted for the specific use requested in the order and for no other use, subject to the conditions below.

1. 2. The Licensor warrants that it has, to the best of its knowledge, the rights to license reuse of the Licensed Material. However, you should ensure that the material you are requesting is original to the Licensor and does not carry the copyright of another entity (as credited in the published version).

1. 3. If the credit line on any part of the material you have requested indicates that it was reprinted or adapted with permission from another source, then you should also seek permission from that source to reuse the material.

2. Scope of Licence

2. 1. You may only use the Licensed Content in the manner and to the extent permitted by these Ts&Cs and any applicable laws.

2. 2. A separate licence may be required for any additional use of the Licensed Material, e.g. where a licence has been purchased for print only use, separate permission must be obtained for electronic re-use. Similarly, a licence is only valid in the language selected and does not apply for editions in other languages unless additional translation rights have been granted separately in the licence. Any content owned by third parties are expressly excluded from the licence.

2. 3. Similarly, rights for additional components such as custom editions and derivatives require additional permission and may be subject to an additional fee. Please apply to Journalpermissions@springernature.com/bookpermissions@springernature.com for these rights.

2. 4. Where permission has been granted **free of charge** for material in print, permission may also be granted for any electronic version of that work, provided that the material is incidental to your work as a whole and that the electronic version is essentially equivalent to, or substitutes for, the print version.

2. 5. An alternative scope of licence may apply to signatories of the STM Permissions Guidelines, as amended from time to time.

3. Duration of Licence

3. 1. A licence for is valid from the date of purchase ('Licence Date') at the end of the relevant period in the below table:

Scope of Licence	Duration of Licence
Post on a website	12 months
Presentations	12 months
Books and journals	Lifetime of the edition in the language purchased

4. Acknowledgement

4. 1. The Licensor's permission must be acknowledged next to the Licenced Material in print. In electronic form, this acknowledgement must be visible at the same time as the figures/tables/illustrations or abstract, and must be hyperlinked to the journal/book's homepage. Our required acknowledgement format is in the Appendix below.

5. Restrictions on use

5. 1. Use of the Licensed Material may be permitted for incidental promotional use and minor editing privileges e.g. minor adaptations of single figures, changes of format, colour and/or style where the adaptation is credited as set out in Appendix 1 below. Any other changes including but not limited to, cropping, adapting, omitting material that affect the meaning, intention or moral rights of the author are strictly prohibited.

5. 2. You must not use any Licensed Material as part of any design or trademark.

5. 3. Licensed Material may be used in Open Access Publications (OAP) before publication by Springer Nature, but any Licensed Material must be removed from OAP sites prior to final publication.

6. Ownership of Rights

6. 1. Licensed Material remains the property of either Licensor or the relevant third party and any rights not explicitly granted herein are expressly reserved.

7. Warranty

IN NO EVENT SHALL LICENSOR BE LIABLE TO YOU OR ANY OTHER PARTY OR ANY OTHER PERSON OR FOR ANY SPECIAL, CONSEQUENTIAL, INCIDENTAL OR INDIRECT DAMAGES, HOWEVER CAUSED, ARISING OUT OF OR IN CONNECTION WITH THE DOWNLOADING, VIEWING OR USE OF THE MATERIALS REGARDLESS OF THE FORM OF ACTION, WHETHER FOR BREACH OF CONTRACT, BREACH OF WARRANTY, TORT, NEGLIGENCE, INFRINGEMENT OR OTHERWISE (INCLUDING, WITHOUT LIMITATION, DAMAGES BASED ON LOSS OF PROFITS, DATA, FILES, USE, BUSINESS OPPORTUNITY OR CLAIMS OF THIRD PARTIES), AND
WHETHER OR NOT THE PARTY HAS BEEN ADVISED OF THE POSSIBILITY OF SUCH DAMAGES. THIS LIMITATION SHALL APPLY NOTWITHSTANDING ANY FAILURE OF ESSENTIAL PURPOSE OF ANY LIMITED REMEDY PROVIDED HEREIN.

8. Limitations

8. 1. _BOOKS ONLY:_ Where **'reuse in a dissertation/thesis'** has been selected the following terms apply: Print rights of the final author's accepted manuscript (for clarity, NOT the published version) for up to 100 copies, electronic rights for use only on a personal website or institutional repository as defined by the Sherpa guideline (www.sherpa.ac.uk/romeo/).

9. Termination and Cancellation

9. 1. Licences will expire after the period shown in Clause 3 (above).

9. 2. Licensee reserves the right to terminate the Licence in the event that payment is not received in full or if there has been a breach of this agreement by you.

Appendix 1 — Acknowledgements:

For Journal Content:
Reprinted by permission from [**the Licensor**]: [**Journal Publisher** (e.g. Nature/Springer/Palgrave)] [**JOURNAL NAME**] [**REFERENCE CITATION** (Article name, Author(s) Name), [**COPYRIGHT**] (year of publication)

For **Advance Online Publication papers:**
Reprinted by permission from [**the Licensor**]: [**Journal Publisher** (e.g. Nature/Springer/Palgrave)] [**JOURNAL NAME**] [**REFERENCE CITATION** (Article name, Author(s) Name), [**COPYRIGHT**] (year of publication), advance online publication, day month year (doi: 10.1038/sj.[JOURNAL ACRONYM].)

For Adaptations/Translations:
Adapted/Translated by permission from [**the Licensor**]: [**Journal Publisher** (e.g. Nature/Springer/Palgrave)] [**JOURNAL NAME**] [**REFERENCE CITATION** (Article name, Author(s) Name), [**COPYRIGHT**] (year of publication)

Note: For any republication from the British Journal of Cancer, the following credit line style applies:

Reprinted/adapted/translated by permission from [**the Licensor**]: on behalf of Cancer Research UK: : [**Journal Publisher** (e.g. Nature/Springer/Palgrave)] [**JOURNAL NAME**] [**REFERENCE CITATION** (Article name, Author(s) Name), [**COPYRIGHT**] (year of publication)

For **Advance Online Publication** papers:
Reprinted by permission from The [**the Licensor**]: on behalf of Cancer Research UK: [**Journal Publisher** (e.g. Nature/Springer /Palgrave)] [**JOURNAL NAME**] [**REFERENCE CITATION** (Article name, Author(s) Name), [**COPYRIGHT**] (year of publication),

advance online publication, day month year (doi: 10.1038/sj.
[JOURNAL ACRONYM])

For Book content:
Reprinted/adapted by permission from [**the Licensor**]: [**Book
Publisher** (e.g. Palgrave Macmillan, Springer etc) [**Book Title**] by
[**Book author**(s)] [**COPYRIGHT**] (year of publication)

Other Conditions:

Version 1.2

Questions? customercare@copyright.com or +1-855-239-3415 (toll free in the US) or +1-978-646-2777.

G.5　Permission to reprint content in appendix F

G.5　Permission to reprint content in appendix F

SPRINGER NATURE ORDER DETAILS	
	Aug 16, 2019

This Agreement between Thierry Fredrich ("You") and Springer Nature ("Springer Nature") consists of your order details and the terms and conditions provided by Springer Nature and Copyright Clearance Center.

Order Number	501507382
Order date	Aug 16, 2019
Licensed Content Publisher	Springer Nature
Licensed Content Publication	The European Physical Journal E - Soft Matter
Licensed Content Title	Tumorcode
Licensed Content Author	Thierry Fredrich, Michael Welter, Heiko Rieger
Licensed Content Date	Jan 1, 2018
Licensed Content Volume	41
Licensed Content Issue	4
Type of Use	Journal Cover
Requestor type	academic/university or research institute
Format	print and electronic
Circulation/distribution	<501
Author of this Springer Nature content	yes
Requestor Location	Thierry Fredrich Campus E2.6 -- 4.27 Saarbrücken, 66125 Germany Attn: Thierry Fredrich
Billing Type	Invoice
Billing Address	Thierry Fredrich Campus E2.6 -- 4.27 Saarbrücken, Germany 66125 Attn: Thierry Fredrich
Total	0.00 USD
Terms and Conditions	

Springer Nature Customer Service Centre GmbH
Terms and Conditions

This agreement sets out the terms and conditions of the licence (the **Licence**) between you and **Springer Nature Customer Service Centre GmbH** (the **Licensor**). By clicking 'accept' and completing the

transaction for the material (**Licensed Material**), you also confirm your acceptance of these terms and conditions.

1. Grant of License

1. 1. The Licensor grants you a personal, non-exclusive, non-transferable, world-wide licence to reproduce the Licensed Material for the purpose specified in your order only. Licences are granted for the specific use requested in the order and for no other use, subject to the conditions below.

1. 2. The Licensor warrants that it has, to the best of its knowledge, the rights to license reuse of the Licensed Material. However, you should ensure that the material you are requesting is original to the Licensor and does not carry the copyright of another entity (as credited in the published version).

1. 3. If the credit line on any part of the material you have requested indicates that it was reprinted or adapted with permission from another source, then you should also seek permission from that source to reuse the material.

2. Scope of Licence

2. 1. You may only use the Licensed Content in the manner and to the extent permitted by these Ts&Cs and any applicable laws.

2. 2. A separate licence may be required for any additional use of the Licensed Material, e.g. where a licence has been purchased for print only use, separate permission must be obtained for electronic re-use. Similarly, a licence is only valid in the language selected and does not apply for editions in other languages unless additional translation rights have been granted separately in the licence. Any content owned by third parties are expressly excluded from the licence.

2. 3. Similarly, rights for additional components such as custom editions and derivatives require additional permission and may be subject to an additional fee. Please apply to Journalpermissions@springernature.com/bookpermissions@springernature.com for these rights.

2. 4. Where permission has been granted **free of charge** for material in print, permission may also be granted for any electronic version of that work, provided that the material is incidental to your work as a whole and that the electronic version is essentially equivalent to, or substitutes for, the print version.

2. 5. An alternative scope of licence may apply to signatories of the STM Permissions Guidelines, as amended from time to time.

3. Duration of Licence

3. 1. A licence for is valid from the date of purchase ('Licence Date') at the end of the relevant period in the below table:

Scope of Licence	Duration of Licence
Post on a website	12 months
Presentations	12 months
Books and journals	Lifetime of the edition in the language purchased

4. Acknowledgement

4. 1. The Licensor's permission must be acknowledged next to the Licenced Material in print. In electronic form, this acknowledgement must be visible at the same time as the figures/tables/illustrations or abstract, and must be hyperlinked to the journal/book's homepage. Our required acknowledgement format is in the Appendix below.

5. Restrictions on use

5. 1. Use of the Licensed Material may be permitted for incidental promotional use and minor editing privileges e.g. minor adaptations of single figures, changes of format, colour and/or style where the adaptation is credited as set out in Appendix 1 below. Any other changes including but not limited to, cropping, adapting, omitting material that affect the meaning, intention or moral rights of the author are strictly prohibited.

5. 2. You must not use any Licensed Material as part of any design or trademark.

5. 3. Licensed Material may be used in Open Access Publications (OAP) before publication by Springer Nature, but any Licensed Material must be removed from OAP sites prior to final publication.

6. Ownership of Rights

6. 1. Licensed Material remains the property of either Licensor or the relevant third party and any rights not explicitly granted herein are expressly reserved.

7. Warranty

IN NO EVENT SHALL LICENSOR BE LIABLE TO YOU OR ANY OTHER PARTY OR ANY OTHER PERSON OR FOR ANY SPECIAL, CONSEQUENTIAL, INCIDENTAL OR INDIRECT DAMAGES, HOWEVER CAUSED, ARISING OUT OF OR IN CONNECTION WITH THE DOWNLOADING, VIEWING OR USE OF THE MATERIALS REGARDLESS OF THE FORM OF ACTION, WHETHER FOR BREACH OF CONTRACT, BREACH OF WARRANTY, TORT, NEGLIGENCE, INFRINGEMENT OR OTHERWISE (INCLUDING, WITHOUT LIMITATION, DAMAGES BASED ON LOSS OF PROFITS, DATA, FILES, USE, BUSINESS OPPORTUNITY OR CLAIMS OF THIRD PARTIES), AND
WHETHER OR NOT THE PARTY HAS BEEN ADVISED OF THE POSSIBILITY OF SUCH DAMAGES. THIS LIMITATION SHALL APPLY NOTWITHSTANDING ANY FAILURE OF ESSENTIAL PURPOSE OF ANY LIMITED REMEDY PROVIDED HEREIN.

8. Limitations

8. 1. *BOOKS ONLY:*Where **'reuse in a dissertation/thesis'** has been selected the following terms apply: Print rights of the final author's accepted manuscript (for clarity, NOT the published version) for up to 100 copies, electronic rights for use only on a personal website or institutional repository as defined by the Sherpa guideline (www.sherpa.ac.uk/romeo/).

9. Termination and Cancellation

9. 1. Licences will expire after the period shown in Clause 3 (above).

9. 2. Licensee reserves the right to terminate the Licence in the event that payment is not received in full or if there has been a breach of this agreement by you.

Appendix 1 — Acknowledgements:

For Journal Content:
Reprinted by permission from [**the Licensor**]: [**Journal Publisher** (e.g. Nature/Springer/Palgrave)] [**JOURNAL NAME**] [**REFERENCE CITATION** (Article name, Author(s) Name), [**COPYRIGHT**] (year of publication)

For **Advance Online Publication papers:**
Reprinted by permission from [**the Licensor**]: [**Journal Publisher** (e.g. Nature/Springer/Palgrave)] [**JOURNAL NAME**] [**REFERENCE CITATION** (Article name, Author(s) Name), [**COPYRIGHT**] (year of publication), advance online publication, day month year (doi: 10.1038/sj.[JOURNAL ACRONYM].)

For Adaptations/Translations:
Adapted/Translated by permission from [**the Licensor**]: [**Journal Publisher** (e.g. Nature/Springer/Palgrave)] [**JOURNAL NAME**] [**REFERENCE CITATION** (Article name, Author(s) Name), [**COPYRIGHT**] (year of publication)

Note: For any republication from the British Journal of Cancer, the following credit line style applies:

Reprinted/adapted/translated by permission from [**the Licensor**]: on behalf of Cancer Research UK: : [**Journal Publisher** (e.g. Nature/Springer/Palgrave)] [**JOURNAL NAME**] [**REFERENCE CITATION** (Article name, Author(s) Name), [**COPYRIGHT**] (year of publication)

For **Advance Online Publication** papers:
Reprinted by permission from The [**the Licensor**]: on behalf of Cancer Research UK: [**Journal Publisher** (e.g. Nature/Springer /Palgrave)] [**JOURNAL NAME**] [**REFERENCE CITATION** (Article name, Author(s) Name), [**COPYRIGHT**] (year of publication), advance online publication, day month year (doi: 10.1038/sj. [JOURNAL ACRONYM])

For Book content:
Reprinted/adapted by permission from [**the Licensor**]: [**Book Publisher** (e.g. Palgrave Macmillan, Springer etc) [**Book Title**] by [**Book author**(s)] [**COPYRIGHT**] (year of publication)

Other Conditions: Reuse cover in dissertation.

Version 1.2

G.6   Permission to reprint figure 1 of [6]

G.6   Permission to reprint figure 1 of [6]

ELSEVIER LICENSE
TERMS AND CONDITIONS

Aug 28, 2019

This Agreement between Thierry Fredrich ("You") and Elsevier ("Elsevier") consists of your license details and the terms and conditions provided by Elsevier and Copyright Clearance Center.

License Number	4657561175790
License date	Aug 28, 2019
Licensed Content Publisher	Elsevier
Licensed Content Publication	Physics Reports
Licensed Content Title	Rheological properties of the Eukaryotic cell cytoskeleton
Licensed Content Author	Pramod A. Pullarkat,Pablo A. Fernández,Albrecht Ott
Licensed Content Date	Sep 1, 2007
Licensed Content Volume	449
Licensed Content Issue	1-3
Licensed Content Pages	25
Start Page	29
End Page	53
Type of Use	reuse in a thesis/dissertation
Portion	figures/tables/illustrations
Number of figures/tables /illustrations	1
Format	both print and electronic
Are you the author of this Elsevier article?	No
Will you be translating?	No
Original figure numbers	figure 1
Title of your thesis/dissertation	Computational studies of vascularized tumors
Publisher of new work	Saarland University
Expected completion date	Jan 2020
Estimated size (number of pages)	1
Requestor Location	Thierry Fredrich Campus E2.6 -- 4.27 Saarbrücken, 66125 Germany Attn: Thierry Fredrich
Publisher Tax ID	GB 494 6272 12
Total	0.00 USD

INTRODUCTION

1. The publisher for this copyrighted material is Elsevier. By clicking "accept" in connection with completing this licensing transaction, you agree that the following terms and conditions apply to this transaction (along with the Billing and Payment terms and conditions established by Copyright Clearance Center, Inc. ("CCC"), at the time that you opened your Rightslink account and that are available at any time at http://myaccount.copyright.com).

GENERAL TERMS

2. Elsevier hereby grants you permission to reproduce the aforementioned material subject to the terms and conditions indicated.

3. Acknowledgement: If any part of the material to be used (for example, figures) has appeared in our publication with credit or acknowledgement to another source, permission must also be sought from that source. If such permission is not obtained then that material may not be included in your publication/copies. Suitable acknowledgement to the source must be made, either as a footnote or in a reference list at the end of your publication, as follows:

"Reprinted from Publication title, Vol /edition number, Author(s), Title of article / title of chapter, Pages No., Copyright (Year), with permission from Elsevier [OR APPLICABLE SOCIETY COPYRIGHT OWNER]." Also Lancet special credit - "Reprinted from The Lancet, Vol. number, Author(s), Title of article, Pages No., Copyright (Year), with permission from Elsevier."

4. Reproduction of this material is confined to the purpose and/or media for which permission is hereby given.

5. Altering/Modifying Material: Not Permitted. However figures and illustrations may be altered/adapted minimally to serve your work. Any other abbreviations, additions, deletions and/or any other alterations shall be made only with prior written authorization of Elsevier Ltd. (Please contact Elsevier at permissions@elsevier.com). No modifications can be made to any Lancet figures/tables and they must be reproduced in full.

6. If the permission fee for the requested use of our material is waived in this instance, please be advised that your future requests for Elsevier materials may attract a fee.

7. Reservation of Rights: Publisher reserves all rights not specifically granted in the combination of (i) the license details provided by you and accepted in the course of this licensing transaction, (ii) these terms and conditions and (iii) CCC's Billing and Payment terms and conditions.

8. License Contingent Upon Payment: While you may exercise the rights licensed immediately upon issuance of the license at the end of the licensing process for the transaction, provided that you have disclosed complete and accurate details of your proposed use, no license is finally effective unless and until full payment is received from you (either by

publisher or by CCC) as provided in CCC's Billing and Payment terms and conditions. If full payment is not received on a timely basis, then any license preliminarily granted shall be deemed automatically revoked and shall be void as if never granted. Further, in the event that you breach any of these terms and conditions or any of CCC's Billing and Payment terms and conditions, the license is automatically revoked and shall be void as if never granted. Use of materials as described in a revoked license, as well as any use of the materials beyond the scope of an unrevoked license, may constitute copyright infringement and publisher reserves the right to take any and all action to protect its copyright in the materials.

9. Warranties: Publisher makes no representations or warranties with respect to the licensed material.

10. Indemnity: You hereby indemnify and agree to hold harmless publisher and CCC, and their respective officers, directors, employees and agents, from and against any and all claims arising out of your use of the licensed material other than as specifically authorized pursuant to this license.

11. No Transfer of License: This license is personal to you and may not be sublicensed, assigned, or transferred by you to any other person without publisher's written permission.

12. No Amendment Except in Writing: This license may not be amended except in a writing signed by both parties (or, in the case of publisher, by CCC on publisher's behalf).

13. Objection to Contrary Terms: Publisher hereby objects to any terms contained in any purchase order, acknowledgment, check endorsement or other writing prepared by you, which terms are inconsistent with these terms and conditions or CCC's Billing and Payment terms and conditions. These terms and conditions, together with CCC's Billing and Payment terms and conditions (which are incorporated herein), comprise the entire agreement between you and publisher (and CCC) concerning this licensing transaction. In the event of any conflict between your obligations established by these terms and conditions and those established by CCC's Billing and Payment terms and conditions, these terms and conditions shall control.

14. Revocation: Elsevier or Copyright Clearance Center may deny the permissions described in this License at their sole discretion, for any reason or no reason, with a full refund payable to you. Notice of such denial will be made using the contact information provided by you. Failure to receive such notice will not alter or invalidate the denial. In no event will Elsevier or Copyright Clearance Center be responsible or liable for any costs, expenses or damage incurred by you as a result of a denial of your permission request, other than a refund of the amount(s) paid by you to Elsevier and/or Copyright Clearance Center for denied permissions.

LIMITED LICENSE

The following terms and conditions apply only to specific license types:

15. **Translation**: This permission is granted for non-exclusive world **English** rights only unless your license was granted for translation rights. If you licensed translation rights you may only translate this content into the languages you requested. A professional translator must perform all translations and reproduce the content word for word preserving the integrity of the article.

16. **Posting licensed content on any Website**: The following terms and conditions apply as follows: Licensing material from an Elsevier journal: All content posted to the web site must maintain the copyright information line on the bottom of each image; A hyper-text must be included to the Homepage of the journal from which you are licensing at http://www.sciencedirect.com/science/journal/xxxxx or the Elsevier homepage for books at http://www.elsevier.com; Central Storage: This license does not include permission for a scanned version of the material to be stored in a central repository such as that provided by Heron/XanEdu.

Licensing material from an Elsevier book: A hyper-text link must be included to the Elsevier homepage at http://www.elsevier.com . All content posted to the web site must maintain the copyright information line on the bottom of each image.

Posting licensed content on Electronic reserve: In addition to the above the following clauses are applicable: The web site must be password-protected and made available only to bona fide students registered on a relevant course. This permission is granted for 1 year only. You may obtain a new license for future website posting.

17. **For journal authors:** the following clauses are applicable in addition to the above:

Preprints:

A preprint is an author's own write-up of research results and analysis, it has not been peer-reviewed, nor has it had any other value added to it by a publisher (such as formatting, copyright, technical enhancement etc.).

Authors can share their preprints anywhere at any time. Preprints should not be added to or enhanced in any way in order to appear more like, or to substitute for, the final versions of articles however authors can update their preprints on arXiv or RePEc with their Accepted Author Manuscript (see below).

If accepted for publication, we encourage authors to link from the preprint to their formal publication via its DOI. Millions of researchers have access to the formal publications on ScienceDirect, and so links will help users to find, access, cite and use the best available version. Please note that Cell Press, The Lancet and some society-owned have different preprint policies. Information on these policies is available on the journal homepage.

Accepted Author Manuscripts: An accepted author manuscript is the manuscript of an article that has been accepted for publication and which typically includes author-incorporated changes suggested during submission, peer review and editor-author communications.
Authors can share their accepted author manuscript:

- immediately
    - via their non-commercial person homepage or blog
    - by updating a preprint in arXiv or RePEc with the accepted manuscript
    - via their research institute or institutional repository for internal institutional uses or as part of an invitation-only research collaboration work-group
    - directly by providing copies to their students or to research collaborators for their personal use
    - for private scholarly sharing as part of an invitation-only work group on commercial sites with which Elsevier has an agreement
- After the embargo period
    - via non-commercial hosting platforms such as their institutional repository
    - via commercial sites with which Elsevier has an agreement

In all cases accepted manuscripts should:

- link to the formal publication via its DOI
- bear a CC-BY-NC-ND license - this is easy to do
- if aggregated with other manuscripts, for example in a repository or other site, be shared in alignment with our hosting policy not be added to or enhanced in any way to appear more like, or to substitute for, the published journal article.

Published journal article (JPA): A published journal article (PJA) is the definitive final record of published research that appears or will appear in the journal and embodies all value-adding publishing activities including peer review co-ordination, copy-editing, formatting, (if relevant) pagination and online enrichment.
Policies for sharing publishing journal articles differ for subscription and gold open access articles:
<u>**Subscription Articles:**</u> If you are an author, please share a link to your article rather than the full-text. Millions of researchers have access to the formal publications on ScienceDirect, and so links will help your users to find, access, cite, and use the best available version.
Theses and dissertations which contain embedded PJAs as part of the formal submission can be posted publicly by the awarding institution with DOI links back to the formal publications on ScienceDirect.
If you are affiliated with a library that subscribes to ScienceDirect you

have additional private sharing rights for others' research accessed under that agreement. This includes use for classroom teaching and internal training at the institution (including use in course packs and courseware programs), and inclusion of the article for grant funding purposes.

Gold Open Access Articles: May be shared according to the author-selected end-user license and should contain a [CrossMark logo](#), the end user license, and a DOI link to the formal publication on ScienceDirect. Please refer to Elsevier's [posting policy](#) for further information.

18. **For book authors** the following clauses are applicable in addition to the above: Authors are permitted to place a brief summary of their work online only. You are not allowed to download and post the published electronic version of your chapter, nor may you scan the printed edition to create an electronic version. **Posting to a repository:** Authors are permitted to post a summary of their chapter only in their institution's repository.

19. **Thesis/Dissertation**: If your license is for use in a thesis/dissertation your thesis may be submitted to your institution in either print or electronic form. Should your thesis be published commercially, please reapply for permission. These requirements include permission for the Library and Archives of Canada to supply single copies, on demand, of the complete thesis and include permission for Proquest/UMI to supply single copies, on demand, of the complete thesis. Should your thesis be published commercially, please reapply for permission. Theses and dissertations which contain embedded PJAs as part of the formal submission can be posted publicly by the awarding institution with DOI links back to the formal publications on ScienceDirect.

Elsevier Open Access Terms and Conditions
You can publish open access with Elsevier in hundreds of open access journals or in nearly 2000 established subscription journals that support open access publishing. Permitted third party re-use of these open access articles is defined by the author's choice of Creative Commons user license. See our [open access license policy](#) for more information.

Terms & Conditions applicable to all Open Access articles published with Elsevier:
Any reuse of the article must not represent the author as endorsing the adaptation of the article nor should the article be modified in such a way as to damage the author's honour or reputation. If any changes have been made, such changes must be clearly indicated.
The author(s) must be appropriately credited and we ask that you include the end user license and a DOI link to the formal publication on ScienceDirect.
If any part of the material to be used (for example, figures) has appeared in our publication with credit or acknowledgement to another source it

is the responsibility of the user to ensure their reuse complies with the terms and conditions determined by the rights holder.

Additional Terms & Conditions applicable to each Creative Commons user license:

CC BY: The CC-BY license allows users to copy, to create extracts, abstracts and new works from the Article, to alter and revise the Article and to make commercial use of the Article (including reuse and/or resale of the Article by commercial entities), provided the user gives appropriate credit (with a link to the formal publication through the relevant DOI), provides a link to the license, indicates if changes were made and the licensor is not represented as endorsing the use made of the work. The full details of the license are available at http://creativecommons.org/licenses/by/4.0.

CC BY NC SA: The CC BY-NC-SA license allows users to copy, to create extracts, abstracts and new works from the Article, to alter and revise the Article, provided this is not done for commercial purposes, and that the user gives appropriate credit (with a link to the formal publication through the relevant DOI), provides a link to the license, indicates if changes were made and the licensor is not represented as endorsing the use made of the work. Further, any new works must be made available on the same conditions. The full details of the license are available at http://creativecommons.org/licenses/by-nc-sa/4.0.

CC BY NC ND: The CC BY-NC-ND license allows users to copy and distribute the Article, provided this is not done for commercial purposes and further does not permit distribution of the Article if it is changed or edited in any way, and provided the user gives appropriate credit (with a link to the formal publication through the relevant DOI), provides a link to the license, and that the licensor is not represented as endorsing the use made of the work. The full details of the license are available at http://creativecommons.org/licenses/by-nc-nd/4.0. Any commercial reuse of Open Access articles published with a CC BY NC SA or CC BY NC ND license requires permission from Elsevier and will be subject to a fee. Commercial reuse includes:

- Associating advertising with the full text of the Article
- Charging fees for document delivery or access
- Article aggregation
- Systematic distribution via e-mail lists or share buttons

Posting or linking by commercial companies for use by customers of those companies.

20. **Other Conditions**:

v1.9

G.7   Permission to reprint figure 5 and 8 of [7]

G.7   Permission to reprint figure 5 and 8 of [7]

IOP Publishing LICENSE
TERMS AND CONDITIONS

Aug 29, 2019

This is a License Agreement between Thierry Fredrich ("You") and IOP Publishing ("IOP Publishing") provided by Copyright Clearance Center ("CCC"). The license consists of your order details, the terms and conditions provided by IOP Publishing, and the payment terms and conditions.

All payments must be made in full to CCC. For payment instructions, please see information listed at the bottom of this form.

License Number	4658150018877
License date	Aug 29, 2019
Licensed content publisher	IOP Publishing
Licensed content title	Reports on Progress in Physics
Licensed content date	Jan 1, 1934
Type of Use	Thesis/Dissertation
Requestor type	Academic institution
Format	Print, Electronic
Portion	image/photo
Number of images/photos requested	2
The requesting person/organization is:	Thierry Fredrich
Title or numeric reference of the portion(s)	Figure 5 and 8
Title of the article or chapter the portion is from	N/A
Editor of portion(s)	N/A
Author of portion(s)	N/A
Volume of serial or monograph.	N/A
Page range of the portion	page 8 and 10
Publication date of portion	N/A
Rights for	Main product
Duration of use	Life of current and all future editions
Creation of copies for the disabled	no
With minor editing privileges	no
For distribution to	Worldwide
In the following language(s)	Original language of publication
With incidental promotional use	no

The lifetime unit quantity of new product	Up to 499
Title	Computational studies of vascularized tumors
Institution name	Saarland University
Expected presentation date	Jan 2020
Total (may include CCC user fee)	0.00 USD
Terms and Conditions	

TERMS AND CONDITIONS
The following terms are individual to this publisher:

These special terms and conditions are in addition to the standard terms and conditions for CCC's Republication Service and, together with those standard terms and conditions, govern the use of the Works.

As the "User" you will make all reasonable efforts to contact the author(s) of the article which the Work is to be reused from, to seek consent for your intended use. Contacting one author who is acting expressly as authorised agent for their co-author(s) is acceptable.

User will reproduce the following wording prominently alongside the Work:

- the source of the Work, including author, article title, title of journal, volume number, issue number (if relevant), page range (or first page if this is the only information available) and date of first publication. This information can be contained in a footnote or reference note; and
- a link back to the article (via DOI); and
- if practicable, and IN ALL CASES for new works published under any of the Creative Commons licences, the words "© IOP Publishing. Reproduced with permission. All rights reserved"

Without the express permission of the author(s) and the Rightsholder of the article from which the Work is to be reused, User shall not use it in any way which, in the opinion of the Rightsholder, could: (i) distort or alter the author(s)' original intention(s) and meaning; (ii) be prejudicial to the honour or reputation of the author(s); and/or (iii) imply endorsement by the author(s) and/or the Rightsholder.

This licence does not apply to any article which is credited to another source and which does not have the copyright line '© IOP Publishing Ltd'. User must check the copyright line of the article from which the Work is to be reused to check that IOP Publishing Ltd has all the necessary rights to be able to grant permission. User is solely responsible for identifying and obtaining separate licences and permissions from the copyright owner for reuse of any such third party material/figures which the Rightsholder is not the copyright owner of. The Rightsholder shall not reimburse any fees which User pays for a republication license for such third party content.

This licence does not apply to any material/figure which is credited to another source in the Rightsholder's publication or has been obtained from a third party. User must check the Version of Record of the article from which the Work is to be reused, to check whether any of the material in the Work is third party material. Third party citations and/or copyright notices and/or permissions statements may not be included in any other version of the article from which the Work is to be reused and so cannot be relied upon by the User. User is solely responsible for identifying and obtaining separate licences and permissions from the copyright owner for reuse of any such third party material/figures where the Rightsholder is not the copyright owner. The Rightsholder shall not reimburse any fees which User pays for a republication license for such third party content.

User and CCC acknowledge that the Rightsholder may, from time to time, make changes or additions to these special terms and conditions without express notification, provided that these shall not apply to permissions already secured and paid for by User prior to such change or addition.

User acknowledges that the Rightsholder (which includes companies within its group and third parties for whom it publishes its titles) may make use of personal data collected through the service in the course of their business.

If User is the author of the Work, User may automatically have the right to reuse it under the rights granted back when User transferred the copyright in the article to the Rightsholder. User should check the copyright form and the relevant author rights policy to check whether permission is required. If User is the author of the Work and does require permission for proposed reuse of the Work, User should select 'Author of requested content' as the Requestor Type. The Rightsholder shall not reimburse any fees which User pays for a republication license.

If User is the author of the article which User wishes to reuse in User's thesis or dissertation, the republication licence covers the right to include the Accepted Manuscript version (not the Version of Record) of the article. User must include citation details and, for online use, a link to the Version of Record of the article on the Rightsholder's website. User may need to obtain separate permission for any third party content included within the article. User must check this with the copyright owner of such third party content. User may not include the article in a thesis or dissertation which is published by ProQuest. Any other commercial use of User's thesis or dissertation containing the article would also need to be expressly notified in writing to the Rightsholder at the time of request and would require separate written permission from the Rightsholder.

User does not need to request permission for Work which has been published under a CC BY licence. User must check the Version of Record of the CC BY article from which the Work is to be reused, to check

whether any of the material in the Work is third party material and so not published under the CC BY licence. User is solely responsible for identifying and obtaining separate licences and permissions from the copyright owner for reuse of any such third party material/figures. The Rightsholder shall not reimburse any fees which User pays for such licences and permissions.

As well as CCC, the Rightsholder shall have the right to bring any legal action that it deems necessary to enforce its rights should it consider that the Work infringes those rights in any way.

For STM Signatories ONLY (as agreed as part of the STM Guidelines) Any licence granted for a particular edition of a Work will apply also to subsequent editions of it and for editions in other languages, provided such editions are for the Work as a whole in situ and do not involve the separate exploitation of the permitted illustrations or excerpts.

Other Terms and Conditions:
STANDARD TERMS AND CONDITIONS

1. Description of Service; Defined Terms. This Republication License enables the User to obtain licenses for republication of one or more copyrighted works as described in detail on the relevant Order Confirmation (the "Work(s)"). Copyright Clearance Center, Inc. ("CCC") grants licenses through the Service on behalf of the rightsholder identified on the Order Confirmation (the "Rightsholder"). "Republication", as used herein, generally means the inclusion of a Work, in whole or in part, in a new work or works, also as described on the Order Confirmation. "User", as used herein, means the person or entity making such republication.

2. The terms set forth in the relevant Order Confirmation, and any terms set by the Rightsholder with respect to a particular Work, govern the terms of use of Works in connection with the Service. By using the Service, the person transacting for a republication license on behalf of the User represents and warrants that he/she/it (a) has been duly authorized by the User to accept, and hereby does accept, all such terms and conditions on behalf of User, and (b) shall inform User of all such terms and conditions. In the event such person is a "freelancer" or other third party independent of User and CCC, such party shall be deemed jointly a "User" for purposes of these terms and conditions. In any event, User shall be deemed to have accepted and agreed to all such terms and conditions if User republishes the Work in any fashion.

3. Scope of License; Limitations and Obligations.

3.1 All Works and all rights therein, including copyright rights, remain the sole and exclusive property of the Rightsholder. The license created by the exchange of an Order Confirmation (and/or any invoice) and payment by User of the full amount set forth on that document includes only those rights expressly set forth in the Order Confirmation and in these terms and conditions, and conveys no other rights in the Work(s) to User. All rights not expressly granted are hereby reserved.

3.2 General Payment Terms: You may pay by credit card or through an account with us payable at the end of the month. If you and we agree that you may establish a standing account with CCC, then the following terms apply: Remit Payment to: Copyright Clearance Center, 29118 Network Place, Chicago, IL 60673-1291. Payments Due: Invoices are payable upon their delivery to you (or upon our notice to you that they are available to you for downloading). After 30 days, outstanding amounts will be subject to a service charge of 1-1/2% per month or, if less, the maximum rate allowed by applicable law. Unless otherwise specifically set forth in the Order Confirmation or in a separate written agreement signed by CCC, invoices are due and payable on "net 30" terms. While User may exercise the rights licensed immediately upon issuance of the Order Confirmation, the license is automatically revoked and is null and void, as if it had never been issued, if complete payment for the license is not received on a timely basis either from User directly or through a payment agent, such as a credit card company.

3.3 Unless otherwise provided in the Order Confirmation, any grant of rights to User (i) is "one-time" (including the editions and product family specified in the license), (ii) is non-exclusive and non-transferable and (iii) is subject to any and all limitations and restrictions (such as, but not limited to, limitations on duration of use or circulation) included in the Order Confirmation or invoice and/or in these terms and conditions. Upon completion of the licensed use, User shall either secure a new permission for further use of the Work(s) or immediately cease any new use of the Work(s) and shall render inaccessible (such as by deleting or by removing or severing links or other locators) any further copies of the Work (except for copies printed on paper in accordance with this license and still in User's stock at the end of such period).

3.4 In the event that the material for which a republication license is sought includes third party materials (such as photographs, illustrations, graphs, inserts and similar materials) which are identified in such material as having been used by permission, User is responsible for identifying, and seeking separate licenses (under this Service or otherwise) for, any of such third party materials; without a separate license, such third party materials may not be used.

3.5 Use of proper copyright notice for a Work is required as a condition of any license granted under the Service. Unless otherwise provided in the Order Confirmation, a proper copyright notice will read substantially as follows: "Republished with permission of [Rightsholder's name], from [Work's title, author, volume, edition number and year of copyright]; permission conveyed through Copyright Clearance Center, Inc. " Such notice must be provided in a reasonably legible font size and must be placed either immediately adjacent to the Work as used (for example, as part of a by-line or footnote but not as a separate electronic link) or in the place where substantially all other credits or notices for the new work containing the republished Work are located. Failure to include the

required notice results in loss to the Rightsholder and CCC, and the User shall be liable to pay liquidated damages for each such failure equal to twice the use fee specified in the Order Confirmation, in addition to the use fee itself and any other fees and charges specified. 3.6 User may only make alterations to the Work if and as expressly set forth in the Order Confirmation. No Work may be used in any way that is defamatory, violates the rights of third parties (including such third parties' rights of copyright, privacy, publicity, or other tangible or intangible property), or is otherwise illegal, sexually explicit or obscene. In addition, User may not conjoin a Work with any other material that may result in damage to the reputation of the Rightsholder. User agrees to inform CCC if it becomes aware of any infringement of any rights in a Work and to cooperate with any reasonable request of CCC or the Rightsholder in connection therewith.

4. Indemnity. User hereby indemnifies and agrees to defend the Rightsholder and CCC, and their respective employees and directors, against all claims, liability, damages, costs and expenses, including legal fees and expenses, arising out of any use of a Work beyond the scope of the rights granted herein, or any use of a Work which has been altered in any unauthorized way by User, including claims of defamation or infringement of rights of copyright, publicity, privacy or other tangible or intangible property.

5. Limitation of Liability. UNDER NO CIRCUMSTANCES WILL CCC OR THE RIGHTSHOLDER BE LIABLE FOR ANY DIRECT, INDIRECT, CONSEQUENTIAL OR INCIDENTAL DAMAGES (INCLUDING WITHOUT LIMITATION DAMAGES FOR LOSS OF BUSINESS PROFITS OR INFORMATION, OR FOR BUSINESS INTERRUPTION) ARISING OUT OF THE USE OR INABILITY TO USE A WORK, EVEN IF ONE OF THEM HAS BEEN ADVISED OF THE POSSIBILITY OF SUCH DAMAGES. In any event, the total liability of the Rightsholder and CCC (including their respective employees and directors) shall not exceed the total amount actually paid by User for this license. User assumes full liability for the actions and omissions of its principals, employees, agents, affiliates, successors and assigns.

6. Limited Warranties. THE WORK(S) AND RIGHT(S) ARE PROVIDED "AS IS". CCC HAS THE RIGHT TO GRANT TO USER THE RIGHTS GRANTED IN THE ORDER CONFIRMATION DOCUMENT. CCC AND THE RIGHTSHOLDER DISCLAIM ALL OTHER WARRANTIES RELATING TO THE WORK(S) AND RIGHT(S), EITHER EXPRESS OR IMPLIED, INCLUDING WITHOUT LIMITATION IMPLIED WARRANTIES OF MERCHANTABILITY OR FITNESS FOR A PARTICULAR PURPOSE. ADDITIONAL RIGHTS MAY BE REQUIRED TO USE ILLUSTRATIONS, GRAPHS, PHOTOGRAPHS, ABSTRACTS, INSERTS OR OTHER PORTIONS OF THE WORK (AS OPPOSED TO THE ENTIRE WORK) IN A MANNER CONTEMPLATED BY USER; USER UNDERSTANDS AND AGREES THAT NEITHER CCC NOR THE RIGHTSHOLDER MAY HAVE

SUCH ADDITIONAL RIGHTS TO GRANT.

7. Effect of Breach. Any failure by User to pay any amount when due, or any use by User of a Work beyond the scope of the license set forth in the Order Confirmation and/or these terms and conditions, shall be a material breach of the license created by the Order Confirmation and these terms and conditions. Any breach not cured within 30 days of written notice thereof shall result in immediate termination of such license without further notice. Any unauthorized (but licensable) use of a Work that is terminated immediately upon notice thereof may be liquidated by payment of the Rightsholder's ordinary license price therefor; any unauthorized (and unlicensable) use that is not terminated immediately for any reason (including, for example, because materials containing the Work cannot reasonably be recalled) will be subject to all remedies available at law or in equity, but in no event to a payment of less than three times the Rightsholder's ordinary license price for the most closely analogous licensable use plus Rightsholder's and/or CCC's costs and expenses incurred in collecting such payment.

8. **Miscellaneous.**

8.1 User acknowledges that CCC may, from time to time, make changes or additions to the Service or to these terms and conditions, and CCC reserves the right to send notice to the User by electronic mail or otherwise for the purposes of notifying User of such changes or additions; provided that any such changes or additions shall not apply to permissions already secured and paid for.

8.2 Use of User-related information collected through the Service is governed by CCC's privacy policy, available online here: http://www.copyright.com/content/cc3/en/tools/footer/privacypolicy.html.

8.3 The licensing transaction described in the Order Confirmation is personal to User. Therefore, User may not assign or transfer to any other person (whether a natural person or an organization of any kind) the license created by the Order Confirmation and these terms and conditions or any rights granted hereunder; provided, however, that User may assign such license in its entirety on written notice to CCC in the event of a transfer of all or substantially all of User's rights in the new material which includes the Work(s) licensed under this Service.

8.4 No amendment or waiver of any terms is binding unless set forth in writing and signed by the parties. The Rightsholder and CCC hereby object to any terms contained in any writing prepared by the User or its principals, employees, agents or affiliates and purporting to govern or otherwise relate to the licensing transaction described in the Order Confirmation, which terms are in any way inconsistent with any terms set forth in the Order Confirmation and/or in these terms and conditions or CCC's standard operating procedures, whether such writing is prepared prior to, simultaneously with or subsequent to the Order Confirmation, and whether such writing appears on a copy of the Order Confirmation or in a separate instrument.

Appendix H

Curriculum Vitae

- born in 1985

- 2005 Abitur (TGI), Georg-Kerschensteiner-Schule, Müllheim

- 2006 - 2008, Undergraduate Studies in Physics, Math and Computer Science, University of Freiburg

- 2009 - 2011, Graduate Studies in Physics and Math, University of Freiburg

- 2012 - 2013, Diploma Thesis, "Statistical aspects of the Global Tracking algorithm (https://freidok.uni-freiburg.de/data/149366)", Medical Physics Freiburg, Prof. Dr. Dr. h.c. Jürgen Hennig

- 2014 - 2019, PhD candidate, "Computational studies of vascularized tumors", Prof. Dr. Dr. h.c. Heiko Rieger

Summary in English

Cancer is a hard problem touching numerous branches of life science. One reason for the complexity of cancer is that tumors act across many different time and length scales ranging from the subcellular to the macroscopic level. Modern sciences still lack an integral understanding of cancer, however in recent years, increasing computational power enabled computational models to accompany and support conventional medical and biological methods bridging the scales from micro to macro. Here I report a multiscale computational model simulating the progression of solid tumors comprising the vasculature mimicked by artificial arterio-venous blood vessel networks. I present a numerical optimization procedure to determine radii of blood vessels in an artificial microcirculation based on physiological stimuli independently of Murray's law. Comprising the blood vessels, the reported model enables the inspection of blood vessel remodeling dynamics (angiogenesis, vaso-dilation, vessel regression and collapse) during tumor growth. We successfully applied the method to simulated tumor blood vessel networks guided by optical mammography data. In subsequent model development, I included cellular details into the method enabling a computational study of the tumor microenvironment at cellular resolution. I found that small vascularized tumors at the angiogenic switch exhibit a large ecological niche diversity resulting in high evolutionary pressure favoring the colonal selecion hypothesis.

Zusammenfassung in Deutsch (Summary in German)

Krebs ist ein schwieriges Thema und tritt in zahlreichen Gebieten auf. Ein Grund für die Komplexität des Tumorwachstums sind die unterschiedlichen Zeit- und Längenskalen. In der aktuellen Forschung fehlt immernoch ein ganzheitliches Verständnis von Krebs, obwohl die computergestützten Methoden in den vergangenen Jahren die konventionellen Methoden der Medizin und der Biologie erweitern und unterstützen. Damit wird die Kluft zwischen subzellulären und makroskopischen Prozessen bereits verringert. In der vorliegenden Arbeit dokumentiere ich ein computergestütztes Verfahren, welches das Tumorwachstum auf mehreren Skalen simuliert. Insbesondere wird das Blutgefäßsystem durch künstliche Gefäße nachgeahmt. Es wurde ein numerisches Optimierungsverfahren zur Bestimmung der Gefäßradien eines künstlichen Blutkreislaufes entwickelt, welches auf physiologischen Reizen basiert und unabhängig von Murray's Gesetz ist. Da das beschriebene Verfahren zur Simulation von Tumoren Blutgefäße beinhaltet, kann die Umbildung des Gefäßbaumes während des Tumorwachstums untersucht werden. Das Modell wurde erfolgreich mit krankhaften Gefäßsystemen verglichen. In der darauffolgenden Weiterentwicklung des Modells berücksichtigte ich zelluläre Feinheiten, die es mir erlaubten das Mikromilieu in zellulärer Auflösung zu untersuchen. Meine Resultate zeigen, dass bereits kleine Tumore eine hohe ökologische Vielfalt besitzen, was den Selektionsdruck erhöht und damit die Klon-Selektionstheorie begünstigt.

Acknowledgments

I thank

- Prof. Dr. Dr. h.c. Heiko Rieger for the opportunity to conduct the documented research independently. In particular I thank him for useful discussions, constructive criticism and financial support enabling my contributions to the scientific community by participating at (inter) national conferences and publishing in peer-reviewed journals.

- my wife Sabrina Fredrich for her relentless support at all times and for giving birth to our dear son.

- my grandfather Hans-Peter Kiefer for his encouragement and his motivation engaging my studies at university level.

- my family and my parents-in-law for their support during my PhD studies.

- Mrs. Susanne Balzert for her help with bureaucracy and all the administrative issues.

- Prof. Dr. Edoardo Milotti for hosting me in Trieste during the Barcolana in 2017.

- Dr. Michael Welter for teaching me *C++* and *Python* at its finest.

- Dr. Karsten Schwarz for showing me the "Nauwieser Viertel" and proofreading this dissertation.

- Benjamin Bogner for sharing the office in a pleasant way, for useful discussions and for receiving my parcels during the past six years.

- Dr. Anne Hafner and Barbara Schmidt for proofreading this dissertation.

- Dr. Adam Wysocki for sharing his scientific insights.

- Robin Jose, Erik Maikranz and Gina Monzon for joining the Cuban German Graduate School 2018.

- Olaf Leidinger for his efforts regarding the "lusi"-cluster at Saarland University.

- Ilaria Maccari for telling me the trust about German coffee.

- Dr. Benjamin Blaß, Dr. Martin Peglow, Dr. Astrid Niederle, Christian Thome, André Winter, Johannes Sicks, Ivan Hornak for all the nice discussions during our common lunch breaks.